Up- and Down- Conversion in Rare Earth-Doped Fluoride Crystalline Materials for Photovoltaic Applications

Zur Erlangung des akademischen Grades eines

DOKTORS DER INGENIEURWISSENSCHAFTEN (Dr.-Ing.)

von der KIT-Fakultät für Maschinenbau des

Karlsruher Instituts für Technologie (KIT)

angenommene

DISSERTATION

von

M. Sc. Eduard Madirov

Tag der mündlichen Prüfung:	16.05.2024
Hauptreferent:	Prof. Dr. Alexander Nesterov-Müller
Korreferenten:	Prof. Dr. Martin Dienwiebel
	Prof. Dr. Bryce S. Richards

Kurzfassung

Die Nachfrage nach erneuerbaren Energien steigt jedes Jahr. Dazu gehören Windkraft, Wasserkraft, Wellenkraft und viele andere, wobei Solarenergie eine der zugänglichsten Quellen für grüne Energie ist. Um Solarenergie erschwinglicher zu machen, muss die Effizienz von Solarzellen weiter verbessert werden. Silizium-Solarzellen, die den Markt dominieren, reagieren am empfindlichsten im nahen Infrarot- und sichtbaren Teil des solaren Spektrums und sind unempfindlich gegenüber dem ultravioletten Teil. Daher sollte der ultraviolette Teil des Spektrums durch einen Prozess namens Downshifting in das Infrarote umgewandelt werden.

Perowskit-Solarzellen sind eine alternative Technologie, die im ultravioletten und sichtbaren Teil des Spektrums anspricht, aber unempfindlich gegenüber dem Infrarotanteil der Solarradiation ist. Um die Effizienz zu steigern, ist eine Umwandlung vom Infraroten zum sichtbaren Teil des Spektrums erforderlich. Dies ist durch einen Prozess namens Upconversion möglich.

Das Ziel dieser Arbeit ist es, neue spektrale Umwandlungsmaterialien zu untersuchen - BaF_2- und PbF_2-Kristalle, dotiert mit Er^{3+} und Yb^{3+} als Upconversion-Materialien sowie BaF_2-Kristalle, dotiert mit Er^{3+} und YF_3-Partikeln, dotiert mit Ce^{3+} und Yb^{3+}, als Downshifting-Materialien. Alle Materialien werden in einem Mehrkanal-Graphittiegel in einem Vakuumofen synthetisiert. Die Dotierungskonzentrationsreihe ermöglicht die Bestimmung der chemischen Zusammensetzungen, die die höchste Umwandlungseffizienz ergeben. Diese wird durch absolute Photolumineszenzquantenausbeutemessungen bestimmt, die mit einem Aufbau um eine Integrationskugel durchgeführt werden.

Im Fall der Upconversion-Materialien wird die Quantenausbeute über einen weiten Intensitätsbereich (0.1 - 350 W/cm^2) der 976-nm-Anregung studiert. Es wird entdeckt, dass die höchste Upconversion-Quantenausbeute in BaF_2 mit 2 Mol% Er^{3+} und 3 Mol% Yb^{3+} bei einer Anregungsintensität von 490 W/cm^2 gefunden wird. Um die Grenzen des Upconversion-Prozesses zu finden, werden die Quantenausbeutewerte

unter direkter Anregung einiger höher liegender Zustände der Er3+-Ionen ebenfalls untersucht. Diese Ergebnisse ermöglichen die Analyse der Energiemigration zwischen den Dotierionen sowie der Populationswege der angeregten Zustände. Einer der mit Er^{3+} und Yb^{3+} dotierten BaF_2-Kristalle wird dann mit einer Perowskit-Solarzelle kombiniert, und der Anstieg des Kurzschlussstroms aufgrund der Upconversion wird analysiert.

Bei der Untersuchung der Downshifting-Materialien wird festgestellt, dass BaF_2-Kristalle im Bereich von 1 - 12 Mol% Quantenausbeutewerte von über 100% und bis zu 153% erreichen können. Um zu untersuchen, wie sich dieser Effekt auf die Leistung eines photovoltaischen Geräts auswirken kann, wird ein Kristall mit einer Ge-Photodiode kombiniert und der Anstieg des Kurzschlussstroms aufgrund der spektralen Umwandlung wird analysiert.

Im Fall von YF_3-Pulvern, dotiert mit Ce^{3+} und Yb^{3+}, wird der Energieübertrag zwischen den Dotantionen untersucht, und es wird festgestellt, dass der Ladungstransfer für den Prozess verantwortlich ist. Die höchste beobachtete Quantenausbeute beträgt nur 0.91%.

Die Verwendung der mit Er^{3+} und Yb^{3+} dotierten SrF_2-Kristalle als Referenz für relative Quantenausbeutemessungen wird ebenfalls untersucht. Es wird mit $NaYF_4$:18%Yb^{3+}2%Er^{3+}@CaF_2 -Nanopartikeln getestet, und es wird eine gute Übereinstimmung zwischen absoluten und relativen Messungen erzielt. Darüber hinaus werden Peptide als vielversprechende neue Gastgeber für die Ionen der Seltenen Erden angeboten, und einige Vorversuche werden durchgeführt.

Zusammenfassend präsentiert diese Arbeit neue spektrale Umwandlungsmaterialien. Einige mögliche Anwendungen werden getestet, und die Ergebnisse zeigen, dass die Materialien in vielen Bereichen von Forschung und Industrie nützlich sein können.

Contents

List of Abbreviations

AD	Acceptor-Donor
CPD	Critical Power Density
CT	Charge Transfer
DA	Donor-Acceptor
DC	Down-Conversion
DD	Donor-Donor
DS	Down-Shifting
ED	Electric Dipole
EQ	Electric Quadrupole
EQE	External Quantum Efficiency
ESA	Excited State Absorption
ET	Energy Transfer
ETU	Energy Transfer Up-Conversion
FRET	Förster Resonant Energy Transfer
GSA	Ground State Absorption
IR	Infrared
JO	Judd-Ofelt
MD	Magnetic Dipole
MQ	Magnetic Quadrupole
ND	Neutral Density
NIR	Near Infrared
PLQY	Photoluminescence Quantum Yield
QC	Quntum-Cutting
R/G	Red-To-Green
SC	Short-Circuit
UC	Up-Conversion
UV	Ultraviolet
Vis	Visible
WDXRF	Wavelength Dispersive X-Ray Fluorescence Spectroscopy

Acknowledgements

I would like to express my deepest gratitude to my supervisor, Alexander Nesterov-Muller, for his mentorship, and new exciting research opportunities that unexpectedly opened towards the end of my work.

I am grateful to the Karlsruhe Institute of Technology for providing the resources and environment conducive to academic research. I would like to thank the Institute of Microstructure Technology and the Nanophotonics for Energy group. I would like to express my gratitude to Prof. Dr Bryce S. Richards, who welcomed me to the group first during my fellowship and then as an employee of the institute. His expertise and sense of humour are essential to the success of the project.

I would like to thank Dr Andrey Turshatov, who was the person most involved in my daily work. Discussing the results helped to identify the most important features of the research. His guidance and support have shaped the current work in many ways.

I would like to thank Dr Dmitry Busko, who was always willing to share his knowledge of optical spectroscopy, which greatly enhanced my experimental skills. The measurement setups he created significantly accelerated the acquisition of experimental data.

I would like to acknowledge Dr. Sergey Kuznetsov for his contribution to the success of this research. His ideas, knowledge and encouragement have been invaluable in my scientific journey.

I express my gratitude to Dr Damien Hudry, Dr Ian Howard, Alexandra Orlova, Fernando Arteaga Cardona, Dr Arzu Ergene, Dr Nisrin Bhiri as well as the team at the Light Technology Institute: Prof. Dr Ulrich W. Paetzold, Roja Singh, Isabel Allegro, Julie Roger and everyone who participated in the research for their invaluable input, commitment and support during the ups and downs of the doctoral journey.

I extend my thanks to the Department of Quantum Electronics and Radiospectroscopy of the Kazan Federal University where this study started and whose

willingness to contribute their time and insights made this research possible. In particular, I would like to acknowledge all the contributions made by Dr Alexey Nizamutdinov, Dr Vadim Semashko, Dr Elena Lukinova, Dr Stella Korableva as well as Amir Khadiev, Alexey Shavelev, Niyaz Rakhimov and Ilnur Farukhshin. Your perspectives have added depth and richness to the findings.

I am indebted to my mum Irina who provided constant love and support and dear friends Timur Absalyamov, Kamila Yunusova, Daria Shakurova, Emil Mamleyev, Julia Schulte-Hermann, Andrey Michailov, Natalia Kiseleva, Anna Vaiman, Sergei Kazantsev and many others for their understanding and encouragement throughout this long and challenging process.

Finally, I want to acknowledge the financial support provided to Dr Andrey Turshatov and Prof. Dr Bryce S. Richards by DFG (project no. TU 487/8-1).

List of Publicatinons

Peer-Reviewed Journals

- Madirov, E.I., Konyushkin, V.A., Nakladov, A.N., Fedorov, P.P., Bergfeldt, T., Busko, D., Howard, I.A., Richards, B.S., Kuznetsov, S.V. and Turshatov, A. "An up-conversion luminophore with high quantum yield and brightness based on BaF_2: Yb^{3+}, Er^{3+} single crystals." *Journal of Materials Chemistry C* 9.10 (2021): 3493-3503.

- Madirov, E.I., et al. "Absolute quantum yield for understanding upconversion and downshift luminescence in PbF_2: Er^{3+}, Yb^{3+} crystals." *Physical Chemistry Chemical Physics* 25.17 (2023): 11986-11997.

- Madirov, Eduard, et al. "Comparison of Quantum Yield of Upconversion Nanocrystals Determined by Absolute and Relative Methods." *Advanced Photonics Research* 4.2 (2023): 2200187.

- Singh, R., Madirov, E., Busko, D., Hossain, I.M., Konyushkin, V.A., Nakladov, A.N., Kuznetsov, S.V., Farooq, A., Gharibzadeh, S., Paetzold, U.W. and Richards, B.S "Harvesting sub-bandgap photons via upconversion for perovskite solar cells." *ACS Applied Materials & Interfaces* 13.46 (2021): 54874-54883. (Shared first authorship together with Roja Singh)

- Nizamutdinov, A.S., Kuznetsov, S.V., Konyushkin, V.A., Nakladov, A.N., Voronov, V.V., Madirov, E.I., Khadiev, A.R., Gorieva, V.G. and Semashko, V.V. "Down-conversion luminescence of Ce-Yb ions in YF_3." *Optical Materials* 95 (2019): 109256.

Conferences:

- Oral presentation. "Optical characterisation and photovoltaic application of up-conversion luminophores based on BaF_2:Yb^{3+}, Er^{3+} single crystals" 07.2022, 9th International Conference on Optical, Optoelectronic and Photonic Materials (ICOOPMA)
- Oral presentation. "Spectral conversion in doped BaF_2 crystals for photovoltaic applications" 05.2022, 9th South African Conference on Photonic Materials 2023 (SACPM 2023)

Co-authored works published during PhD:

- Nizamutdinov, A. S., et al. "Down-conversion luminescence of Yb^{3+} in novel $Ba_4Y_3F_{17}$: Yb: Ce solid solution by excitation of Ce^{3+} in UV spectral range." *Optical Materials* 108 (2020): 110185.
- Nasrabadi, Hossein Beygi, et al. "Coordination mechanism of cyanine dyes on the surface of core@ active shell β-$NaGdF_4$: Yb^{3+}, Er^{3+} nanocrystals and its role in enhancing upconversion luminescence." *Journal of Materials Chemistry C* 9.45 (2021): 16313-16323.
- Gao, Guojun, et al. "Ratiometric luminescent thermometry with excellent sensitivity over a broad temperature range utilizing thermally-assisted and multiphoton upconversion in triply-doped La_2O_3: Yb^{3+}/Er^{3+}/Nd^{3+}." *Advanced Optical Materials* 9.5 (2021): 2001901.
- Douzi, Abir, et al. "Structure and luminescence properties of Dy^{3+} doped quaternary tungstate $Li_3Ba_2Gd_3(WO_4)_8$ for application in wLEDs." *RSC advances* 13.34 (2023): 23772-23787.

- Niyom, Yupaporn, et al. "Absolute quantum yield of short-wave infrared luminescence of $GdVO_4$: Yb^{3+}, Er^{3+}, Zn^{2+} nano-and microparticles." *Optical Materials* 140 (2023): 113833.
- Arteaga Cardona, Fernando, et al. "Preventing cation intermixing enables 50% quantum yield in sub-15 nm short-wave infrared-emitting rare-earth based core-shell nanocrystals." *Nature communications* 14.1 (2023): 4462.
- Rajagopalan, Krishnan, et al. "High Quantum Yield Shortwave Infrared Luminescent Tracers for Improved Sorting of Plastic Waste." *ACS Applied Materials & Interfaces* 15.37 (2023): 43985-43993.

Introduction

The search for efficient sources of renewable energy has been a hot topic for many years. There are a lot of ways to generate energy from renewable sources: wind power, hydropower, wave power, and many more. One of the fastest-growing areas of renewable energy is solar power. By the end of 2021, the total installed capacity of solar power increased to 945 gigawatts[1].

However, despite rapid growth, the solar power industry faces several challenges that severely limit the future development of the entire industry. The first one is the limited maximum efficiency of solar cells [2]. According to the latest Photovoltaic Report of the Fraunhofer Institute for Solar Energy Systems [1] the best-performing samples of the mono-crystalline solar cells is 26.7%, whereas the best modules demonstrate the efficiency equal to 24.4%. Alternative technologies such as perovskite solar cells demonstrate an efficiency equal to 23.7% while perovskite modules show an efficiency of 17.9%.

The second one is the spectral response of solar cells. Silicon solar cells currently account for more than 95% of the solar cell market [3]. Their spectral response has a maximum in the infra-red (IR) region of the spectrum (800 – 1000 nm), where the sunlight does not have the highest intensity. Perovskite solar cells are an alternative technology for photovoltaic systems. They have completely different spectral properties with a maximum sensitivity in the visible range of the spectrum. There are several ways to overcome the limitations of single-bandgap solar cells: tandem structures [4], multiple exciton generation [5], solar concentrators [6] as well as the use of spectral conversion materials [7]. So far, the best results are obtained with the multi-junction concentrator solar cells. A device that consists of six junctions is reported to have an efficiency of 47.1% [8]. However, this technology faces some challenges mostly related to a complicated manufacturing process as well as the high cost of a unit compared to other technologies [9].

The approach that utilizes the spectral conversion materials does not require significant modification of the already existing photovoltaic technologies which makes it favourable compared to the alternatives. Thus, the search for new efficient spectral conversion materials is still an urgent task today. In order to tailor the solar spectrum to the response of different types of photovoltaic devices both up- and down-conversion materials are needed.

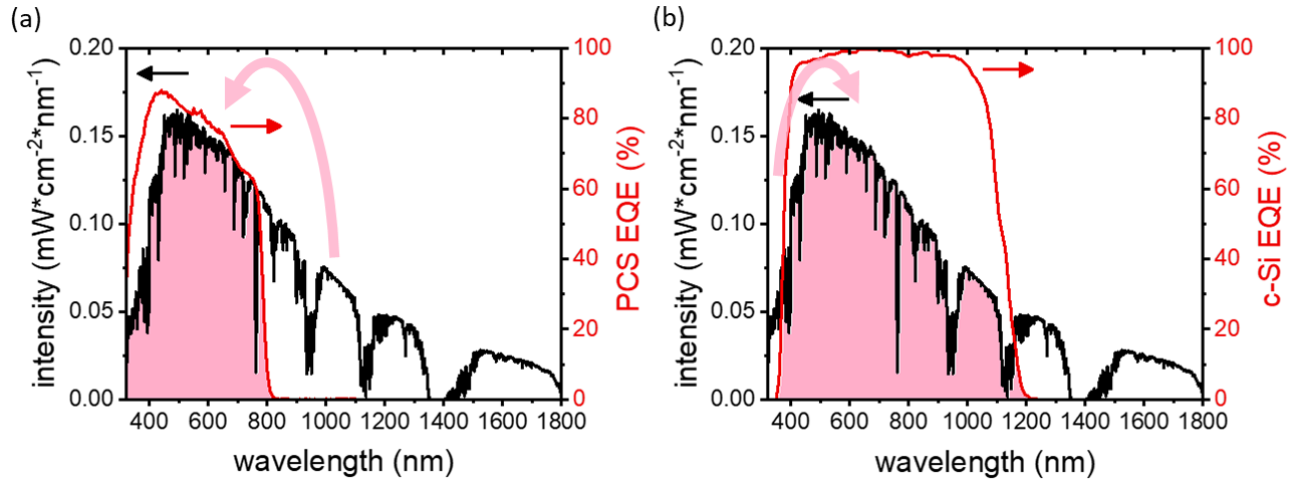

Figure 1 – AM 1.5G solar spectrum (black line) and external quantum efficiency (EQE) of a) perovskite and b) crystalline-silicon (c-Si) solar cells (red line). Highlighted area shows a part of the solar spectrum that can be used by solar cells.

To illustrate the concept the spectral response of a perovskite and c-Si solar cells are presented on top of a solar spectrum in Figure 1. In the case of silicon solar cells, radiation from the ultraviolet (UV) and visible (Vis) range must be converted into the near-infrared (NIR) range, whereas perovskite solar cells require conversion from the NIR to the Vis range. Materials doped with the ions of rare-earth elements can achieve these types of spectral conversion[10]. The complex structure of the excited states of these ions provides the opportunity to have emission bands in a wide wavelength range while co-doping with two or more ions adds additional possibilities for excitation.

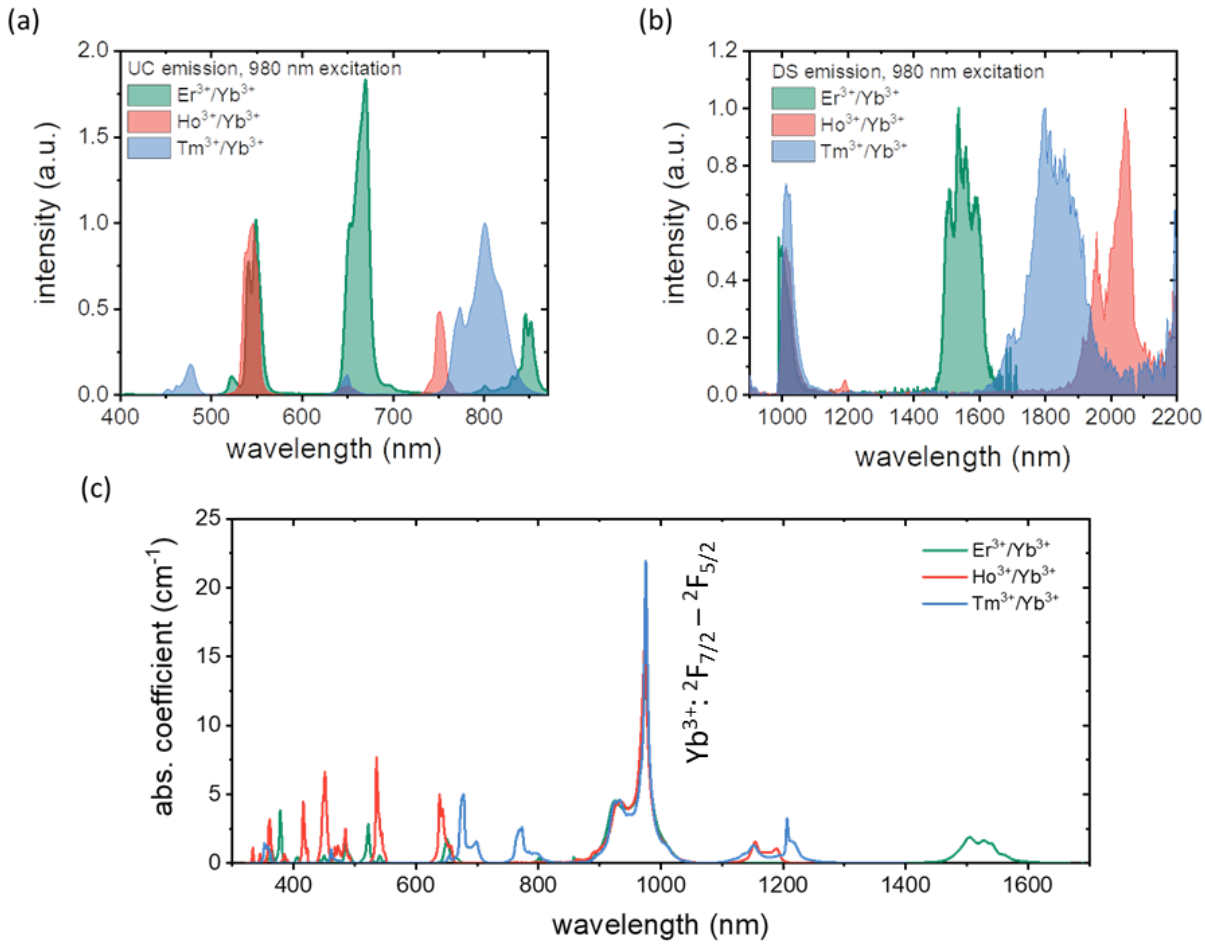

Figure 2 – a) Up-conversion (UC) and b) downshifting (DS) emission under 976 nm excitation; c) absorption spectra of materials co-doped with Er^{3+}/Yb^{3+}, Ho^{3+}/Yb^{3+} and Tm^{3+}/Yb^{3+}.

Figure 2a, b shows typical emission spectra of the materials doped with Er^{3+}, $Ho^{3+,}$ or Tm^{3+} ions. It can be observed that several emission bands can be obtained with these ions both in the Vis and NIR ranges. All materials are also co-doped with Yb^{3+} ions as it has an intense absorption band in the NIR with a maximum at 980 nm (Figure 2c) and can efficiently transfer energy to Er^{3+}, $Ho^{3+,}$ or Tm^{3+}.

Another factor that affects the performance of the spectral conversion materials is the host into which the ions are doped. Among a plethora of available options, fluoride crystals stand out due to several features. First, high chemical stability[11] allows the use of these materials in various environments. Potential use in photovoltaic

systems might leave the materials exposed to different conditions like extreme temperatures or humidity for extended periods, thus, requiring the ability to withstand it. Second, a wide band gap makes fluorides transparent up to the VUV range[12]. As demonstrated in Figure 1a, b spectral conversion materials might require absorption and emission bands anywhere from UV to NIR range. The third feature is low phonon energy, compared to other crystalline materials [13], which should decrease the non-radiative losses. It is generally considered that non-radiative losses lead to lower values of the photoluminescence quantum yield (PLQY) – a ratio of the emitted and absorbed ions, which is used as the chief metric of spectral conversion performance. Due to the combination of all these features fluoride crystalline materials doped with rare earth ions often act as light converters [14–19].

Recent studies show that high values of quantum yield are found in the MF_2 (M = Ca, Sr) crystals doped with Er^{3+} and Yb^{3+} ions [20,21,22,23]. The next hosts in this series are BaF_2 [24] and PbF_2 [25]. The up-conversion efficiency in these hosts is expected to be even higher as previous studies show that an increase in the ionic radius of the host cations allows higher values of luminescence quantum yield [20,22].

Currently, there are little to no published results of the up- and down-conversion properties of BaF_2:Er^{3+}, Yb^{3+} or PbF_2:Er^{3+}, Yb^{3+}. Single crystals seem to be the best option for the study of new materials of this type. Not only the surface effects are minimised in single crystals, but also this form allows for easier estimation of absorption cross-section.

To test up-conversion performance two series of BaF_2:Er^{3+}, Yb^{3+} samples are investigated - with the amount of Er^{3+} ions fixed at 2 mol. % and Yb^{3+} concentration varying from 2 to 15 mol. %, as well as a series with the amount of Yb^{3+} ions fixed at 3 mol. % and Er^{3+} concentration varying from 2 to 15 mol. %. As well as this a series of PbF_2:Er^{3+}, Yb^{3+} samples with an amount of Er^{3+} ions fixed at 2 mol. % and Yb^{3+} concentration varying from 2 to 7.5 mol. % is also synthesized.

For the down-conversion application, a series of BaF_2:Er^{3+}crystals doped with 1 – 25 mol.% of Er^{3+} ions as well as two series of YF_3:Ce^{3+}, Yb^{3+} powders with concentration of Ce^{3+} ions equal to 0.05 mol % and 0.1 mol % and Yb^{3+} concentration in the range from 1 to 10 mol % are prepared. YF_3 host also has a relatively low phonon energy (~500 cm^{-1}), which reduces the probability of losses due to non-radiative transitions [26], and the substitution of the Y^{3+} ion by Ce^{3+} ions or Yb^{3+} does not require additional charge compensation or valence change [27,28].

Objectives and Outline of the thesis

The goal of the current work is to demonstrate that fluoride crystalline materials doped with a combination of rare-earth ions are efficient spectral conversion systems and can then be combined with photovoltaic devices to enhance their response.

Based on the available data the following objectives can be formulated:

1. Determine how efficiently the Er^{3+}/Yb^{3+} co-doped and Er^{3+} single-doped BaF_2 and PbF_2 crystals grown by Bridgeman method can efficiently perform as up- and down-conversion materials
2. Determine the photoluminescence quantum yield (PLQY) values and determine the doping concentrations that provide the most efficient spectral conversion in the case of each crystalline host.
3. Find the value of the maximum enhancement of the response of the Ge – photodiode when combined with a BaF_2:Er down-converting crystal.
4. Determine how efficiently Ce^{3+}/Yb^{3+} - doped YF_3 powders can perform as downshifting materials, estimate the spectral conversion efficiency, and determine the energy transfer mechanism.

The work consists of an introduction, seven chapters, and a conclusion.

Chapter 1 of this work discusses the existing results devoted to the study of optical properties of materials activated by rare-earth elements. A wide range of studies devoted to the study of different types of transitions in lanthanide ions is covered.

Chapter 2 is devoted to the description of the synthesis methods of the studied samples, as well as the tools used to study the physicochemical and spectral-kinetic properties. The growth of crystals by the Bridgman method and the synthesis of powders are briefly described. **Chapter 3** presents the main results of the study of BaF_2: Er^{3+}, Yb^{3+}, namely the analysis of the spectral conversion properties of the

concentration series. **Chapter 4** presents the main results of the down-conversion study of BaF_2: Er^{3+} crystals such as quantum yield values under different excitation wavelengths and estimation of the enhancement of the Ge – photodiode performance. **Chapter 5** presents the main results of the study of PbF_2: Er^{3+}, Yb^{3+}. It includes the analysis of the spectral conversion properties of the concentration series and the comparison of the performance of bulk crystals and powders of the same chemical composition. **Chapter 6** presents the main results of the study of YF_3: Ce^{3+}, Yb^{3+} powders, namely the analysis of the spectral conversion properties of the concentration series and the study of the energy transfer mechanisms. **Chapter 7** studies the possibility of application of an SrF_2: Er^{3+}, Yb^{3+} crystal as a reference for relative quantum yield measurements. **Chapter 8** outlines new promising hosts for the rare-earth ions.

1. State of the Art

1.1 Luminescence and energy transfer mechanisms in rare earth ions.

The spectroscopy of lanthanide ions is a scientific field that constantly continues to expand and develop as it still has areas that require further research. There are three main types of optical transitions in lanthanides: allowed f - d transitions, charge-transfer transitions, and forbidden f - f transitions. Below, each of these types of transitions is discussed in more detail.

1.1.1 Intra-configuration f - f transitions

The transition between the two electronic levels can be realised via several mechanisms. Four main mechanisms can be distinguished: electric dipole (ED), magnetic dipole (MD), electric quadrupole (EQ), and magnetic quadrupole (MQ).

The transition probability between two states is described as $\int \psi_1^* \mu \psi_2 dt$ where ψ - are the wave functions of states between which the transition takes place, μ - is the transition moment operator. If the function $\psi_1^* \mu \psi_2$ is even, the integral is nonzero and the transition is possible, otherwise the transition is forbidden. The parity inversion in quantum mechanics is a change of sign of one of the spatial coordinates. If the wave function does not change its sign when all coordinates are inverted, then it is called even, otherwise, the state is called odd. Since the functions describing 4f orbitals are even, and the dipole moment transfer operator is odd, the resulting function is odd and the integral is zero. Thus, the parity selection rules dictate that f - f transitions are forbidden for the electric dipole mechanism. However, when the lanthanide ions are in a crystalline host, they are exposed to ligand fields and non-centrally symmetric interactions lead to the mixing of electronic levels with opposite parity into the wave functions. This weakens the selection rules and the transitions become partially allowed. Magnetic dipole transitions are allowed, but their probability is low, although in some f - f spectra their intensity is comparable with electric dipole transitions.

Quadrupole transitions are also partially allowed (although they have a low probability compared to allowed transitions), but they are much less intense than magnetic dipole transitions, so they are not usually observed. Selection rules for quantum numbers S, L, and J are given in the Table 1.1.

Table 1.1 - Conditions for allowed transitions for quantum numbers S, L, and J in case of f-f and f-d transitions [29].

Transition	**ΔS**	**|ΔL|**	**|ΔJ|**	**Approximate oscillator strength**
ED (f-d)	0	≤1	≤1	0.01-1
ED (f-f)	0	≤6 (2, 4, 6 with L or L' = 0)	≤6 (2, 4, 6 with J or J' = 0)	10^{-4} - 10^{-5}
MD (f-f)	0	0	0, ±1	10^{-5} - 10^{-6}
EQ (f-f)	0	0, ±1,±2	0, ±1, ±2	10^{-10}

A theory to predict the intensities of f-f transitions was independently presented in 1962 by two scientists within one month[30,31]. Now known as the Judd-Ofelt (JO) theory, it is developed in the crystal field approximation and provides a simple method for calculating intensities of absorption lines corresponding to f-f transitions as well as probabilities of radiative transitions. The main drawback of this theory is that it allows only the 4f configuration of electrons to be taken into account, while it is not possible to do the same analysis of the 4f - 5d transitions.

The standard analysis within the framework of Judd-Ofelt theory provides values of the emission intensity as well as the radiative lifetimes based on absorption spectra recorded at room temperature.

To perform the analysis, the spectral line intensities determined experimentally as

$$S_{exp}(J-J') = \frac{3ch(2J+1)n}{8\pi^3\bar{\lambda}e^2N_0}\left[\frac{9}{(n^2+2)^2}\right]\int \alpha(\lambda)d\lambda\,, \qquad 1$$

where J, J' is the quantum number of the total angular momentum of the initial and final states respectively, n is the refractive index, N_0 is the concentration of rare-earth ions , $\bar{\lambda}$ - is the average wavelength of the absorption band, $\int \alpha(\lambda) d\lambda$ - integral absorption coefficient, are compared with the values of spectral line intensities determined theoretically as

$$S_{theory}(J - J') = \sum_{t=2,4,6} \Omega_t \mid < (S, L)J|U^{(t)}|(S', L')J' > |^2, \quad 2$$

where Ω_2, Ω_4, Ω_6 - are the intensity parameters of Judd-Offelt theory, and $U^{(t)}$ - are the matrix elements of rank t (t = 2, 4, 6) between the states characterized by quantum numbers (S, L, and J), and (S', L' and J').

This allows determining the values of the Ω_2, Ω_4, Ω_6 parameters which are then used to predict the transition probability between any two states as

$$A(J - J') = \frac{64\pi^4 e^3}{3h(2J+1)\bar{\lambda}^3} \frac{n(n^2+2)^2}{9} S_{thery}(J - J'). \quad 3$$

As has been already mentioned above Judd-Ofelt theory can provide an insight into the optical properties of materials. When combined with experimentally obtained luminescence decay times it allows easily estimating the quantum efficiency of the radiative transitions without complex experimental procedures. Judd-Ofelt analysis can be easily performed when the studied material is in the form of single crystals or glasses because in this case absorption cross-section, doping ion concentration, and refractive index are easily estimated. However, oftentimes the newly synthesized materials come in the form of either micro- or nanoparticles. In this case, it is significantly more difficult to experimentally obtain an absorption cross-section. There are various ways to overcome this limitation and still perform the Judd-Ofelt analysis. If the studied material is doped with certain lanthanide ions, namely Eu^{3+}, Dy^{3+}, Tb^{3+}, and Sm^{3+} the Judd-Ofelt parameters can be calculated only using the emission spectrum as these ions have purely magnetic-dipole-allowed transitions [32]. Unfortunately, the Judd-Ofelt parameters of the rest of the lanthanide ions in the powder samples cannot be obtained

so easily. Thus, the search for methods that can provide reliable Judd-Offelt parameters of powders doped with different rare-earth ions is still actively going.

There are several works dedicated to the realization of Judd-Ofelt analysis with Er^{3+} doped powders. First, the *Method A* is described in the paper [32]. It uses the excitation spectrum recorder while monitoring the emission of the $^4S_{3/2} - {}^4I_{15/2}$ transition. The JO parameters Ω_t are calculated in arbitrary units and then recalculated using the radiative lifetime of the $^4I_{13/2} - {}^4I_{15/2}$ transition. These parameters are then used to estimate the transition probabilities and radiative lifetimes of other transitions.

Secondly, the *Method B* is described in the paper [33]. This approach uses the diffuse reflectance spectrum of the powder sample. To convert from arbitrary units of the diffuse reflectance spectrum to cm^2 of the absorption cross-section, the experimentally determined oscillator strength of the $^4I_{15/2} - {}^4I_{13/2}$ transition is calibrated to the radiative lifetime of the $^4I_{13/2} - {}^4I_{15/2}$ transition. The treated spectrum is then used to calculate the JO parameters Ω_t.

The final approach is *Method C* described in [34]. Unlike the previous case, here the absorption in arbitrary optical density units is used to calculate the relative intensity parameters. The actual JO parameters Ω_t are calculated afterwards using the radiative lifetime of the $^4I_{13/2} - {}^4I_{15/2}$ transition. In this case, a diffuse reflectance spectrum is used in combination with Kubelka-Munk theory to perform the calculations in arbitrary units.

It can be seen that all mentioned methods require the luminescence decay time of the $^4I_{13/2} - {}^4I_{15/2}$ transition. Thus, it is crucial to determine this decay time reliably. There is a number of factors such as concentration quenching, and cross- or multiphonon relaxation that have an effect on the observed decay times. Reabsorption effects can also have a noticeable change in the measured luminescence decay times[35,36], but its effect can be taken into account. One way to minimize the reabsorption is to dilute the studied material with optically inactive powder. This way the emission

will have a lower probability of hitting an optically active particle when propagating through the material and subsequently lower probability of being reabsorbed.

1.1.2 Allowed f-d transitions

It should be noted that the spin selection rule $\Delta S = 0$ is important since the f-d transitions for which this condition is not fulfilled have an extremely low emission intensity. The f-d transitions are observed in the following lanthanide ions: Ce^{3+}, Pr^{3+}, Tb^{3+} as well as in some divalent ions: Sm^{2+}, Eu^{2+}, Tm^{2+}, Yb^{2+}. In other trivalent ions, these transitions are often quenched by cross-relaxation with the $4f^n$ configuration. Typically, f-d transitions have high energies of >50000 cm^{-1} (<200 nm). These transitions have been both calculated theoretically and observed experimentally in various hosts, e.g. CaF_2, $LiYF_4$, or $Y_3Al_5O_{12}$. [37]. As an example, the energies of the first f-d spin-allowed transition of the lanthanide ions in the CaF_2 host are given in the Figure 1.1. The fact that the d orbitals, in contrast to the f orbitals, are not shielded, accounts for several features of f-d transitions. The field generated by the surrounding ligands is in the range of 10^3 - 10^4 cm^{-1}. This value is significantly higher than the case of f orbitals. This, in turn, leads to an energy difference between the higher and lower spin levels of about 8000 cm^{-1}. In addition, the Stokes shift is much larger than the corresponding values for the f levels and is usually in the range of 1000 - 3000 cm^{-1}. Since f-d transitions are much more sensitive to the surroundings, it is possible to change the transition energy by placing the ion in different hosts. A stronger ligand field will lead to a bigger splitting and the lowest d level will shift to a lower energy region.

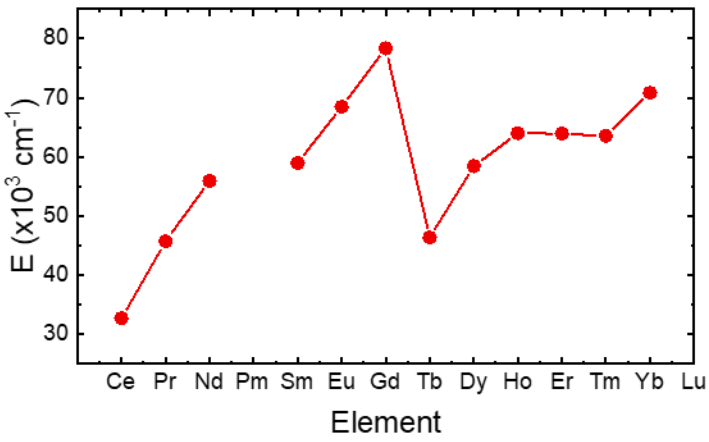

Figure 1.1 - Energy of the first spin allowed the transition of the trivalent lanthanide ions in the CaF_2 host [38].

The nature of f-d transitions has been studied quite thoroughly. An important parameter is the position of the lowest d level in relation to the valence and conduction bands, as this parameter determines the optical properties of the dopant. A phenomenological expression was obtained by Dorenbos to determine the energy with respect to the d level position of the Ce^{3+} ion.

$$E(Ln, A) = 49340\ cm^{-1} - D(A) + \Delta E^{Ln,Ce}. \qquad 4$$

Here $E(Ln, A)$ - maximum energy of the lowest f-d transition of the trivalent lanthanide ion placed in host *A*. $D(A)$ - lowering of the d level of the Ce^{3+} ion by the ligand field with respect to the position of the level in a free ion. $\Delta E^{Ln,Ce}$ - difference in the lower d level position of the trivalent lanthanide ion and Ce^{3+} ion, which is independent of the host. These parameters were determined for many materials.

f-d transitions generally show absorption cross-section values that are significantly higher than the ones found in the f-f transitions. This feature makes ions that demonstrate f-d transitions an attractive sensitizer, as these ions can absorb a large number of excitation photons. If combined with an appropriate emitter such a system might be capable of efficient energy conversion.

1.2 Energy transfer mechanisms

In 1942 Weissman discovered that luminescence of lanthanide ions can be observed when excited at the absorption wavelength of ligands [39]. This effect was called luminescence sensitization. It greatly influenced all subsequent research and development in the field of luminescent materials containing lanthanide ions.

Another important step was the development of the theory of resonant energy transfer. In 1948 Theodore Förster suggested the existence of transfer of electron excitation between molecules based on the available experimental data [40]. Förster's theory is discussed in more detail in the following section.

The next step was to directly investigate the energy transfer mechanisms. In 1953 D.L. Dexter further developed Förster's theory describing a dipole-dipole energy transfer mechanism for the case of forbidden transitions in solids [41]. Dexter distinguished several possible mechanisms, each with a specific distance dependence (see Table 1.2). The mechanisms include the dipole-dipole mechanism, already known from Förster's theory, as well as the electric dipole-quadrupole and quadrupole-quadrupole mechanisms, the magnetic dipole mechanism, and the exchange mechanism. To determine the relative role of each mechanism, the number of centres that can be excited from a single donor has been calculated. These estimates were made for the model host with NaCl structure and corresponding lattice parameters. It is worth noting that the exchange mechanism has an efficiency comparable to the dipole-quadrupole mechanism. Thus, the distance between the donor and the acceptor can be experimentally determined from the dependence of the luminescence intensity on the acceptor concentration, since the luminescence intensity of the acceptor directly depends on the energy transfer efficiency which, in turn, is related to the distance separating the donor and the acceptor (see Table 1.2).

Table 1.2 - Energy transfer mechanisms between donor and acceptor.

Mechanism	Dependence on distance
Dipole dipole (el.)	$\mathbf{r_{DA}^{-6}}$
Dipole quadrupole (el.)	$\mathbf{r_{DA}^{-8}}$
Exchange (spin)	$\mathbf{exp(-r_{DA})}$
Quadrupole-quadrupole (el.)	$\mathbf{r_{DA}^{-10}}$

1.2.1 Förster energy transfer

Förster's theory of the resonant energy transfer is a key to any study of sensitised luminescence. This topic occupies a special place because it often arises in both theoretical and experimental research, extending from basic fields such as theoretical physics to applications in electronics, chemistry, medicine, and biology.

Before proceeding to describe methods of resonant energy transfer estimation, it is necessary to outline the framework within which Förster's theory can be applied. Förster resonant energy transfer (FRET) is a mechanism strongly dependent on the distance between the optical centres. The resonant energy transfer process is only feasible if the distance between the optical centres is less than 20 nm. Otherwise, the theory will not provide reliable results. If the distance requirements are met, then two optical centres, e.g. two molecules, must be present in the medium to realize the resonant energy transfer. The energy donor must be a phosphor and the energy acceptor must be capable of absorbing light in the emission range of the donor. Energy transfer is carried out non-radiatively through the dipole-dipole mechanism. The presence of resonant energy levels in the donor and acceptor is a requirement for this. It must also be noted that the optical properties of the donor-acceptor pair must be maintained throughout the entire volume of the medium under study. Typically, the averaged luminescence parameters of a large ensemble of donor-acceptor pairs are used to evaluate the efficiency of the resonant energy transfer process. Since there are always

additional processes in the system that lead to energy loss, the probability of resonant energy transfer is usually lower than the probability of spontaneous emission of an individual donor or acceptor.

The Förster energy transfer coefficient has a dependence on the distance between donor and acceptor as r_{DA}^{-6}. This theory is based on the dipole-dipole approximation, which can be represented as a Coulomb interaction. Thus, the Förster energy transfer can be written down as:

$$k_{FRET} = \frac{2\pi}{\hbar}|V|^2\rho. \quad 5$$

Here V is the electrical interaction between the donor and acceptor, ρ - is the density of states of initial and final interacting levels, which is proportional to the spectral overlap integral J that describes the overlap between the emission spectrum of the donor and the absorption spectrum of the acceptor. In turn, the parameter V can be represented as

$$V_{Col} = \frac{\kappa|\overrightarrow{\mu_D}||\overrightarrow{\mu_A}|}{3\pi\varepsilon_0 n^2 r^3}, \quad 6$$

where $\overrightarrow{\mu_D}$, $\overrightarrow{\mu_A}$ - are the dipole moments of the donor and the acceptor, κ is determined by the orientation between them, r is the distance between the pair.

By combining the last two expressions, the familiar expression as r_{DA}^{-6} is obtained:

$$k_{FRET} = \frac{9(Ln\ 10)\kappa^2\Phi_D}{128\pi^5 N_A n^4 r^6} J\ . \quad 7$$

At the distance at which the Förster energy transfer and other processes are in balance, the resonance transfer efficiency is 50%. This distance is called the Förster distance or radius, which is defined as

$$R_0 = \left(\frac{9(Ln\ 10)\kappa^2\Phi_D}{128\pi^5 N_A n^4} J\right)^{1/6}, \quad 8$$

where J is the integral of spectral overlap calculated as:

$$J = \int \bar{I_D}(\lambda)\varepsilon_A(\lambda)\lambda^4 d\lambda = \int \bar{I_D}(\tilde{\nu})\varepsilon_A(\tilde{\nu}) d\frac{\tilde{\nu}}{\tilde{\nu}^4}\,. \qquad 9$$

This integral depends on the extinction coefficient of the acceptor ε_A and the normalized per unit emission spectrum of the donor $\bar{I_D}$.

$$\int \bar{I_D}(\lambda) d\lambda = 1. \qquad 10$$

It is also possible to express the resonance energy transfer rate with the donor's luminescence lifetime:

$$k_{FRET} = \tau_D^{-1}\left[\frac{R_0}{r}\right]^6\,, \qquad 11$$

and the efficiency of the Förster energy transfer as

$$\eta_{FRET} = \frac{k_{FRET}}{k_{FRET}+\tau_D^{-1}} = \frac{1}{1+(r/R_0)^6}\,. \qquad 12$$

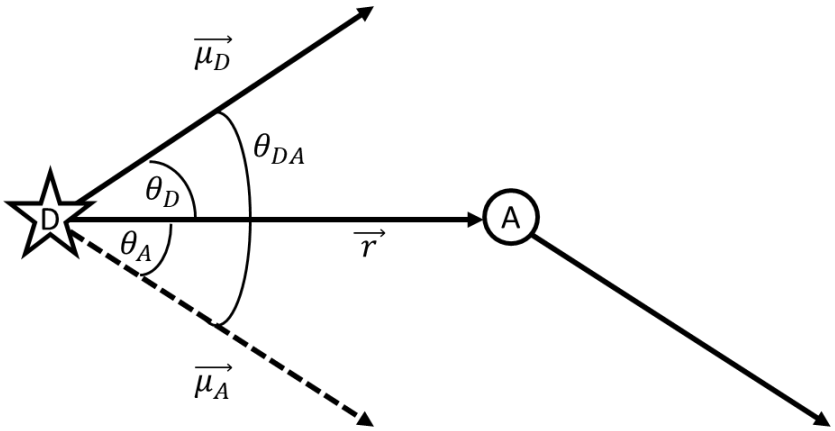

Figure 1.2 - Orientation of donor emission dipole moment $\overrightarrow{\mu_D}$, the absorption dipole moment of the acceptor $\overrightarrow{\mu_A}$, as well as the vector connecting the donor and acceptor, necessary to calculate the parameter k.

The last important parameter for estimating the Förster energy transfer is the so-called orientation factor. To estimate it, one can get away with a fairly simple averaging. Figure 1.2 shows the possible orientations of the donor and acceptor. The orientation factor can be calculated as

$$\kappa = \widehat{\mu_D} * \widehat{\mu_A} - 3\,(\widehat{\mu_D} * \hat{r})(\widehat{\mu_A} * \hat{r}) = cos\theta_{DA} - 3cos\theta_D * cos\theta_A. \qquad 13$$

Here $\widehat{\mu_D}$ $\widehat{\mu_A}$ and $\hat{r}$- unit vectors corresponding to $\overrightarrow{\mu_D}$, $\overrightarrow{\mu_A}$ and $\vec{r}$; angles θ_{DA}, θ_D и θ_A are shown in the Figure 1.2.

For most scenarios, it is possible to use an approximation which gives a good estimation of the parameter κ^2. If during the Förster energy transfer time that is equal to $1/k_{FRET}$ the acceptors and donors can take all possible positions, then the system is in the dynamic averaging mode and κ^2 = 2/3. If one of the centres can take any orientation, while the other has a fixed orientation, the parameter κ^2 takes values between 1/3 and 4/3 (in this case 2/3 is still a good approximation). However, if both centres have a fixed orientation, the picture gets noticeably more complicated, as the parameter κ^2 takes on values between 0 and 4.

1.2.2 Charge transfer transitions

Charge transfer is a complex phenomenon that can manifest itself in different ways. Sometimes, these transitions are necessary for the sensitisation of luminescence of inorganic phosphors containing lanthanides, but in other cases, they can lead to quenching of luminescence. Charge transfer transitions, like f - d transitions, are partially allowed. There are several basic types of charge transfer transitions.

The first type is charge transfer from a ligand to a metal. This process consists of the transfer of an electron from a ligand to a metal ion. Like the f-d transitions, the energy of this process is relatively high, so the corresponding absorption bands are usually observed in the UV region of the spectrum. The lowest transition energies are observed in easily reduced ions such as Sm^{3+}, Eu^{3+}, Tm^{3+} and Yb^{3+}. In Figure 1.3 one can see calculated energies of (2p)O-Ln^{3+} transition in inorganic phosphors. However, the energy of this transition is highly dependent on the host in which the ion is placed and, for example, for the Eu^{3+} ion in europium azide in water the energy is 31250 cm^{-1} [42]. The contribution of covalent bonding with organic ligands significantly lowers the charge transfer transition energy to 18000-25000 cm^{-1}, and the energy can be additionally controlled by changing the ligands [43]. Mixing charge transfer transitions

and 4f states leads to an increased probability of electric dipole transitions. For example, a weak $^5D_0$ - $^7F_0$ europium absorption band with an extinction coefficient of about 10^{-3} M^{-1} cm^{-1} in the aqueous ion $[Eu(H_2O)_9]^{3+}$, located at 17212 cm^{-1} not only shifts to higher energies up to 17330 cm^{-1} in the p-But-calix[8]arene H8L bi-core complex, $[Eu_2(H_2L)(DMF)_5]$, but also becomes 5000 times more intense, reaching values of 5 M^{-1} cm^{-1}[44].

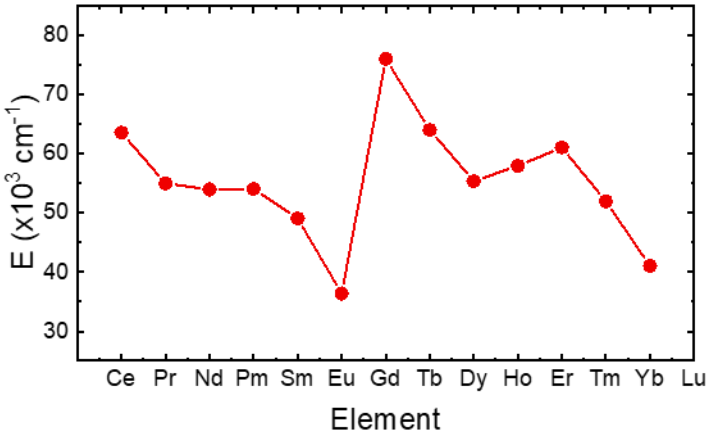

Figure 1.3 - Calculated energies of charge transfer transition of (2p)O-Ln^{3+} [45].

The second type is charge transfer from metal to a ligand. Such transitions, as a rule, are observed in d-elements and are rarely observed in spectra of lanthanide ions except for Ce^{3+}, which is easily oxidized to the 4+ state.

The third type is charge transfer between ligands. If a ligand has regions of opposite charge, the transfer can take place between these regions. Sometimes this process is also called intramolecular charge transfer. These states are well suited for sensitising lanthanide luminescence, as they have high absorption, at low energies. In addition, the transition energy can be modulated by changing the surrounding ligands [46].

There are several examples where charge transfer plays an important role in the optical properties of the materials in question. The charge transfer scenario is most likely to occur in Yb^{3+} and Eu^{3+} ions. The Yb^{3+} ion additionally stands out because it

has only one excited 4f state - $^2F_{5/2}$, which is located 10 000 cm^{-1} above the ground state $^2F_{7/2}$. The large difference between the energy of the excited state and the charge transfer band makes it possible to observe luminescence from this band.

The results presented in the paper [47] demonstrate that in the Yb^{3+} ion, the excitation energy of the charge transfer state is higher than that of the Eu ion^{3+} (49000 cm^{-1} vs. 45000 cm^{-1}), which has the lowest charge transfer energy among the rare-earth ions. However, due to a large number of excited 4f states, some of which are comparable with the energy of the charge transfer, in the Eu^{3+} ion the charge transfer state excitation energy will dissipate non-radiatively, in contrast to the Yb^{3+} ion, whose only excited state corresponds to an energy of 10000 cm^{-1} over the ground state.

The charge transfer process does not involve the transfer of a single electron from the ligand to the metal ion but results in a significant redistribution of the charge density. This in turn leads to an increase in the bonding between the ion and the ligand in the excited state, which can manifest itself in large Stokes shifts and broadening of the luminescence bands [48].

In the work [49,] the emission of the charge transfer band of Yb^{3+} ions in orthophosphates, lithium and rare earth oxides as well as oxysulfides is investigated. In these materials, the emission depends on the size and position of the cation and shifts towards longer wavelengths with the increase in cation size. The ion radius increases from 0.87 Å for Sc^{3+}, to 0.97 Å for Lu^{3+}, 1.01 Å for Y^{3+} and 1.18 Å for La^{3+}. The position of the Yb^{3+} ion determines the relaxation pattern. When a larger cation is substituted, the radiative relaxation of the excited state is larger, which manifests itself in a larger observed Stokes shift.

The quenching temperature of the luminescence of a charge transfer band can be estimated with a relatively simple configuration-coordinate model since the efficient relaxation leads to a fast transition to the ground state. If Yb^{3+} replaces a La^{3+} ion, the luminescence of a charge transfer band can be quenched at a relatively low temperature.

However, this model is not able to predict the quenching temperature for all crystal lattices.

Changing the cation from Sc to Lu or Y in orthophosphates increases the quenching temperature (from 225 K to 250 or 290 K respectively). A similar effect exists for Eu^{3+} ions. This might be explained by greater distortion of the local environment of the ions. Another explanation is that the quenching is not due to a thermally activated transition to the ground state but to photoionization. At the same time, the $^5D_0 \rightarrow ^7F_J$ luminescence transition of the Eu^{3+} ion is quenched at higher temperatures. This may be related to the fact that the Yb^{2+} ion has lower stability in comparison to the Eu^{2+} ion (the most stable divalent lanthanoid). The lower stability is since the charge transfer state is located closer to the valence band, hence photoionization can take place at a lower temperature. The effect is similar for both Yb^{3+} and Eu^{3+} ions. In some hosts where Eu^{3+} has a high luminescence quenching temperature when excited into the charge transfer band, Yb^{3+} has a quenching temperature below room temperature. An exception is the YBO_3 host, in which the luminescence quenching temperature of Eu^{3+} is > 850 K, whereas Yb^{3+} charge-transfer luminescence is not observed at all. To sum up, it is possible to say that charge transfer luminescence from Yb^{3+} is observed only in hosts in which the quenching temperature for Eu^{3+} is higher than 500 K. An alternative explanation of the observed effect could be that in the Yb^{3+} ion the radiative decay from the charge transfer state is about 150 ns, whereas in the Eu^{3+} ion luminescence is observed when the$^5 D_0$ states are populated by rapid non-radiative decay ($\tau \sim$ ps).[50].

Table 1.3 shows the position of the Eu^{3+} ion charge transfer band and the quenching temperature of the $^5D_0 \rightarrow ^7F_J$ luminescence when excited into the Eu^{3+} charge transfer band in different hosts. In some hosts marked in the Table 1.3 with [a], the luminescence is not completely quenched at high temperatures but remains at more than a quarter of the maximum intensity.

Table 1.3 - Position of the charge transfer band in Eu^{3+} and Yb^{3+} ions and quenching temperature of the $^5D_0 \rightarrow ^7F_J$ luminescence of Eu^{3+} or quenching temperature of Yb^{3+} emission after excitation in the charge transfer band.

	Eu^{3+} CT excitation band (nm)	Eu^{3+} T (K)	Yb^{3+} CT absorption band (nm)	T_q (K)
$ScPO_4$	205	760 [a]	195	225
LuPO	215	850 [a]	210	250
YPO	218	>850	210	290
$LaPO_4$	251	400	228	<10
$NaScO_2$	225	650	208	225
$NaLaO_2$	264	320	262	<10
$LiScO_2$	223	>850	206	180
LiYO	247	600	214	125
$LiLaO_2$	274	475	252	<10
Y_2O_3	250	>850	227	130
Y_2O_2S	334	725	310	140
LaOS	347	480	317	150
YAG	237	>850	212	<80
$LaAlO_3$	306	500	244	<10
$ScBO_3$	218	420		<10
YBO_3	228	>850	216	<10
$LaBO_3$	275	350	-	<10

1.3 Up-conversion luminescence

Luminescence of materials doped with rare-earth ions can be generally divided into two large groups: stokes and anti-stokes luminescence. Most of the known luminescent materials belong to the first group that demonstrates Stokes luminescence.

This means that the wavelength of the radiation emitted by the material is longer than the wavelength of absorbed excitation. Fewer known optical materials exhibit anti-stokes luminescence. In this scenario, the wavelength of the emitted radiation is shorter than the absorbed excitation wavelength. Such processes are also often referred to as up-conversion (UC).

Until the 1960s all known materials exhibiting anti-stokes radiation had emission energies exceeding the excitation energy by only a few kT. This energy was due to the thermal population of the energy states above the excited states. This was a well-known case of anti-stokes radiation for the so-called thermal bands or Raman effect for the well-known anti-stokes side bands. Thermoluminescence, where excited trap states are emptied by excitation energy on the order of kT, also represents a separate field of study of anti-stokes radiation. Superexcitation, i.e. the rise of an already excited electron to an even higher level due to absorption from the excited state (ESA), was also known, but the observed emission intensity in this case was extremely low.

Both the advent of new excitation sources and the development of optical materials uncovered new up-conversion materials in which the anti-stokes shift had a value of 10-100 kT and the quantum efficiency was in the units of per cent at relatively low excitation intensities (<40 W/cm^2) [51, 23]. To explain the observed effects, a new approach to the interpretation of up-conversion processes was needed.

It has been recognised that several different mechanisms are individually or in combination involved in up-conversion processes. In the Figure 1.4 there is a schematic representation of the up-conversion processes, the corresponding typical efficiency values according to [52], as well as the materials in which each of the named processes can be observed.

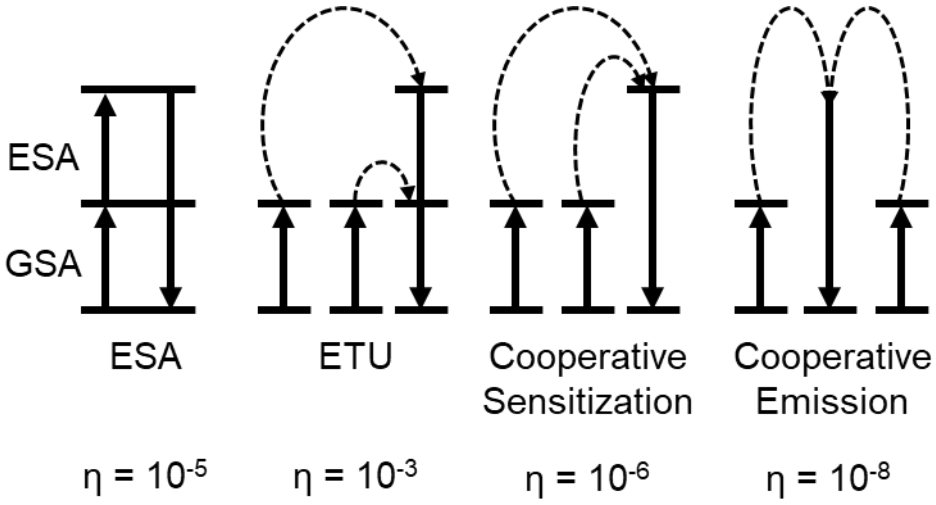

Figure 1.4 - The main types of up-conversion processes and the characteristic efficiency values (η) of each process and the materials in which they can be observed [52].

One of the historically first models to describe the up-conversion process is the excited state absorption (ESA) model. This process was first described as the basis of the infrared quantum counter [53]. To realize ESA, only one ion is needed, whose state absorbs one photon while in the ground and is excited to the excited state with a relatively long lifetime. Then, from this state the ion absorbs another excitation photon, moving to an even higher-lying excited level, from where it emits radiation. This is often the only process observed in samples with low concentrations of doping ions.

In addition to the multistep excitation realised via ESA, there is a very efficient up-conversion process by sequential energy transfer, which has been termed the energy transfer up-conversion (ETU). This mechanism requires the presence of two ions near each other, thus this process prevails in materials with a relatively high concentration of activators. When the ETU process is described, a distinction is normally made between donor ions and acceptor ions. Donor ions absorb excitation while in their ground state. Once in the excited state, they transfer energy to an acceptor, which goes to an intermediate excited state. Then, the energy transfer from another donor propagates the acceptor to an even higher state, from which radiation is emitted.

To demonstrate what provides the high efficiency of an ETU we can consider a simple system shown in the Figure 1.5.

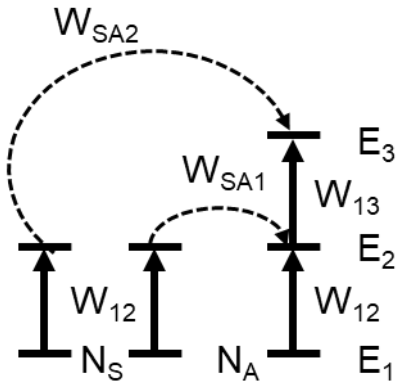

Figure 1.5 - Simplified diagram of levels used to illustrate ESA and ETU processes.

The probability of ESA can simply be described as the product of the probabilities of the intermediate steps:

$$W_{13} = W_{12} * W_{23} \quad (14)$$

In the case of the ETU process, the probability of a population of the same level is defined as:

$$W_{13} = (N_S * W_{12})^2 * W_{SA1} * W_{SA2} \quad (15)$$

Here W_{SA1} and W_{SA2} are the energy transfer probabilities at each stage, and the product ($N_S * W_{12}$) can be interpreted as the concentration of excited donor ions.

Given that the probabilities W_{ij} have the same order of magnitude as W_{SA1} and W_{SA2}, then in the case of ESA $W_{13} \sim W_{12}^2$, and in the case of ETU $W_{13} \sim N_S^2 * W_{12}^2 * W_{SA}^2$.

From this, it is clear that the higher efficiency of the ETU process is due to the multiplier $N_S^2 * W_{SA}^2$, which can take any value.

The ETU phenomenon must be distinguished from the third process, namely cooperative up-conversion between either two ions or a pair of ions and a third. Although some aspects of it are theoretically quite similar to ETU, its efficiency is

usually much lower. This is due to the fact that this process requires the existence of quasi-virtual paired levels, the transitions between which must be described in a higher-order perturbation due to their two-operator nature.

In addition, a fourth process must be mentioned: the photon avalanche effect, also based on sequential energy transfer, but of the down-conversion type (commonly referred to as cross-relaxation), while the up-conversion process itself is driven by ESA.

1.4 Energy transfer mechanisms in materials doped with ions Er^{3+}/Yb^{3+}

There are many different implementations of up-conversion materials. There are known materials based on transition metal ions such as Ni^{2+}[54], Ti^{2+}[55]Os^{4+}[56] and Mo^{3+}[57]. A great deal of work is also carried out on up-conversion in organic materials [58][59]. Up-conversion materials containing trivalent ions of rare earth elements deserve special attention. The electronic structure of rare earth elements, namely the presence of a valence 4f shell, determines the unique optical properties of materials containing these ions. Absorption and emission spectra of such materials consist of a series of narrow lines defined by transitions inside the 4f shell. Up-conversion materials doped with Er^{3+}[60], Ho^{3+}[61] or Tm^{3+}[62] are well known. To increase the efficiency of such up-conversion, co-activation with an ion (called a sensitizer) that has a high absorption cross-section is often used. If the goal is to achieve conversion from the near-infrared to the visible range, co-doping with Yb^{3+} ions is often used. The $^2F_{7/2} \longrightarrow {}^2F_{5/2}$ transition in Yb^{3+} is resonant with certain f-f transitions of Er^{3+}, Tm^{3+} and Ho^{3+} ions, which ensures efficient energy transfer. Thus, Er^{3+}/Yb^{3+}, Ho^{3+}/Yb^{3+}, and Tm^{3+}/Yb^{3+} pairs are often used [63–67].

In the work by Oliveira et al. [68] the population of excited states of Er^{3+} ion in chalcogenide glass doped with Er^{3+}/Yb^{3+} is investigated in the case of the excitation with a continuous wave laser at a wavelength of 1.06 μm with intensity up to 500 mW. The intensity of up-conversion luminescence of samples doped with only Er^{3+} ions is

an order of magnitude lower than one of the samples co-doped with Er^{3+} and Yb^{3+}, indicating the importance of the energy transfer process between the ions.

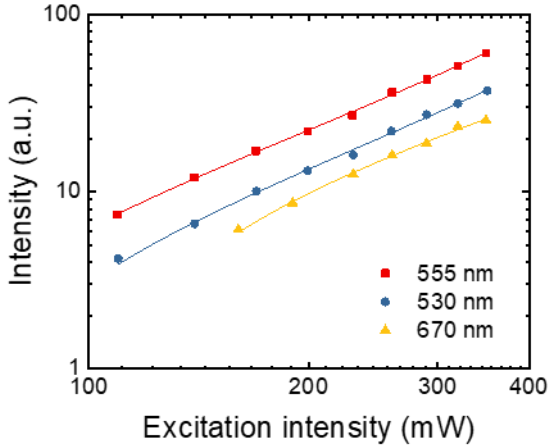

Figure 1.6 - Dependence of luminescence intensity of different Er^{3+} ion bands on pump power in chalcogenide glass doped with Er^{3+} /Yb^{3+} ions [68].

Figure 1.6 shows the dependence of luminescence intensities of different emission bands of Er^{3+} ions on the pump power in co-doped samples. The dependence shows that the population of all observed levels $^2H_{11/2}$ (530 nm),$^4S_{3/2}$ (555 nm) and $^4F_{9/2}$ (670 nm) occurs via the absorption of two photons. The authors suggest that the $^2H_{11/2}$ level is populated as follows. First, the Yb^{3+} ion absorbs a photon and is excited from the ground state $^2F_{7/2}$ to the level $^2F_{5/2}$. From there the excitation is transferred to the Er^{3+} ion, which transitions from the ground state $^4I_{15/2}$ to the excited state $^4I_{11/2}$. In the next stage the same or neighbouring Yb^{3+} ion absorbs another photon of excitation and by transferring energy to the same Er^{3+} ion excites it from the state $^4I_{11/2}$ to the state $^2H_{11/2}$. The level $^4S_{3/2}$ is populated from the level $^2H_{11/2}$ via multi-phonon relaxation. Several ways to populate the state $^4F_{9/2}$ are suggested. The first involves multi-phonon relaxation from the level $^4S_{3/2}$. However, the authors call this option unlikely, as the energy difference between the levels is around 3200 cm^{-1}. The second pathway suggests that first the level $^4I_{13/2}$ is populated by transitions from the levels $^4I_{11/2}$ and $^4S_{3/2}$, and then, after an energy transfer of another excitation photon, the state $^4F_{9/2}$ is populated

via the $^4I_{13/2} \rightarrow {}^4F_{9/2}$ transitions. This process must lead to a linear dependence of the luminescence intensity at 670 nm on the concentration of Yb^{3+} ions, which is investigated separately in [69].

In the work by Da Vila et al. [70] the values of critical distance and energy transfer constant, describing the efficiency of energy transfer processes between the states $Yb(^2F_{7/2}) \rightarrow Yb(^2F_{5/2})$, $Yb(^2F_{5/2}) \rightarrow Er(^4I_{11/2})$, and $Er(^4I_{11/2}) \rightarrow Yb(^2F_{5/2})$ in fluorocirconate glasses doped with Er^{3+} /Yb^{3+} ions are calculated. The values are determined using the spectral overlap integral method in the case of resonant energy transfer.

The results of the calculations are shown in the Table 1.4. The values of the energy transfer constant indicate that processes such as the migration of excitation between Yb^{3+} ions, and the reverse energy transfer from Er^{3+} to Yb^{3+} play an important role in the transfer of energy between the ions.

Table 1.4 - Microparameters of resonant energy transfer between Er^{3+} and Yb^{3+} ions in fluorine zirconate glasses [70].

Energy transfer	Transfer constant ($cm^6 \times s^{-1}$)	R_c(Å)
$Yb(^2F_{7/2}) \rightarrow Yb(^2F_{5/2})$	$C_{DD} = (6.77 \pm 0.94) \times 10^{-39}$	16.2
$Yb(^2F_{5/2}) \rightarrow Er(^4I_{11/2})$	$C_{DA} = (1.76 \pm 0.24) \times 10^{-39}$	13.0
$Er(^4I_{11/2}) \rightarrow Yb(^2F_{5/2})$	$C_{AD} = (1.18 \pm 0.16) \times 10^{-39}$	14.3

The study of luminescence decays at 2.7 μm shows that there is a process of rapid diffusion of excitation energy which occurs in a very short time, affecting the initial distribution of excitation between Yb^{3+} ions, which strongly affects the mechanism of Yb - Er energy transfer. This manifests itself in the fact that the probability of the presence of an excited Yb^{3+} ion near the Er^{3+} ion is higher than predicted by the Inokuti-Hirayama model.

In the article by Aarts et al. [15] energy transfer mechanisms are studied in $NaYF_4$ powders doped with 1 mol% Er^{3+} and 1, 5, 10, 30 mol% Yb^{3+} under excitation at 380 nm. The dependence of luminescence intensity of Er^{3+} emission bands on Yb^{3+} concentration showed that effective cross-relaxation between Er^{3+} and Yb^{3+} ions is present from the states $^4G_{11/2}$ and $^4S_{3/2}$ of Er^{3+}, and there is no cross-relaxation from the state $^4F_{9/2}$. It is shown that in co-doped samples the $^4F_{9/2}$ level is predominantly populated by the Er^{3+} ($^4G_{11/2} \rightarrow {}^4F_{9/2}$) - Yb^{3+} ($^2F_{7/2} \rightarrow {}^2F_{5/2}$) cross-relaxation process. In addition, the absence of luminescence from the level $^4F_{7/2}$ suggests that in these samples the non-radiative relaxation process prevailed over the emissive transition from the level. However, the authors suggest that luminescence can be observed in crystals with even lower phonon energy (<250 cm^{-1}).

The work by Xu et al. [71] is devoted to determining the population of the excited states of Er^{3+} ions in two series of GdF_3 nanoparticles co-doped with Er^{3+} and Yb^{3+} ions. The first concentration series consists of samples containing 20 mol% Yb^{3+} and, 2, 3, 5 mol% Er^{3+}, and the second consists of 2 mol% Er^{3+} and 10, 20, 40, 60 mol% Yb^{3+}. Using the dependencies of luminescence intensity on doping concentration, and excitation intensity, as well as rate equations describing the population of excited states of Er^{3+} ion, an excitation propagation model shown in Figure 1.7 is developed.

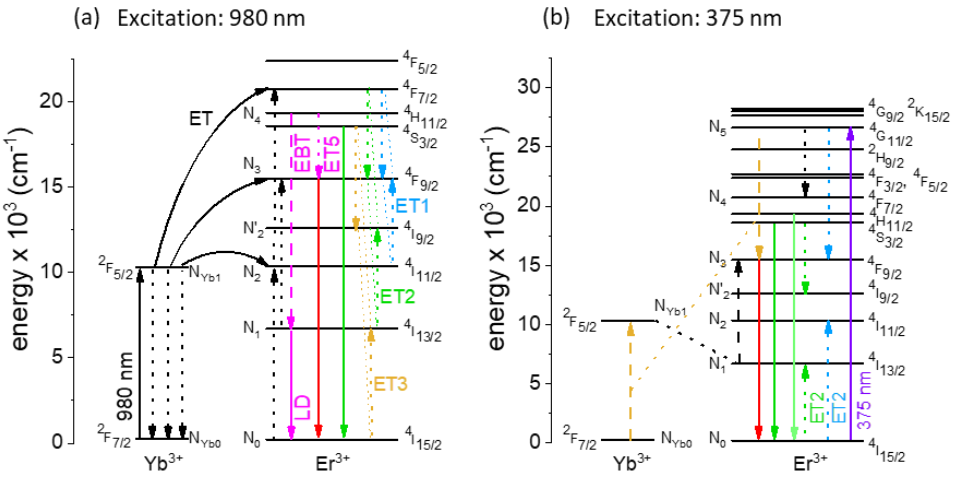

Figure 1.7 - Excitation energy transfer processes between Er^{3+} and Yb^{3+} ions under a) 976 nm and b) 378 nm excitation [71].

It was discovered that the $^4F_{9/2}$ level is populated via the route indicated in Figure 1.7a as ET5. This process involves a combination of reverse energy transfer, multi-phonon relaxation and depopulation of the intermediate state $^4I_{13/2}$.

The result of the study of pump excitation propagation at 378 nm is shown in Figure 1.7b. It is shown that cross-relaxation processes that lead to the decrease in the population of the levels $^2H_{11/2}$ and $^4S_{3/2}$ and an increase in the population of the level $^4I_{13/2}$ also play a decisive role in the energy transfer processes.

In the work by Yu et al. [72] the parameters describing the cross relaxation between Er^{3+} and Yb^{3+} ions from $^2H_{9/2}$, $^2H_{11/2}$ and $^4S_{3/2}$ excited states in β-NaYF4:Yb, Er particles are determined. The Dornauf-Heber model based on the same principles as the Inokuchi-Hiroyama model is used. This model additionally takes into account the fact that the donor-acceptor distances can only take discrete values proportional to the lattice parameters. The critical energy transfer distances in Er - Er and Er - Yb pairs are 4 and 3 Å, respectively, for cross-relaxation processes from the Er^{3+}:$^2H_{9/2}$ level, and 9 and 4 Å for transitions from the Er^{3+}:$^2H_{11/2}$, $^4S_{3/2}$ levels. This suggests that the quenching of the luminescence of Er^{3+} ions is predominantly carried out by other Er^{3+} ions rather than by Yb^{3+} ions. This is a fundamental result since the Er^{3+}:$^2H_{11/2}$ and $^4S_{3/2}$ levels are intermediate for populating the $^4F_{9/2}$ and $^2H_{9/2}$ levels during up-conversion processes.

The article by Fan et al.[73] is devoted to the study of up- and down-conversion in β-$NaYF_4$:Yb, Er microcrystals under excitation at wavelengths of 488, 940 and 980 nm. The proposed excitation migration pathways are shown in Figure 1.8

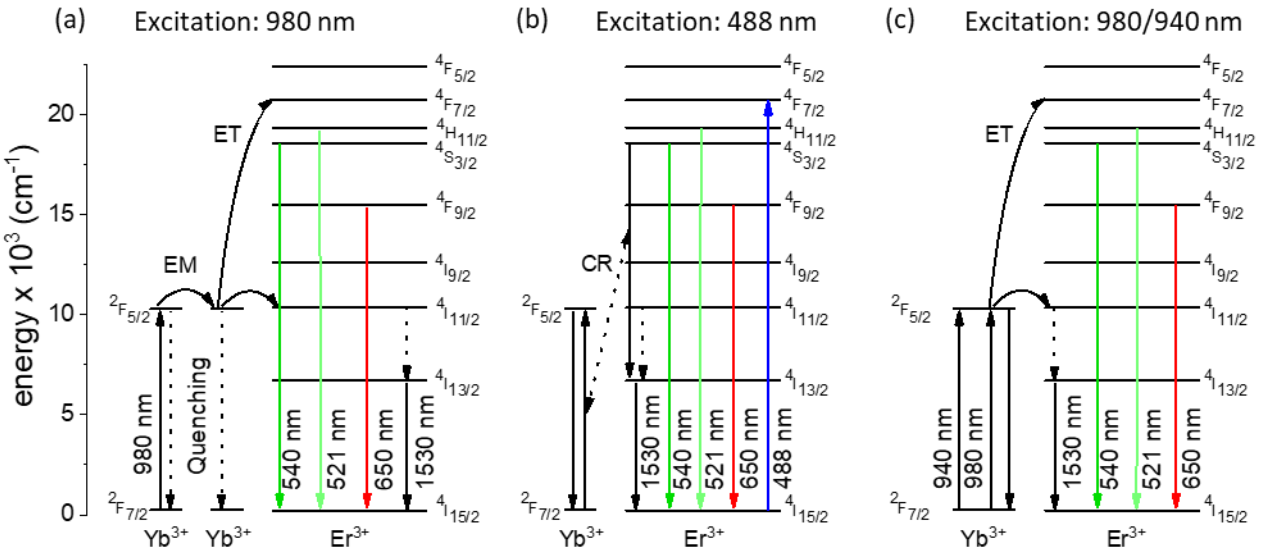

Figure 1.8 - Mechanisms of up- and down-conversion luminescence of the Er^{3+} and Yb^{3+} ions when excited at a) 980 nm, b) 488 nm and c) 980, 940 nm [73].

One of the main results obtained in this study is the conclusion that when excited at 980 nm, up-conversion and down-conversion processes occur simultaneously. Due to the nonlinear nature of up-conversion, these processes manifest differently depending on the excitation intensity. At relatively low excitation intensities (<1 W/cm^2), down-conversion processes dominate. In turn, up-conversion becomes more prominent at pumping intensities exceeding 10 W/cm^2.

Another feature of the up-conversion process is the so-called up-conversion saturation. It is known that in up-conversion the emission intensity can nonlinearly depend on the excitation and the form of the dependence will be determined by the number of photons needed to excite the corresponding emissive level. This dependence has the form of $I \sim P^n$, where I is the luminescence intensity, P is the excitation intensity, and n is the number of excitation photons needed to populate the excited state [74]. However, a deviation from this dependence is observed at high excitation intensities. The paper by Suyver et al. [75] outlines the basic principles explaining such behaviour. For any level involved in the up-conversion, several processes take place simultaneously: the population comes from the excitation from the lower-lying levels

and the depopulation occurs via spontaneous transitions to the lower-lying levels. At low pumping intensities, the spontaneous transitions play the dominant role in level population change and the dependence will be of the form $I \sim P^n$. At high excitation intensities, up-conversion processes begin to play an increasing role in influencing the type of dependence. In the case of saturation of the population of lower levels, the dependence takes the form $I \sim P^n$. Schematically the described processes are shown in the Figure 1.9

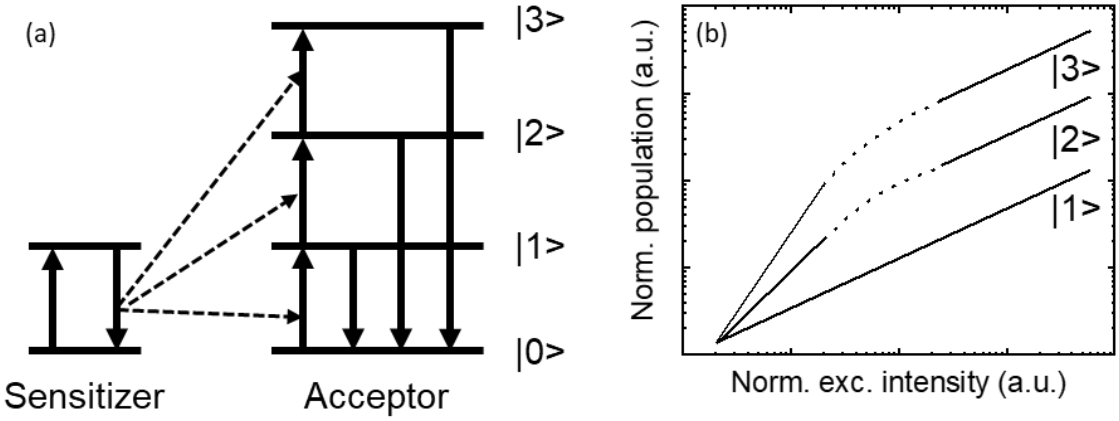

Figure 1.9 - a) Schematic representation of the energy levels of the up-conversion system, b) dependence of the population of the levels of this system on the excitation intensity [75].

1.5 Up-conversion in the MF_2: Er, Yb (M = Ca, Sr, Ba, Pb) crystals

One of the key characteristics of up-conversion material is the internal photoluminescence quantum yield (PLQY). The internal quantum yield is defined as the ratio of the number of emitted and absorbed photons. It characterises the efficiency of the conversion of absorbed excitation photons into up-conversion emission. However, this is not the only figure of merit that can be used to describe the energy conversion in a material. External quantum yield is another value that is defined as a ratio of the number of emitted and incident photons. Another similar parameter parameter is brightness. It is defined as a product of internal quantum yield and

absorption coefficient at the excitation wavelength. PLQY of any particular emission band can be estimated under a number of various conditions. Resonance excitation is the case when the excitation wavelength corresponds to the energy gap between the ground state and the emissive level. Downshifting quantum yield is defined when the excitation wavelength corresponds to the level located at higher energy than the emissive one, whereas the up-conversion quantum yield is the opposite case when the excitation wavelength corresponds to the level located at lower energy.

To date, the record value of up-conversion quantum yield under excitation at a wavelength of about 980 nm for a material doped with Er^{3+} and Yb^{3+} ions is 10.5% and is obtained in β-$NaYF_4$: 21.4 mol.% Yb^{3+}, 2.2 mol.% Er^{3+} particles at a pump intensity of 35 W/cm[276]. Other published works on efficient up-conversion materials include BaY_2ZnO_5: 7 mol% Yb^{3+}, 3 mol% Er^{3+} phosphors with a luminescence quantum yield value as high as 5% at 2.2 W/cm[251] as well as La_2O_2S: 9 mol.% Yb^{3+}, 1 mol.% Er^{3+}, where the quantum yield is 5.8% at an excitation power density of 13 W/cm^2 [77].

Even from a brief overview, it is evident that the efficiency of the up-conversion process is influenced by a large number of factors. The crystal host is one of the most important elements in obtaining efficient up-conversion since it determines the environment of the optical centres and the crystal field, which directly affects the probability of electronic transitions in rare earth ions. Also, the crystal host should have low phonon energy. This allows for minimizing non-radiative losses and enhances radiative transitions. A wide variety of matrices can be doped with Er^{3+} and Yb^{3+} ions. Materials containing these ions can be based on glasses [687879] as well as oxide crystals [80,81,82]. Among all possible variants of crystal hosts, fluorides are optimal candidates because of their relatively low phonon energy and good chemical stability [83, 84]. At the moment quite a few papers have been published on the up-conversion properties of the fluoride materials doped with Er^{3+} and Yb^{3+} ions.

For example, several papers investigating the efficiency of up-conversion processes in fluoride crystals with the MF_2 (M = Ca, Sr) structure have been recently

published [20, 21, 22, 23]. In the works [21, 22] possibility of efficient up-conversion luminescence in CaF_2:Er,Yb particles when excited at 980 nm is shown. In the work [20] luminescence quantum yield of SrF_2 microparticles doped with 2 mol% Er^{3+} and 2 mol% Yb^{3+} is reported to be 2.8% at a pump intensity of 10 W/cm^2. In a later article [23] properties of SrF_2 single crystals doped with Er ions^{3+} and Yb^{3+} are reported. The maximum value of luminescence quantum yield mentioned in the article is 6.5%. This result is obtained under excitation at a wavelength of 976 nm with a power density of 230 W/cm^2. These results show promise for the use of crystalline materials with similar structures for efficient up-conversion.

The next compound in the MF_2 series is the BaF_2 crystal. According to the data available in the literature, the phonon energy in this crystal is ~240 cm^{-1} [24, 85]. This value is somewhat lower than the similar parameter in the materials mentioned above. The value of phonon energy is 360 cm^{-1} in β-$NaYF_4$ [86], 350 cm^{-1} in LaF_3 [87] 320 cm^{-1} in CaF_2 [83] and 284 cm^{-1} in SrF_2 crystals [83].

Thus, the BaF_2 crystalline host has great potential for applications in efficient up-conversion materials, as similar materials already exhibit rather high values of luminescence quantum yield, and the lower phonon energy of BaF_2 allows expecting lower non-radiative losses and higher luminescence quantum yield [24].

Whereas optical materials doped with Er^{3+} and Yb^{3+} ions such as CaF_2: Er^{3+}, Yb^{3+} and SrF_2: Er^{3+}, Yb^{3+} are quite well studied and many of their up-conversion characteristics can be found in published articles, barium fluoride remains a relatively under-researched host for similar applications. There are only a few papers where the optical characteristics of BaF_2 crystals doped with Er^{3+} or Yb^{3+} ions are investigated in detail.

In the paper "Spectroscopic investigation of Er^{3+} doped BaF_2 single crystal" [88] the basic luminescence characteristics of BaF_2 single crystal, doped with 2 mol% Er^{3+} ions are investigated. In this work absorption spectra in the UV to NIR range, as well as excitation spectra when detected at a wavelength of 530 nm are given. Using

absorption spectra and Judd-Ofelt theory the authors calculate the Ω parameters and lifetimes of excited states. The luminescence decay times of the $^4S_{3/2} \rightarrow ^4I_{15/2}$ and $^4F_{9/2} \rightarrow ^4I_{15/2}$ transitions were also experimentally determined. The authors do not explain the difference from the mono-exponential appearance of the decay curve the of $^4S_{3/2} \rightarrow ^4I_{15/2}$ transition and further use the value of the effective decay time. Comparing the calculated lifetime and the luminescence decay time determined experimentally, the authors obtained the $^4S_{3/2} \rightarrow ^4I_{15/2}$ transition quantum efficiency value as 70%. This value is in good agreement with the results known for other fluoride hosts doped with Er^{3+} ions.

Up-conversion in the BaF_2: Er^{3+} material was investigated in the article [89]. It is shown that when excited at a wavelength of 976 nm, up-conversion is observed in samples with an erbium content of 5 to 35 mol%. The dependence of luminescence intensity at 528, 550 and 660 nm on the excitation intensity showed that the population of excited states happens due to the absorption of two photons. In addition, the phonon energy in the BaF_2 host (~240 cm^{-1}), as well as the luminescence decay times at 410 nm under 808 nm excitation (1.4 ms) and 496 nm for 976 nm excitation (0.87 ms) are determined.

The distribution of the Er^{3+} ion in the BaF_2 crystal is studied in the "Growth and characterization of ErF_3 doped BaF_2 crystals" article. [90]. In this work the distribution of impurity in crystals is investigated in a series of samples with various Er^{3+} concentrations from 0.05 to 0.5 mol.%. It is shown that the absorption coefficient depends not only on the amount but also on the position of doping ions in the crystal lattice. In addition, it is shown that the absorption bands contain bands from both trigonal centres and clusters, and the absorption intensities of bands associated with clusters increase with concentration much faster than the intensities of peaks from C_{3v} centres. These dependencies of the absorption coefficient value on the position in the crystal lattice allow estimating the impurity distribution coefficient in the range from 0.6 to 0.86 for clusters and from 0.76 to 0.98 for C_{3v} centres.

In addition, there are several papers devoted to the synthesis of BaF_2 crystalline particles, doped with Er^{3+} ions. In the work [91], the synthesis of BaF_2 particles containing Er^{3+} ions by an ultrasonic pulse method is demonstrated. As proof of successful synthesis, the paper presents X-ray diffraction patterns of the samples containing peaks characteristic of BaF_2 lattice, as well as absorption and emission spectra showing lines corresponding to transitions in the erbium ion.

Separately the works devoted to the study of the formation of optical centres in BaF_2 crystals doped with rare-earth ions should be mentioned. In the article [92] the structure of optical centres is investigated in a series of BaF_2 samples doped with a small amount of Er^{3+} ions (0.01 - 1 mol%). Using a selective laser excitation method, it is discovered that in the BaF_2 host, only one charge-compensated centre consisting of Er^{3+} - F^- ions pair is formed, whereas in the CaF_2 host, there are 2, and in the SrF_2 host there are 4 centres. The remaining centres found in the BaF_2 host turned out to be clusters consisting of two or more Er^{3+} ions, between which efficient energy transfer is possible. The authors point out that the clusters largely determine the optical properties of the material as the luminescence intensity of cluster centres increases with concentrations of Er^{3+} ions and at 0.2 mol.% it exceeds the intensity of luminescence of Er^{3+} - F^- single pairs by more than 100 times. The main difference between materials based on BaF_2 from similar materials based on CaF_2 and SrF_2 hosts is a lower non-radiative relaxation rate.

In the work [93], the structure of Er^{3+} - F^- centres with charge compensation is investigated in more detail using selective laser excitation. The BaF_2 sample, doped with 0.05 mol.% Er^{3+} is used for the measurements. The authors can experimentally demonstrate that such centres consist of a single rare-earth ion whose charge is compensated by an F^- ion located on the adjacent position along 111 crystallographic axes. It is confirmed that the environment of this centre has C_{3v} symmetry. However, the study of the luminescence intensity dependence on polarization in a high magnetic

field revealed that the environment has small distortions. The crystal field analysis in the C_{3v} symmetry approximation provided results comparable to the experimental data.

The article [94] further discusses the role of clusters of doping ions. The authors showed that although some lines in the absorption spectrum could be interpreted as single centres in different environments, the close arrangement of the lines is explained by the fact that the ions in the cluster could efficiently exchange energy and thus the number of lines increases.

Similarly, the formation of impurity centres of Yb^{3+} ions in the BaF_2 host is studied. In the work [95,] the change in the absorption cross-section of Yb^{3+} ions in CaF_2, SrF_2 and BaF_2 hosts is considered. The results clearly show an increase in the absorption cross-section when transitioning from Ca to Sr and then to Ba cation. The value of the absorption cross-section of the sample with 2 mol% Yb^{3+} in the BaF_2 host is $9.4*10^{-21}$ cm^2. At the same time, the observed luminescence decay time in all samples remained approximately the same: 2.8 ms in SrF_2, 2.6 ms in BaF_2 and 2.4 ms in the CaF_2 host.

The structure of the Yb^{3+} optical centres in the BaF_2 crystal is discussed in more detail in [96]. At low concentrations of the doping ions (<0.01%) the absorption spectrum contains one peak with a maximum around 968 nm. This peak is attributed to the centre with trigonal C_{3v} symmetry consisting of Yb^{3+} ion and F^- ion which compensates the charge. When the doping concentration is increased, a second peak with a maximum around 976 nm appears in the absorption spectrum. The intensity of this peak rapidly grows with an increase in concentration and at 0.2 mol % its intensity exceeds the value of the C_{3v} peak. This new peak is associated with clusters of doping ions. In addition, another absorption band with a maximum around 920 nm becomes intense when Yb^{3+} concentration exceeds 2%. This band is formed due to the absorption of optical centres with cubic O_h symmetry. Using the dependence of the absorption coefficient value on the position in the crystal, it is determined that the distribution coefficient of Yb^{3+} ions in the BaF_2 crystal is in the range of 0.7 - 0.84.

Another host for Er^{3+} and Yb^{3+} ions that might facilitate an efficient up-conversion process is lead fluoride. PbF_2 can have two types of unit cells – orthorhombic (α phase) and cubic (β phase). Only the cubic phase can form under the atmosphere pressure. It has several properties that allow expecting high up-conversion quantum yield values from the PaF_2 crystals doped with Er^{3+} and Yb^{3+} ions. First, the material is reported to demonstrate low phonon energy values (257 cm^{-1})[25] which are similar to ones observed in other MF_2 hosts. Additionally, as has been stated above transition from CaF_2 to SrF_2 and then to BaF_2 leads to higher up-conversion quantum yield values in Er^{3+} and Yb^{3+} ions suggesting that heavier cations might help achieve greater quantum yield values. Pb^{2+} divalent ion is the next step in this series.

Currently, there are only a few published works dedicated to the study of the optical properties of PbF_2 crystals doped with rare-earth ions. Types of the doping centres in the PbF_2:Yb single crystals are studied in the work [97]. Two types of centres are discovered: Yb^{3+} ions in a cubic symmetry site are revealed with electron paramagnetic resonance spectroscopy, whereas Yb^{3+} ions in clusters are discovered with site-selective laser spectroscopy. It is also noted that the second type dominates in the samples with a concentration of Yb^{3+} ions equal to 2 mol.%. This result is similar to the conclusions drawn during the study of impurity centres in BaF_2 host that say that if the concentration of rare-earth exceeds 1 mol.% then the optical properties are defined by clusters. Clustering of trivalent ions is further proved in the work [98] using the simulation of the diffuse scattering.

The optical properties of the PbF_2:Er particles are studied in the work [99]. A study of the up-conversion emission spectra under 1560 nm excitation shows that the optimal concentration of the Er^{3+} ions is 5 mol.%. Additionally, the combination of PbF_2:Er particles with bifacial Si-solar cells resulted in the 0.5% enhancement of the efficiency of the solar cell under co-excitation with AM1.5 and laser irradiation.

Work [100] presents the comparison between the emission of Er^{3+}-doped PbF_2 particles in glass ceramics and single crystals under 488 nm excitation. Even though all

studied samples have similar emission bands the relative intensity of these bands somewhat varies. The emission from the $^4S_{3/2}$ level is the most prominent in particles in glass ceramics whereas in the single crystal samples, the emission from the $^4F_{9/2}$ and $^4I_{9/2}$ dominates the spectrum. This once again shows that in PbF_2 single crystals rare-earth ions tend to form clusters that facilitate cross-relaxation processes that manifest in redistribution of energy between the excited states.

The up-conversion emission of the Er^{3+}-doped PbF_2 nanocrystals in glass ceramics is discussed in the work [101]. The emission spectra in the visible range obtained under 980 nm excitation show bands originating from $^2H_{9/2}$, $^2H_{11/2}$, $^4S_{3/2}$ and $^4F_{9/2}$ excited states. Intensity dependence of the $^4S_{3/2} - {}^4F_{15/2}$ and $^4F_{9/2} - {}^4F_{15/2}$ emission bands demonstrates that these excited states are populated via a stepwise process and that multiphonon as well as cross-relaxation are present.

The up-conversion performance of the PbF_2 nanoparticles doped with Er^{3+} and Yb^{3+} ions is discussed in the works [102,103]. Both papers present similar emission spectra. The effect of the concentration is studied and it is highlighted that PbF_2 nanoparticles can be doped with Yb^{3+} or Er^{3+} ions to a very high doping level of 10 at.% with no concentration quenching. It is also predicted that this material can achieve high values of the luminescence quantum yield, but no experimental proof is presented.

To sum up, the available data confirms the assumptions made above that BaF_2 crystals, doped with Er^{3+} and Yb^{3+} ions can be promising up-conversion materials. This is evidenced, for example, by the low phonon energy of the BaF_2 crystal host, as well as by the relatively high absorption cross-section of Yb^{3+} ions and their long excited state lifetime. Besides, the very structure of optical centres in BaF_2 crystals may be favourable for efficient up-conversion in the pair of Er^{3+} - Yb^{3+} ions. Several papers show that when the concentration of doping ions exceeds 1%, the optical properties of the material are determined mainly by the ion clusters. Since up-conversion in materials containing Er^{3+} and Yb^{3+} ions is realized by the ETU mechanism, clustering of ions that reduces the distance between them should lead to higher energy transfer efficiency and,

hence, up-conversion. However, there are no comprehensive studies of the BaF_2 crystals co-doped with Er^{3+} and Yb^{3+} ions. To determine the highest achievable up-conversion quantum yield concentration effects of both doping ions should be studied.

A similar conclusion can be drawn in the case of PbF_2 crystals. The data currently available in the published works suggests that PbF_2 crystals doped with Er^{3+} and Yb^{3+} ions should have similar behaviour to extensively studied CaF_2 and SrF_2 crystals with the same doping ions as well as BaF_2:Er^{3+}, Yb^{3+} material. It has been reported in several papers that in the PbF_2 host doping ions form clusters which can be beneficial for the up-conversion process. This as well as low phonon energy makes PbF_2 a promising host for up-conversion. However, a comprehensive study of the energy transfer processes is needed to confidently answer this question.

1.6 Down-conversion in the Er^{3+} - doped crystals

UC emission is not the only feature of Er^{3+} ions. A complex system of the energy levels of the Er^{3+} ions makes it possible to suggest the possibility of the quantum-cutting process (QC). QC is a process during which the absorption of one high-energy excitation photon leads to the emission of two or more photons with lower energy. In theory, if a QC is realized in a material, then the observed internal PLQY should exceed 100% making such material a great spectral converter.

Generally, three main processes are differentiated [104]. The first one is quantum cutting via host lattice sites. Quantum cutting on host lattice sites involves the generation of multiple lower-energy electron-hole pairs per higher-energy photon through impact ionization. Certain luminescent materials, like europium-doped yttrium oxide (Y_2O_3:Eu^{3+}), have demonstrated high visible external quantum efficiency (EQE) reaching 240%. However, achieving such value has required an exceptionally high excitation energy of 23 eV. Additionally, energy of at least 15 eV was necessary to achieve an EQE greater than unity [105]. The limited performance of phosphors in the near-bandgap region can be attributed to surface recombination effects[106].

The second type is Quantum-cutting on single rare-earth ions. This process is possible thanks to narrow energy levels of rare-earth ions that are separated by large energy gaps. In the mid-1970s, two research groups discovered the phenomenon described as the first instance of quantum cutting in rare earths. They utilized Pr^{3+} as the activator ion in their experiments. The process involves the initial absorption of an 185nm photon by the YF_3 host lattice. The absorbed energy is then transferred to the lower-lying $^1S_0$ state via a 4f-5d transition. Subsequently, a blue photon (408 nm) is emitted through the $^1S_0$-$^1I_6$ transition, and a red photon (620 nm) through the $^3P_0$-$^3H_6$ transition. This process exhibited an impressive external quantum efficiency (EQE) of about 140% [107].

The last type uses pairs of rare-earth ions. This is the method mainly realized in systems doped with Er^{3+} ions. The term down-conversion (DC) is misused in the literature, sometimes meaning QC while on other occasions simply DS. To avoid confusion, here the term 'DC' is defined in a manner consistent with the definition used by Meijerink and co-workers[108–110], referring to a process whereby the emission of multiple lower-energy photons is achieved via cross-relaxation between two ions. This mechanism originated in the 1950s when Dexter formulated the concept of achieving two-photon emission through energy transfer [111], and it can be treated as the opposite of the energy transfer up-conversion (ETU) process [112]. Figure 1.10 shows some of the possible ways to achieve DC from the visible to the NIR spectral range in the Er^{3+} ions.

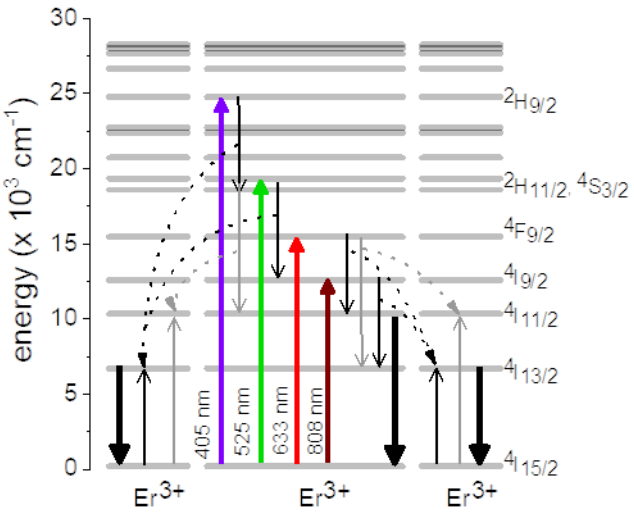

Figure 1.10 - Energy level diagram of an Er^{3+} ion with possible mechanisms of DC and cross-relaxation between Er^{3+} ions.

The DC processes in Er^{3+} have already attracted a bit of attention. In the work [113], the possibility of a visible DC process in the $LiGdF_4$ codoped with Er^{3+} and Tb^{3+} is studied upon Er^{3+} $4f^{11} \rightarrow 4f^{10}5d$ excitation. It is shown that 150 nm excitation might lead to the emission of two green photons – one by Er^{3+} ion and the second one by Tb^{3+} ion.

The next article [114] is dedicated to the study of DC in the Er^{3+} and Yb^{3+} $Cs_3Y_2Br_9$ crystals. Using luminescence decay times and emission spectra it is demonstrated that intrinsic DC efficiency of the 1000 nm emission of Yb^{3+} is as high as 95%.

Additionally, DC in Er^{3+} and Yb^{3+} doped $CsPbCl_3$ perovskite thin films is analyzed in [115]. Absolute quantum yield measurements demonstrate that under 300 nm excitation, the luminescence quantum yield of either Er^{3+} or Yb^{3+} emission can exceed 100% depending on the concentration ratio of the doping ions.

DC properties of the Er^{3+}/Yb^{3+} pair of doping ions in the La_2O_2S host is researched in the article [116]. As in the previous work, the absolute quantum yield measurements show that total emission yield in both Vis and NIR spectral ranges

exceeds 100% under 523 nm excitation. However, none of the emission bands has a quantum yield value higher than 100%.

Emission of Er^{3+} doped $NaYF_4$ nanostructured glass ceramics is studied in the work [117]. Here efficiency of the DC process is estimated using luminescence decay times of the Er^{3+}:$^4S_{3/2} \rightarrow {}^4I_{15/2}$ transition under 485 nm excitation. It is concluded that the efficiency can go up to 150% in the sample doped with 4% of Er^{3+} ions.

To sum up, an overview of the published results makes it clear that efficient DC in Er^{3+} ions with a quantum yield value above 100% is possible. It is shown that hosts with low phonon energy are crucial for efficient DC process. However, a comprehensive analysis of a wide concentration series of Er^{3+}-doped samples under various excitation wavelengths is still required to answer the question if such light conversion is useful for photovoltaic applications.

2. Sample synthesis and research methodology

2.1 Sample synthesis methodology

The YF_3: Ce^{3+}, Yb^{3+} samples were synthesised from yttrium fluoride, cerium fluoride and ytterbium fluoride (purity 99.99%, LANHIT). The initial components were mixed in appropriate proportions and put inside a multi-channel graphite crucible placed inside a vacuum furnace. The furnace chamber was pumped out to 10^{-3} torr and then slowly heated to 1000° C. When the temperature was reached, the vacuum pump was stopped and a CF_4 and Ar gas mixture was pumped into the chamber until a pressure of 380 torr was reached. The temperature was then raised to the melting point of 1155° C and kept at this point for 30 minutes, after which it was cooled back to room temperature in time of three hours. The crystalline samples were then ground to a powder in an agate mortar.

Crystalline barium fluoride samples were synthesised according to the following procedure. Powders of barium fluoride, ytterbium fluoride and erbium fluoride of high purity (99.99% LANHIT, Russia) were taken as initial components. Preliminarily, the powders were melted in a fluorinating atmosphere of CF_4. Then, crystals were synthesised in a vacuum furnace in a CF_4 atmosphere. The heater, crucible as well as the temperature gradientor (60-80 K/cm) were made of graphite. The temperature (1350° C) and crystallization rate (6.5 mm/hr) were chosen based on the phase diagrams of BaF_2 -Ln^{3+} [118, 119]. The obtained crystals were 5 cm in length and 10 mm in diameter. The crystals were sawed in a plane perpendicular to the long axis of the crystal and the resulting discs (~2 mm thick and 10 mm in diameter) were polished before optical measurements.

Two series of BaF_2 crystalline samples doped with Er^{3+} and Yb^{3+} ions as well as a series of BaF_2 samples single doped with Er^{3+} ions were prepared for the study. The first series consisted of samples with a nominal content of activator ions equal to 2 mol% Er^{3+} and 2, 3, 5, 7.5, 10 or 15 mol% Yb^{3+}. Hereafter, the mol.% denotes the

nominal concentration of rare earth ions used in crystal growth. The second series consisted of crystals containing 3 mol % Yb^{3+} and 3, 5, 10 or 15 mol % Er^{3+}. The series of single-doped crystals consisted of samples with 1, 2, 3, 4, 5, 12, 14, 18, 20 and 25 mol.% Er^{3+}. These concentration series were chosen based on previous studies, which showed that significant concentration quenching of luminescence and deterioration of up-conversion characteristics of the materials would take place if the concentration of any of the ions exceeded 15 mol %[120,121].

Single PbF_2 crystals, doped with Yb^{3+} and Er^{3+}, were grown in multichannel graphite crucibles using the Bridgman technique under a vacuum environment. The growth process involved employing a CF_4 fluorination atmosphere and a temperature gradient of 7 degrees per millimetre. The growth rate was set to be 7 millimetres per hour based on analyzing the stability function of a flat crystallization front[119]. The choice of the growth temperature (870°C) was determined on the PbF_2-RF_3 (R=Yb, Er) phase diagrams[122]. The resulting crystalline samples were shaped into disks 10 mm in diameter and approximately 1.7 mm in thickness. These disks were cut perpendicular to the long axis of the crystal boule.

2.2 Methodology of sample examination

2.2.1 Physico-chemical analysis

The lattice parameters of the YF_3: Ce^{3+}, Yb^{3+} samples are determined with X-ray diffractometer Bruker D8 Advanced (CuKα radiation). To calculate the lattice parameters the Powder 2.0 ($\Delta Q<10$) program is used. Particle size and morphology are determined with a Carl Zeiss NVision 40 scanning electron microscope with an energy dispersive spectrometer. To determine the crystal structure of the BaF_2, a small portion of the samples is ground to powder and X-ray diffraction patterns were recorded with a Bruker D2 Phaser diffractometer (CuKα radiation source). The patterns are recorded in the 2Θ angle range of 10 - 70^0.

The actual concentration of Ba^{2+}, Er^{3+} and Yb^{3+} ions is determined using wavelength dispersive X-ray fluorescence spectroscopy (WDXRF) (Pioneer S4, Bruker AXS). Three samples from each crystal are analysed to obtain the result. 25 mg of sample material (± 0.05 mg) is dissolved in 6 g of EQF-TML-5050-5 (49.75% $Li_2 B_4 O_7$ + 49.75% $LiBO_2$ + 0.5% LiBr) in a platinum crucible at 1373 K. After cooling in the platinum cell, the resulting alloy is analysed. Four standard samples adapted for the studied host (BaF_2, Er_2O_3, Yb_2O_3) are melted for calibration. Two to three energy lines of the elements are used for the calculation. The standard deviation of the chemical composition does not exceed 0.6 wt% for barium 0.07 wt% for erbium and 0.05 wt% for ytterbium.

The Raman spectrum for the undoped BaF_2 sample is recorded with the i-Raman instrument from Polytec (excitation 785 nm, resolution 3.5 cm^{-1}).

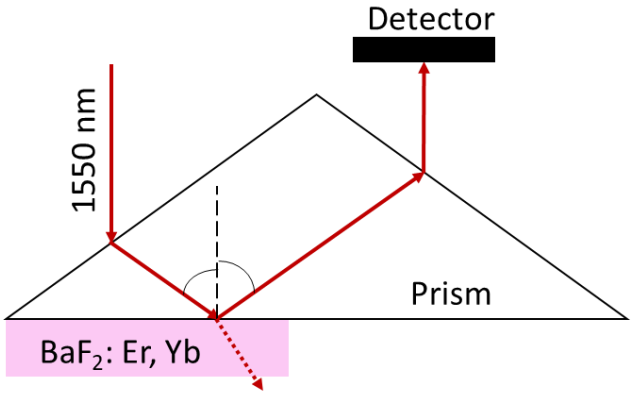

Figure 2.1 - Schematic diagram of refractive index measurement.

The refractive indices of the samples are determined using the Metricon 2010/M prism coupling element using 1550 nm laser emission (Thorlabs, TLK-L1550R). The Metricon 2010/M operates as follows. Through a prism with a known refractive index, the laser beam is directed towards the studied sample. Depending on the angle of incidence, the total internal reflection may be disturbed and the detected intensity may fall. The measured reflection profile is used to calculate n with a high accuracy (usually ±0,0005). A schematic of the instrument is shown in the Figure 2.1.

2.2.2 Spectral-kinetic analysis

The absorption spectra of all samples were recorded using a Perkin Elmer Lambda 950 spectrophotometer. The instrument recorded the value of optical density (A), which is then converted into an absorbtion coefficient using the following expression:

$$\alpha = -\frac{1}{d} ln(10^{A}). \quad 16$$

Here α - is the absorption coefficient of the sample in units of cm^{-1}, d is the thickness of the sample in centimetres. Excitation spectra were recorded using a pre-calibrated Varian Cary Eclipse spectrofluorimeter.

The luminescence quantum yield of BaF_2: Er^{3+}, Yb^{3+} samples is measured as follows. The sample is placed in the centre of an integrating sphere (Labsphere, 6 in. Ø, 3 P-LPM-060-SL) in a special holder. The luminescence spectrum of the sample is recorded with an Avantes, AvaSpec-ULS2048 × 64TEC spectrometer, and the excitation laser intensity is detected with a Thorlabs spectrometer, CCS200/M. Both spectrometers are calibrated and coupled to an optical sphere system using an Ocean Optics calibration lamp, HL-3plus-INT-CAL-EXT. The luminescence quantum yield is calculated after integrating the corresponding region of the luminescence spectrum and the excitation laser spectrum. The calculations are carried out using the well-known 3M algorithm [123124]. The whole system is controlled with the software implemented in the LabVIEW environment (National Instruments, LabVIEW Software) and developed at Karlsruhe Institute of Technology.

The following excitation sources are used to measure the luminescence quantum yield. A 375 nm LED is used to excite the $^4G_{11/2}$ level of the Er^{3+} ion, which is controlled by the Thorlabs control unit, ITC4001. To excite $^4S_{3/2,}$ $^4F_{9/2}$ Er^{3+} ion levels a tunable continuous wave laser at 522 nm and 652 nm is used (Solstis with EMM-Vis module, M-Squared Lasers Ltd). It uses a 532 nm laser (Verdi-V18, Coherent) as a

pump. The $^4I_{13/2}$ level of Er^{3+} ion is excited with a tunable laser (Thorlabs, TLK-L1550M) operating at a wavelength of 1520 nm. A schematic representation of the setup is shown in Figure 2.2

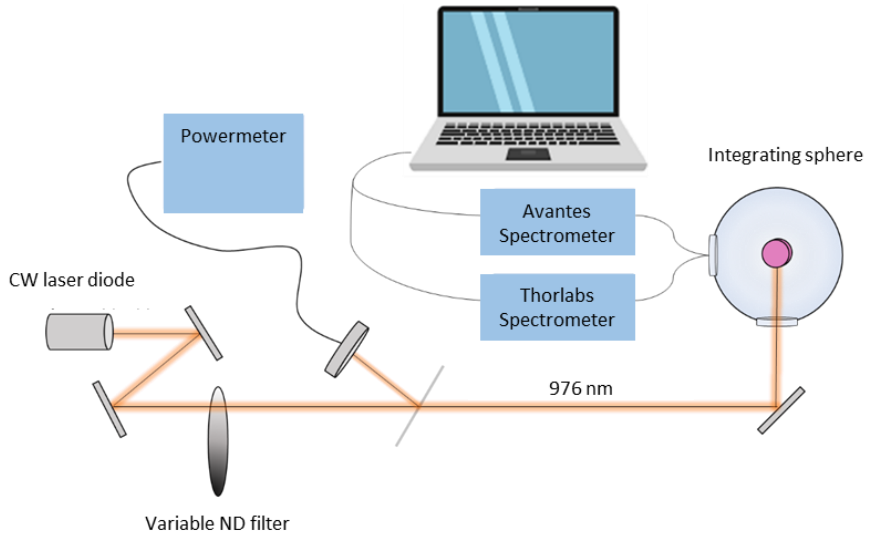

Figure 2.2 - Schematic of the luminescence quantum yield measurement setup.

When excited at 976 nm the quantum yield of the luminescence is recorded as a function of the excitation intensity. The excitation source is a Thorlabs L980P200 laser diode, operating in continuous wave mode. It is mounted in a temperature-controlled mount (Thorlabs, TCLDM9) and controlled by the Thorlabs ITC4001 control unit. The intensity of the laser was varied using a motorised continuously variable neutral density (ND) Filter (Thorlabs, NDC-100C-2). The excitation laser intensity is monitored using a Thorlabs PM320E power meter. For this purpose, a quartz plate is placed in the path of the laser beam, which reflects part of the beam and directs it to the powermeter. The intensity of the beam reflected from the plate is estimated as 8% of the total power. To determine the intensity of the excitation laser, the size of the laser spot is also monitored. For this purpose, a Thorlabs laser beam profiler, BP209-IR/M and a standard 2σ determination for beam axis size are used. In the Figure 2.3 there is an image of the beam profile of a diode laser with a wavelength of 976 nm. The intensity distribution along the X and Y axes is fitted with a Gaussian function. The

approximation results give 2σ values equal to 1922.84 and 3840.62 μm in the X and Y axes without focusing and 252.67 and 223.38 μm in the X and Y axes in case of focusing with a lens with a focal length of 20 cm, respectively. The corresponding areas are 0.0515 cm^2 without additional focusing and 0.000487 cm^2 when focused with a 20 cm lens.

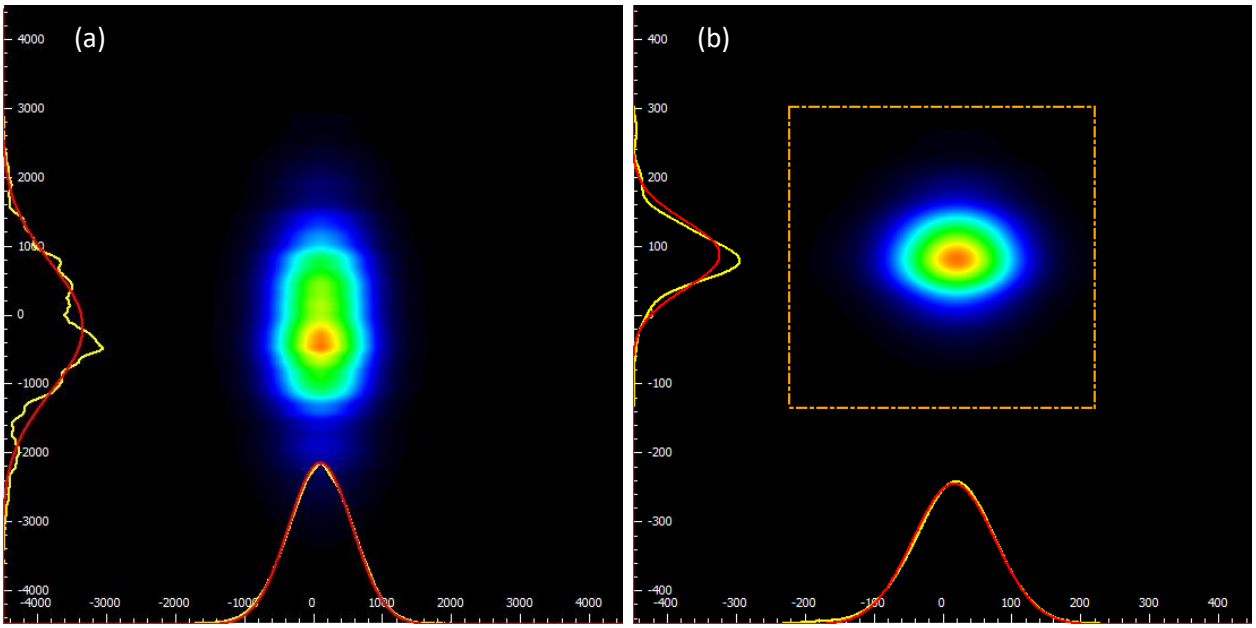

Figure 2.3 - Laser beam profile of the used excitation source at 976 nm a) without focusing, b) in the focus of the collecting lens with a focal length of 20 cm.

When up-conversion luminescence spectra of BaF_2: Er, Yb samples are obtained, a 950 nm short pass filter (Semrock, FF01-950/SP-25) is placed between the integrating sphere and the detector to keep the pump radiation from entering the detection path.

The characterization of quantum yield using the absolute method involves measuring the number of absorbed and emitted photons, denoted as N_a and N_e, respectively.

$$\phi_{UC}^{(a)} = \frac{N_e}{N_a}. \qquad 17$$

However, there are several factors to take into account when determining the number of photons in the integrating sphere. When the excitation light passes through the sample, it reflects multiple times inside the sphere, which can result in two effects

for Stokes luminescence: an increase in the number of absorbed photons and the generation of additional emitted photons. For up-conversion emission, only the first effect is relevant, as scattered light with a low intensity does not produce up-conversion. To address the first effect, a method called 3M, which involves three measurements, is utilized [125].

$$\phi_{UC}^{(a,exp)} = \left(PD - \frac{LD}{LI} \times PI\right) / \left(\left(1 - \frac{LD}{LI}\right) \times ES\right). \quad 18$$

In this context, PD refers to Photoluminescence Direct, which represents the number of photons emitted when the sample is directly excited. PI stands for Photoluminescence Indirect, which denotes the number of photons emitted when the sample is excited indirectly. ES is an abbreviation for Empty Sphere, which represents the number of excitation photons measured in an empty sphere without a sample. LD (Laser Direct) represents the number of excitation photons measured during direct excitation of the sample, while LI (Laser Indirect) represents the number of excitation photons measured during indirect excitation of the sample. It is important to note that to obtain the internal quantum yield $\phi_{UC}^{(a)}$ that is independent of sample geometry, an additional correction is required for the value $\phi_{UC}^{(a,exp)}$, which will be described in detail later in the section.

Further analysis highlights that measurements using an integrating sphere may slightly underestimate the $\phi_{UC}^{(a,exp)}$, and several potential causes of this deviation have been identified.

Similarly to excitation photons, emitted photons can also undergo reflection inside the integrating sphere, causing them to pass repeatedly through the sample and undergo reabsorption. Additionally, reabsorption might take place while emission propagates through the bulk of the crystalline sample. However, the transition Er^{3+}:$^4S_{3/2} \rightarrow {}^4I_{13/2}$ (at 845 nm) is not susceptible to reabsorption because it is a transition between two excited states. Therefore, two measurements can be conducted to estimate

the percentage of reabsorbed light inside the integrating sphere, assuming that the luminescent peak shape corresponding to the $^4S_{3/2} \rightarrow {}^4I_{13/2}$ transition remains unaltered. The first emission spectrum is obtained with the sample as is, while the second one is obtained with a sample ground to powder and then diluted with optically inactive particles in the ratio of 1-to-9. This method was proposed and tested by Meijerink et. al. [35,36]

Another reason for the underestimation of $\phi_{UC}^{(a)}$ is the non-linear nature of the UC process, where the up-conversion yield is dependent on the excitation intensity ($\phi_{UC} \sim I^n$). As light propagates through a crystal with finite thickness, the excitation intensity decreases, leading to a higher value of $\phi_{UC}^{(a,exp)}$ for thinner crystals. To quantify this phenomenon, the following calculations are conducted. A sample is assumed as a seamless stack of 100 layers with the same absorption and UC PLQY behaviour ($\phi_{UC} \propto I^m$, where I is the incident intensity and *m* can range from 0 at high excitation intensity to 1 at low excitation intensity). These assumptions allow obtaining the following dependence of the decrease in the observed UC PLQY on the total absorptance of the sample at different values of *m*.

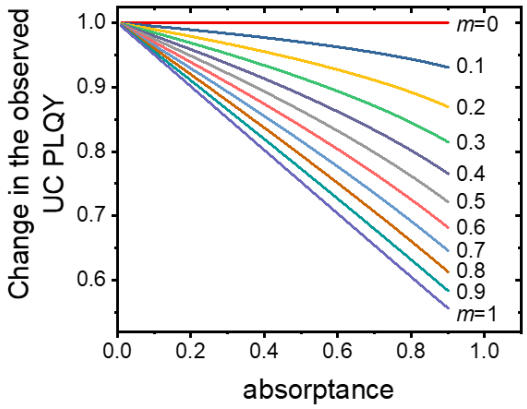

Figure 2.4 - The decrease in the observed UC PLQY as a function of sample absorptance and the slope (m).

The data in Figure 2.4 shows that if *m = 0*, i.e. PLQY is not intensity-dependent, there is no decrease in the observed PLQY regardless of the absorptance. The higher

the value of *m*, the more pronounced the absorptance dependence is. In the case of *m = 1* and absorptance of 0.5, only 75% of the actual PLQY value is observed experimentally.

One more effect that may lead to underestimation of $\phi_{UC}^{(a)}$ is local heating within the excitation spot, as reported by Joseph et al.[126]. This effect can be corrected by using a coefficient to account for temperature changes. The local temperature can be determined with the ratio of emission intensity of two thermally coupled Er^{3+} levels, namely $^2H_{11/2}$ and $^4S_{3/2}$. An increase in temperature should lead to an increase in the intensity ratio of the $^2H_{11/2} \rightarrow {}^4I_{15/2}$ and $^2S_{3/2} \rightarrow {}^4I_{15/2}$ transitions.

The experiments to determine the luminescence decay time use additional excitation sources. Excitation at 375 and 976 nm uses sources similar to those in the luminescence quantum yield experiments. To excite $^4S_{3/2,}$ and $^4F_{9/2}$ levels of Er^{3+} ion Roithner laser diodes operating at wavelengths of 525 and 639 nm, respectively are used. Their operation is also controlled by the Thorlabs, ITC4001 unit. The radiation from all sources is modulated with a frequency in the range of 100 to 10 Hz with a fill factor of 30%.

When measuring the luminescence quantum yield of the YF_3:Ce^{3+},Yb^{3+} samples the technique from [127] involving correction of the spectral response of the luminescence registration system and calibration of the optical system using light sources of a given intensity is used. Direct measurement of the quantum yield of Stokes luminescence is carried out using a Thorlabs IS200 integrating sphere and a Stellarnet EPP2000 spectrometer with 0.5 nm spectral resolution, calibrated with a TRJ-2850 lamp and an optical filter ZhS-16. A fourth harmonic YAG: Nd crystal laser with a wavelength of 266 nm and a pulse duration of 7 ns (LS-2147, Lotis TII) is used as an excitation source.

Decay times of BaF_2: Er^{3+}, Yb^{3+} samples are measured with a PicoQuant, TimeHarp 260 multi-channel scaling card. The triggering signal from Thorlabs, ITC4001 unit is sent to the card to start the detection. The required detection wavelength

is selected with a dual monochromator (Bentham, DTMS300). From the monochromator, the signal went either to a photomultiplier tube (R928P, Hamamatsu) when the detection wavelength is less than 850 nm or to an infrared photon detector (ID Quantique, ID220). From the detectors, the signal, previously attenuated to the appropriate level, is sent to the multichannel scaling card. A schematic representation of the setup is shown in the Figure 2.5

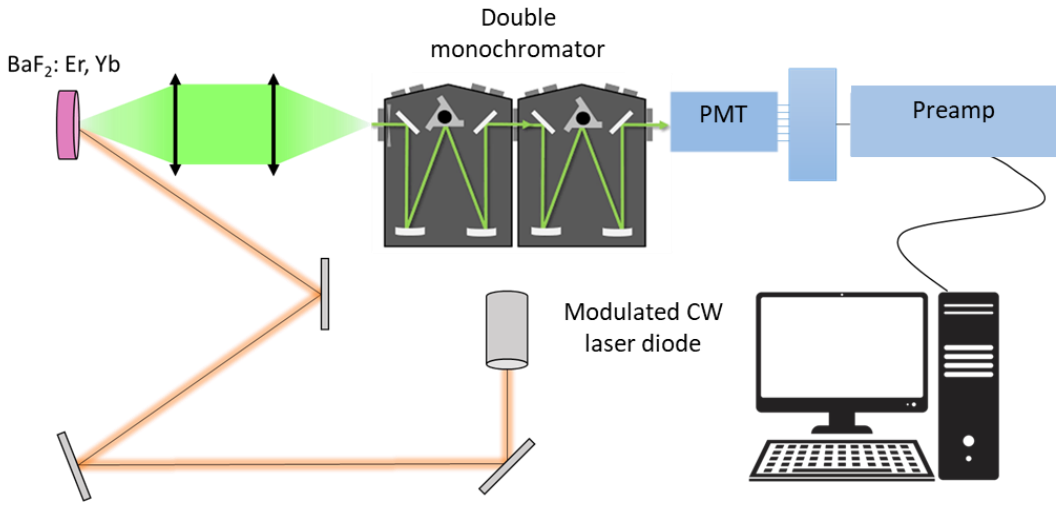

Figure 2.5 - Schematic of the setup used to measure the luminescence decay time.

Luminescence decays of YF_3: Ce^{3+}, Yb^{3+} samples are recorded using MDR-23 and MDR-3 monochromators, FED-100 is used as a photodetector in the visible region of the spectrum, FED-62 in the IR region of spectrum. The time sweep of the luminescence decay signals is carried out by a BORDO digital oscilloscope with a bandwidth of 200 MHz and a dynamic range of 10 bits. For excitation at a wavelength of 266 nm the fourth harmonic of the YAG: Nd laser with a pulse duration of 7 ns (LS-2147, Lotis TII) is used, and for excitation at 930 nm a wavelength-tunable OPO Lotis TII laser system with a pulse duration of the same 7 ns is used.

3. Study of BaF_2: Er^{3+}, Yb^{3+} crystals.

The results in the following section have already been published.

Sections 3.2 and 3.3. The results are presented in the paper J. Mater. Chem. C, 2021, 9, 3493-3503 [128]*. The co-authors from the Prokhorov General Physics Institute have synthesized the samples, Thomas Bergfeldt performed the WDXRF analysis, Dmitry Busko and Ian A. Howard participated in the setup of the optical characterization systems, Bryce S. Richards, Sergey V. Kuznetsov and Andrey Turshatov were involved in the coordination of the work and the interpretation of the results.*

Section 3.3. The results are presented in the paper ACS Appl. Mater. Interfaces 2021, 13, 46, 54874–54883 [129]*. Eduard Madirov and Roja Singh have equally contributed to the paper. The co-authors from the Prokhorov General Physics Institute have synthesized the samples, co-authors from the Light Technology Institute of Karlsruhe Institute of Technology have participated in the development and characterization of the perovskite solar cell, Dmitry Busko helped with the characterization of the BaF_2 crystal, Ulrich W. Paetzold, Bryce S. Richards, and Andrey Turshatov were involved in the coordination of the work and the interpretation of the results.*

3.1 Introduction

In the State of the Art chapter of the current work, it is outlined that Er^{3+}/Yb^{3+}-doped BaF_2 crystals meet all of the requirements for efficient up-conversion materials. However, a comprehensive study of the effects of doping concentration on UC performance is still lacking. To fill this gap, two concentration series of Er^{3+}/Yb^{3+}-doped BaF_2 crystals are synthesised. One series has a fixed amount of Er^{3+} ions (2 mol%) and a varying number of Yb^{3+} ions (2-15% mol.%), while the second series has a fixed amount of Yb^{3+} ions (3 mol%) and a varying number of Er^{3+} ions (2-15% mol.%).

To carry out the study, the following objectives are set for this chapter:

- To demonstrate that the Bridgeman method can yield Er^{3+}/Yb^{3+}-doped BaF_2 crystals that are capable of efficient up-conversion.

- To find the optimum doping concentration that gives the highest ϕ_{UC} value.
- To study the emission of the samples under excitation of different levels ($^4G_{11/2}$, $^2H_{11/2}$, $^4F_{9/2}$, $^4I_{9/2}$, $^4I_{11/2}$, $^4I_{13/2}$) and determine the excitation migration paths.
- To study the behaviour of the intensity ratio of the $^4S_{3/2} \longrightarrow {}^4I_{15/2}$ and $^4F_{9/2} \longrightarrow {}^4I_{15/2}$ UC emission in different excitation scenarios.
- To investigate the possibility of enhancing the perovskite solar cell performance by combining it with an Er^{3+}/Yb^{3+}-doped BaF_2 crystal.

3.2 Physico-chemical properties

X-ray diffraction patterns of BaF_2: Er^{3+}, Yb^{3+} samples are shown in Figure 3.1 together with JCPDS card 04-0452 (BaF_2).

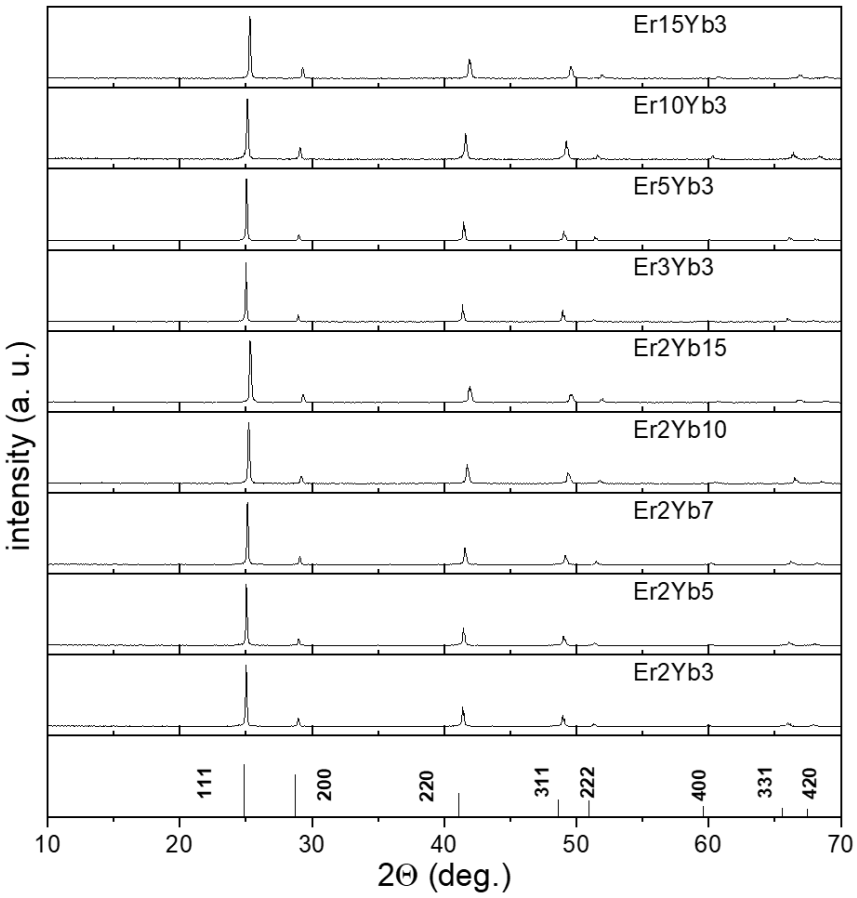

Figure 3.1 - X-ray diffraction patterns of BaF_2: Er^{3+}, Yb^{3+} samples.

The results show that the obtained samples have unit cells with cubic symmetry, which is an expected result for BaF_2 samples. The data obtained with X-ray diffraction analysis allows calculating the parameters of the unit cell (*a*). The results of the calculations are shown in Table 3.1. They are in good agreement with the value of the barium fluoride unit cell parameter available in the literature (a = 6.200 Å) [85].

Table 3.1 - Nominal concentration of doping ions in molar %, concentration in molar % based on WDXRF results and, number of ions per cm^3, unit cell parameter, and refractive index measured at 1520 nm.

Sample name	**Er**		**Yb**		**a, Å**	**n**
	mol.,%	N, 10^{20} cm^{-3}	mol.,%	N, 10^{20} cm^{-3}		
Er2Yb2	1,96	3.42	1,69	2.91	6.1785(2)	1.472
Er2Yb3	2.00	3.44	2.59	4.40	6.1645(4)	1.473
Er2Yb5	1.73	2.98	3.93	6.70	6.1588(8)	1.474
Er2Yb7	1.72	2.94	5.58	9.47	6.1442(9)	1.475
Er2Yb10	1.76	2.99	9.40	15.83	6.118(1)	1.475
Er2Yb15	1.86	3.15	11.98	20.06	6.100(2)	1.475
Er3Yb3	2.50	4.35	2.15	3.71	6.1664(4)	1.475
Er5Yb3	4.09	7.10	2.16	3.72	6.1560(6)	1.478
Er10Yb3	8.14	13.83	2.08	3.50	6.1320(8)	1.488
Er15Yb3	12.82	21.67	2.40	4.01	6.0961(7)	1.495

The unit cell parameter was calculated using the equation for a cubic crystal system:

$$\frac{1}{d^2} = \frac{h^2+k^2+l^2}{a^2}. \qquad 19$$

Here, *h, k, l* are Miller indices, and *d* is the interplanar distance. The parameter *d* was obtained from the Bragg-Wulff equation:

$$n\lambda = 2\,sin\,\theta\,. \qquad 20$$

Where n is the order of reflection, in this case, it is equal to 1, λ is the wavelength of the X-ray radiation, equal, in the case of the CuKα source, to 1.54051 Å, and θ is the position of the reflection peak. The parameters were calculated by the least squares

method, and the calculation error (ΔQ) was less than 10 $\Delta Q=10^4/d^2_{theoretical} - 10^4/d^2_{experimental}$.

From the data in the Table 3.1, we can see that the unit cell parameter drops with the increase in the number of both Yb^{3+}, and Er^{3+} ions. This can be explained by the fact that the ionic radius of the trivalent ions of the rare-earth elements is smaller than one of the Ba^{2+} ions, whose position they occupy [130]. This change in crystal structure leads to a decrease in the volume of the unit cell, which in turn affects the distance between the activator ions, reducing it. Due to this, the local concentration of rare earth ions increases.

To determine the phonon energy of barium fluoride lattice, the Raman spectrum of an undoped BaF_2 crystal is recorded. The obtained spectrum is shown in Figure 3.2. It consists of only one narrow band with a peak located at 240 cm^{-1} and a width at half maximum equal to 13 cm^{-1}. The obtained values are in good agreement with the value of the phonon energy of the BaF_2 crystal (240 cm^{-1}) available in the literature. [131, 132]. This indicates the low phonon energy of the BaF_2 lattice.

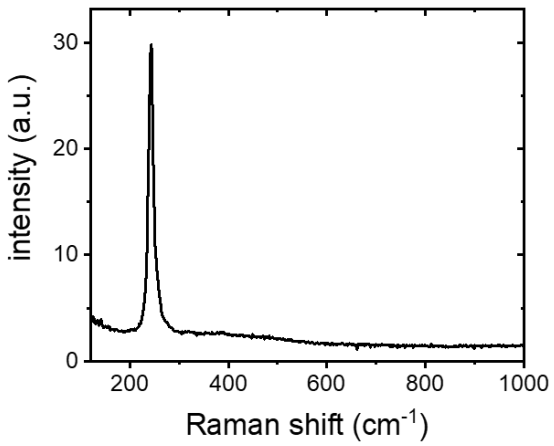

Figure 3.2 - Raman spectrum of an undoped BaF_2 crystal under 785 nm excitation.

In addition to this, the exact chemical composition of the samples is investigated with WDXRF. This method gives the concentration of elements as a weight percentage,

which is then converted into molar percentages (mol%) and the number of ions per cm^3. The mol.% indicates the proportion of Ba^{2+} cations replaced by doping ions. The total values are given in the Table 3.1. The errors are 0.30, 0.02 and 0.02 weight % for barium, erbium and ytterbium ions, respectively. For the sake of simplicity, the nominal concentration values of Yb^{3+} and Er^{3+} ions (first column in Table 3.1) will be used in all further discussions.

3.3 Spectral and kinetic properties

3.3.1 Absorption spectra

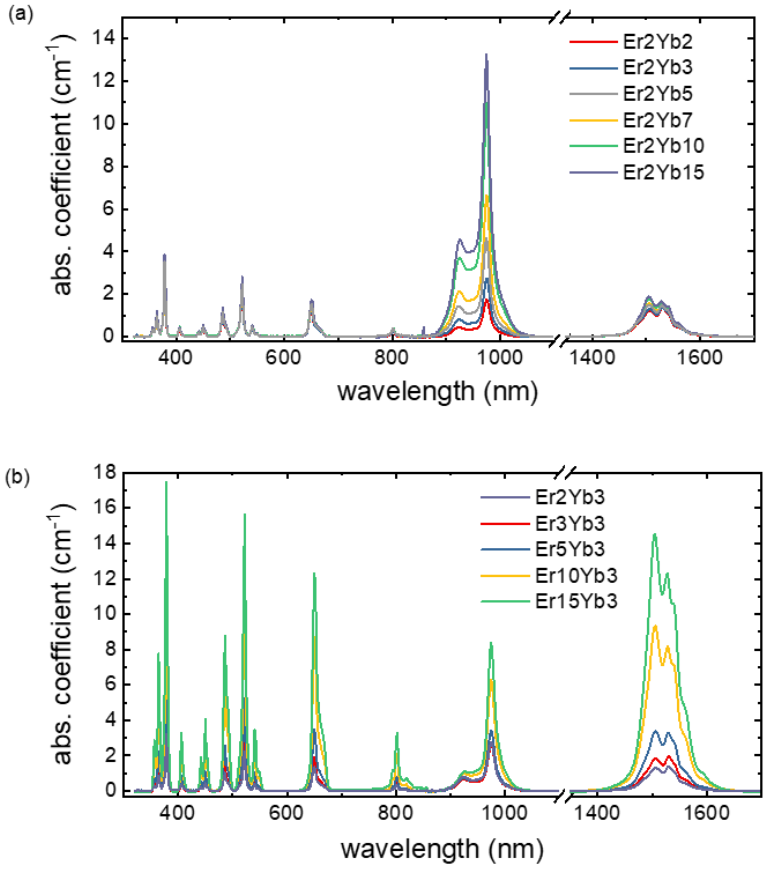

Figure 3.3 - Absorption spectra of two series of BaF_2: Er^{3+}, Yb^{3+} samples a) series with a fixed concentration of Er^{3+} ions (2 mol.%) and concentration of Yb^{3+} varying from 2 to 15 mol.%; b) series with a fixed concentration of Yb^{3+} ions (3 mol.%) and concentration of Er ions^{3+} varying from 2 to 15 mol.%.

Absorption spectra of BaF_2: Er^{3+}, Yb $^{3+}$ samples are shown in Figure 3.3. The spectra contain narrow absorption bands located in the UV, visible and IR regions of the spectrum. These bands are characteristic of the transitions within the 4f shell of trivalent Er and Yb ions. The most intense absorption bands are observed at 378 nm (transition $^4I_{15/2} \longrightarrow ^4G_{11/2}$ of Er^{3+}), 522 nm (transition $^4I_{15/2} \longrightarrow ^2H_{11/2}$ of Er^{3+}), 650 nm (transition $^4I_{15/2} \longrightarrow ^4F_{9/2}$ of Er^{3+}) and 1506 nm (transition $^4I_{15/2} \longrightarrow ^4I_{13/2}$ of Er^{3+}). An absorption band with its maximum at 974-976 nm should be mentioned separately. It is a superposition of two absorption bands, one relates to the $^4I_{15/2} \longrightarrow ^4F_{9/2}$ transition of the Er^{3+} ion, and the other one relates to the $^2F_{7/2} \longrightarrow ^2F_{5/2}$ transition of the Yb^{3+} ion.

The position of the absorption bands is similar to one observed in other hosts [23,133,134]. Once the values of the absorption coefficient and the true concentration of the doping ions are determined (Table 3.1) it is then possible to calculate the absorption cross-section of the observed transitions.

Table 3.2 - Peak absorption cross-section of some transitions of Er^{3+} ions, pm^2.

	378 nm	**522 nm**	**650 nm**	**1506 nm**
	$^4I_{15/2} \longrightarrow ^4G_{11/2}$	$^4I_{15/2} \longrightarrow ^2H_{11/2}$	$^4I_{15/2} \longrightarrow ^4F_{9/2}$	$^4I_{15/2} \longrightarrow ^4I_{13/2}$
Er2Yb2	0.91	0.64	0.40	0.37
Er2Yb3	0.98	0.68	0.42	0.40
Er2Yb5	1.25	0.87	0.54	0.52
Er2Yb7	1.23	0.89	0.55	0.56
Er2Yb10	1.31	0.97	0.61	0.62
Er2Yb15	1.28	0.94	0.58	0.62
Er3Yb3	1.01	0.73	0.46	0.44
Er5Yb3	0.99	0.76	0.51	0.49
Er10Yb3	0.99	0.86	0.64	0.68
Er15Yb3	0.81	0.73	0.57	0.67

The Table 3.2 shows the peak values of the absorption cross section of some transitions of the Er^{3+} ion: $^4I_{15/2} \longrightarrow {}^4G_{11/2}$,$^4I_{15/2} \longrightarrow {}^2H_{11/2}$,$^4I_{15/2} \longrightarrow {}^4F_{9/2}$ and $^4I_{15/2} \longrightarrow {}^4I_{13/2}$. By comparison, the absorption cross-section of the $^4I_{15/2} \longrightarrow {}^4I_{13/2}$ transition in the CaF_2 crystal is 0.55 pm [2135], in the SrF_2 host it is about 0.5 pm[223] and in the $SrGdGa_3O_7$ crystal it is also 0.5 pm[2 136]. The values presented above show that in the studied samples the absorption cross-section values are either comparable or even exceed similar parameters in other hosts. The absorption cross-section value around 980 nm is of particular interest. Since the absorption band at this wavelength is a superposition of two absorption bands, it is not possible to determine the absorption cross-section corresponding to each transition.

An important conclusion to be drawn from the data in the Table 3.2 is the change in the absorption cross-section of all observed bands with the concentration of the doping ions. It can be seen that an increase in the concentration of any of the doping ions leads to a significant increase in the peak absorption cross-section. This phenomenon has also been studied earlier [137]. As already discussed in Chapter 2, the trivalent Er^{3+} and Yb^{3+} ions replace the divalent Ba^{2+} ion in the crystal lattice, thereby leading to local distortion of the crystal field, which in turn increases the probability of f-f transitions. This effect will only become more pronounced with increasing concentration of the doping ions.

3.3.2 Mechanisms of down-shifting luminescence

Luminescence spectra under excitation of $^4H_{11/2}$ and $^4F_{9/2}$ states of Er^{3+}

The next step in the study of the spectral properties of BaF_2: Er^{3+}, Yb^{3+} crystals is the analysis of the emission spectra under excitation at different wavelengths. It is important to determine the luminescence properties under resonant excitation of emissive levels, namely $^4H_{11/2}$ (522 nm) and $^4F_{9/2}$ (652 nm). First, it is required to study the emission spectra under 522 nm excitation.

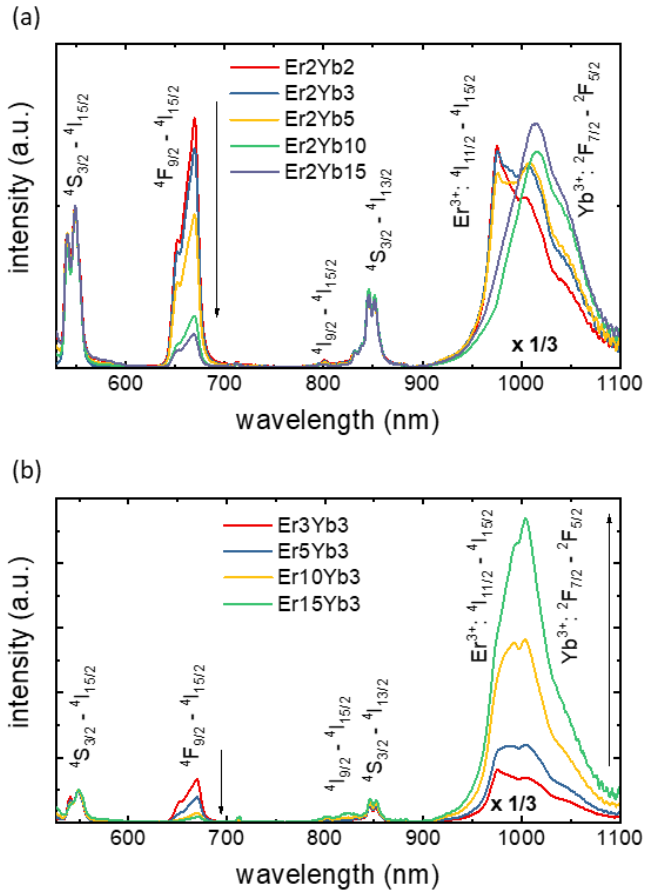

Figure 3.4 - Emission spectra of the BaF_2: Er^{3+}, Yb^{3+} samples under 522 nm excitation. The intensity of the emission band in the 900 - 1100 nm range is reduced by a factor of 3 in all spectra.

Figure 3.4 shows the emission spectra of the investigated samples under 522 nm excitation. Emission bands with a maximum at 540 nm ($^4S_{3/2} \longrightarrow {}^4I_{15/2}$), 650 nm ($^4F_{9/2} \longrightarrow {}^4I_{15/2}$), 810 nm ($^4I_{9/2} \longrightarrow {}^4I_{15/2}$) and 850 nm ($^4S_{3/2} \longrightarrow {}^4I_{13/2}$) are observed. The relative intensity of the emission lines depends on the concentration of both Er^{3+}, and Yb^{3+} ions. An increase in the concentration of either of the doping ions leads to a significant decrease in the relative emission intensity of the $^4F_{9/2} \longrightarrow {}^4I_{15/2}$ band, while the emission intensity of the transition located near 1000 nm rises, especially with an increase in the concentration of Er^{3+} ions. It is assumed that this line originates from the $^4F_{9/2} \longrightarrow {}^4I_{15/2}$ transition in the Er^{3+} ion, and the $^2F_{5/2} \longrightarrow {}^2F_{7/2}$ transition in the Yb^{3+} ion. Hereafter this line will be denoted as {Er^{3+}:$^4I_{11/2}$ & Yb^{3+}:$^2F_{5/2}$}. Such dependence can be explained

by the presence of cross-relaxation processes involving the levels $^2H_{11/2}$ and $^4S_{3/2}$ and leading to an increase in the population of the {Er^{3+}:$^4I_{11/2}$ & Yb^{3+}:$^2F_{5/2}$} level. Besides, in samples with high Er^{3+} content, there is an increase of luminescence intensity around 810 nm. For a more detailed discussion of the processes, it is necessary to consider the energy level diagram of Er^{3+} and Yb^{3+} ions that is given in Figure 3.5.

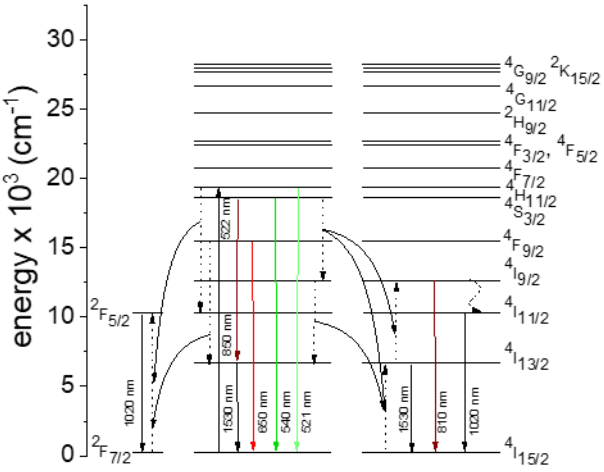

Figure 3.5 - Energy migration between the excited states of Er^{3+} - Yb^{3+} ions under 522 nm excitation.

A 522 nm photon is absorbed by the Er^{3+} ion, after which it is excited to the $^4H_{11/2}$ state that is thermally bound to the $^4S_{3/2}$ state. From this level transitions to the ground state with emission of a 540 nm photon and to the $^4I_{13/2}$ state with emission of an 850 nm photon are possible. In addition, the following cross-relaxation processes between Er $^{3+}$ ions ($^4S_{3/2} \longrightarrow {}^4I_{9/2}$ -$^4I_{15/2} \longrightarrow {}^4I_{13/2}$,$^4S_{3/2} \longrightarrow {}^4I_{9/2}$ -$^4I_{13/2} \longrightarrow {}^4I_{9/2}$) and between Er^{3+} - Yb^{3+} ions (Er^{3+} :$^4H_{11/2} \longrightarrow {}^4I_{11/2}$ - Yb^{3+} :$^2F_{7/2} \longrightarrow {}^2F_{5/2}$) are possible.

As discussed above, the probability of non-radiative relaxation from the $^4H_{11/2}$ and $^4S_{3/2}$ levels to the $^4F_{9/2}$ level remains a matter of discussion due to a relatively large distance between the excited states (~ 3200 cm^{-1}). However the presence of an emission band around 650 nm under 522 nm excitation suggests that such a non-radiative process is present in the BaF_2: Er^{3+}, Yb^{3+} crystals. At the same time, besides the radiative

transition to the ground state from the $^4F_{9/2}$ level there is a cross-relaxation process Er^{3+}:$^4F_{9/2}$ ⟶ $^4I_{13/2}$ - Yb^{3+}:$^2F_{7/2}$ ⟶ $^2F_{5/2}$.

This leads to the conclusion that non-radiative relaxation from $^4S_{3/2}$ to $^4F_{9/2}$ is probable but competes with several cross-relaxation processes both between Er^{3+} - Yb^{3+} ions, and between Er^{3+} - Er^{3+} ions. The probability of these processes rises with an increase in the concentration of doping ions, leading to a drop in the intensity of $^4F_{9/2}$ ⟶ $^4I_{15/2}$ luminescence. Additionally, a cross-relaxation process is present, leading to a decrease in the population of the $^4F_{9/2}$ level and an increase in the intensity of the emission band originating from the {Er^{3+} :$^4I_{11/2}$ & Yb^{3+}:$^2F_{5/2}$} state.

The next excitation wavelength is 652 nm. This corresponds to the excitation of an Er^{3+} ion from the ground state to the $^4F_{9/2}$ level.

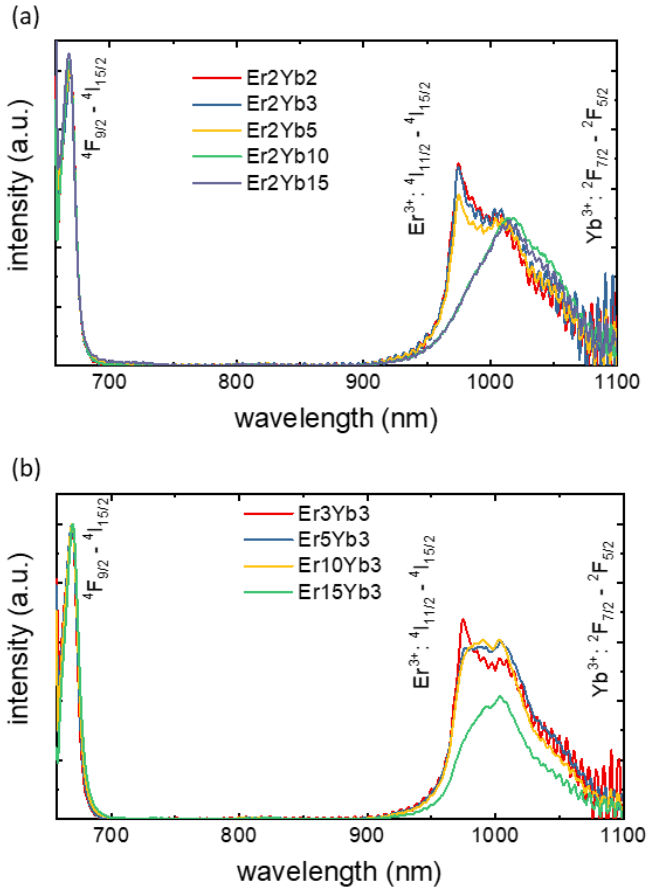

Figure 3.6 - Emission spectra of the BaF_2: Er^{3+}, Yb^{3+} samples under 652 nm excitation.

Figure 3.6 shows the emission spectra of the samples under 652 nm excitation. Emission bands with maximum at wavelengths of 650 nm ($^4F_{9/2} \longrightarrow {}^4I_{15/2}$), and 1000 nm {$Er^{3+}$:$^4I_{11/2}$ & Yb^{3+}:$^2F_{5/2}$} are observed. All spectra are normalized to the emission intensity at 669 nm. In this excitation scenario, the emission spectra have a rather simple outline as they contain only 2 bands: Er^{3+}:$^4F_{9/2} \longrightarrow {}^4I_{15/2}$ and the transition to the ground state from the {Er^{3+}:$^4I_{11/2}$ & Yb^{3+}:$^2F_{5/2}$} manifold. Like the 522 nm excitation scenario, under 652 nm excitation, the most intense emission band is the one located around 1000 nm. The emission spectra can be explained by analysing the energy level diagram of Er^{3+} and Yb^{3+} ions which is shown in Figure 3.7.

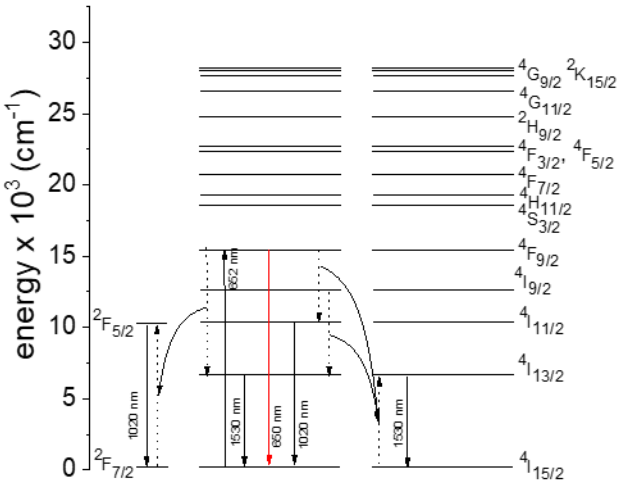

Figure 3.7 - Energy migration between the excited states of Er^{3+} - Yb^{3+} ions under 652 nm excitation.

After absorption of a 652 nm photon, the Er^{3+} ion is excited to the $^4F_{9/2}$ state. From there it can radiatively relax to the $^4I_{15/2}$ ground state with the emission of a photon or it can go to the $^4I_{13/2}$ state via the cross-relaxation process Er^{3+}:$^4F_{9/2} \longrightarrow {}^4I_{13/2}$ - Yb^{3+}:$^2F_{7/2} \longrightarrow {}^2F_{5/2}$. The absence of the $^4I_{9/2} \longrightarrow {}^4I_{15/2}$ emission band suggests that the non-radiative relaxation from the $^4F_{9/2}$ level to the $^4I_{9/2}$ state is not efficient, even though the distance between the levels is about 2800 cm^{-1}. Thus, as suggested above, the main mechanism of the population of the $^4I_{9/2}$ level is cross-relaxation from higher levels, and

emission at 1000 nm appears primarily due to the following cross-relaxation process Er^{3+}:$^4F_{9/2} \longrightarrow {}^4I_{13/2}$ - Yb^{3+}:$^2F_{7/2} \longrightarrow {}^2F_{5/2}$.

Luminescence quantum yield under excitation of $^4H_{11/2}$ and $^4F_{9/2}$ states of Er^{3+}

Next, the luminescence quantum yield under excitation of the $^4H_{11/2}$ (522 nm) and $^4F_{9/2}$ (652 nm) levels is analyzed. The obtained results are shown in the Table 3.3.

Table 3.3 - Luminescence quantum yield values under 522 and 652 nm excitation.

Excitation	**522 nm**			**652 nm**	
	$^4S_{3/2} \longrightarrow {}^4I_{15/2}$	$^4F_{9/2} \longrightarrow {}^4I_{15/2}$	{Er^{3+}:$^4I_{11/2}$ Yb^{3+}:$^2F_{5/2}$}	$^4F_{9/2} \longrightarrow {}^4I_{15/2}$	{Er^{3+}:$^4I_{11/2}$ Yb^{3+}:$^2F_{5/2}$}
Er2Yb2	0.04	0.088	0.769	0.24	0.62
Er2Yb3	0.04	0.067	0.757	0.22	0.59
Er2Yb5	0.03	0.050	0.818	0.26	0.65
Er2Yb10	0.03	0.014	0.687	0.24	0.56
Er2Yb15	0.03	0.009	0.776	0.25	0.56
Er3Yb3	0.03	0.060	0.799	0.21	0.59
Er5Yb3	0.02	0.022	0.849	0.21	0.60
Er10Yb3	0.02	0.003	0.715	0.19	0.49
Er15Yb3	0.01	0.001	0.434	0.15	0.22

The main relaxation channel is the emission from the {Er^{3+}:$^4I_{11/2}$ & Yb^{3+}:$^2F_{5/2}$} manifold. When the $^4H_{11/2}$ state (522 nm) is excited, the luminescence quantum yield of the $^4F_{9/2} \longrightarrow {}^4I_{15/2}$ transition is comparable, and in some cases even exceeds the quantum yield of the $^4S_{3/2} \longrightarrow {}^4I_{15/2}$ transition, which proves the efficiency of phonon-assisted relaxation $^4S_{3/2}$ - $^4F_{9/2}$. It is worth noting that the luminescence quantum yield of the $^4S_{3/2} \longrightarrow {}^4I_{15/2}$ and $^4F_{9/2} \longrightarrow {}^4I_{15/2}$ transitions under resonant excitation (522 and 652 nm, respectively) is independent of the concentration of Yb^{3+} ions and is weakly dependent

on the content of Er^{3+} ions, indicating that in these excited states the interaction between Er^{3+} - Er^{3+} ions appears stronger than one of the Er^{3+} - Yb^{3+} ions.

Luminescence quantum yield values under resonant excitation of Er^{3+}:$^4H_{11/2}$ and $^4F_{9/2}$ levels show the maximum achievable value of ϕ_{UC}. Since the up-conversion process requires the absorption of at least two excitation photons, the maximum up-conversion quantum yield value of an emission band is half the value of the quantum yield under resonant excitation of the corresponding level. In the case of the $^4S_{3/2} \longrightarrow {}^4I_{15/2}$ transition the quantum yield under resonant excitation does not exceed 0.04, and in the case of the $^4F_{9/2} \longrightarrow {}^4I_{15/2}$ transition, the highest observed value is 0.26. It can be concluded that the observed ϕ_{UC} value of $^4S_{3/2} \longrightarrow {}^4I_{15/2}$ transition is close to the maximum achievable in this material, whereas, in the case of $^4F_{9/2} \longrightarrow {}^4I_{15/2}$ transition, there are processes leading to a decrease in the ϕ_{UC}.

Luminescence spectra at Er^{3+}: $^4G_{9/2}$ state excitation

Next, it is necessary to study the emission spectra as well as the energy migration scenarios under 375 nm excitation (excitation of the $^4G_{9/2}$ state).

Figure 3.8 shows the emission spectra in the 400 - 1100 nm range obtained under 375 nm excitation. The intensity of all spectra is normalised to the intensity of the peak at 549 nm. All spectra show emission lines of Er^{3+} and Yb^{3+} ions. Lines associated with transitions in the Er^{3+} ion are observed at wavelengths of 405 nm ($^2H_{9/2} \longrightarrow {}^4I_{15/2}$), 521 nm ($^2H_{11/2} \longrightarrow {}^4I_{15/2}$), 540 nm ($^4S_{3/2} \longrightarrow {}^4I_{15/2}$), 650 nm ($^4F_{9/2} \longrightarrow {}^4I_{15/2}$), 810 nm ($^4I_{9/2} \longrightarrow {}^4I_{15/2}$) and 850 nm ($^4S_{3/2} \longrightarrow {}^4I_{13/2}$). In addition to the indicated emission bands, all spectra show a broad band located in the range of 900 to 1100 nm with a maximum around 1020 nm - {Er^{3+}:$^4I_{11/2}$ & Yb^{3+}:$^2F_{5/2}$}. The change in the short-wave edge of emission bands is noticeable in all spectra, especially at high concentrations of doping ions (>5 mol%). This indicates the presence of strong reabsorption in the studied samples. Change in the shape of the emission bands in the samples doped with Yb^{3+} ions due to reabsorption has already been observed, even at a low doping concentration

of only 1 mol.%.[138]. It is crucial to highlight the change in the shape of the emission band originating from the {Er^{3+}:$^4I_{11/2}$ & Yb^{3+}:$^2F_{5/2}$} manifold, especially in the series of samples with variable concentrations of Yb^{3+} ions. This change is due to the overlap of the Er^{3+}:$^4I_{11/2} \longrightarrow {}^4I_{15/2}$ and Yb^{3+}:$^2F_{5/2} \longrightarrow {}^2F_{7/2}$ emission bands. As the concentration of the doping ions changes, the contribution from the corresponding transition becomes more prominent.

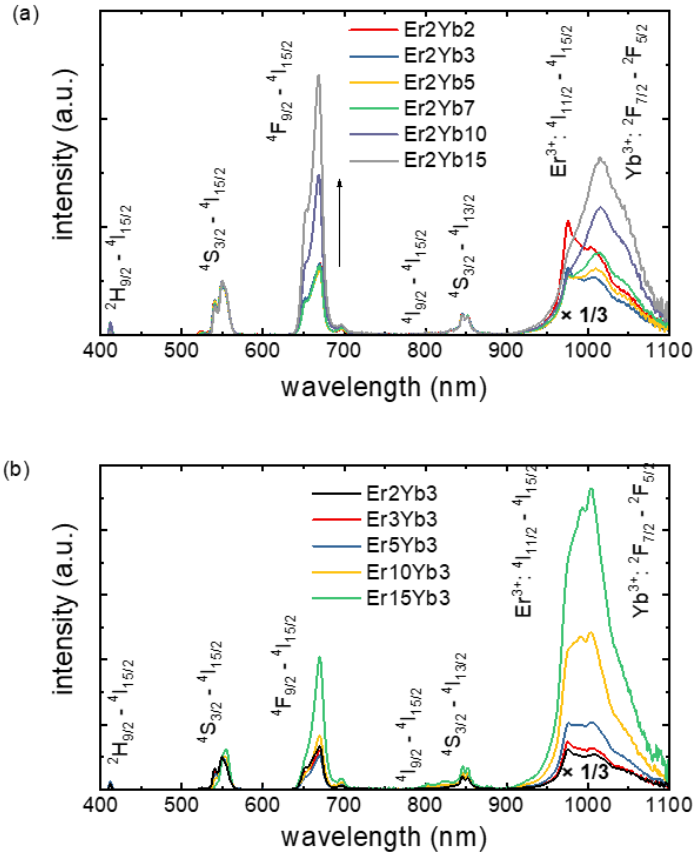

Figure 3.8 - Emission spectra of the BaF_2: Er^{3+}, Yb^{3+} samples under 375 nm excitation. The intensity of the emission band in the 900 - 1100 nm range is reduced by a factor of 3 in all spectra.

The relative intensity of the emission bands is dependent on the concentration of the doping ions. Noticeable change occurs only when the concentration of any of the doping ions reaches 10 mol.%. In this case, the relative intensity of the $^4F_{9/2} \longrightarrow {}^4I_{15/2}$ transition significantly increases. The observed effect can be caused by either of two

processes: a decrease in the population of the $^4S_{3/2}$ level and/or an increase in the population of the $^4F_{9/2}$ level. Also, in samples with high Er^{3+} content increase in relative intensity of the $^4I_{9/2} \longrightarrow {}^4I_{15/2}$ band is noticeable.

To better understand energy migration processes in the Er^{3+} - Yb^{3+} system it is necessary to consider the energy levels diagram of the ions.

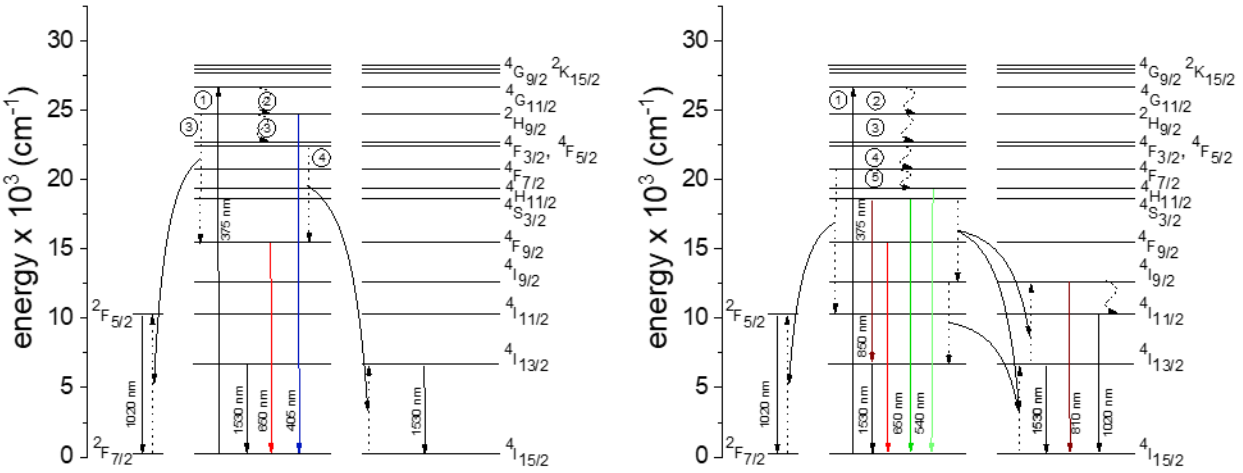

Figure 3.9 - Energy migration between the excited states of Er^{3+} - Yb^{3+} ions under 375 nm excitation.

Figure 3.9 shows a diagram of the energy levels of the Er^{3+} and Yb^{3+} ions, as well as the transitions due to excitation at a 375 nm wavelength. A 375 nm photon is absorbed by the Er^{3+} ion, which then transitions to the $^4G_{11/2}$ excited state. The transitions following this are shown in the Figure 3.9a. There is a non-radiative relaxation to the $^4H_{9/2}$ state from the $^4G_{11/2}$ level (2 in Figure 3.9a). The distance between the levels is about 1900 cm^{-1}, which is equal to the energy of 8 phonons. There are several possible transitions from the $^2H_{9/2}$ level. They are indicated by number 3 in Figure 3.9a. The first option is non-radiative relaxation to the $^4F_{3/2}$ level, the distance to which is 2000 cm^{-1}, from the $^4F_{3/2}$ level a $^4F_{3/2} \longrightarrow {}^4F_{9/2}$ - $^4I_{15/2} \longrightarrow {}^4I_{13/2}$ cross-relaxation process is possible. The other option is a radiative transition to the $^4I_{15/2}$ ground state, accompanied by the emission of a photon with a wavelength of 405 nm. The third

option is the Er^{3+}:$^4H_{9/2} \longrightarrow {}^4F_{9/2}$ - Yb^{3+}:$^2F_{7/2} \longrightarrow {}^2F_{5/2}$ cross-relaxation, which leads to a transition of a Yb^{3+} ion to an excited state.

The following transitions are shown in Figure 3.9b. A non-radiative relaxation to the level $^4F_{7/2}$ is possible from the $^4F_{3/2}$ and $^4F_{5/2}$ levels. The distance of this transition is 1300 cm^{-1}. From the $^4F_{7/2}$ level Er^{3+}:$^4F_{7/2} \longrightarrow {}^4I_{11/2}$ - Yb^{3+}:$^2F_{7/2} \longrightarrow {}^2F_{5/2}$ cross relaxation that leads to excitation of Yb^{3+} ion, and non-radiative transition to the $^4H_{11/2}$ level (distance 1300 cm^{-1}) can occur. From the pair of $^4H_{11/2}$ and $^4S_{3/2}$ thermally bound levels, radiative transitions to the ground state are probable, with emission of photons at wavelengths of 521 and 540 nm, respectively. In addition, from the $^4S_{3/2}$ level, a radiative transition to the $^4I_{13/2}$ state with the emission of a photon at a wavelength of 850 nm is also possible. There are several probable cross-relaxation processes from the $^4S_{3/2}$ excited state: $^4S_{3/2} \longrightarrow {}^4I_{9/2}$ - $^4I_{15/2} \longrightarrow {}^4I_{13/2}$ and $^4S_{3/2} \longrightarrow {}^4I_{9/2}$ - $^4I_{13/2} \longrightarrow {}^4I_{9/2}$. The population mechanism of the $^4F_{9/2}$ level is the subject of active discussion[139, 71] and several mechanisms of its population have already been described above. The non-radiative $^4S_{3/2} \longrightarrow {}^4F_{9/2}$ transition is one of the possible population pathways. In the section above it has been demonstrated that in the studied samples this non-radiative process is possible despite the large energy gap. From the level $^4F_{9/2}$, in turn, there is a radiative transition to the $^4I_{15/2}$ ground state.

Transitions from $^4I_{9/2}$ state and below are also shown in Figure 3.9b. There can be non-radiative relaxation to the $^4I_{11/2}$ level (2200 cm^{-1}), radiative transition to the ground state (810 nm), or $^4I_{9/2} \longrightarrow {}^4I_{13/2}$ - $^4I_{15/2} \longrightarrow {}^4I_{13/2}$ cross-relaxation from the $^4I_{9/2}$ level. From the $^4I_{11/2}$ and $^4I_{13/2}$ levels, the excitation can relax to the ground state with the emission of photons at wavelengths of about 1000 and 1530 nm, respectively. In addition, from the $^2F_{5/2}$ excited state of the Yb^{3+} ion, there is an emissive transition to the ground state with the emission of a photon with a wavelength of about 1000 nm.

Several conclusions can be drawn from the considered excitation migration scenario. First, the increase in the emission intensity of the bands around 650 and 1000 nm is explained by the fact that the probability of cross-relaxation processes between

Er^{3+} and Yb^{3+} ions rises with the increase in the concentration of doping ions. Second, the increase in the intensity of the $^4I_{9/2} \longrightarrow {}^4I_{15/2}$ transition in samples with high content of Er^{3+} ions is explained by the presence of several cross-relaxation processes between Er^{3+} ions that lead to a higher population of the excited state.

Luminescence quantum yield upon excitation of Er^{3+}:$^4G_{9/2}$ state

Table 3.4 - Luminescence quantum yield values under 375 nm excitation.

	$^2H_{9/2}$ -^{4} $I_{15/2}$	$^4S_{3/2}$ -^{4} $I_{15/2}$	$^4F_{9/2}$ -^{4} $I_{15/2}$	$^4S_{3/2}$ -^{4} $I_{13/2}$	{Er^{3+} :^{4} $I_{11/2}$ Yb^{3+} :^{2} $F_{5/2}$}
Er2Yb2	<0.01	0.04	0.10	0.03	1.317
Er2Yb3	<0.01	0.02	0.06	0.02	0.872
Er2Yb5	<0.01	0.03	0.07	0.02	1.197
Er2Yb7	<0.01	0.03	0.06	0.02	1.372
Er2Yb10	<0.01	0.02	0.09	0.01	1.397
Er2Yb15	<0.01	0.01	0.08	0.01	0.985
Er3Yb3	<0.01	0.03	0.05	0.02	1.118
Er5Yb3	<0.01	0.02	0.03	0.02	1.266
Er10Yb3	0	0.01	0.02	0.01	1.295
Er15Yb3	0	<0.01	0.02	<0.01	1.078

The quantum yield values obtained under 375 nm are presented in the Table 3.4. The first thing that can be noticed is that the emission band located around 1000 nm has the highest quantum yield in all samples. Its quantum yield value is close to or even exceeds unity. This suggests that the {Er^{3+}:$^4I_{11/2}$&Yb^{3+}:$^2F_{5/2}$} state is the main metastable level to which the excitation relaxes. This is also facilitated by a large number of cross-relaxation processes between Er^{3+} and Yb^{3+} ions, which lead to the population of the {Er^{3+}:$^4I_{11/2}$&Yb^{3+}:$^2F_{5/2}$} state as discussed above. It can also be noted

that under 375 nm excitation, the quantum yield does not change significantly with an increase in doping ion concentration. The transitions from the $^4S_{3/2}$ level are most sensitive to the number of rare-earth ions. For example, when the amount of Yb^{3+} ions changes from 2 to 15 mol.% quantum yield decreases from 0.04 to 0.01, and with a similar change in Er^{3+} content - from 0.03 to less than 0.01. At the same time, the quantum yield of the $^4F_{9/2}$ - $^4I_{15/2}$ band is almost completely unaffected by doping concentration. This once again confirms that the $^4S_{3/2}$ level is part of a large number of cross-relaxation processes, the probability of which changes with the number of rare-earth ions.

Excitation spectra

To complete the study of the down-shifting spectra of the samples it is necessary to pay attention to the excitation spectra. For this purpose, excitation spectra were recorded in the range 320 - 525 nm when detected at wavelengths of 552 and 660 nm.

The resulting excitation spectra are shown in the Figure 3.10. As can be seen from Figure 3.10a, b the emission at 552 nm has no pronounced dependence on the concentration of either Er^{3+} or Yb^{3+} ions. This observation provides further evidence that the population of the $^4S_{3/2}$ level of Er^{3+} happens via a series of non-radiative multiphonon relaxation transitions and does not include energy transfer or cross-relaxation processes.

The excitation spectra look quite different when detected at 660 nm (Figure 3.10c, d). In this case, there is a pronounced dependence on the concentration of both Er^{3+} and Yb^{3+} ions. A change in the concentration of any of the two ions has a different effect on the observed spectrum. In samples with high concentrations of Yb^{3+} ions, an increase in the intensity of excitation bands located in the spectral range shorter than 400 nm is observed (Figure 3.10c). This proves that the $^4F_{9/2}$ level is efficiently populated via the following cross-relaxation process Er^{3+}:$^2H_{9/2} \longrightarrow {}^4F_{9/2}$ - Yb^{3+}:$^2F_{7/2} \longrightarrow {}^2F_{5/2}$. The probability of this process goes up with the increase in Yb^{3+} concentration.

The almost complete absence of excitation bands around 450 nm in samples with a high content of Yb^{3+} indicates that there is no resonance transition from the $^4F_{5/2}$ and $^4F_{3/2}$ levels.

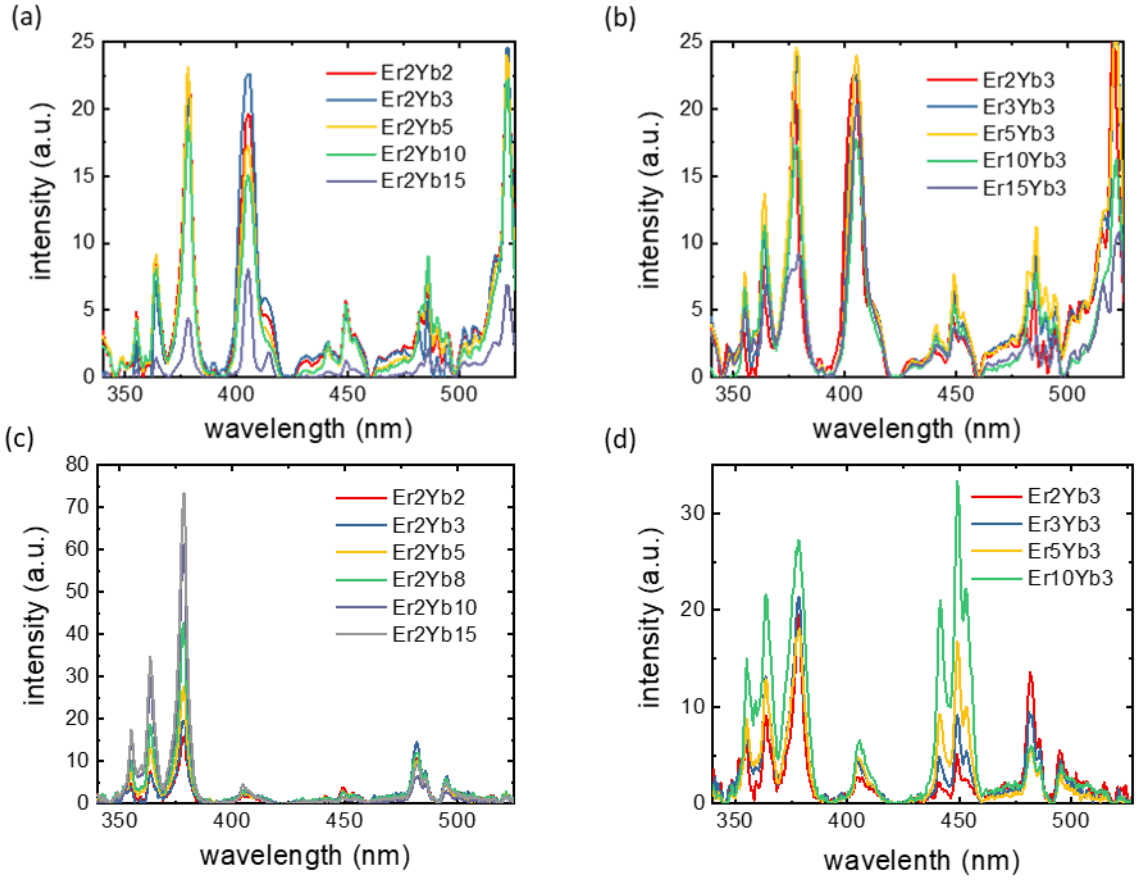

Figure 3.10 - Excitation spectra of BaF_2: Er^{3+}, Yb^{3+} samples when detected at a), b) 552 nm, c), d) 660 nm.

In turn, an increase in the concentration of Er^{3+} ions leads to a slight increase in the intensity of the excitation bands located in the spectral range shorter than 400 nm. There is also a significant increase in the intensity of the band near 450 nm. This dependence indicates that in samples with high content of Er^{3+} ions, there is an efficient cross-relaxation process between Er^{3+} ions that leads to the population of the $^4F_{9/2}$ state from the $^4F_{5/2}$ or $^4F_{3/2}$. This is in line with the $^4F_{3/2} \longrightarrow {}^4F_{9/2}$ - $^4I_{15/2} \longrightarrow {}^4I_{13/2}$ process that is proposed above and is presented in Figure 3.9a.

Thus, all of the energy transfer routes in the Er^{3+} - Yb^{3+} ion system that are proposed during the study of the emission spectra are also present in the excitation spectra of the two most intense emission lines of the Er^{3+} ion, which indicates the correctness of the conclusions drawn so far.

3.3.3 Up-conversion luminescence mechanisms

In the previous chapter, there is a lot of data showing that the materials doped with Er^{3+} and Yb^{3+} ions exhibit up-conversion luminescence. Various wavelengths can be used for its excitation, but the most intense up-conversion luminescence is observed when the material is excited at a wavelength around 980 nm, which simultaneously corresponds to the maximum absorption band of $^4I_{15/2} \longrightarrow ^4I_{1/2}$ transition of Er^{3+} ions and $^2F_{7/2} \longrightarrow ^2F_{5/2}$ band of the Yb^{3+} ions. Thus, a diode laser with a wavelength of 976 nm is used as the excitation source to study the up-conversion luminescence spectra.

The Figure 3.11 shows the emission spectra from 400 to 900 nm in the case of the 976 nm excitation with an intensity of 490 W/cm^2. All spectra are normalised to the emission intensity at 549 nm. Emission bands at 405 nm ($^2H_{9/2} \longrightarrow ^4I_{15/2}$), 521 nm ($^2H_{11/2} \longrightarrow ^4I_{15/2}$), 540 nm ($^4S_{3/2} \longrightarrow ^4I_{15/2}$), 650 nm ($^4F_{9/2} \longrightarrow ^4I_{15/2}$), 810 nm ($^4I_{9/2} \longrightarrow ^4I_{15/2}$) and 850 nm ($^4S_{3/2} \longrightarrow ^4I_{13/2}$) are observed. The relative intensities of the luminescence bands have a pronounced dependence on the concentration of both doping ions. It is shown that an increase in the concentration of both Er^{3+} and Yb^{3+} ions leads to a decrease in the relative intensity of the luminescence band corresponding to the $^4F_{9/2} \longrightarrow ^4I_{15/2}$ transition.

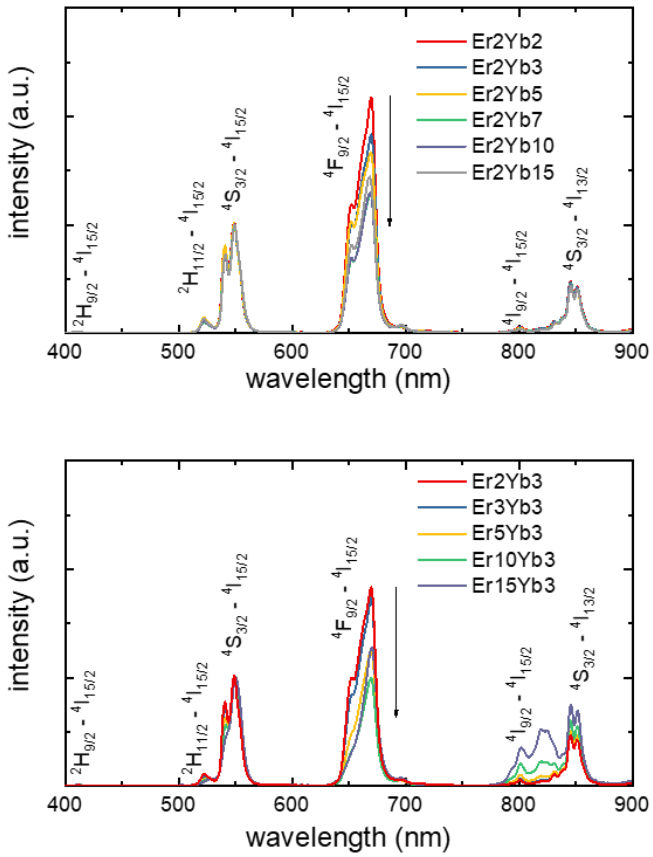

Figure 3.11 - Luminescence spectrum of BaF_2: Er^{3+}, Yb^{3+} samples when excited at 976 nm with an intensity of 490 W/cm^2.

On the other hand, this behaviour of the relative intensity of the emission lines is similar to the case of excitation at a wavelength of 522 nm. To better understand the mechanisms of excitation propagation it is necessary to consider the energy levels diagram of the Er $^{3+}$ - Yb^{3+} ion system. In Figure 3.12 The energy diagram of Er^{3+} - Yb^{3+} ions, as well as the transitions associated with excitation at a wavelength of 976 nm are shown.

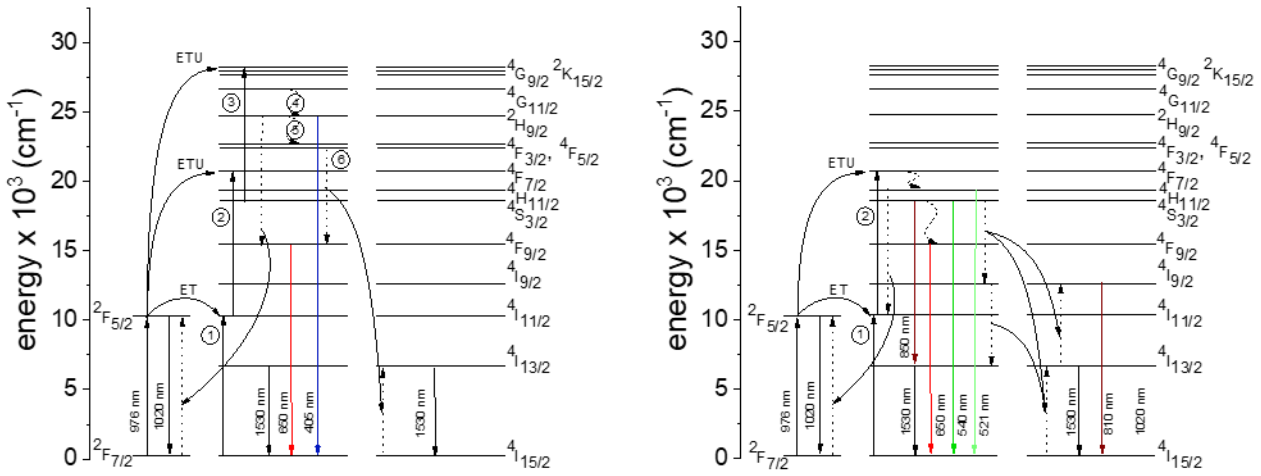

Figure 3.12 - Energy migration between the excited states of Er^{3+} - Yb^{3+} ions under 976 nm excitation.

As already discussed in the State of the Art section, up-conversion luminescence requires the absorption of two or more excitation photons per one emitted. It is known that in the Er^{3+} - Yb^{3+} ion pair the ETU mechanism is realized [52]. Excitation photons are absorbed by Yb^{3+} ions and then the energy is transferred to Er^{3+} ions. In the energy diagram of the Er^{3+} ion, there are several transitions resonant with the $^2F_{5/2}$ - $^2F_{7/2}$ transition of the Yb^{3+} ion. In the Figure 3.12 they are marked as 1, 2 and 3. Thus, up-conversion can be divided into two- and three-photon processes. Here, the act of up-conversion refers to the absorption of an excitation photon by an Yb^{3+} ion followed by energy transfer to Er^{3+} ions. First, the scenario involving the absorption of three photons should be considered. This process is illustrated in Figure 3.12a. The first photon is absorbed by the Yb^{3+} ion, and then the energy is transferred to the Er^{3+} ion, which transitions to the $^4I_{11/2}$ state. Another Yb $^+$ ion, excited by the absorption of another photon, transfers energy to the same Er^{3+} ion and thereby transfers it from the $^4I_{11/2}$ state to the $^4F_{7/2}$, from which non-radiative transition to the level $^4S_{3/2}$ is possible. From this state, the Er^{3+} ion can go to the $^4G_{9/2}$ state after excitation from the third Yb^{3+} ion is received. Then a series of non-radiative relaxation processes brings the excitation to the $^2H_{9/2}$ level of Er^{3+}. From this level a radiative transition to the ground state with the

emission of a 405 nm photon, a non-radiative relaxation to the $^4F_{3/2}$,$^4F_{5/2}$ levels, as well as Er^{3+}:$^4H_{9/2} \longrightarrow {}^4F_{9/2}$ - Yb^{3+}:$^2F_{7/2} \longrightarrow {}^2F_{5/2}$ cross relaxation process are possible. There is a cross-relaxation process between the two Er^{3+} ions: $^4F_{3/2} \longrightarrow {}^4F_{9/2}$ - $^4I_{15/2} \longrightarrow {}^4I_{13/2}$ from the $^4F_{3/2}$, $^4F_{5/2}$ excited states. From the $^4F_{9/2}$ level, a radiative transition to the ground state with the emission of a 650 nm photon is possible. Thus, it can be summarized that the absorption of three photons leads to emissive transitions $^2H_{9/2} \longrightarrow {}^4I_{15/2}$ and $^4F_{9/2} \longrightarrow {}^4I_{15/2}$, with wavelengths of 405 and 650 nm, respectively.

The next step is to consider the two-photon scenario (Figure 3.12b). In general, the two-photon excitation scenario is similar to excitation at 522 nm. After absorption of two excitation quanta, an Er^{3+} ion is in the $^4F_{7/2}$ state, from which it can either non-radiatively relax to a $^4H_{11/2}$, $^2S_{3/2}$ pair of levels, or transition in the $^4I_{11/2}$ state via the Er^{3+}:$^4H_{11/2} \longrightarrow {}^4I_{11/2}$ - Yb^{3+}:$^2F_{7/2} \longrightarrow {}^2F_{5/2}$ cross-relaxation. From the $^4H_{11/2}$ level, there is a radiative transition to the ground state (521 nm) and from the $^2S_{3/2}$ level there are possible transitions to the $^4I_{13/2}$,$^4I_{15/2}$ levels with emission of 850 nm and 550 nm photons respectively. In addition, several cross-relaxation processes between Er^{3+} ions are possible: $^4S_{3/2} \longrightarrow {}^4I_{9/2}$ - $^4I_{15/2} \longrightarrow {}^4I_{13/2}$,$^4S_{3/2} \longrightarrow {}^4I_{9/2}$ -$^4I_{13/2} \longrightarrow {}^4I_{9/2}$. Also, it must be considered that the $^4H_{11/2}$ and $^2S_{3/2}$ states can be efficient sources of the population of the $^4F_{9/2}$ level. The radiative transfer to the ground state from this level leads to the emission around 650 nm.

Both the two- and three-photon processes depend on the excitation intensity and the order of this dependence will be different for the two cases. It has been demonstrated that some bands in the up-conversion luminescence spectra of the samples are related to the absorption of three excitation photons and some are related to the absorption of two. Additionally, in the spectrum, there is a luminescence band ($^4F_{9/2} \longrightarrow {}^4I_{15/2}$) which is associated with both scenarios.

Quantum yield of up-conversion luminescence.

As has already been discussed in Chapter Two, one of the key parameters determining the utility of luminescent materials is the luminescence quantum yield. This value can also shed additional light on the energy transfer processes that take place in the investigated material.

In the case of the excitation of up-conversion luminescence (976 nm), it is not sufficient to consider the luminescence quantum yield at a single excitation intensity. Since up-conversion is a non-linear process that depends on the excitation intensity, the up-conversion luminescence quantum yield (ϕ_{UC}) will also be a function of the excitation intensity. For this purpose, the luminescence quantum yield is obtained over a wide range of excitation intensities, from 0.01 to 490 W/cm^2. The results are presented in Figure 3.13.

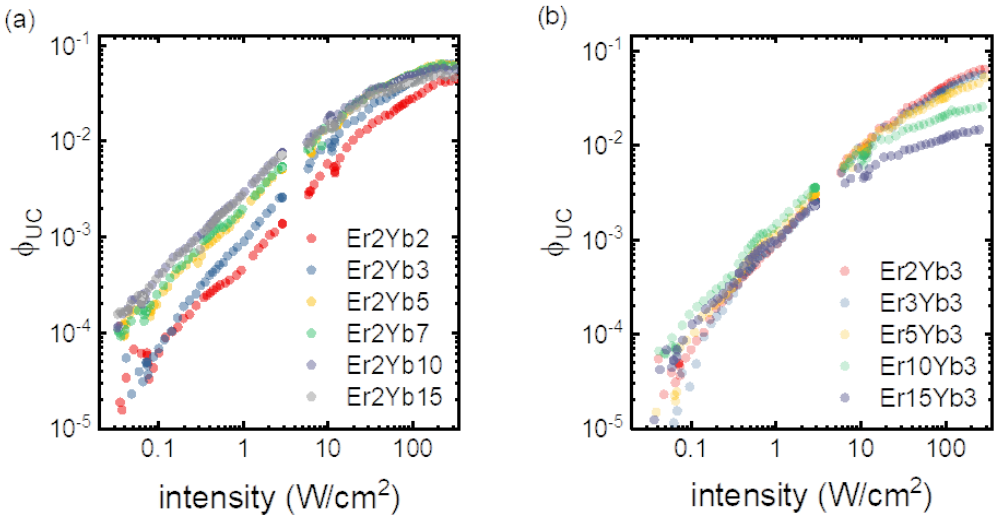

Figure 3.13 - Luminescence quantum yield values under 976 nm excitation at different intensities in the BaF2 samples with various Er^{3+}/Yb^{3+} doping levels.

Several conclusions can be drawn from the data presented in the Figure 3.13. First, all samples show a monotonic increase in the value of ϕ_{UC} as the excitation intensity increases. Second, when the excitation intensity is less than 100 W/cm^2 an increase in the concentration of Yb^{3+} ions leads to higher ϕ_{UC} values. However, when

the intensity exceeds 100 W/cm^2 the behavior is reversed and the ϕ_{UC} value drops in samples with high Yb^{3+} ion content. In addition, a change in the number of Er^{3+} ions also affects the value of the quantum yield. At relatively low excitation intensities (<10 W/cm^2) samples with high Er $^{3+}$ content show higher ϕ_{UC} values, whereas, in the remaining range of investigated intensities (10 - 300 W/cm^2), the maximum quantum yield is observed in samples with a lower number of Er^{3+} ions. These observations are similar to the concentration effects observed in previously studied materials such as SrF_2[23] and $NaYF_4$ [140].

When the dependence of ϕ_{UC} on the excitation intensity is investigated, the heating of the sample must be considered since it is well known that the value of ϕ_{UC} also depends on the temperature of the sample[126]. In the Er^{3+} ion, there are 2 thermally bound levels ($^4H_{11/2}$ and $^4S_{3/2}$). The ratio of the intensities of these levels is proportional to the temperature of the sample and these levels can be used for luminescence thermometry in the temperature range of 283-393 K [141]. Thus, up-conversion luminescence spectra can be used to determine the temperature of the samples and study its effect on the quantum yield of up-conversion luminescence. This approach has already been discussed in detail in [126].

There is the intensity dependence of the ratio of the $^4S_{3/2} \longrightarrow {}^4I_{15/2}$ and $^4H_{11/2} \longrightarrow {}^4I_{15/2}$ emission bands in the Figure 3.14. The distance between the $^4S_{3/2}$ and $^4H_{11/2}$ levels is about 800 cm^{-1}. This distance can be bridged by several phonons and the probability of this process increases with temperature. Thus, the intensity of the luminescence from a higher $^4H_{11/2}$ level will increase relative to the luminescence from a lower $^4S_{3/2}$ level at higher temperatures. Consequently, the ratio of the luminescence intensities of the $^4S_{3/2} \longrightarrow {}^4I_{15/2}$ (I_{521}) and $^4H_{11/2} \longrightarrow {}^4I_{15/2}$ (I_{545}) transitions is proportional to the temperature of the samples.

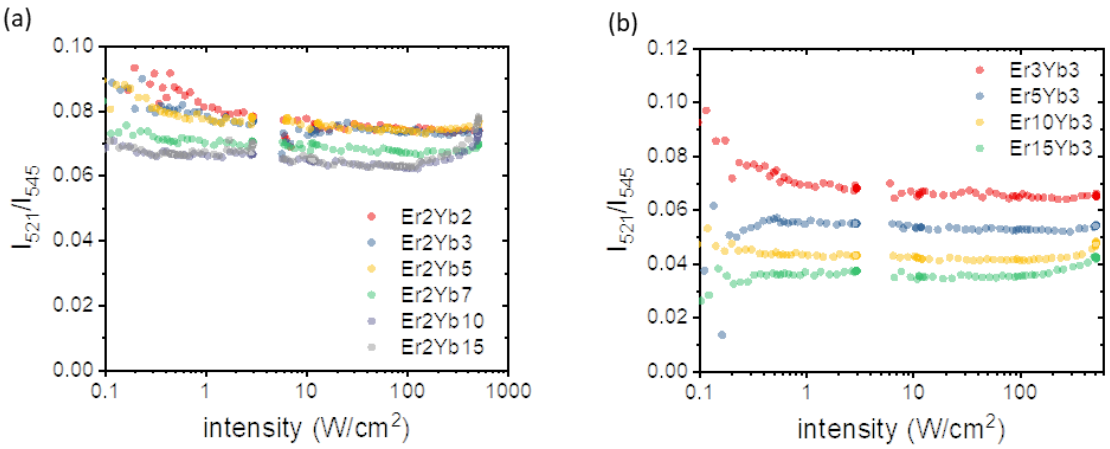

Figure 3.14 - Dependence of the ratio of transition luminescence intensities $^4S_{3/2} \rightarrow {}^4I_{15/2}$ *(*I_{521}*) and* $^4H_{11/2} \rightarrow {}^4I_{15/2}$ *(*I_{545}*) on the pump intensity at 976 nm.*

The data in the Figure 3.14 shows that in the majority of the samples, the temperature does not significantly deviate from room temperature even at high excitation intensities, since the I_{521} / I_{545} ratio remains the same over the entire range of studied intensities. A noticeable deviation of this ratio from the initial one, and hence an increase in temperature, is only observed in samples with the maximum content of Yb $^{3+}$ ions namely 10 and 15 mol %.

For certain applications, the total number of emitted up-conversion photons is more important than the conversion efficiency of absorbed radiation. For this purpose, the brightness parameter is used as defined in[142]:

$$B = \phi_{UC} * \alpha. \qquad 21$$

Here α - is the absorption coefficient. The values of the maximum quantum yield of several transitions of Er^{3+} ions and total UC emission in the 400 – 900 nm range, as well as brightness under 976 nm excitation, are given in the Table 3.5. The data shows that the maximum ϕ_{UC} value is achieved in Er2Yb2 and Er2Yb3 samples and equals 0.099 and 0.100, respectively. These values are comparable with the maximum ϕ_{UC} values known in the literature. The highest brightness is observed in a different sample – Er2Yb10. Despite having an average ϕ_{UC} value high absorption at the excitation wavelength makes this sample the brightest.

Table 3.5 – Maximum ϕ_{UC} value (at excitation intensity of 490 W/cm^2) of $^4S_{3/2} \longrightarrow {}^4I_{15/2}$, and $^4F_{9/2} \longrightarrow {}^4I_{15/2}$ transitions, total emission in the 400 - 900 nm range and brightness under 976 nm excitation.

	$^4S_{3/2} \longrightarrow {}^4I_{15/2}$	$^4F_{9/2} \longrightarrow {}^4I_{15/2}$	Total	Brightness, cm^{-1}
Er2Yb2	0.021	0.063	0.099	0.121
Er2Yb3	0.023	0.061	0.100	0.192
Er2Yb5	0.021	0.053	0.088	0.262
Er2Yb7	0.023	0.043	0.081	0.374
Er2Yb10	0.019	0.036	0.068	0.495
Er2Yb15	0.013	0.027	0.048	0.419
Er3Yb3	0.018	0.043	0.064	0.120
Er5Yb3	0.017	0.03	0.062	0.148
Er10Yb3	0.008	0.01	0.026	0.121
Er15Yb3	0.002	0.004	0.011	0.065

To better understand which features of the studied materials allow achieving high ϕ_{UC} values and to find the factors that limit the ϕ_{UC} additional experiments are required. A study of the luminescence lifetimes under different excitation wavelengths can provide additional insight into the energy migration in the investigated materials.

3.3.4 Physical reasons for the increased lifetime of Er^{3+} states

Luminescence decay

The next step in the spectral characterization of the samples is the analysis of luminescence decays. Luminescence decay can provide a great deal of additional information about the energy migration pathways in the system of doping ions. Similar to the study of emission spectra, luminescence decays are recorded under 375 nm excitation. Decays at wavelengths of 550 nm ($^4S_{3/2} \longrightarrow {}^4I_{15/2}$ transition), 660 nm ($^4F_{9/2}$

$\longrightarrow {}^4I_{15/2}$ transition) and 990 nm (transition from the $\{Er^{3+}:{}^4I_{11/2}\&Yb^{3+}:{}^2F_{5/2}\}$ manifold) are obtained.

The resulting curves are shown in Figure 3.15. It can be seen that the curves obtained at wavelengths of 660 and 990 nm have a shape close to mono-exponential, so in order to determine the average luminescence decay time these curves are fitted with a following function

$$I = A \ e^{-\frac{t}{\tau}}. \quad 22$$

However, the luminescence decay curves at 540 nm have a different from mono-exponential shape. A good agreement between the experimental results and the fitting is obtained with a bi-exponential function:

$$I = A_1 e^{-\frac{t}{\tau_1}} + A_2 e^{-\frac{t}{\tau_2}} . \quad 23$$

The average lifetime is defined as [143]

$$\bar{\tau} = \frac{A_1\tau_1 \ + A_2\tau_2}{A_1 + A_2}. \quad 24$$

Here τ, τ_1, τ_2 are the decay times and A, A1 and A2 are the amplitudes of the corresponding decays. These parameters are adjusted during the fitting procedure.

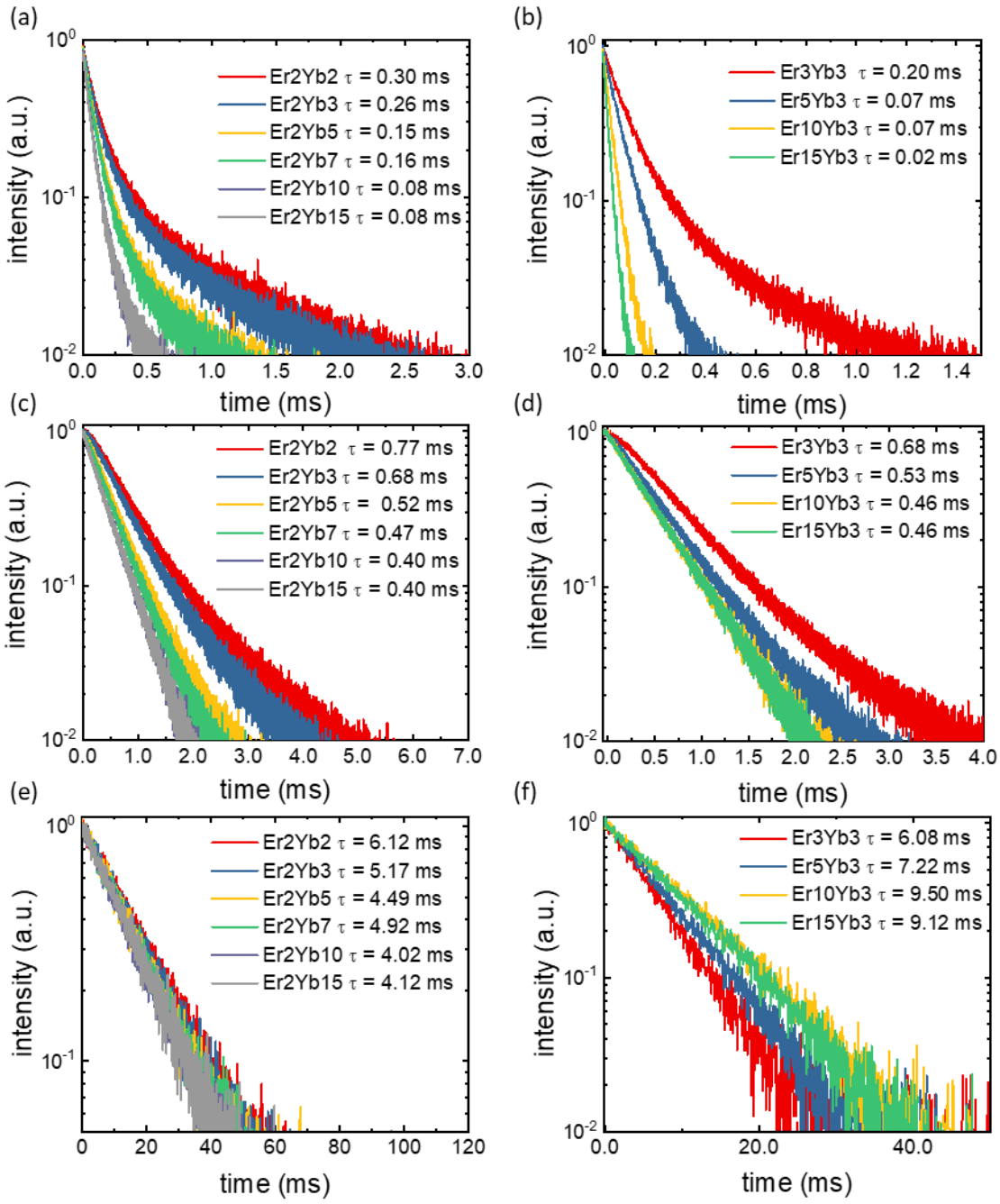

Figure 3.15 - Luminescence decay curves of the transition a, b) $^4S_{3/2} \longrightarrow {}^4I_{15/2}$ *at 540 nm; c, d)* $^4F_{9/2} \longrightarrow {}^4I_{15/2}$ *at 660 nm; e, f) from* $\{Er^{3+}:{}^4I_{11/2}\&Yb^{3+}:{}^2F_{5/2}\}$ *manifold at 990 nm under 375 nm excitation.*

Then the luminescence decay curves of the $^4S_{3/2} \longrightarrow {}^4I_{15/2}$ (550 nm), $^4F_{9/2} \longrightarrow {}^4I_{15/2}$ (660 nm) transitions and from $\{Er^{3+}:{}^4I_{11/2}\&Yb^{3+}:{}^2F_{5/2}\}$ manifold (990 nm) under 976 nm excitation are then recorded. The curves are presented in Figure 3.16.

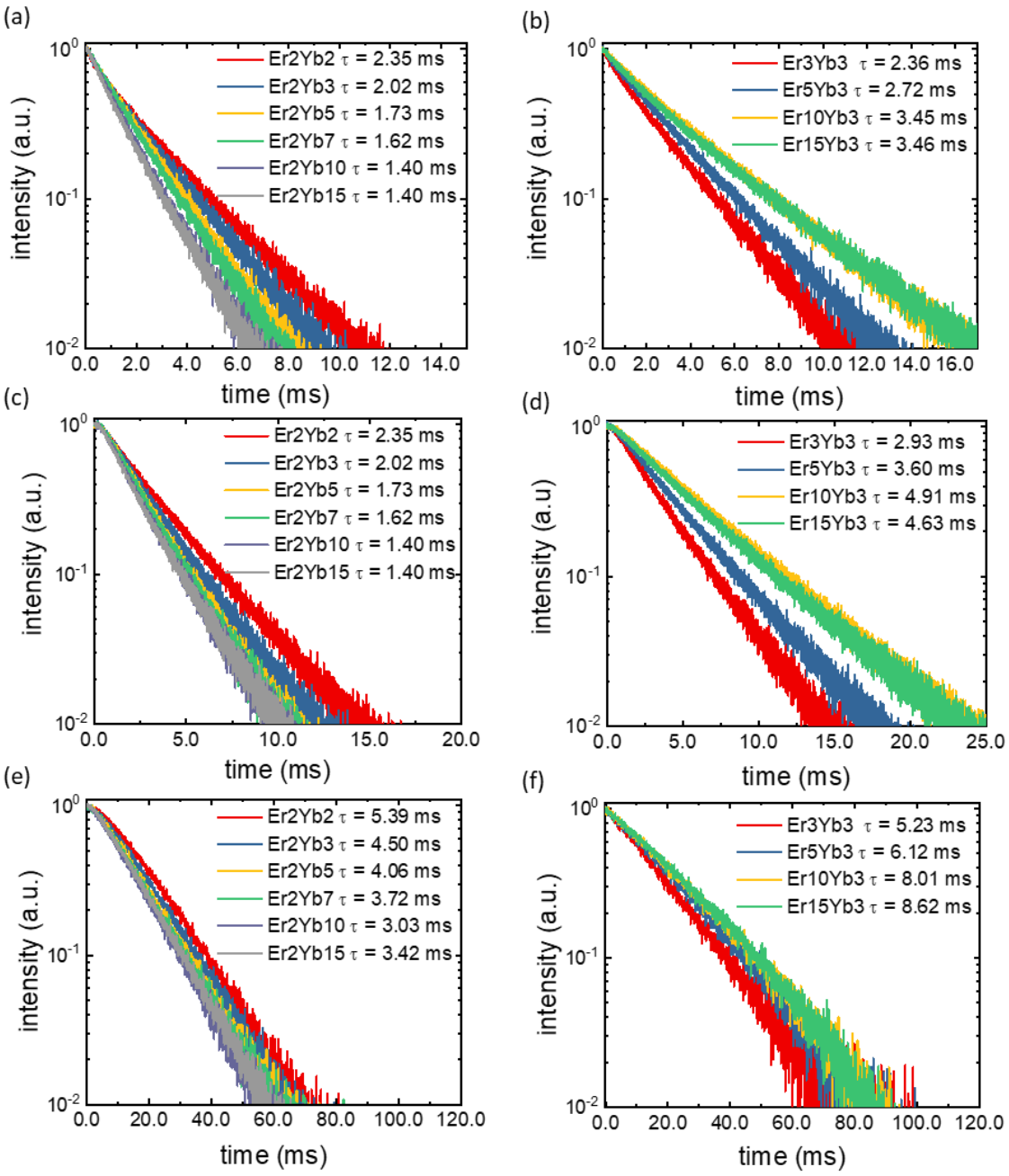

Figure 3.16 - Luminescence decay curves of the transition a, b) $^4S_{3/2} \longrightarrow {}^4I_{15/2}$ *at 540 nm; c, d)* $^4F_{9/2} \longrightarrow {}^4I_{15/2}$ *at 660 nm; e, f) from* $\{Er^{3+}:{}^4I_{11/2}\&Yb^{3+}:{}^2F_{5/2}\}$ *manifold at 990 nm under 976 nm excitation.*

In this case, the shape of the decay curves differs significantly from the one observed under UV or visible excitation. The decay curves obtained under 976 nm excitation have a shape close to exponential, therefore the formula 22 can be used to

determine the average luminescence decay time. The resulting decay times are shown in the corresponding figures. All times are also presented in the Table 3.6.

Table 3.6 - Average luminescence decay time under 976 nm excitation, ms.

	Er^{3+} :$^4S_{3/2} \rightarrow {}^4I_{15/2}$ (540 nm)		Er^{3+} :$^4F_{9/2} \rightarrow {}^4I_{15/2}$ (660 nm)		{Er^{3+} :$^4I_{11/2} \rightarrow {}^4I_{15/2}$ Yb^{3+} :$^2F_{5/2} \rightarrow {}^2F_{7/2}$ } (990 nm)	
Excitation, nm	**375**	**976**	**375**	**976**	**375**	**976**
Er2Yb2	0.30	2.35	0.77	2.86	6.12	5.39
Er2Yb3	0.26	2.02	0.68	2.39	5.17	4.50
Er2Yb5	0.15	1.73	0.52	2.11	4.49	4.06
Er2Yb7	0.16	1.62	0.47	2.05	4.92	3.72
Er2Yb10	0.08	1.40	0.40	1.94	4.02	3.03
Er2Yb15	0.08	1.40	0.40	1.95	4.12	3.42
Er3Yb3	0.20	2.36	0.68	2.93	6.08	5.23
Er5Yb3	0.07	2.72	0.53	3.60	7.22	6.12
Er10Yb3	0.07	3.45	0.46	4.91	9.50	8.01
Er15Yb3	0.02	3.46	0.46	4.63	9.12	8.62

The data in the table highlights several trends in the decay time when the concentration of the doping ions is varied. An increase in the content of either Yb^{3+} or Er^{3+} ions leads to a drop in the luminescence decay time of the $^4S_{3/2}$ and $^4F_{9/2}$ levels under 375 nm excitation. The simplest explanation of this effect is the concentration quenching of luminescence. However, there could be other processes, which lead to a decrease in the luminescence decay time. Cross-relaxation that involves emissive levels, such as Er^{3+}:$^4S_{3/2}$ $\rightarrow$ $^4I_{9/2}$ - Er^{3+}:$^4I_{13/2}$ $\rightarrow$ $^4I_{9/2}$, Er^{3+}:$^4H_{11/2}$ $\rightarrow$ $^4I_{9/2}$ - Er^{3+}:$^4I_{15/2}$ $\rightarrow$ $^4I_{13/2}$ and Er^{3+}:$^4F_{9/2}$ $\rightarrow$ $^4I_{13/2}$ - Yb^{3+}:$^2F_{7/2}$ $\rightarrow$ $^2F_{5/2}$ can act as such processes. In addition, the luminescence decay times can change if the increase in the concentration leads to a

distortion of the crystal lattice and hence a change in the radiative transition probability. A similar effect has already been observed during the analysis of the absorption cross-sections of some transitions of the Er^{3+} ion.

The role of cross-relaxation has already been discussed during the analysis of luminescence spectra. For example, cross-relaxation processes between Er^{3+} ions: $^4S_{3/2} \longrightarrow {}^4I_{9/2}$ - $^4I_{15/2} \longrightarrow {}^4I_{13/2}$, $^4S_{3/2} \longrightarrow {}^4I_{9/2}$ - $^4I_{13/2} \longrightarrow {}^4I_{9/2}$ leads to a drop in the luminescence lifetime of the $^4S_{3/2} \longrightarrow {}^4I_{15/2}$ transition, as they serve as alternative channels of luminescence level depopulation. In addition, a process between Er^{3+}:$^4S_{3/2} \longrightarrow {}^4I_{11/2}$ and Yb^{3+}:$^2F_{7/2} \longrightarrow {}^2F_{5/2}$ ions, which also leads to a shortening of the luminescence decay, can be identified using the luminescence spectra.

During the analysis of possible processes that involve the Er^{3+}:$^4F_{9/2}$ state cross-relaxation between both Er^{3+} ions:$^4F_{9/2} \longrightarrow {}^4I_{9/2}$ - $^4I_{15/2} \longrightarrow {}^4I_{13/2}$, $^4F_{9/2} \longrightarrow {}^4I_{9/2}$ - $^4I_{13/2} \longrightarrow {}^4I_{9/2}$, as well as Er^{3+}:$^4F_{9/2} \longrightarrow {}^4I_{13/2}$ and Yb^{3+}:$^2F_{7/2} \longrightarrow {}^2F_{5/2}$ ions is identified as one that can lead to decrease in the luminescence decay time.

The luminescence decay time of the $^4S_{3/2}$ and $^4F_{9/2}$ levels under 976 nm excitation is significantly longer than the one discussed previously. As it was settled in the previous chapter, in a system consisting of Er^{3+} and Yb^{3+} ions the energy transfer up-conversion scenario is realized. In such systems, the luminescence decay time is dependent not only on the lifetime of the emissive levels of the acceptor ion but also on the lifetime of the intermediate levels of the donor ion involved in up-conversion. This is because the probability of energy transfer between a donor and an acceptor is lower than the probability of the radiative decay of the excited state of the donor. Thus, the observed luminescence decay time is dependent on the lifetime of the excited state of the donor. In the studied system, this intermediate state is the {Er^{3+}:$^4I_{11/2}$&Yb^{3+}:$^2F_{5/2}$} manifold. This once again proves the fact that under such excitation the population of the higher levels of the Er^{3+} ion takes place via the transfer of energy from the long-lived lower states.

The luminescence decay time of the $\{Er^{3+}:{}^4I_{11/2}\&Yb^{3+}:{}^2F_{5/2}\}$ manifold should be discussed separately. The luminescence decay time of this state has similar values and the concentration dependence both under 375 nm and 976 nm excitation. At high concentrations of Yb^{3+} ions, the decay time decreases, which is primarily due to a rise in the intensity of the ETU process. This also leads to a drop in the luminescence decay time from the ${}^4S_{3/2}$ and ${}^4F_{9/2}$ levels. The luminescence decay of the $\{Er^{3+}:{}^4I_{11/2}\&Yb^{3+}:{}^2F_{5/2}\}$ manifold is out of the trend when the number of Er^{3+} ions is increased. In these samples the luminescence decay time of the $\{Er^{3+}:{}^4I_{11/2}\&Yb^{3+}:{}^2F_{5/2}\}$ manifold increases under both wavelengths. Under 976 nm excitation, high Er^{3+} content also leads to an increase in the luminescence decay time of the ${}^4S_{3/2} \longrightarrow {}^4I_{15/2}$, ${}^4F_{9/2} \longrightarrow {}^4I_{15/2}$ transitions, which is expected given the population pathway of the upper levels.

This behaviour of the luminescence decay time of the $\{Er^{3+}:{}^4I_{11/2}\&Yb^{3+}:{}^2F_{5/2}\}$ manifold is a rather interesting phenomenon, which has not been discussed in detail in the literature before. Several factors can lead to an increase in the decay time when the number of Er^{3+} ions is increased. For example, this effect can be caused by the re-absorption process in which a photon can be re-absorbed and re-emitted several times before it leaves the crystal. For example, in the work [144,] the effect of Yb^{3+} concentration on the luminescence decay time is shown. The investigated samples were YAG single crystals doped with Yb^{3+} ions. In the concentration range from 2 to 30 mol.% the decay time varies from 1.1 to 1.5 ms, which cannot explain the observed effect. Another explanation of this behaviour of the luminescence decay time dependence is that the $Er^{3+}:{}^4I_{11/2}$ level decay time is much longer than the decay time of the Yb^{3+} excited state. For example, in

Figure *3.17* the luminescence decay curves of BaF_2 crystals single-doped with 2, 3 or 5 mol% of Er^{3+} or Yb^{3+} ions are shown. All curves have an exponential decay, which allows to estimate the decay time using the formula 22.

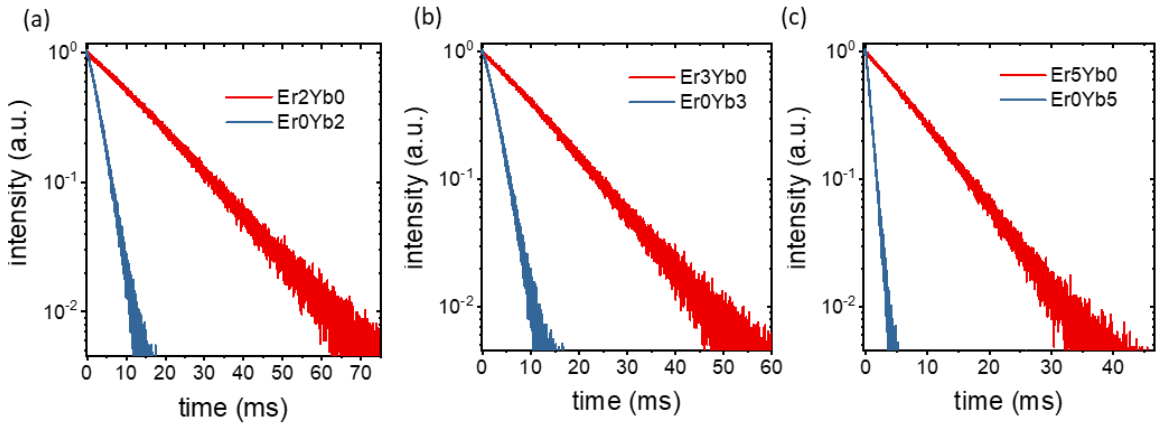

Figure 3.17 - Luminescence decay curves at 990 nm in samples doped with (a)2, (b)3, (c) 5 mol% of Er^{3+} or Yb^{3+} ions.

The fitting results show that the decay times of the two ions differ significantly at all investigated concentrations. It is 14.55, 10.73 and 7.41 ms for Er^{3+} concentrations of 2, 3 and 5% mol% and 2.77, 2.44 and 0.77 ms for similar concentrations of Yb^{3+} respectively. However, the Er^{3+} ion concentration series shows that an increase in the content of the doping ion leads to a drop in the luminescence decay time. Thus, there must still be a mechanism which leads to an increase in the decay time of the $\{Er^{3+}:{}^4I_{11/2}\&Yb^{3+}:{}^2F_{5/2}\}$ manifold.

Such a mechanism could be the influx of population to the $^4I_{11/2}$ from the $^4I_{9/2}$ level. This process can be particularly intense at high concentrations of Er^{3+} ions. During the analysis of the luminescence and excitation spectra several cross-relaxation processes which lead to an increase in the population $^4I_{9/2}$ state have been highlighted. In crystals with low phonon energy such as BaF_2 the multiphonon relaxation rates are relatively low and thus the decay time of the $^4I_{11/2}$ level will approach the values of the lifetime of the $^4I_{9/2}$ state, which may exceed 10 ms [88]. All of the above suggests that this level, possessing weak emission but a long lifetime, can be considered as another metastable level (similar to the $\{Er^{3+}:{}^4I_{11/2}\&Yb^{3+}:{}^2F_{5/2}\}$ manifold and $^4I_{13/2}$ state) that affects both up- and down-shifting processes. Thus, an increase in the content of Er^{3+} ions leads to an increase in the population probability of the $^4I_{9/2}$ level, which, in turn,

causes an increase in the luminescence decay time of the $^4S_{3/2}$, $^4F_{9/2}$ states, and $\{Er^{3+}:{}^4I_{11/2}\&Yb^{3+}:{}^2F_{5/2}\}$ manifold.

Judd – Ofelt calculations

To explicitly answer the question of whether the relaxation from the $^4I_{9/2}$ level can have the suggested effect on the luminescence decay time, the radiative lifetime values of the $^4I_{9/2}$ and $^4I_{11/2}$ states of the Er^{3+} ion are calculated using the standard Judd-Offelt theory [145,146]. A detailed description of the calculations has already been given in chapter two of this paper. In the first stage of calculations, the values of $\Omega_{(\lambda)}$ intensity parameters are obtained. The results are shown in the Table 3.7.

Table 3.7 - Intensity parameters Ω_2, Ω_4, Ω_6.

	Ω_2	Ω_4	Ω_6
Er2Yb2	0.95	0.49	1.45
Er2Yb3	1.01	0.50	1.54
Er2Yb5	1.18	0.74	1.94
Er2Yb10	1.31	0.71	2.12
Er2Yb15	1.32	0.60	2.16
Er3Yb3	1.07	0.58	1.71
Er5Yb3	1.04	0.70	1.88
Er10Yb3	1.06	0.80	2.44
Er15Yb3	0.94	0.63	2.36

Intensity parameters $\Omega_{(\lambda)}$ can be used to estimate the environment of an emitting centre. There are several works devoted to the investigation of the dependence of the Ω_2 parameter on the symmetry of the impurity centre environment [147–149]. In these works, it is shown that an increase in the Ω_2 parameter correlates with a decrease in the symmetry of the impurity centre environment. The data in Table 3.7 shows that the Ω_2

parameter increases in samples containing more Yb^{3+} ions. This is in line with the assumption made during the study of the absorption cross-sections that an increase in the concentration of doping ions leads to greater distortion of the local crystal field, which, in turn, increases the probability of f-f transitions.

Using the obtained $\Omega_{(\lambda)}$ values and the least squares method the values of spontaneous emission probability, branching ratios as well as radiative lifetimes are obtained.

Table 3.8 - Radiative lifetimes of the $^4S_{3/2}$, $^4F_{9/2}$, $^4I_{9/2}$ and $^4I_{11/2}$ levels of Er^{3+} ions obtained with Judd-Ofelt theory, ms.

	Er2Yb2	**Er2Yb3**	**Er2Yb5**	**Er2Yb10**	**Er2Yb15**
Er^{3+} :^{4} $S_{3/2}$	1.13	1.06	0.84	0.77	0.76
Er^{3+} :^{4} $F_{9/2}$	2.25	2.15	1.63	1.55	1.59
Er^{3+} :^{4} $I_{9/2}$	21.09	20.34	15.23	14.73	15.42
Er^{3+} :^{4} $I_{11/2}$	12.74	12.10	9.83	9.05	8.92
	Er3Yb3	**Er5Yb3**	**Er10Yb3**	**Er15Yb3**	
Er^{3+} :^{4} $S_{3/2}$	0.95	0.87	0.67	0.69	
Er^{3+} :^{4} $F_{9/2}$	1.91	1.69	1.35	1.47	
Er^{3+} :^{4} $I_{9/2}$	17.98	15.82	12.91	14.35	
Er^{3+} :^{4} $I_{11/2}$	10.99	10.12	8.02	8.32	

A comparison of the calculated values and the luminescence decay times under 375 nm excitation (Figure 3.15) reveals that the luminescence decay time of the $^4S_{3/2}$ and $^4F_{9/2}$ states, obtained experimentally, is significantly lower than the radiative lifetime obtained from the Judd-Ofelt theory. This indicates a low efficiency of the radiative process. When comparing the experimental and theoretical values, it is

important to know that the radiative lifetime obtained from the Judd-Ofelt theory does not consider the multiphonon and cross-relaxation processes, which play a significant role in the studied samples. Thus, it is shown that these processes cause quenching of luminescence, which also leads to a decrease in the luminescence quantum yield.

To determine the cause of the increase of luminescence decay time of $\{Er^{3+}:{}^4I_{11/2}\&Yb^{3+}:{}^2F_{5/2}\}$ manifold radiative lifetimes of $Er^{3+}:{}^4I_{11/2}$ and ${}^4I_{9/2}$ levels should be analyzed. The calculated radiative lifetime of each of the two levels drops with an increase in the number of doping ions. It should also be noted that in the sample with the highest content of Er^{3+} ions, the calculated radiative lifetime is shorter than that observed experimentally. In turn, the lifetime of the ${}^4I_{9/2}$ state is much longer than the observed decay of other studied levels. This fact allows concluding that the ${}^4I_{9/2} \longrightarrow {}^4I_{11/2}$ relaxation process assumed above may be responsible for an additional prolongation of the luminescence decay time of the $\{Er^{3+}:{}^4I_{11/2}\&Yb^{3+}:{}^2F_{5/2}\}$ manifold.

3.3.5 Ratio of $Er^{3+}:{}^4S_{3/2} \longrightarrow {}^4I_{15/2}$ and $Er^{3+}:{}^4F_{9/2} \longrightarrow {}^4I_{15/2}$ transition intensities

In this work, it has been repeatedly stated that the ${}^4S_{3/2}$ and ${}^4F_{9/2}$ energy levels of the Er^{3+} ion have different population pathways. Thus, analysis of the luminescence intensity ratio of the ${}^4S_{3/2} \longrightarrow {}^4I_{15/2}$ and ${}^4F_{9/2} \longrightarrow {}^4I_{15/2}$ transitions can provide additional information on the excitation energy distribution. The dependence of this relationship on the excitation intensity under 976 nm excitation is of particular interest. This dependence is plotted in Figure 3.18.

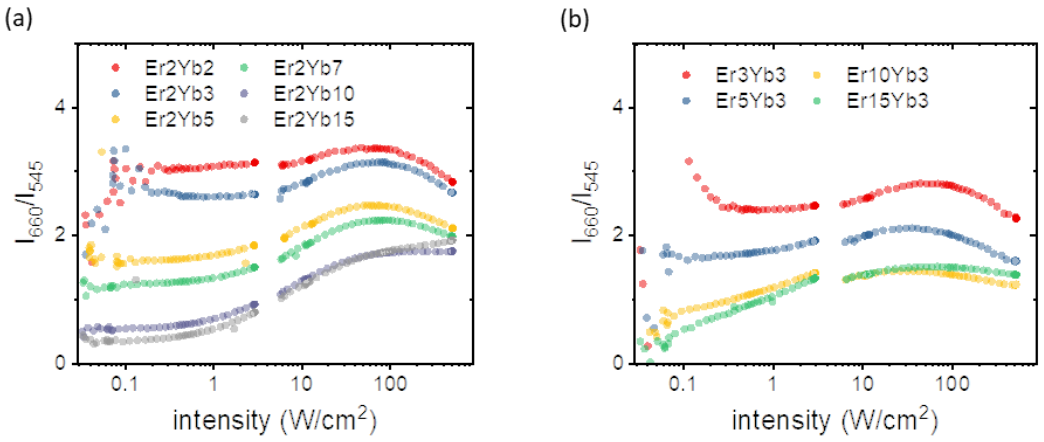

Figure 3.18 - Dependence of the intensity ratio of $^4S_{3/2} \longrightarrow {}^4I_{15/2}$ (I_{545}) and $^4F_{9/2} \longrightarrow {}^4I_{15/2}$ (I_{660}) transitions on the excitation intensity at 976 nm.

From the data in the Figure 3.18, several conclusions can be drawn. First, in a series of samples with different concentrations of Yb^{3+} ions, the dependence on the excitation intensity is not observed at low doping content. Then, in the range from 1 to 100 W/cm^2, there is an increase in the intensity ratio, followed by a drop, except for the sample with maximum Yb^{3+} content. This can be explained by the fact that at low intensities the absorption probability of three photons is low and the level $^4F_{9/2}$ is populated via the relaxation from the $^4S_{3/2}$ level, whereas at higher intensities the three-photon process begins to play a bigger role. The subsequent drop can be explained by the different saturation of $^4S_{3/2}$ and $^4F_{9/2}$ levels of Er^{3+} ion [76] as well as the competition between up-conversion and spontaneous emission [150]. If the processes of up-conversion excitation and spontaneous emission occur simultaneously, they will compete and the dependence of the luminescence intensity on the excitation will be determined by the dominant process. If spontaneous emission of photons dominates, the luminescence intensity will depend on excitation as $I \sim P^n$, where I is the luminescence intensity, P *is* the excitation intensity and n is the number of excitation photons needed to populate the excited state. If up-conversion dominates, the dependence will look like $I \sim P^{n-1}$.

The data presented in the Figure 3.18 shows that the luminescence intensity of the $^4S_{3/2} \longrightarrow {}^4I_{15/2}$ and $^4F_{9/2} \longrightarrow {}^4I_{15/2}$ transitions has a different dependence on the

excitation intensity. In most cases, the intensity of the $^4F_{9/2} \longrightarrow {}^4I_{15/2}$ transition grows faster than that of the $^4S_{3/2} \longrightarrow {}^4I_{15/2}$ transition when excitation intensity is increased. In all but one sample, the ratio of intensities reaches a maximum value in the intensity range of 50 to 100 W/cm^2, after which it decreases. In the literature, this effect is often referred to as up-conversion intensity saturation [74].

Only one sample, doped with 2 mol.% Er^{3+} and 15 mol.% Yb^{3+}, shows a monotonic increase in the intensity ratio of red to green bands over the entire studied excitation intensity range. This suggests the possibility of application of such samples as a reference for determining the incident radiation intensity, using the intensity ratio of the bands as a metric. However, for this approach to be feasible, the results must be reproducible over a wide range of excitation wavelengths. To test this, the dependence of the intensity ratio of red and green bands on the excitation wavelength in the range of the Yb^{3+} :$^2F_{7/2} \longrightarrow {}^2F_{5/2}$ absorption is obtained.

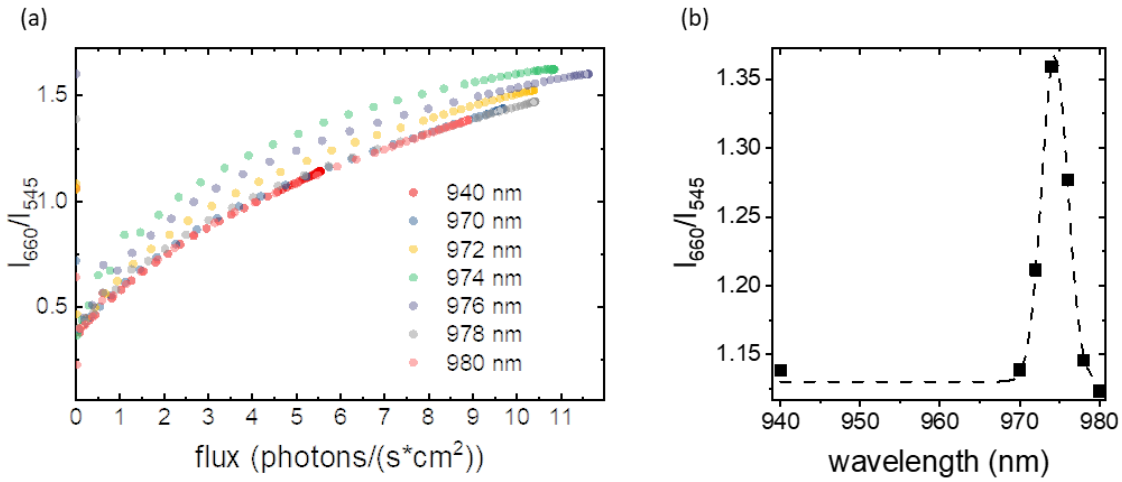

Figure 3.19 - Dependence of the intensity ratio of $^4S_{3/2} \longrightarrow {}^4I_{15/2}$ (I_{545}) and $^4F_{9/2} \longrightarrow {}^4I_{15/2}$ (I_{660}) transitions on the excitation intensity in the 940 - 980 nm wavelength range.

The resulting dependencies are shown in Figure 3.19a. To take into account the different values of the absorption coefficient, the dependence on the absorbed photon flux is presented. It was expected that in this case, the intensity ratio of the red and

green bands would behave the same under every excitation wavelength. However, as can be seen in Figure 3.19 the dependence strongly deviates from the general trend under some excitation wavelengths (972, 974, 976 nm). For the same number of absorbed photons, the intensity ratio of red and green bands is significantly greater under these excitation wavelengths. To clearly show this dependency, the same data is presented in a different format in Figure 3.19b. This figure shows the dependency of the intensity ratio of red/green emission on wavelength for the same number of absorbed photons. It is assumed that the observed dependence corresponds to the Er^{3+}:$^4I_{15/2} \longrightarrow {}^4I_{11/2}$ absorption band. All of this suggests a serious limitation on the possible application of the material for the estimation of the incident intensity. On the other hand, this demonstrates that the up-conversion process occurs differently when the Er^{3+}:^{4} $I_{11/2}$ state is excited directly. Since in the proposed ETU scenario the population of the higher levels occurs via several energy transfer steps between the Er^{3+} and Yb^{3+} ions, the direct population of the excited state of Er^{3+} changes the population pathway, which affects the observed intensity ratio. It has been reported that there is a possible cross-relaxation process of Er^{3+}:$^4S_{3/2} \longrightarrow {}^4I_{13/2}$ - Yb^{3+}:$^2F_{7/2} \longrightarrow {}^2F_{5/2}$ that leads to a decrease in the population of the $^4S_{3/2}$ state and an increase in the population of the $^4F_{9/2}$ state in the case of up-conversion excitation [73].

Another important parameter that might affect the applicability of the studied material as an incident intensity reference is the excitation mode. There are studies devoted to the determination of the influence of the excitation mode on the spectral and kinetic properties of materials doped with Er^{3+} and Yb^{3+} ions. In the paper [151] the excitation modulation effect is studied in more detail. It is shown that an increase in both pulse duration and repetition rate significantly affects the observed up-conversion spectrum of $NaYF_4$:Er/Tm (2/0.5%)@$NaYF_4$ core-shell nanoparticles, leading to an increase in the relative intensity of the red emission band.

In the current work, a different approach is used to investigate the dependence of the red and green intensity ratio on the excitation mode. Continuous radiation was

modulated so that the average pump power is constant, i.e. there is a constant duty cycle. In this experiment, the duty cycle is set to 10.

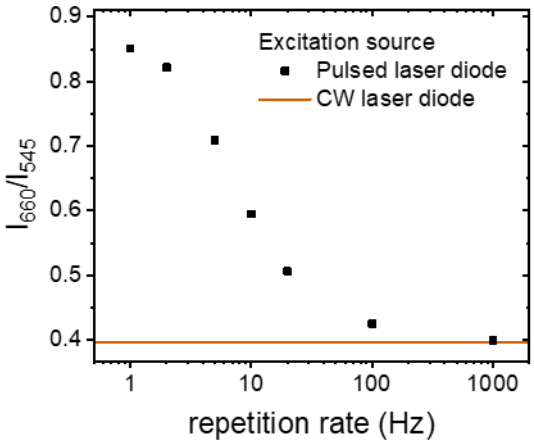

Figure 3.20 - Dependence of the intensity ratio of $^4S_{3/2} \longrightarrow {}^4I_{15/2}$ (I_{545}) and $^4F_{9/2} \longrightarrow {}^4I_{15/2}$ (I_{660}) transitions in a sample with 2 mol.% Er^{3+} and 15 mol.% Yb^{3+} on the excitation pulse frequency at 976 nm.

The results are shown in Figure 3.20. The results show that the intensity ratio of red and green emission has a strong dependence on the frequency of pulsed excitation. A monotonous drop in the value of the ratio of intensities with an increase in pulse repetition frequency is observed. The observed dependence can be explained as follows. It is shown above that the luminescence lifetime under up-conversion excitation exceeds 1 ms for both $^4S_{3/2}$ and $^4F_{9/2}$ levels. In addition, the discussion of the luminescence and excitation spectra has shown that one of the main population pathways of the $^4F_{9/2}$ state is relaxation from higher levels, including $^4S_{3/2}$. Thus, when the pulse repetition rate is comparable to the luminescence decay time, the next excitation pulse arrives before the upper state has had time to completely empty, thus creating a near-continuous wave mode. At lower frequencies, the relative intensity of the red band becomes larger, since in the time between the pulses all the relaxation processes that lead to redistribution of the population have time to occur.

3.4 Enhancement of the perovskite solar cell performance via UC of the sub-bandgap photons

The final step of the research is to study the spectral response of a perovskite solar cell combined with an Er^{3+}/Yb^{3+}-doped BaF_2 crystal. It is crucial to study this effect under the excitation conditions as close as possible to the solar spectrum. The sample doped with 2 mol.% of Er^{3+} and 10 mol.% of Yb^{3+} ions provides the highest PLQY values in this low-intensity excitation range. To test the combined device (perovskite solar cell + crystal), the short-circuit current (J_{sc}) is chosen as a figure of merit. It is proposed to use two excitation sources. One is a solar simulator operating in the 350 – 850 nm range to simulate the Vis part of the solar spectrum, which will set the baseline J_{sc} level. The second excitation source is a CW laser operating at 976 nm, the intensity of which can be varied. This source is responsible for the NIR part of the excitation. The scheme of the setup is shown in Figure 3.21.

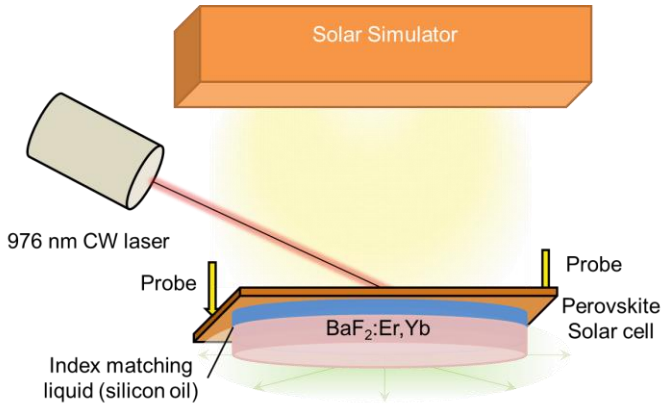

Figure 3.21 - Setup for the estimation of the enhancement of the short-circuit current of the perovskite solar cell.

Using the setup described above it is found that at the intensity of the 976 nm excitation equal to 0.6 W/cm^2 (corresponding to 120 intensities of the solar radiation) the J_{sc} enhancement is 0.38 mA/cm^2. This demonstrates the possibility of improving the spectral response of the perovskite solar cells by combining them with up-conversion material.

3.5 Summary

The following conclusions can be drawn at the end of this chapter:

- The Bridgeman method provides Er^{3+}/Yb^{3+}-doped bulk BaF_2 crystals that can function as efficient up-conversion materials.
- The highest ϕ_{UC} value is detected under 490 W/cm^2, 976 nm excitation in the sample doped with 2 mol.% of Er^{3+}, 3 mol.% of Yb^{3+} ions and equals to 10%.
- Different population scenarios of Er^{3+} ions are discussed and it is found that both two- and three-photon processes take place in the case of UC in BaF_2:Er, Yb crystals.
- The role of the weakly emitting Er^{3+}:$^4I_{9/2}$ level is discussed and its role in the population of the lower levels $^4I_{11/2}$ and $^4I_{13/2}$ is demonstrated using Judd-Ofelt analysis.
- The intensity ratio of the $^4S_{3/2} \longrightarrow {}^4I_{15/2}$ and $^4F_{9/2} \longrightarrow {}^4I_{15/2}$ UC emission is studied. It is shown that both the excitation wavelength and the excitation mode (CW or pulsed) affect this value. This gives additional insight into the population dynamics of the Er^{3+}/Yb^{3+}-doped materials.
- It is shown that the addition of the BaF_2 crystal doped with 2 mol.% of Er^{3+} and 10 mol.% of Yb^{3+} ions provides an increase in the J_{sc} of a perovskite solar cell equal to 0.38 mA/cm^2 under 976 nm excitation with an intensity of 0.6 W/cm^2.

4. Down-conversion in Er^{3+} and possible enhancement of the Ge diode performance

4.1 Introduction

The energy level structure of the Er^{3+} ion shows that several pathways can lead to down-conversion, which should manifest itself in PLQY values above 100%. As this effect depends on cross-relaxation between different ions, it should be influenced by the concentration of the doping ions. To prove this, a wide concentration range of the Er^{3+}-doped samples is required. To perform the study a series of the Er^{3+}-doped BaF_2 crystals is synthesised with the doping concentration in the range of 1-25 mol.%.

To carry out the study, the following objectives are set for this chapter:

- To prove that the Bridgeman method can provide Er^{3+}-doped BaF_2 crystals that are capable of efficient down-conversion.
- To find the optimal doping concentration that gives the highest PLQY value of the NIR emission under different excitation wavelengths (405nm, 525 nm, 633 nm, 808 nm).
- To calculate the maximum achievable enhancement of the J_{sc} of the Ge-photodiode due to the DC in the BaF_2:Er from the PLQY data.
- To experimentally check the maximum achievable enhancement of the J_{sc} of the Ge-photodiode due to DC in the BaF_2:Er crystal.

4.2 Down-conversion in BaF_2:Er^{3+} crystals

It is considered that several absorption transitions can lead to the realization of down-conversion. It is assumed that in Er^{3+} ions down-conversion is dependent on cross-relaxation processes between different Er^{3+} ions. Thus, the concentration of the doping ions should have a significant effect on the probability of such a process. To find the optimal concentration of Er^{3+} ions, $\phi_{DC}$is estimated in a wide concentration series of single crystal samples (1 – 25 mol.%). The obtained ϕ_{DC}values are presented in Figure 4.1.

A typical emission spectrum of a BaF_2 crystal doped with 12 mol.% of Er^{3+} ions under 405 nm excitation is shown in Figure 4.1a. The spectrum has several bands that correspond to the transitions in Er^{3+} ion, namely $^4S_{3/2} – {}^4I_{15/2}$ (545 nm), $^4F_{9/2} – {}^4I_{15/2}$ (660 nm), $^4S_{3/2} – {}^4I_{13/2}$ (850 nm), $^4I_{11/2} – {}^4I_{15/2}$ (990 nm), and $^4I_{13/2} – {}^4I_{15/2}$ (1550 nm).

To determine the most efficient composition, the PLQY values are assessed in all single-crystal samples. The resulting data is depicted in Figure 4.1 (b-d). Figure 4.1b shows that under 405 nm excitation, some samples doped with 5 and 12 mol.% of Er^{3+} ions demonstrate PLQY values of the $^4I_{13/2} – {}^4I_{15/2}$ emission over unity (104 and 110%, respectively). This confirms the presence of the DC process in BaF_2:Er^{3+} crystals. However, Er^{3+} concentrations below 5% and above 12%, lead to the PLQY values below unity. A similar concentration-dependent trend (with the optimum concentration of 10%) has been previously observed in the Gd_2O_2S: Tm^{3+} samples[152]. In the work [152] it is observed that at low concentrations, cross-relaxation is outperformed by radiative or non-radiative relaxation, whereas at significantly higher concentrations, luminescence decreases due to concentration quenching.

Under 525 nm excitation, PLQY of the $^4I_{13/2} – {}^4I_{15/2}$ band is 92% in the sample doped with 5 mol.% of Er^{3+}. It should be noted that in the samples with low doping concentration (< 5 mol.%), 405 nm excitation provides lower PLQY values than 525

nm excitation. In the case of 405 nm excitation, the Er^{3+} ion is excited to the $^2H_{9/2}$ state. Unlike the $^2H_{11/2}$ state to which the ion is excited with a 525 nm excitation, energy gaps in the 25000 – 17000 cm^{-1} region are rather small (<2000 cm^{-1}) and can be bridged by several phonons which makes multiphonon relaxation probable [153]. Thus, in the samples with lower doping concentrations under 405 nm excitation cross-relaxation competes with multiphonon processes leading to lower PLQY values.

At the other studied excitation wavelengths, 633 nm and 808 nm, notably lower PLQY values are observed, 35% and 46%, respectively. These excitation wavelengths are not favourable for cross-relaxation with the $^4I_{13/2}$ level, offering fewer opportunities for the DC process compared to 405 nm and 525 nm. 1510 nm emission resonantly excites the $^4I_{13/2}$ level. In this case PLQY of the samples with a doping level lower than 5 mol.% is near 100%, indicating the absence of quenching. Higher doping levels lead to the appearance of the concentration quenching.

The $^4I_{11/2}$ - $^4I_{15/2}$ transition is the second most intense emission band. It can be also harvested to enhance the response of the systems sensitive to NIR radiation. The PLQY values (Figure 4.1c) can reach 50%. The concentration dependence of the $^4I_{11/2}$ - $^4I_{15/2}$ band PLQY has a trend similar to $^4I_{11/2}$ - $^4I_{15/2}$. The values go up until 5 – 12 mol.% where the highest values are observed. Higher doping concentrations lead to a decrease in the observed values.

The total emission of the two NIR emission bands (Figure 4.1d) shows PLQY above unity in several samples– namely crystals doped with 3 – 14 mol.% in the case of 405 nm excitation and 1 – 5 mol.% under 525 nm excitation. The highest value (153%) is observed in the sample doped with 5 mol.% of Er^{3+} under 405 nm excitation. Compared to the NIR emission (see Figure 4.1a) visible emission accounts for a small fraction of total yield.

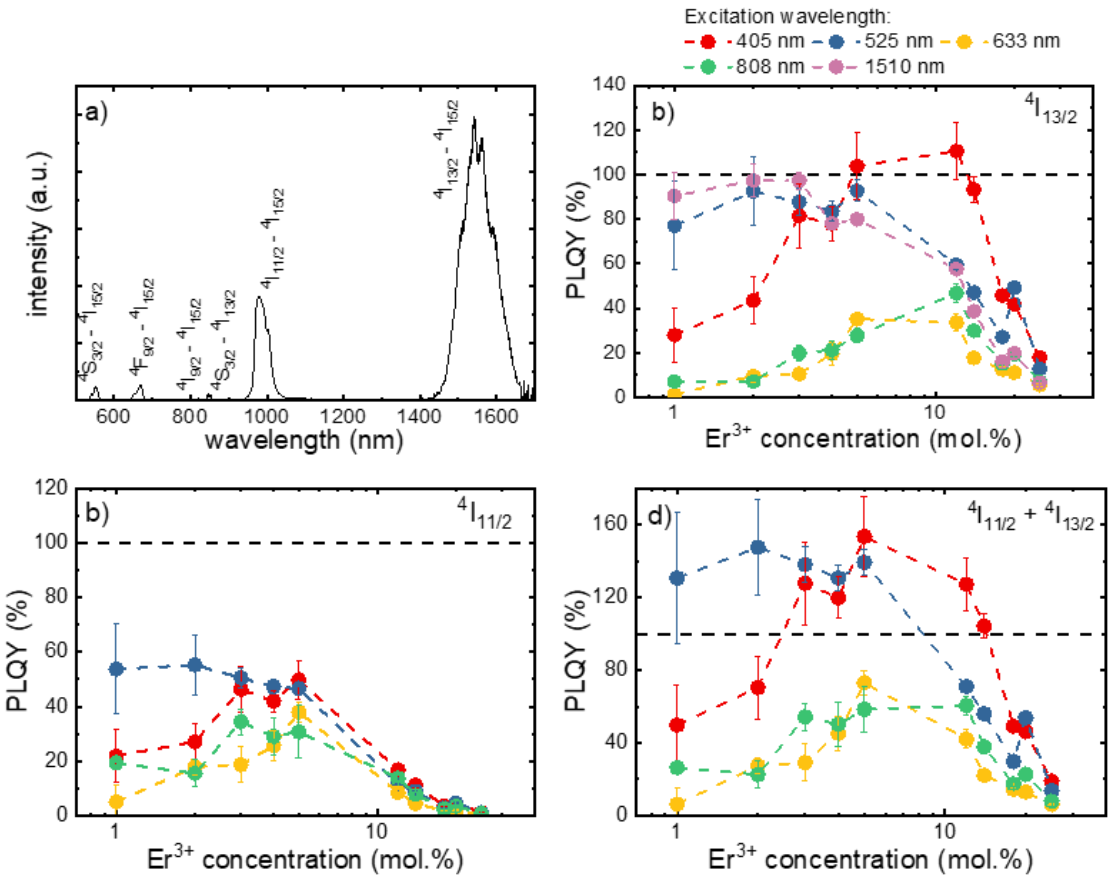

Figure 4.1 - a) Emission spectrum of the BaF_2:Er (12 mol.%) sample under 405 nm excitation; PLQY of the b) $^4I_{13/2} - {}^4I_{15/2}$ c) $^4I_{11/2} - {}^4I_{15/2}$, d) total NIR emission of the $BaF_2:Er^{3+}$ single crystals under different visible range excitation.

4.3 Enhancement of the short-circuit current of the Ge-photodiode

Such high spectral conversion efficiency can be utilized in different ways. However, if the proposed application of a material is in the area of photovoltaics, then it should perform well under the excitation intensity equivalent to solar illumination. Thus, to estimate the efficiency of the $BaF_2:Er^{3+}$ crystal in somewhat real-life conditions it was decided to calculate the change in the short-circuit current of a commercially available Ge-photodiode under 1 Sun illumination when combined with the studied crystals. Ge-photodiode is chosen as the model photovoltaic system because the maximum of its spectral response matches with the NIR emission band of Er^{3+} ions.

Four BaF_2 crystals (doped with 3, 4, 5 and 12 mol.% of Er^{3+} ions) that demonstrated the highest quantum yield values were selected for further analysis.

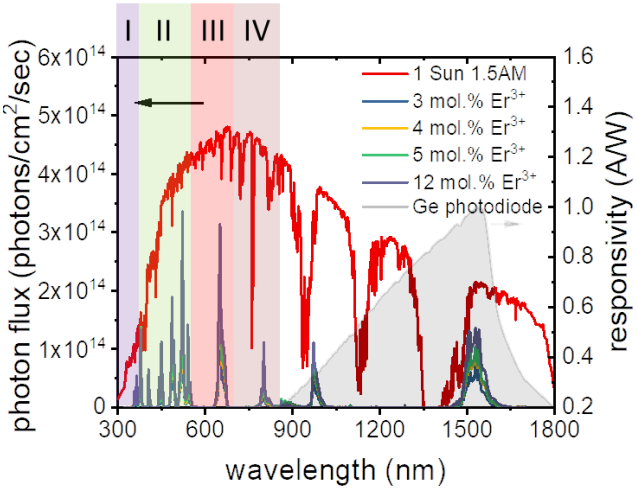

Figure 4.2 - 1.5 am solar spectrum as well as the number of photons absorbed by $BaF_2:Er^{3+}$ crystals under solar irradiation.

Figure 4.2 shows the number of photons absorbed by the studied crystals under 1 Sun illumination. To estimate the number of photons emitted by the crystals, the visible part of the solar spectrum is split into 4 regions and it is considered that the DC PLQY of the crystals stays the same for any excitation wavelength in the corresponding range. DC PLQY in the range I is taken as one estimated under 405 nm excitation, in the range II – under 522 nm, range III – under 652 nm and range IV – under 808 nm excitation. With the number of the absorbed photons as well as DC PLQY settled it is possible to know the number of photons emitted in the NIR range. Considering the isotropic nature of the emission, when the crystal is positioned atop a Ge-photodiode, only half of the emitted photons can effectively reach the photovoltaic device. Thus, only half of the number of the emitted photons should be considered during short-circuit current calculations. When this value is then combined with a known spectral response of a Ge-photodiode the short-circuit current provided by spectral conversion in the crystals can be obtained.

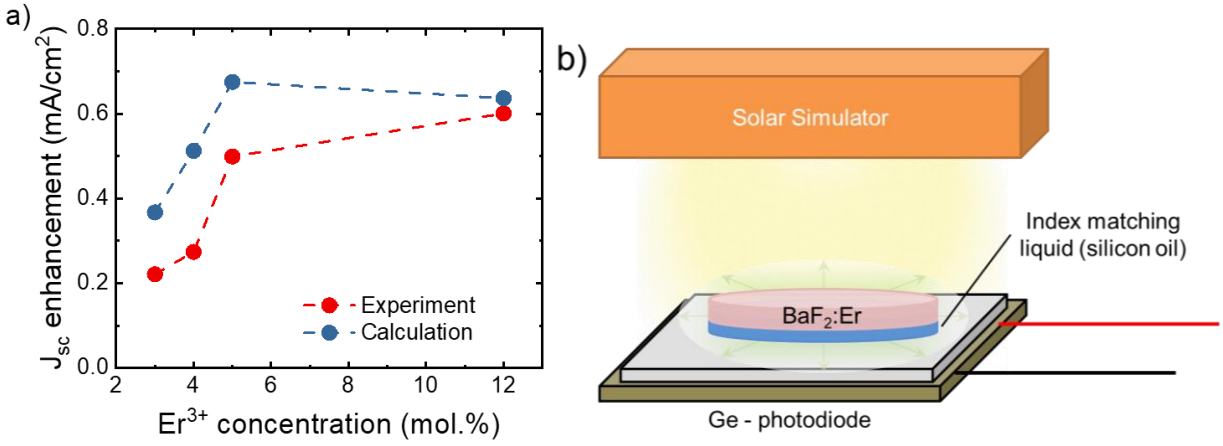

Figure 4.3 - a) measured and calculated short-circuit current density enhancement; b) setup for the estimation of the enhancement of the short-circuit current of the Ge – photodiode.

Figure 4.3a shows the results of the calculations. It can be seen that the predicted short-circuit current enhancement reaches 0.67 mA/cm^2. To put this value into some context, the current generated in the Ge photodiode by the NIR (>850 nm) part of the solar spectrum is estimated. Using a typical response of a Ge photodiode the calculated value is 6 mA/cm^2. It can be calculated that the enhancement is up to 11% of the initial current.

The proposed setup for the measurement of J_{sc} enhancement is presented in Figure 4.3b. Er^{3+} doped BaF_2 crystals are placed on top of the Ge – photodiode with silicon oil serving as the refractive index matching liquid. The whole assembly is then placed under a solar simulator and the J-V curves are obtained.

An undoped BaF_2 crystal on top of the photodiode increases the observed Jsc due to the better light coupling as in the 1500 nm region the refractive index of Ge is 4.21, whereas the refractive index of BaF_2 is 1.46 and one of the silicon oil is 1.41. The increase in the J_{sc} introduced by the doped crystals is estimated in relation to the measurement with an undoped crystal. The highest value of the J_{sc} enhancement (0.6 mA/cm^2) is detected when the crystal doped with 12 mol.% of Er^{3+} ions is used.

A comparison of the experimental results and the calculations shows that even though there is a refractive index matching liquid (silicon oil) between the crystal and photodiode some boundary reflections are still present as well as waveguiding in the crystal that can help the emission to escape through the crystal sides and lead to loss of emission. In this case, the obtained results exhibit reasonable agreement with the predictions.

4.4 Summary

To summarise the chapter, the main results can be outlined as follows:

- The Bridgeman method provides Er^{3+}-doped BaF_2 bulk crystals that can function as efficient down-conversion materials.
- The down-conversion in a concentration series of the Er^{3+}-doped BaF_2 samples is studied. It is shown that the PLQY value of the NIR emission can exceed 100%. The highest PLQY is 153% and it is obtained in the sample doped with 5 mol.% of Er^{3+} under 405 nm excitation.
- The maximum enhancement of the J_{sc} of the Ge-photodiode due to the DC in the BaF_2:Er crystal is theoretically estimated. It is 0.67 mA/cm^2 for the sample doped with 5 mol.% of Er^{3+}.
- The enhancement of the J_{sc} of the Ge-photodiode due to the DC in the BaF_2:Er crystal is estimated experimentally. The highest observed value is 0.6 mA/cm^2 in the case of the sample doped with 12 mol.% of Er^{3+}.

5. Study of PbF_2: Er^{3+}, Yb^{3+} crystals

Sections 5.2 and 5.3. The results are presented in the paper Phys. Chem. Chem. Phys., 2023, 25, 11986-11997 [154]*. Dmitry Busko and Ian A. Howard participated in the optical characterization of the samples, Bryce S. Richards and Andrey Turshatov were involved in the coordination of the work and the interpretation of the results.*

5.1 Introduction

The available data shows that it is reasonable to expect efficient UC from the PbF_2 crystals doped with Er^{3+}/Yb^{3+} ions. The published works rarely discuss the absolute PLQY values as well as the effect of the doping concentration. Therefore, it is necessary to study the UC performance over a wide concentration range. To this end, a series of PbF_2 crystals doped with a fixed amount of Er^{3+} ions (2 mol%) and a varying number of Yb^{3+} ions (2-7.5% mol.%) is synthesised.

To carry out the study, the following objectives are set for this chapter:

- To prove that the Bridgeman method can yield Er^{3+}/Yb^{3+}-doped PbF_2 crystals that are capable of efficient up-conversion.
- To find the optimum doping concentration that gives the highest ϕ_{UC} value.
- To study the relationship between the radiative lifetimes, branching ratios, luminescence decay times and PLQY values.
- Compare three different methods of Judd-Ofelt analysis of the powder samples and check the agreement with the results of the bulk crystal of the same chemical composition.

5.2 Physico-chemical properties

The XRD diffraction patterns of the PbF_2: Er, Yb samples are presented in Figure 5.1a. All diffractograms show a pattern characteristic of a cubic unit cell that is expected in a PbF_2 crystal (JCPDS card # 76-1816). It can be observed that the position of the diffraction peaks slightly changes with the doping concentration. Figure 5.1b shows the position of the [111] peak vs. the doping concentration. It changes towards the bigger angles in the samples with higher doping content.

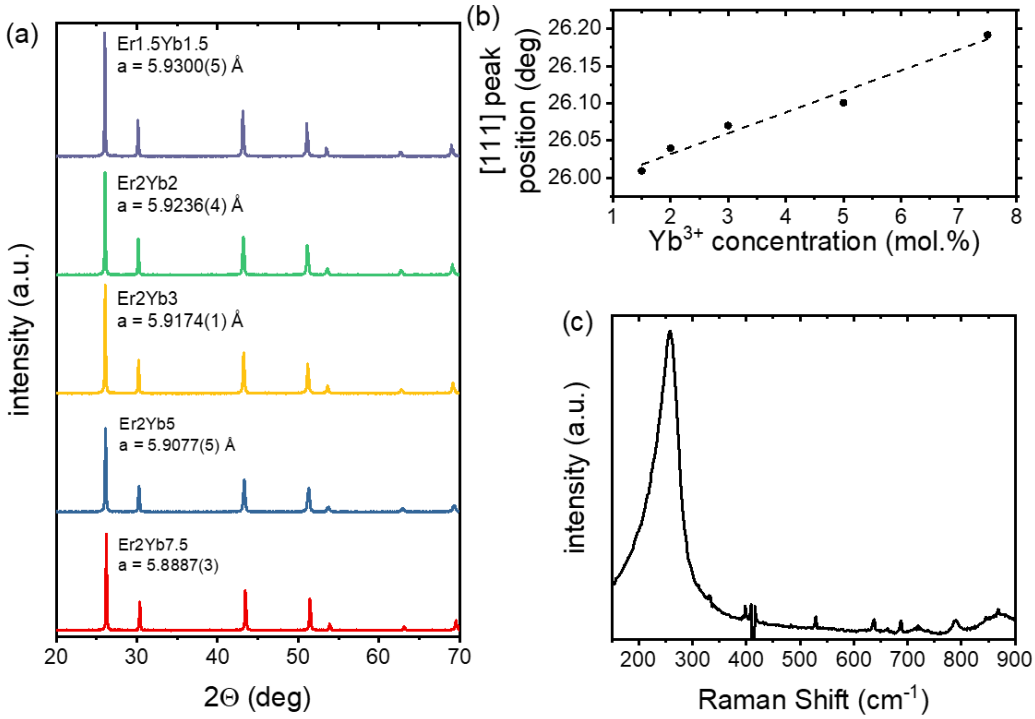

Figure 5.1 - a) Powder XRD patterns of the PbF_2:Yb^{3+},Er^{3+} samples; b) change in the [111] peak position with increasing Yb^{3+} concentration; c) room temperature Raman spectrum of the undoped PbF_2 crystal.

The unit cell parameter is then calculated using the diffraction patterns. The values are shown in Figure 5.1a. They become smaller with the increase in the doping concentration. This as well as the previously discussed change in the peak positions is due to the fact that the ionic radius of the Er^{3+} and Yb^{3+} ions is smaller than that of the

Pb^{2+} ions, which causes the shrinking of the unit cell in samples with higher doping concentration.

Additionally, the Raman spectrum of an undoped PbF_2 crystal is presented in Figure 5.1c. It has one band with a maximum located at 260 cm^{-1}. This value corresponds well to the phonon energy of 257cm^{-1} reported in previous studies [25]. The band is broader than one found in BaF_2 crystal.

Table 5.1 - Concentrations of the doping ions based on WDXRF, unit cell parameters of the PbF_2 doped with Er^{3+}, Yb^{3+}.

Sample name	**Er^{3+}**		**Yb^{3+}**		**a, Å**
	mol.,%	**N, $\times10^{20}cm^{-3}$**	**mol.,%**	**N, $\times10^{20}cm^{-3}$**	
Er1.5Yb1.5	1.61	3.34	1.436	2.98	5.9301
Er2Yb2	2.106	4.36	2.141	4.44	5.9236
Er2Yb3	2.186	4.53	3.285	6.81	5.9174
Er2Yb5	2.116	4.38	5.142	10.66	5.9078
Er2Yb7.5	2.116	4.38	7.713	15.99	5.8887

5.3 Spectral and kinetic properties

5.3.1 Absorption spectra and Judd-Ofelt calculations

The absorption spectra of the samples, presented in Figure 2, exhibit absorption bands in the UV, Vis, and NIR regions, which are typical for Er^{3+} and Yb^{3+} ions. The transitions corresponding to the most intense bands are labelled in the figure. All bands exhibit consistent positions across all samples and are consistent with literature data [23,24].

The absorption data is then utilized in the JO method to calculate key features of the excited states of Er^{3+} ions, such as radiative lifetime and branching ratios. The comparison of these radiative lifetimes with experimentally obtained luminescence decays allows for the determination of the fraction of excitation energy emitted via radiative processes. This information can be used to predict both the down-shifting ϕ_{DS}.and the up-conversion quantum yield ϕ_{UC}[155,156].

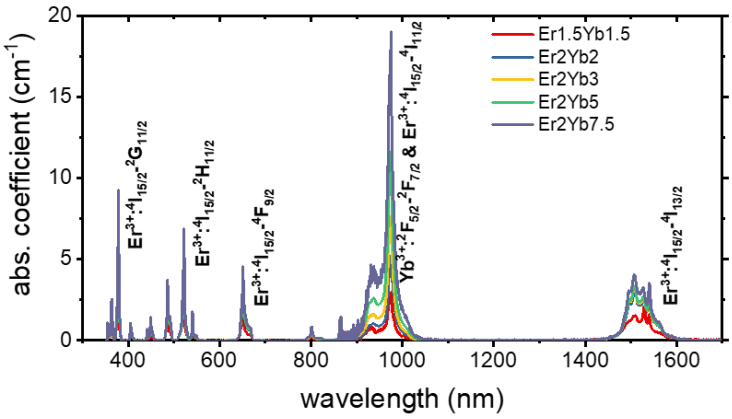

Figure 5.2 - Absorption spectra of the PbF_2: Er^{3+},Yb^{3+} crystals.

Table 5.2 - Integrated absorption cross-section of the PbF_2:Er^{3+},Yb^{3+} samples used in the Judd-Ofelt calculations, $\times 10^{-20}$ cm^2.

	Er1.5Yb1.5	Er2Yb2	Er2Yb3	Er2Yb5	Er2Yb7
$^4G_{11/2}$	5.982	6.628	6.628	6.757	7.825
$^4F_{7/2}$	2.797	3.860	3.911	3.931	4.782
$^2H_{11/2}$	6.099	6.860	6.715	6.747	8.450
$^4S_{3/2}$	0.972	1.649	1.361	1.293	1.727
$^4F_{9/2}$	5.624	7.443	7.789	7.964	9.657
$^4I_{13/2}$	34.724	41.620	42.104	44.380	54.139

In the present study, the JO parameters are obtained using a standard procedure[145,146]. Oscillator strengths are determined by absorption cross-sections, as shown in Table 5.2. These oscillator strengths are then used to calculate the Ω_t values, which allow radiative transitions between different levels to be described. Before determining the Ω_t values, several additional parameters, including the barycentre wavelength, doping concentration of Er^{3+} ions, refractive index, and reduced matrix elements, must be accurately estimated. These estimated values are given in Table 5.3, with reduced matrix elements obtained from literature sources [157] and refractive index data [158] being universal across all samples. The concentrations of doping ions are estimated using the WDXRF method and reported in Table 5.1.

Table 5.3 - Barycentre wavelength (λ_b), along with literature values for the reduced matrix elements (U) and refractive index (n) of the transitions used in the JO calculations.

Excited state	**λ_b, nm**	**$[U^{(2)}]$**	**$[U^{(4)}]$**	**$[U^{(6)}]$**	***n***
$^4G_{11/2}$	378.5	0.9156	0.5263	0.1167	1.8314
$^2H_{9/2}$	406.5	0	0.0243	0.2147	1.8149
$^4F_{7/2}$	487.0	0	0.1465	0.6272	1.7857
$^2H_{11/2}$	522.0	0.7158	0.4128	0.0927	1.7774
$^4S_{3/2}$	542.0	0	0	0.2235	1.7740
$^4F_{9/2}$	653.0	0	0.55	0.4621	1.7593
$^4I_{13/2}$	1520.0	0.0195	0.1172	14.325	1.7335

Table 5.4 - Radiative lifetimes (τ_{rad}) and branching ratios (β) of some transitions of the $PbF_2:Er^{3+}$, Yb^{3+} samples.

		Er1.5Yb15	Er2Yb2	Er2Yb3	Er2Yb5	Er2Yb7.5
$^4S_{3/2}$-$^4I_{15/2}$	τ_{rad}, ms	1.12	0.5	0.81	0.82	0.63
	β	0.67	0.67	0.67	0.67	0.67
$^4F_{9/2}$-$^4I_{15/2}$	τ_{rad}, ms	1.47	1.11	1.06	1.03	0.86
	β	0.91	0.91	0.91	0.91	0.92
$^4I_{13/2}$-$^4I_{15/2}$	τ_{rad}, ms	9.71	8.38	8.75	8.17	7.00
	β	1	1	1	1	1

Table 5.4 summarizes the values of radiative lifetimes (τ_{rad}) and branching ratios (β) that are important for further discussion as obtained with JO calculations. Several observations can be made from the results. Firstly, an increase in the doping concentration of Yb^{3+} results in higher transition probabilities and, consequently, shorter radiative times However, the branching ratios remain similar across all samples. Unfortunately, determining a simple relationship between the radiative lifetime and the number of emitted photons is challenging, as non-radiative relaxation and various quenching processes need to be considered. Nonetheless, studying luminescence decay and understanding the radiative lifetime can provide valuable insights into the quantum yield of luminescent materials.

5.3.2 Down-shifting luminescence in PbF_2: Yb^{3+}, Er^{3+} crystals

The luminescence spectra of the PbF_2: Er^{3+}, Yb^{3+} crystals excited at a wavelength of 375 nm are demonstrated in Figure 5.3a. Peaks corresponding to different transitions are observed in the emission spectra.

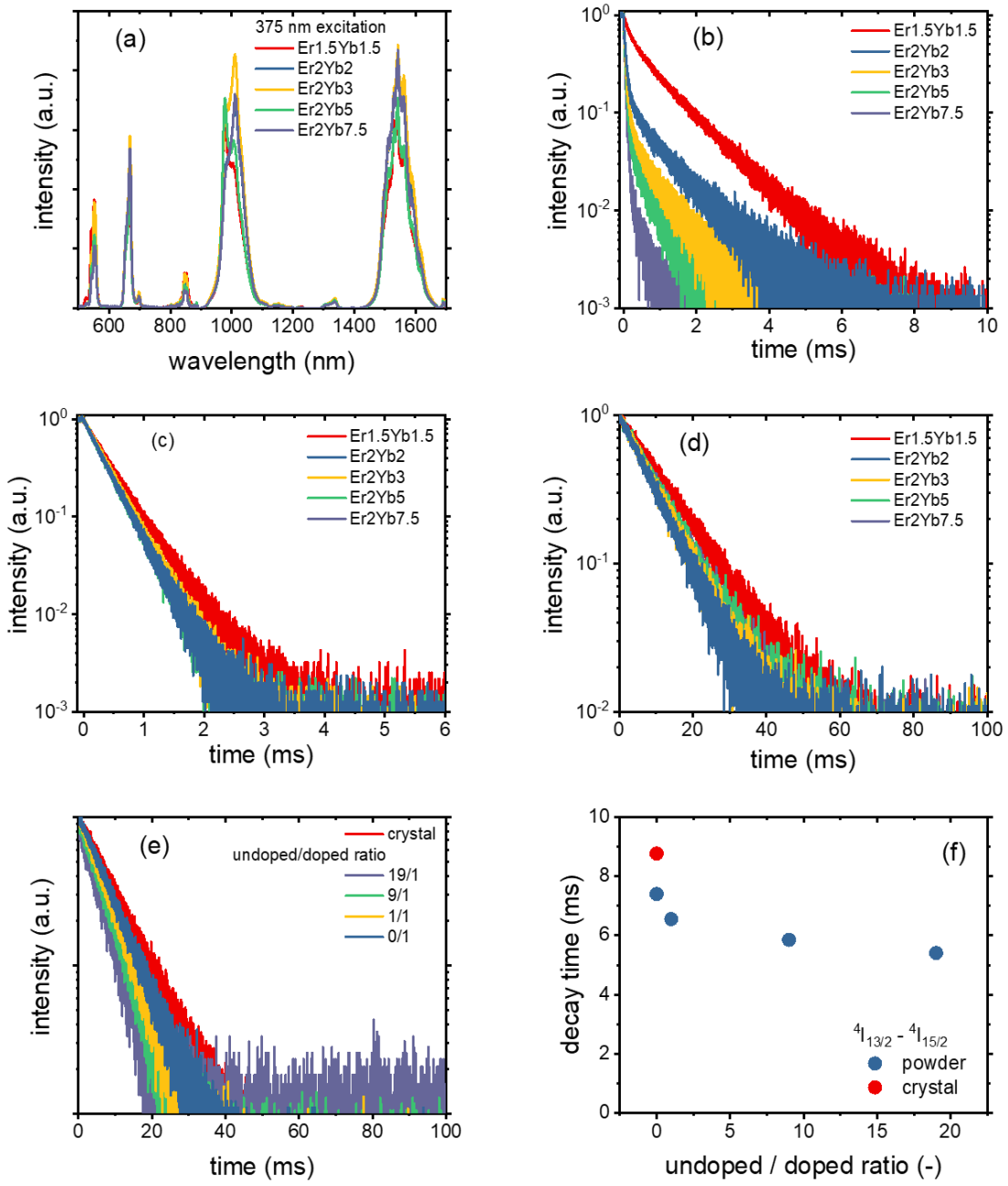

Figure 5.3 - (a) Emission spectra under 375 nm excitation, (b) luminescence decay of the Er^{3+}:$^4S_{3/2}$ – $^4I_{15/2}$ transition under 525 nm excitation, (c) luminescence decay of the Er^{3+}:$^4F_{9/2}$ – $^4I_{15/2}$ transition under 640 nm excitation, (d) luminescence decay of the Er^{3+}:$^4I_{13/2}$ – $^4I_{15/2}$ transition under 1535 nm excitation in the PbF_2:Er^{3+},Yb^{3+} samples; (e) luminescence decay and (f) luminescence decay time of the Er^{3+}:$^4I_{13/2}$ – $^4I_{15/2}$ of the PbF_2:2 mol. % Er^{3+}, 5 mol. % Yb^{3+} crystal and diluted powders under 1535 nm excitation.

To correlate the experimental results with the JO calculations, the luminescence decays of three states ($^4S_{3/2}$, $^4F_{9/2}$, and $^4I_{13/2}$) were studied using direct excitation of the aforementioned states (Figure 5.3b-d). The observation from these decays is that the decay time of the $^4I_{13/2}$-$^4I_{15/2}$ transition is consistently longer than the radiative lifetime calculated by the JO model (Table 5.4). This extension of decay time may be attributed to the re-absorption of emitted photons within the crystal[35,36]. To test this hypothesis, two exemplary crystals (Er2Yb5 and Er2Yb2) are carefully ground and diluted with undoped PbF_2 powder until the undoped/doped ratio is 19 to 1. The local concentration of Er^{3+} and Yb^{3+} remained unchanged, but the re-absorption is significantly reduced by dilution. This resulted in a pronounced decrease in the decay time (Figure 5.3e), which dropped from 8.8 ms in a crystalline sample to 5.4 ms for the most diluted powders (Figure 5.3f). The luminescence decays of the other two transitions ($^4S_{3/2}$-$^4I_{15/2}$ and $^4F_{9/2}$-$^4I_{15/2}$) were also prolonged in the crystal, suggesting the presence of re-absorption, but to a much lesser extent.

Figure 5.3b exhibits a second phenomenon, which is the multi-exponential behaviour of all the decays. Cross-relaxation between the $^4S_{3/2}$ state of Er^{3+} and the ground states of Er^{3+} ($^4I_{15/2}$) and Yb^{3+} ($^2F_{5/2}$) is well known [159]. This cross-relaxation rate can vary due to the distribution of the inter-ion distance (Er^{3+}-Er^{3+} or Er^{3+}-Yb^{3+}), resulting in a multi-exponential decay. To simplify the analysis, a bi-exponential model was used to fit the decays in Figure 5.3b, and the results are presented in Table 5.5. It is worth noting that crystals with the lowest Er^{3+} concentration (Er1.5Yb1.5 and Er2Yb2) exhibit a short-lived component with decay times of 0.18 and 0.08 ms, respectively, and a substantial contribution from the long-lived component with decay times of 1.08 and 0.94 ms while JO calculation predicts radiative lifetimes of 1.12 and 0.85 ms (Table 5.4). Therefore, a closer examination of the decays of Er1.5Yb1.5 and Er2Yb2 crystals shows that the long-lived component of the decay is close to or even

exceeds the radiative lifetime obtained with the JO method, which cannot be attributed to simple re-absorption and demands an explanation.

Table 5.5 - Decay times obtained after fitting the experimental decays in Figures 3b-3d with single-exponential ($^4I_{13/2}$-$^4I_{15/2}$ and $^4F_{9/2}$-$^4I_{15/2}$ transitions) and bi-exponential ($^4S_{1/2}$-$^4I_{15/2}$ transition) functions.

crystal	t ($^4I_{13/2}$-$^4I_{15/2}$), ms	t ($^4F_{9/2}$-$^4I_{15/2}$), ms
Er1.5Yb1.5	11.9	0.44
Er2Yb2	8.4	0.36
Er2Yb3	8.9	0.38
Er2Yb5	9.5	0.36
Er2Yb7.5	9.6	0.37

$^4S_{1/2}$-$^4I_{15/2}$

crystal	t_1, ms	A_1	t_2, ms	A_2
Er1.5Yb1.5	0.18	0.37	1.08	0.58
Er2Yb2	0.075	0.94	0.936	0.12
Er2Yb3	0.055	1.00	0.635	0.08
Er2Yb5	0.047	0.96	0.561	0.05
Er2Yb7.5	0.039	1.01	0.254	0.03

The distribution of radiative decay times in MF_2 (M = Ca, Sr, Ba, Pb)[160,161] may be multi-exponential due to the formation of clusters of lanthanide ions. Such clusters can affect radiative transitions, leading to different symmetries for Er^{3+} ions. In the highly symmetric environment of the cubic PbF_2 crystal structure, the long-lived component of the decay could correspond to individual Er^{3+} ions. In contrast, the short-lived component could correspond to Er^{3+} ions in a less symmetric environment, such as ion clusters. Luminescence decays are capable of distinguishing between these two

symmetries because of the strong cross-relaxation of the $^4S_{3/2}$ state, which is expected for the cluster environment due to the shorter interionic distance. However, detecting the two different environments for the $^4F_{9/2}$ and $^4I_{13/2}$ states is more challenging because these states do not participate in cross-relaxation, and the difference in radiative lifetimes is hardly noticeable in experimental decays.

By analyzing the amplitude ratio (A_i) of the short-lived and long-lived components (as shown in Table 5.5), one can determine the fraction of Er^{3+} ions distributed in the two distinct crystalline environments. For crystals with lower doping concentrations like Er1.5Yb1.5 and Er2Yb2, the values of A_1 and A_2 (which correspond to the amplitudes of the short-lived and long-lived components, respectively) are comparable. In such cases, the JO model may provide an "average" value of the radiative lifetime, although the applicability of the JO model to a material with two radiative lifetimes is uncertain. With an increase in Yb^{3+} concentration (such as in Er2Yb3, Er2Yb5, and Er2Yb7.5 crystals), the number of Er^{3+} ions in the cluster fraction increases, and it becomes more than 95% for the Er2Yb5 crystal. Therefore, for further analysis of the correlations between JO calculations and experimental results, the Er2Yb5 crystal with a dominant radiative lifetime is selected.

Under the assumptions that (i) each $^4S_{3/2}$, $^4F_{9/2}$, and $^4I_{13/2}$ state in the Er2Yb5 crystal has a single radiative lifetime value, (ii) there exists a constant quenching rate for these states, where the quenching mechanism for the $^4S_{3/2}$ state is cross-relaxation with the ground states ($^4I_{15/2}$ or $^2F_{5/2}$), and (iii) the measurement artefact associated with re-absorption of emitted photons is eliminated, a simple equation binds the radiative lifetime, decay time, and quantum yield:

$$\phi_{DS} = \beta \frac{\tau}{\tau_{rad}} . \qquad 25$$

Here, β represents the branching ratio, τ_{rad} is the radiative decay time derived from the JO analysis, and τ is the decay time measured experimentally.

For the $^4S_{3/2}$ - $^4I_{13/2}$ transition in the Er2Yb5 sample, it is highly probable that the requirements (i)-(iii) are satisfied, as this transition is less impacted by re-absorption. With a decay time (τ) of 0.04 ms, a radiative lifetime (τ_{rad}) of 0.82 ms, and a branching ratio (β) of 0.28, the quantum yield of the $^4S_{3/2}$ - $^4I_{13/2}$ luminescence can be calculated as ϕ_{DS}= 1.4% using Eqn.25, which closely matches the measured value of ϕ_{DS}= 1.3% (Table 5.6).

Table 5.6 - ϕ_{DS} (%) of some transitions in the PbF_2:Er^{3+}, Yb^{3+} samples upon excitation of the $^4S_{3/2}$, $^4F_{9/2}$, Er^{3+}:$^4I_{11/2}$ & Yb^{3+}:$^2F_{7/2}$ and $^4I_{13/2}$ levels.

Excitation	Emission	Er1.5Yb1.5	Er2Yb2	Er2Yb3	Er2Yb5	Er2Yb7.5
522 nm 0.1 W/cm²	$^4S_{3/2} - {}^4I_{15/2}$	5.4	3.2	3.5	3.1	2.5
	$^4S_{3/2} - {}^4I_{13/2}$	2.0	1.2	1.5	1.3	0.9
	$^4F_{9/2} - {}^4I_{15/2}$	8.7	7.6	7.0	4.0	1.7
	{Er^{3+}:$^4I_{11/2}$ & Yb^{3+}:$^2F_{7/2}$}	46.7	51.9	57.0	48.3	42.0
652 nm 0.3 W/cm²	$^4F_{9/2} - {}^4I_{15/2}$	22.0	23.5	28.2	24.7	23.4
	{Er^{3+}:$^4I_{11/2}$ & Yb^{3+}:$^2F_{7/2}$}	29.5	31.9	31.5	29.4	18.9
940 nm 0.1 W/cm²	{Er^{3+}:$^4I_{11/2}$ & Yb^{3+}:$^2F_{7/2}$}	37.3	60.6	69.4	52.9	43.2
	$^4I_{13/2} - {}^4I_{15/2}$	3.0	4.4	4.5	2.7	3.0
1495 nm 0.1 W/cm²	$^4I_{13/2} - {}^4I_{15/2}$	85.1	74.8	69.2	68.6	69.5

When the same equation 25 is applied to the $^4S_{3/2}$ - $^4I_{15/2}$ and $^4F_{9/2}$ - $^4I_{15/2}$ transitions, the calculated quantum yield values are ϕ_{DS}= 3.3% and ϕ_{DS} = 29.2%, respectively. However, the measured quantum yields using an integrating sphere and

correction procedure (iperWilson and Richards [162]) are lower, with values of ϕ_{DS} = 3.1% and ϕ_{DS}= 24.7%, respectively (Table 5.6). It is believed that the difference between the predicted quantum yields (based on lifetime) and the experimentally measured quantum yields (3.3% vs. 3.1% for the $^4S_{3/2}$ - $^4I_{13/2}$ transition, and 29.2% vs. 24.7% for the $^4F_{9/2}$ - $^4I_{15/2}$ transition) represents the level of agreement that can be realistically expected between the JO calculations and the experimental results.

Using the data in Table 5.6, one can estimate the transition probabilities for $^4S_{3/2}$ – $^4F_{9/2}$ and {Er^{3+}:$^4I_{11/2}$ & Yb^{3+}:$^2F_{7/2}$} – $^4I_{13/2}$ based on the values of ϕ_{DS}. The three energy level model shown in Figure 5.4 can be used to calculate the probability of the transition φ_{2-1} as the sum of radiative and non-radiative transitions, using the quantum yields of the radiative transition (ϕ_{1-0}) at excitations (0-1) and (0-2):

$$\varphi_{2-1} = \frac{\phi_{1-0(0-2)}}{\phi_{1-0(0-1)}}. \qquad 26$$

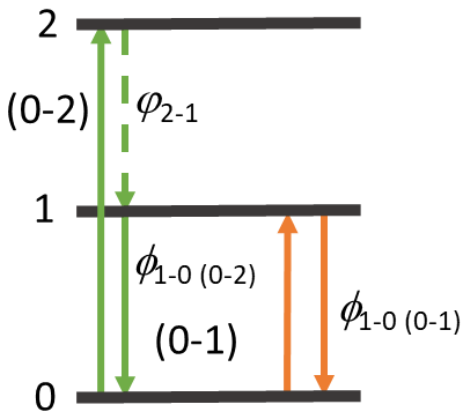

*Figure 5.4 - Energy transfer diagrams for the case of DC emission, where the ground state **0** is Er^{3+}:$^4I_{15/2}$, excited state **1** is either Er^{3+}:$^4I_{13/2}$ or Er^{3+}:$^4I_{9/2}$ and excited state **2** is either Er^{3+}:$^4I_{11/2}$ or Er^{3+}:$^4S_{3/2}$.*

As the branching ratio (β) for the $^4S_{3/2}$ - $^4F_{9/2}$ transition is very small ($3\cdot10^{-4}$), φ_{2-1} for the $^4S_{3/2}$ state denotes the proportion of all excited $^4S_{3/2}$ states that undergo non-radiative decay (via multiphonon relaxation) to the $^4F_{9/2}$ state. On the other hand,

in the case of $\{Er^{3+}:{}^4I_{11/2}$ & $Yb^{3+}:{}^2F_{7/2}\}$ - $^4I_{13/2}$, the value of β is unknown, and hence φ_{2-1} represents the fraction of all excited $\{Er^{3+}:{}^4I_{11/2}$ & $Yb^{3+}:{}^2F_{7/2}\}$ states that undergo both radiative and non-radiative relaxation to the $^4I_{13/2}$ state.

The information presented in Table 5.7 indicates that φ_{2-1} for the $\{Er^{3+}:{}^4I_{11/2}$ & $Yb^{3+}:{}^2F_{7/2}\}$ - $^4I_{13/2}$ transition remains nearly constant (0.036 – 0.065) for all Yb^{3+} concentrations, and is slightly lower than the probability of the $^4I_{11/2}$-$^4I_{13/2}$ radiative transition. This is consistent with previous findings that the branching ratio for the $^4I_{11/2}$-$^4I_{13/2}$ transition in Er^{3+} doped fluorides falls within the range of 0.11-0.15[155,163,164]. In contrast, the value of φ_{2-1} for the $^4S_{3/2}$ – $^4F_{9/2}$ transition decreases as the Yb^{3+} concentration grows, indicating that cross-relaxation becomes more prevalent than non-radiative relaxation in crystals with high Yb^{3+} doping concentration.

Table 5.7 - Transition probabilities between certain Er^{3+} excited states in the PbF_2:Er^{3+}, Yb^{3+} samples in the low excitation intensity range (0.1 – 0.3 W/cm^2).

φ_{2-1}	**Er1.5Yb1.5**	**Er2Yb2**	**Er2Yb3**	**Er2Yb5**	**Er2Yb7.5**
$^4S_{3/2} - {}^4F_{9/2}$	0.395	0.323	0.248	0.136	0.073
$\{Er^{3+}:{}^4I_{11/2}$ & $Yb^{3+}:{}^2F_{7/2}\} - {}^4I_{13/2}$	0.036	0.059	0.065	0.039	0.043

5.3.3 Judd-Ofelt calculations for powder samples.

The use of JO calculations is beneficial for predicting parameters such as radiative transition rates, branching ratios, and quantum efficiencies, providing insights into material applicability. However, obtaining single crystals for JO analysis can be challenging, as new materials are often synthesized as micro- or nanoparticles. Absorption cross-section determination for JO analysis requires knowledge of the light propagation path, which is difficult to determine in powder samples. Consequently, powder samples are usually analyzed using excitation [32] and diffuse reflection [33,34,165]

spectra. To evaluate the accuracy of JO calculations for powder samples, we assumed that known JO calculation results for equivalent crystals could be used. To test this approach, a portion of the Er2Yb5 crystal is ground into microparticles and analyzed using excitation and diffuse reflectance spectra.

In the context of Er^{3+} ions, various methods of JO analysis for powder samples rely on the luminescence decay time of the $^4I_{13/2} - {}^4I_{15/2}$ transition to calibrate the JO parameters Ω_t. However, this approach assumes that the luminescence decay time of the $^4I_{13/2} - {}^4I_{15/2}$ transition is equal to the radiative lifetime and that the ϕ_{DS} of the transition is 100% when the $^4I_{13/2}$ state is excited. These assumptions do not account for possible non-ideal sample and quenching processes that may occur. To address this issue, the ϕ_{DS} of the $^4I_{13/2} - {}^4I_{15/2}$ transition is experimentally determined to be 62.4% using 1495 nm excitation. Moreover, our previous results have shown that the decay times obtained for crystal and powder samples of the same chemical composition differ significantly due to reabsorption effects [166]. For instance, the decay time of the $^4I_{13/2} - {}^4I_{15/2}$ transition in the Er2Yb5 crystal is 8.8 ms, while the same transition in the powder has a decay time of 7.4 ms (and 5.4 ms for the diluted powder (Figure 5.3f). Notably, the experimentally measured lifetime in the crystal exceeds the radiative lifetime obtained from JO analysis, which is 8.4 ms.

By using Eq. 25 with β=1, the radiative lifetime of the $^4I_{13/2} - {}^4I_{15/2}$ transition is experimentally determined to be 7.9 ms (with ϕ_{DS}=68.6% and τ=5.4 ms), which agrees well with the value of 8.4 ms obtained from JO calculations for the crystal. It is interesting to note that quenching reduces the luminescence decay time, while reabsorption increases it. To simplify matters, the radiative lifetime of 8.4 ms obtained for the crystal was used in further calculations for the powder sample.

Three methods described previously in the state-of-the-art section of this work are tested with an Er2Yb5 sample as a reference. The spectra used in the calculations are shown in Figure 5.5.

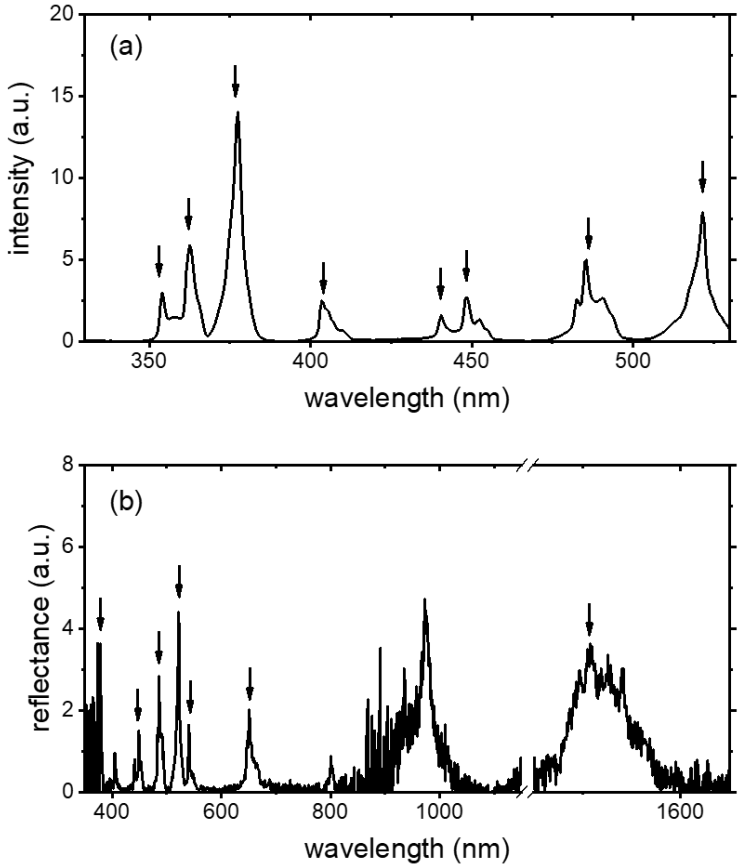

Figure 5.5 - a) the excitation spectrum of the $^4S_{3/2} - {}^4I_{15/2}$ transition (detection at 540 nm); b) the reflectance spectrum of the Er2Yb5 powder sample.

To compare the results obtained from three different methods, the root mean square (RMS) values of the radiative lifetimes obtained for the crystalline and powder samples were calculated (shown in Table 5.8). The comparison of Ω_t values in Table 5.9 further highlights the differences between the three methods.

Table 5.8 - Comparison of the radiative lifetime of Er2Yb5 powder obtained with different approaches based on the JO theory.

Emission band	**Lifetime, ms**			
	Crystal	Method A [32]	Method B [33]	Method C [34,165]
$^4G_{9/2} - {}^4I_{15/2}$	0.562	0.399	0.585	0.501
$^2H_{11/2} - {}^4I_{15/2}$	0.617	0.355	0.892	0.767
$^4S_{3/2} - {}^4I_{15/2}$	0.820	0.734	0.710	0.611
$^4F_{9/2} - {}^4I_{15/2}$	1.031	0.509	1.661	1.428
$^4I_{9/2} - {}^4I_{15/2}$	8.425	3.814	17.556	14.688
$^4I_{11/2} - {}^4I_{15/2}$	9.020	8.438	9.012	7.263
$^4I_{13/2} - {}^4I_{15/2}$	8.174	8.194	12.715	8.094
Relative RMS (with $^4I_{9/2}$)		**0.914**	**1.440**	**0.936**
Relative RMS (w/o $^4I_{9/2}$)		**0.732**	**0.949**	**0.568**

Table 5.9 - The comparison of Ω_t parameters of Er2Yb5 powder obtained by different methods.

	Lifetime, ms			
	Crystal	Method A [32]	Method B [33]	Method C [34,165]
Ω_2	1.342×10^{-20}	1.085×10^{-20}	6.782×10^{-21}	7.267×10^{-21}
Ω_4	4.696×10^{-21}	1.789×10^{-20}	3.144×10^{-21}	3.368×10^{-21}
Ω_6	1.795×10^{-20}	9.519×10^{-21}	1.004×10^{-20}	1.076×10^{-20}
Relative RMS		2.856	0.740	0.671

Although none of these approaches provides perfect consistency between transition probabilities, both Method A [32] and Method C [34,165] show acceptable agreement between values calculated on a single crystal sample and results obtained on powder. Considering the differences in Ω_t values, Method C [34,165] is a better choice. It

is worth noting that the radiative lifetime of a weak $^4I_{9/2} - {}^4I_{15/2}$ transition displays the greatest difference between the methods. This state has lower absorption and emission intensity and worse agreement between experimental and calculated transition probabilities compared to other excited states of Er^{3+}[164]. However, even when excluding this transition from the calculation of RMS (Table 5.8), the conclusion that Method C [34,165] provides a better fit for the parameters calculated for the single crystal remains unchanged.

5.3.4 Up-conversion luminescence in PbF_2: Yb^{3+}, Er^{3+} crystals

Knowing the ϕ_{DS} values for the emitting states $^4S_{3/2}$ and $^4F_{9/2}$, as well as the decay times of the intermediate states $\{Er^{3+}{:}^4I_{11/2}$ & $Yb^{3+}{:}^2F_{7/2}\}$, and $^4I_{13/2}$, one can estimate the efficiency of the UC process that occurs via excited state energy transfer. Generally, the efficiency of UC, denoted by ϕ_{UC}, should not exceed $0.5\phi_{DS}$, as UC involves a two- or three-photon process. Moreover, a longer decay time of the intermediate states $\{Er^{3+}{:}^4I_{11/2}$ & $Yb^{3+}{:}^2F_{7/2}\}$, and $^4I_{13/2}$ increases the likelihood of UC at lower excitation intensities, which is significant for various applications.

The up-conversion emission spectra under 976 nm excitation with an intensity of 350 W/cm^2 are shown in Figure 5.6a, with all spectra normalized to the maximum intensity of the $^4F_{9/2} - {}^4I_{15/2}$ transition. In this study, the UC properties of the crystals are experimentally investigated using a direct approach, wherein ϕ_{UC} was measured in the integrating sphere at varying excitation intensities of the 976 nm laser. However, it is crucial to note that the measurement results of ϕ_{UC} may be biased in several ways [167].

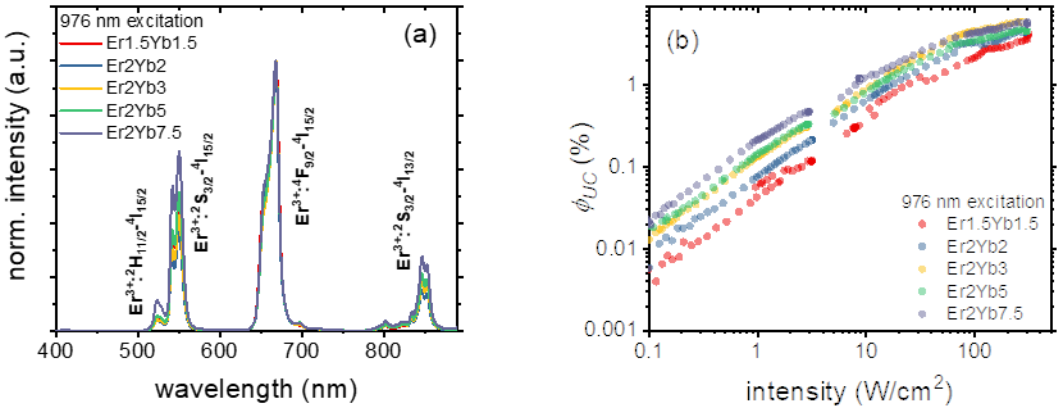

Figure 5.6 - a) UC emission spectra under the 976 nm excitation (intensity of 350 W/cm^2); b) ϕ_{UC} in the intensity range of 0.1 – 350 W/cm^2.

One possible solution to the first issue is to estimate the sample's temperature by analyzing the ratio of the $^2H_{11/2}$ – $^4I_{15/2}$ and $^4S_{3/2}$ – $^4I_{15/2}$ emission bands, which are thermally linked. The temperature can be determined using the following equation:

$$\frac{1}{T} = \frac{1}{T_0} - \frac{k_B}{\Delta E} \cdot \ln\left(\frac{I_{520} I^0_{550}}{I_{550} I^0_{520}}\right). \qquad 27$$

Here, k_B is the Boltzmann constant, ΔE denotes the energy difference between the $^2H_{11/2}$ and $^4S_{3/2}$ levels, I_{520} and I_{550} refer to the emission intensities of the $^2H_{11/2}$ and $^4S_{3/2}$ levels respectively, T_0 is the initial temperature in the absence of excitation and I^0_{520} and I^0_{550} are the emission intensities at the initial temperature.

The literature provides a detailed description of the procedure, as outlined in work [168], and the results obtained with Eqn. 27 are presented in Figure 5.7b. It is evident from the figure that only the sample with the highest concentration of Yb^{3+} (Er2Yb7.5) experienced any noticeable temperature change. The issue of re-absorption in the integrating sphere can be addressed using the same methodology as for ϕ_{DS}, as illustrated in Table 5.6. To account for the impact of sample size on the calculated ϕ_{UC} values, some assumptions must be made. A crystalline sample with a given thickness is assumed to be a seamless stack of layers. The ϕ_{UC} of each layer is assumed to be proportional to I^n, where I is the incident intensity, and n is varied from 0 to 1 to

demonstrate various power dependencies of ϕ_{UC}. It is then feasible to calculate the number of incident and absorbed photons for each layer, as well as the ϕ_{UC} of the layer. The combination of these two values (ϕ_{UC} and n) gives the number of photons emitted by each layer. By summing the emitted and absorbed photons in each layer, the ϕ_{UC} of the sample can be estimated based on the measured ϕ_{UC}.

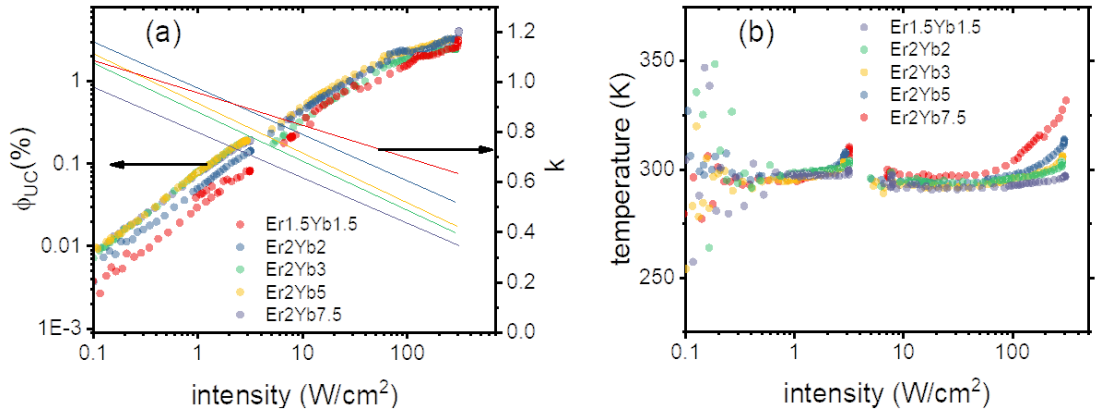

Figure 5.7 - ϕ_{UC} and slopes (k) of the ϕ_{UC} dependence of a) total UC emission in the 400 – 900 nm range, b) Sample temperature as a function of incident 976 nm intensity.

The ϕ_{UC} values are presented in Figure 5.7 after the aforementioned corrections (similar to the detailed explanation given in [167]). It is observed from the data in Figure 5.7a that ϕ_{UC} increases as the incident intensity increases, reaching its maximum value of 5.9% at 350 W/cm^2 for the Er2Yb3 crystal. As with other materials studied with the same structure, such as BaF_2: Er^{3+}, Yb^{3+} [24] and SrF_2:Er^{3+}, Yb^{3+}[169] , the highest ϕ_{UC} is observed in the samples with the maximum amount of Yb^{3+} ions (7.5%) at low intensities (< 10 W/cm^2), whereas at higher intensities (> 10 W/cm^2), samples with a lower concentration (3%) of Yb^{3+} demonstrate the highest ϕ_{UC}.

In order to examine the experimental dependence of ϕ_{UC} on excitation intensity, a method proposed by Joseph et al. [170] is used to estimate a single figure of merit parameter of the UC process - critical power density (CPD). The maximum value of

the quantum yield (ϕ_{UCsat}) and the energy transfer rate between donor and acceptor ions (k_{12}) can be derived from the CPD value. It is worth noting that the CPD concept was developed for a two-photon UC process, such as population and emission from the $^4S_{3/2}$ state, and not for a three-photon process, which refers to emission from the $^4F_{9/2}$ state. Table 5.10 displays experimental values of the UC quantum yield at a maximum intensity of 350 W/cm^2 (Max ϕ_{UC}), CPD values, $\phi_{UC\,CPD}$ (UC quantum yield at an intensity corresponding to the CPD), as well as ϕ_{UCsat} and k_{12} derived from the CPD.

Table 5.10 - Maximum (at 350 W/cm^2) ϕ_{UC} values for UC emission in the 400 – 900 nm range (Max ϕ_{UC} total) and for the $^4S_{3/2} - {}^4I_{15/2}$ emission (Max ϕ_{UC} $^4S_{3/2} - {}^4I_{15/2}$); CPD; ϕ_{UC} at CPD ($\phi_{UC\,CPD}$); and saturation ϕ_{UC} (ϕ_{UCsat}) as well as energy transfer rate (k_{12}) of the $^4S_{3/2} - {}^4I_{15/2}$ transition.

	Er1.5Yb1.5	**Er2Yb2**	**Er2Yb3**	**Er2Yb5**	**Er2Yb7.5**
Max ϕ_{UC} total, %	4.3	4.7	5.9	4.4	5.8
Max ϕ_{UC} $^4S_{3/2} - {}^4I_{15/2}$, %	1.0	0.9	1.2	1.1	1.3
CPD $^4S_{3/2} - {}^4I_{15/2}$, W/cm^2	48.4	37.9	17.8	16.0	9.2
$\phi_{UC\,CPD}$, %	0.4	0.3	0.4	0.2	0.2
ϕ_{UCsat} $^4S_{3/2} - {}^4I_{15/2}$, %	2.7	1.3	2.6	1.2	1.3
k_{12}, *10^{-17} cm^3/s	0.6	1.5	2.1	1.9	5.4

From the data presented in Table 5.10, several conclusions can be drawn. Firstly, the CPD value decreases as the concentration of Yb^{3+} ions in the sample increases, with the Er2Yb7.5 sample demonstrating the lowest CPD value of 9.2 W/cm^2. Previous studies have reported lower CPD values of approximately 1 W/cm^2 for highly efficient hosts such as $NaYF_4$, YF_3, YCl_3, and La_2O_3, but these values are observed at much higher Yb^{3+} concentrations (18%) [170]. Therefore, a high concentration of Yb^{3+} ions is preferred to obtain a high quantum yield at a lower excitation intensity. Secondly, the

sample with the lowest doping concentration (Er1.5Yb1.5) is expected to have the highest value of ϕ_{UCsat}, indicating that cross-relaxation has a significant impact on the UC process. Interestingly, ϕ_{UCsat} values in Table 5.10 are approximately 0.5 times the values of ϕ_{DS} presented in Table 5.6 for most samples, with slightly larger deviations for the Er2Yb7.5 sample. This suggests that in the case of the $^4S_{3/2}$ state, the relatively low ϕ_{DS} may limit the achievement of high ϕ_{UC} values.

The two-photon process responsible for green UC emission from the $^4S_{3/2}$ state is widely recognized, but the origin of the red UC emission from the $^4F_{9/2}$ state is more complex. One hypothesis suggests that if the $^4F_{9/2}$ state is populated through relaxation of the $^4S_{3/2}$ state, as well as a two-photon process, then the red-to-green (R/G) ratio in the UC spectra should be similar to the R/G ratio obtained from direct excitation of the $^4S_{3/2}$ state. To investigate this possibility, a comparison of the R/G ratios for the UC and DC processes is conducted, which may help to determine the mechanism of the $^4F_{9/2}$ state population. Figure 5.8a shows that the R/G ratio changes as a function of excitation intensity in the UC process for the Er2Yb5 sample. At low excitation intensities (<1 W/cm^2), the R/G ratio in the UC spectra corresponds well to the R/G value obtained by direct excitation of the $^4S_{3/2}$ state. Therefore, it is likely that the $^4F_{9/2}$ state originates from the $^4S_{3/2}$ state via non-radiative relaxation. However, increasing the excitation intensity (>1 W/cm2) leads to an increase in the R/G ratio, which may be explained by either the Berry and May model [171], where the $^4F_{9/2}$ state results from the three-photon process of populating the $^2H_{9/2}$ state and the subsequent back energy transfer to Yb^{3+}, or the ETU process involving the $^4I_{13/2}$ state. In turn, the $^4I_{13/2}$ state can arise either by radiative transition from the $^4I_{11/2}$ or $^2S_{3/2}$ states or by cross-relaxation of the $^4S_{3/2}$ state. Although it is difficult to determine the best model, an interesting observation was made in Figure 5.8b: the quantum yield of the $^4I_{13/2}$ state increases sublinearly with the excitation intensity, which indicates that the concentration of $^4I_{13/2}$ states also increases sublinearly. This suggests that the $^4F_{9/2}$ state is mainly populated

by the ETU process: $^4I_{13/2} + {}^2F_{5/2} \rightarrow {}^4F_{9/2} + {}^2F_{7/2}$. Figure 5.8 also confirms similar trends in the R/G ratio and ϕ_{DS} for other investigated samples, which supports the assumption that additional population of the $^4F_{9/2}$ state due to cross relaxation may be valid for a wide range of Yb^{3+} concentrations (1.5 – 7.5%).

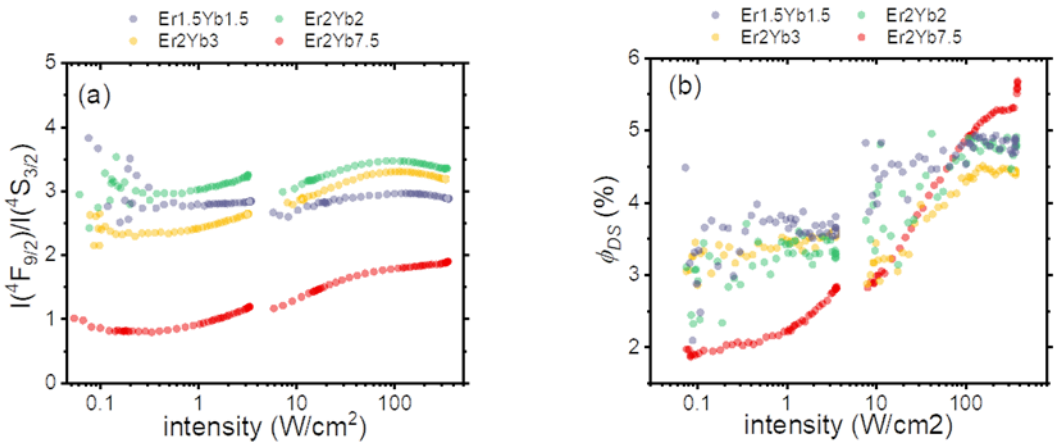

Figure 5.8 - (a) Ratio of the intensities of the $^4F_{9/2} - {}^4I_{15/2}$ (Red) transition and the $^4S_{3/2} - {}^4I_{15/2}$ (Green) transition as a function of 976 nm excitation intensity in the 0.1 – 350 W/cm^2; (b) ϕ_{DS} of the Er^{3+}:$^4I_{13/2} - {}^4I_{15/2}$ transition as a function of intensity at 940 nm excitation.

The results of the investigation reveal that the ϕ_{UC} of PbF_2:Er^{3+}, Yb^{3+} crystals does not surpass that of the SrF_2:Er^{3+}, Yb^{3+} (ϕ_{UC}= 6.5 %) and BaF_2:Er^{3+}, Yb^{3+} (ϕ_{UC}= 10.0 %) crystal series. Nevertheless, the extensive data set presented in this study of PbF_2:Er^{3+}, Yb^{3+} crystals can contribute significantly to the current understanding of UC phenomena and serve as a reference data set for the practical applications of UC materials. By providing a thorough analysis of the UC behaviour in these crystals, this work sheds light on the underlying mechanisms governing the UC process in rare-earth-doped fluorides, which is critical for developing new and more efficient UC materials. Moreover, these findings open new avenues for future research in this area and offer valuable insights for the optimization of UC materials for a wide range of applications.

5.4 Summary

The main results presented in this chapter are:

- The Bridgeman method provides Er^{3+}/Yb^{3+}-doped PbF_2 bulk crystals that can function as efficient up-conversion materials.
- The highest ϕ_{UC} value is detected under 350 W/cm^2, 976 nm excitation in the sample doped with 2 mol.% of Er^{3+}, 3 mol.% of Yb^{3+} ions and is equal to 5.9%.
- The analysis of the radiative lifetimes and branching ratios obtained by Judd-Ofelt theory and the luminescence decay times obtained experimentally reveal a simple method for estimating the PLQY value of the emission levels of Er^{3+} under resonant excitation.
- Three methods of the Judd-Ofelt analysis of the Er^{3+}-doped powder are studied. It is shown that the method using the emission spectra gives the best agreement between the results obtained in the powder and the crystal of the same chemical composition

6. Study of YF_3: Ce^{3+}, Yb^{3+} powders

Sections 6.2 through 6.4. The results are presented in the paper Opt. Mat., 2019, 95, 109256 [172]*. The co-authors from the Prokhorov General Physics Institute synthesized the samples, A.R. Khadiev and V.G. Gorieva participated in the optical characterization, A.S. Nizamutdinov and V.V. Semashko were involved in the coordination of the work and the interpretation of the results.*

6.1 Introduction

The combination of the Ce^{3+} and Yb^{3+} ions can theoretically allow the observation of quantum cutting under UV excitation. YF_3 is a suitable host for this doping ion pair due to its low phonon energy and the same valence of Y^{3+} and Ce^{3+}/Yb^{3+} ions. To perform a complex analysis two series of samples are synthesised. One series has a fixed amount of Ce^{3+} ions (0.05 mol%) and a varying number of Yb^{3+} ions (0-10% mol.%), while the second series has a fixed amount of Ce^{3+} ions (0.1 mol%) and a varying number of Yb^{3+} ions (0-10% mol.%).

To carry out the study, the following objectives are set for this chapter:

- To prove that efficient down-shifting is possible in the Ce^{3+}/Yb^{3+}-doped YF_3 powders.
- To study the energy transfer between the doping ions: determine the energy transfer mechanism and the energy transfer coefficient.
- Find the optimum doping concentration that gives the highest PLQY value.

6.2 Physico-chemical properties

A characteristic X-ray diffraction pattern of the YF_3:Yb, Ce samples is presented in Figure 6.1.

All YF_3: Yb, Ce samples are single-phase and have an orthorhombic symmetry, which corresponds to the low-temperature β-YF_3 type structure [173,174]. The unit cell parameters are calculated using X-ray diffraction data. The results are given in the Table 6.1. The formation of a solid solution is confirmed by the change in the unit cell parameters of samples containing doping ions in comparison with undoped samples. (*a* = 6.353 Å, *b* = 6.850 Å, *c* = 4.393 Å, JCPDS card # 74-0911).

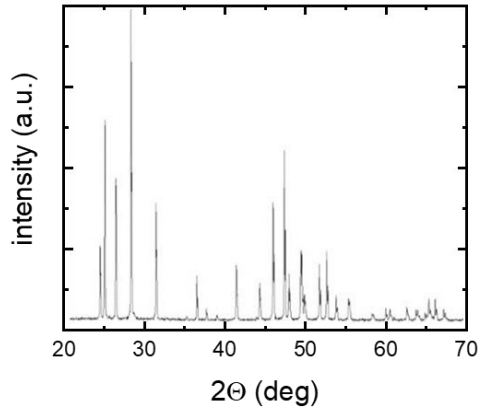

Figure 6.1 - X-ray diffraction patterns of the YF_3; Ce(0.05 mol.%), Yb(10.0 mol.%) sample.

Table 6.1 -Unit cell parameters of the YF_3 Ce, Yb samples.

Sample	Cell parameters, Å		
	a	*b*	*c*
Ce0.05	6.346(2)	6.832(2)	4.386(1)
Ce0.1	6.358(1)	6.851(2)	4.3862(8)
Ce1	6.359(1)	6.852(2)	4.3873(7)
Ce0.1Yb1	6.359(1)	6.853(2)	4.3870(7)
Ce0.1Yb5	6.354(1)	6.849(1)	4.3886(7)
Ce0.1Yb10	6.350(2)	6.843(2)	4.390(1)
Ce0.05Yb1	6.348(2)	6.841(3)	4.382(1)
Ce0.05Yb5	6.3576(9)	6.855(1)	4.3921(6)
Ce0.05Yb10	6.3563(5)	6.8491(7)	4.3934(3)

6.3 Spectral and kinetic properties

4f - 5d transitions are dipole-dipole allowed and their cross sections are several orders of magnitude higher than those of 4f - 4f transitions. Usually, the absorption bands corresponding to the 4f - 5d transitions of the Ce^{3+} ion are located in UV or blue spectral regions [175]. The lowest energy absorption bands of the Ce^{3+} ion in the YF_3 host are located around 250 nm [176]. Intense emission at a wavelength of about 300 nm, which corresponds to the 4f - 5d transition of the Ce^{3+} ion, as well as much weaker emission of the Yb^{3+} ion at a wavelength of about 980 nm (see Figure 6.2) is observed under 266 nm laser excitation. One can notice that with an increase in the concentration of Yb^{3+} ions, the relative intensity of emission of these ions becomes comparable with the intensity of luminescence of Ce^{3+} ions.

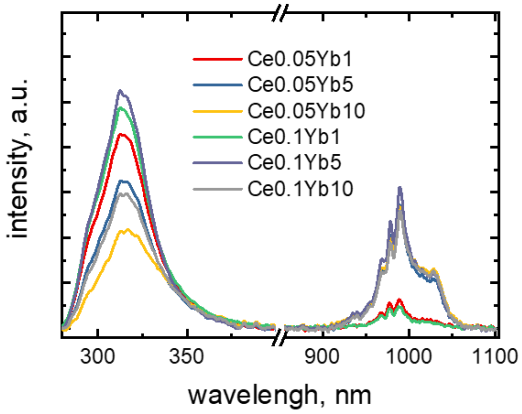

Figure 6.2 - Emission spectra of YF_3: Ce^{3+}, Yb^{3+} samples under 266 nm excitation.

The internal luminescence quantum yield is estimated using an integrating sphere. The excitation wavelength is 266 nm. The low emission intensity of the samples with the concentration of Yb^{3+} ions below 1 mol.% is not sufficient to calculate the quantum yield values. The results of the remaining measurements are given in the Table 6.2.

Table 6.2. Internal luminescence quantum yield of Yb^{3+} ions in YF_3 host.

REE content, mol %	**Ce0.05**	**Ce0.1**
Yb5	0.8	0.5
Yb10	0.9	0.6

Luminescence decay curves of Ce^{3+} ions are detected at a wavelength of 290 nm. All samples are excited with 266 nm pulsed laser emission. In the Figure 6.3, it is seen that the luminescence decay curve of Ce^{3+} ions has a non-mono-exponential behaviour in the samples with higher Yb^{3+} concentration. This can be explained by the fact that the main channel of excitation loss is the energy transfer between the ions as well as the complex nature of the energy transfer mechanism. The average luminescence lifetimes are calculated using the following formula:

$$\tau_{avg} = \frac{\int t*I(t)dt}{\int I(t)dt}. \quad (28)$$

Here I(t) is the intensity of the luminescence of the Ce^{3+} ions at time t.

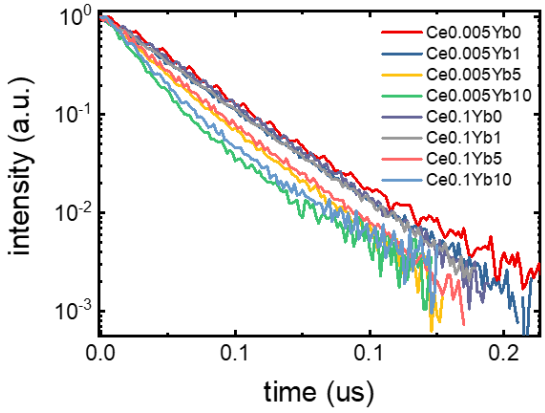

Figure 6.3 - Luminescence decay curves corresponding to the 5d-4f transition of Ce^{3+} ions in the YF_3:Ce^{3+}, $Yb3^+$ samples under 266 nm excitation.

The obtained average luminescence decay time makes it possible to estimate the energy transfer coefficients from the Ce^{3+} to the Yb ions^{3+} using the following expression:

$$k_{ET} = 1 - \frac{\tau_{xYb}}{\tau_{0Yb}}. \qquad 29$$

Here τ_{xYb} is the luminescence decay time of a sample co-doped with Ce^{3+} and Yb^{3+} ions; τ_{0Yb} is the luminescence decay time of a sample doped with only Ce^{3+}ions.

Table 6.3. Average luminescence decay time of the 5d-4f transition of Ce^{3+} ions and energy transfer coefficients in the YF_3:Ce^{3+}, $Yb3^+$ samples under 266 nm excitation.

REE content, mol %	**Ce0.05**		**Ce0.1**	
	t_{avg}, ns	k_{ET}, %	t_{avg}, ns	k_{ET}, %
Yb0	24	-	23	-
Yb1	22	8.3	22	4.3
Yb5	18	25.0	19	17.4
Yb10	15	37.5	16	30.4

Average luminescence decay time as well as energy transfer between Ce^{3+} and Yb^{3+} ions are shown in the Table 6.3. The data in the table shows that the highest energy transfer coefficient (37.5%) is observed in the sample with Ce^{3+}/Yb^{3+} doping concentration = 0.05/10 mol.%.

Luminescence decay curves of the $^2F_{5/2}$ - $^2F_{7/2}$ transition of the Yb^{3+} ions are recorded at 1022 nm. 266 nm and 976 nm wavelengths are used as excitation. The obtained results are presented in the Figure 6.4.

The luminescence decay curves have a shape close to the mono-exponential, and luminescence lifetime drops with an increase in Yb^{3+} concentration. This effect can be explained by the concentration quenching of luminescence. The average luminescence decay time of Yb^{3+} ions is given in the Table 6.4. The data in the table shows that the concentration of Ce^{3+} ions has no noticeable influence on the luminescence lifetime of Yb^{3+} ions. In addition, the obtained luminescence decay time of Yb^{3+} stays the same and exhibits the same concentration quenching under both excitation wavelengths.

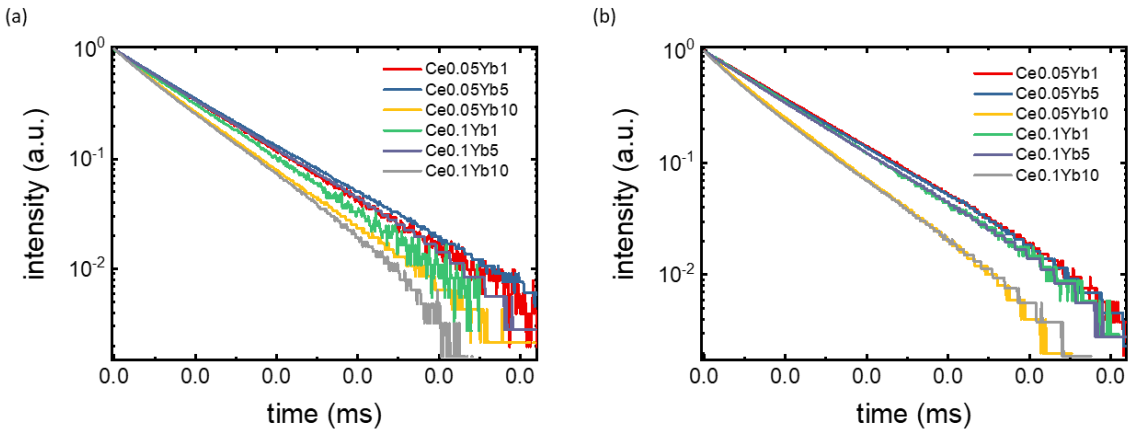

Figure 6.4 - Luminescence decay curves corresponding to the $^2F_{5/2}$ - $^2F_{7/2}$ transition of Yb^{3+} ions in the $YF_3:Ce^{3+},Yb^{3+}$ samples, observed at 1022 nm under (a) 266 nm and (b) 976 nm excitation.

Table 6.4 - Average luminescence decay time of the $^2F_{5/2}$ - $^2F_{7/2}$ transition of Yb^{3+} ions in the $YF_3:Ce^{3+},Yb^{3+}$ samples under 266 nm and 976 nm excitation.

REE content, mol %	Ce0.05		Ce0.1	
	t_{avg} (ms) 266 nm excitation	t_{avg} (ms) 976 nm excitation	t_{avg} (ms) 266 nm excitation	t_{avg} (ms) 976 nm excitation
Yb1	1.8	2.0	1.7	1.8
Yb5	1.9	1.9	1.9	1.9
Yb10	1.6	1.5	1.5	1.5

6.4 Energy transfer mechanism

To study the mechanisms of down-conversion processes in the studied samples in more detail, the dependence of the luminescence intensity of Ce^{3+} and Yb^{3+} ions on the 266 nm excitation intensity is investigated. The obtained dependence is fitted with a function 30. This approach was used earlier in the work [177].

$$I_{norm}(E_{norm}) = E_{norm}^{p} . \quad (30)$$

Here I_{norm} is the normalised luminescence intensity and E_{norm} is the normalised per excitation intensity.

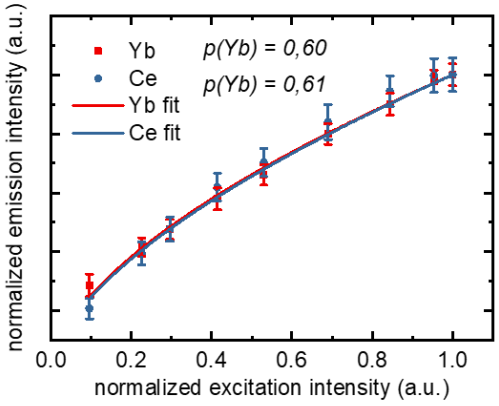

Figure 6.5 - Dependence of luminescence intensity of Yb^{3+} and Ce^{3+} ions in the $YF_3:Ce^{3+}$(0.05%), Yb^{3+}(5.0%) sample on 266 nm excitation intensity.

The dependence of I_{norm} on E_{norm} is presented in Figure 6.5. It has a nonlinear shape with a *p* coefficient equal to 0.60 and 0.61 for the luminescence of Ce^{3+} and Yb^{3+} ions respectively. According to the theory presented in the works [177,178] the dependence of the luminescence intensity of Yb^{3+} ions should have a power factor equal to 0.5 as Yb^{3+} ions act as acceptors in the process of down-conversion. This is an indication that in this case, the Yb^{3+} ion is excited through a down-conversion process in such a way that the energy of one quant of excitation is redistributed between two Yb^{3+} ions. At the same time, the dependence of the luminescence intensity of Ce^{3+} ions under 266 nm excitation has a non-linear shape with a power factor different from 1. This can be explained by the fact that there is an additional process that repopulates the excited state of Ce^{3+} ions.

The YF_3: Ce, Yb material is expected to exhibit a quantum splitting scenario where the absorption of one high-energy photon results in the emission of two or more photons with lower energy. In this case, internal luminescence quantum yield can exceed 100%. As can be seen from quantum yield studies, no such effect is observed. The study of diffuse reflectance spectra of the samples single-doped with Ce^{3+} showed the formation of colour centres when the samples are irradiated with UV light. The formation of colour centres results in the appearance of an absorption band in the 520 – 650 nm range. Diffused reflectance spectra of the YF_3:Ce^{3+} sample before and after laser irradiation are presented in the Figure 6.6a.

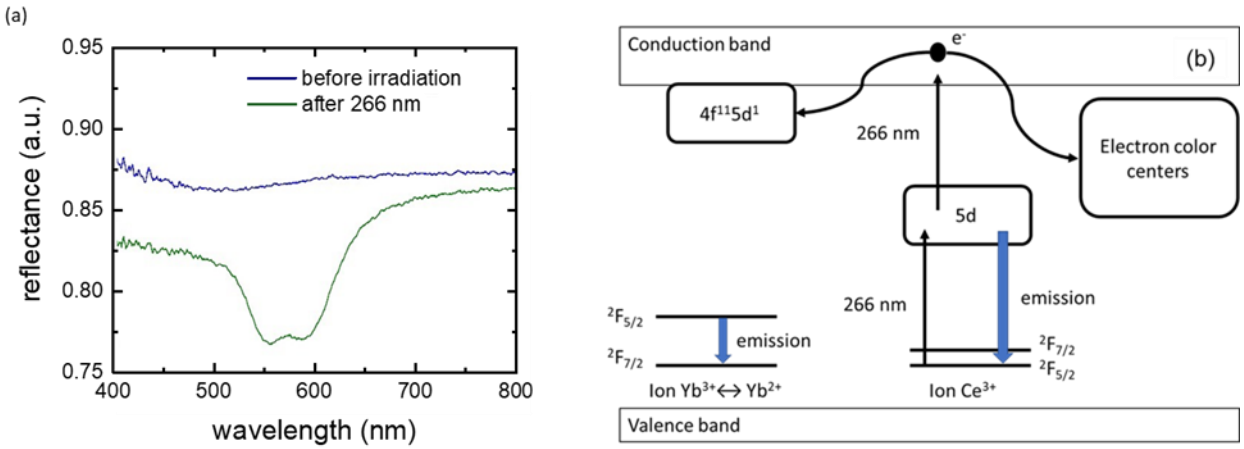

Figure 6.6 - a) Diffused reflectance spectra of the $YF_3:Ce^{3+}$ sample; b) diagram of photodynamic processes in fluoride crystals co-doped with Ce^{3+} and Yb^{3+} ions under UV irradiation, based on [179].

The observed absorption band likely corresponds to transitions in the colour centres that form via a multistep process. This process consists of the following steps: excitation of the Ce^{3+} ion to the 5d state by the first 266 nm photon, absorption of the second 266 nm photon by the excited Ce^{3+} ion and the appearance of free charge carriers, relaxation of free charge carriers on host defects. This is a well-known model of the colour centre formation, the so-called solarisation of crystals doped with Ce^{3+} ions under UV excitation. During this process, Ce^{4+} ions are formed due to electron loss and are then reverted to the Ce^{3+} state, due to hole capture, thus leading to the formation of colour centres of both electronic and hole nature[180–183]. The added Yb^{3+} ions can trap both electrons and holes. The probability of this process is higher than the probability of electron capture by defects. Thus, the ions remain in a trivalent state, resulting in a lowering of the solarisation level[180,184–188]. For example, solarization is not observed in the reflectance spectra of samples of $LiYF_4$ crystals doped with 1 - 2 mol.% of Yb^{3+} ions [189,190]. This may explain the lack of gradual decrease in the intensity of the absorption band of the colour centres since there are no samples with less than 1 mol % of Yb^{3+} ions in the studied series. Energy transfer from the 5d level of Ce^{3+} ion to the 4f ($^1S_0$) level of Yb^{2+} ion is probably a reason for the observed quenching of

luminescence of Ce^{3+} ions [191,192]. As a result of this process, the Yb^{3+} ions remain in the excited $^2F_{5/2}$ state, leading to the increase in the luminescence intensity with a peak at 980 nm [193]. The Ce^{3+} impurity centres, probably end up in an excited 5d state as the result of the following process. First, the thermalized charge carriers can still return to Ce impurity [191], i.e. the process is irreversible at room temperature. Second, at room and higher temperatures, the colour centres can migrate to Ce^{3+} ions, thus transferring the excitation to them and increasing the luminescence quantum yield [194]. Finally, excitons which may be formed as a result of conjugation of free charge carriers may resonantly transfer energy to Ce^{3+} ions as a result of recombination [195,196]. All the described processes lead to an increase in the quantum yield of the luminescence of Ce^{3+} ions, but further research is needed to have a complete picture.

6.5 Summary

Finally, it is possible to highlight the main results of this chapter:

- The possibility of down-sifting emission is shown in the Ce^{3+}/Yb^{3+}-doped YF_3 powders.
- The values of the energy transfer between Ce3+ and Yb3+ ions are estimated with the highest one equal to 37.5% obtained in the sample doped with 0.05 mol.% of Ce^{3+} and 10 mol.% of Yb^{3+} ions. The PLQY value in the same sample is 0.91% under 266 nm excitation.
- It is found that complex photochemical processes take place in the studied samples and charge transfer is identified as the main energy transfer mechanism.

7. Rare-earth -doped fluoride crystal as an UC PLQY reference

Sections 7.2 through 7.4. The results are presented in the paper Advanced Photonics Research, 2023, 4, 2, 2200187 [197] *The co-authors from the Prokhorov General Physics Institute have synthesized the single crystal, Fernando Arteaga Cardona and Damien Hudry synthesized the nanoparticles, Dmitry Busko and Ian A. Howard participated in the optical characterization, Bryce S. Richards and Andrey Turshatov were involved in the coordination of the work and the interpretation of the results.*

7.1 Introduction

Application to photovoltaic devices is not the only possible use of the materials under investigation. Another possible application of the rare–earth–doped fluoride crystals is the UC PLQY reference. The chemical stability of fluoride crystals, the reliability of the PLQY measurements and the ability to cut them into a convenient shape make Er^{3+}/Yb^{3+} - doped SrF_2 an excellent candidate for an UC PLQY reference. To test the performance of the material as a UC PLQY reference, it is necessary to perform a PLQY measurement of a known material with a new reference and then compare it with the absolute PLQY values.

To carry out this study, the following objectives of this chapter are as follows:

- To study the UC PLQY of the Er^{3+}/Yb^{3+} - doped SrF_2 crystal over a wide intensity range.
- To perform a PLQY measurement of the α-$NaYF_4$:18%Yb^{3+},2%Er^{3+}@CaF_2 nanocrystals using the Er^{3+}/Yb^{3+} - doped SrF_2 crystal as a reference.
- To perform an absolute PLQY measurement of the α-$NaYF_4$:18%Yb^{3+},2%Er^{3+}@CaF_2 nanocrystals and compare the results with the relative method.
- Estimate the uncertainties of both methods of PLQY determination.

So far, the only approach to PLQY measurement that has been discussed in the current work is the so-called absolute method. It is based on the measurement of the emission intensity of a sample under investigation and the absorbed amount of the excitation in an integrating sphere. An alternative approach is the relative PLQY ($\phi^{(r)}$) measurement. In this case, the emission intensities of a sample under investigation and a sample with a previously reported PLQY are compared under the same excitation and collection conditions. This method requires a simpler experimental setup than the first one.

$$\phi^{(r)} = \phi_{ref}\left({A_{ref}}/{A_s}\right)\left({E_s}/{E_{ref}}\right)\left({n_s}/{n_{ref}}\right)^2, \quad 31$$

where ϕ_{ref} is the PLQY of the reference, A_s and A_{ref} are the absorptance of the sample and the reference at the excitation wavelength, respectively, E_s and E_{ref} are the integrated emission intensities of the sample and the reference, n_s and n_{ref} are the refractive indices of the sample and the reference at the emission wavelength.

As it has been discussed in the Methodology chapter of the current work, the measurement of UC PLQY is subject to certain additional complications compared to Stokes emission due to the non-linear intensity dependence of the UC process. This imposes limitations on the UC reference material. To minimise the effects of the non-linear nature of the UC process the reference material should have the lowest possible optical density, while still providing reliable absorption and PLQY data. Therefore, a doping concentration of 1 mol.% of Er^{3+} and 1 mol.% of Yb^{3+} is chosen. The SrF_2 is chosen as the host crystal as it has been well-studied for UC applications[198,199]. For ease of use, the size and shape of the reference should be compatible with standard spectroscopy equipment. Therefore, the reference crystal was cut into a 3x3x20 mm parallelepiped and placed in a standard 1 cm quartz cuvette with 3x3 mm internal dimensions and filled with toluene.

7.2 UC PLQY of the Er^{3+}/Yb^{3+} - doped SrF_2 reference crystal

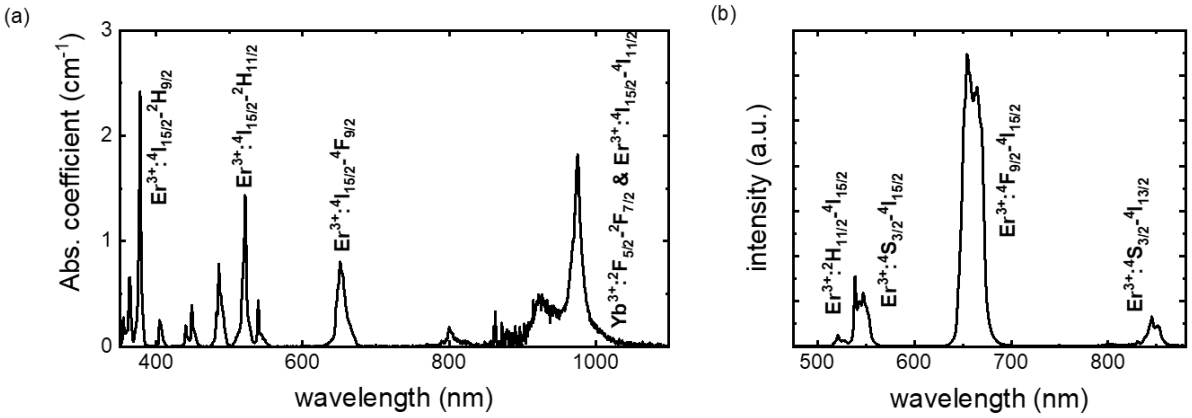

Figure 7.1 – a) Absorption spectrum; b) emission spectrum under 976 nm, 10 W/cm² excitation of the SrF_2: 1 %Yb^{3+},1%Er^{3+} crystal.

The spectroscopic data of the SrF_2:Yb^{3+},Er^{3+} crystal is shown in Figure 7.1. The absorption spectrum shows that at 976 nm the absorption coefficient is 1.74 cm^{-1} which gives an absorption of 39% in a 3 mm thick sample while maintaining the UC emission intensity shown in Figure 7.1b.

Next, the UC PLQY of the crystal should be considered. The values obtained with an absolute method are shown in Figure 7.2.

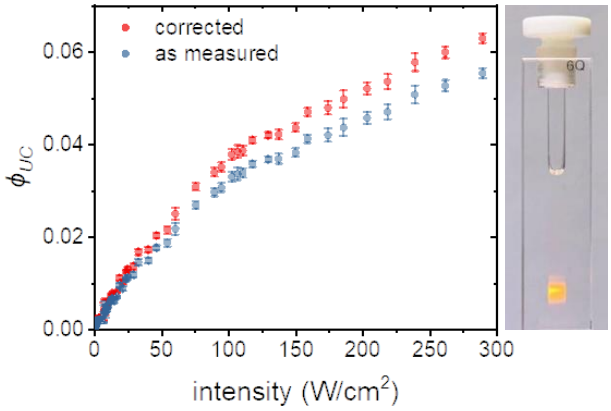

Figure 7.2 – a) Absorption spectrum; b) emission spectrum under 976 nm, 10 W/cm² excitation of the SrF_2: 1 %Yb^{3+},1%Er^{3+} crystal.

It can be seen that the crystal shows a reasonable PLQY value of 0.07% at a relatively low intensity of 1 W/cm^2, which then increases to a value of 5.5% at the highest available intensity of 290 W/cm^2. However, when the sources of error in the PLQY measurement are analysed, the PLQY values change significantly. It should be noted that the correction of the PLQY values of the three Er^{3+} emission bands shown in Figure 7.1b ($^2H_{11/2}$&$^4S_{3/2}\rightarrow{}^4I_{15/2}$, $^4F_{9/2}\rightarrow{}^4I_{15/2}$ and $^2H_{11/2}$&$^4S_{3/2}\rightarrow{}^4I_{13/2}$) is done separately, due to the different intensity dependence of each band. The total UC PLQY changes from 0.07% to 0.09% at 1 W/cm^2 and from 5.5% to 6.3% at 290 W/cm^2.

Once the UC PLQY of the reference crystal is known it is possible to proceed to the PLQY measurement of a new sample using a relative method. $NaYF_4$:18%Yb^{3+}2%Er^{3+}@CaF_2 nanoparticles are chosen as the test material for several reasons. Firstly, its UC emission is defined by Er^{3+} ions, which makes the performance of the relative measurement additionally simple and secondly, heterogeneous core-shell nanocrystals show great promise as efficient UC systems[200].

7.3 UC PLQY of the $NaYF_4$:18%Yb^{3+}2%Er^{3+}@CaF_2 nanoparticles

To perform the relative PLQY measurement the emission of both the reference and the sample must be characterised outside the integrating sphere. This raises the question of the appropriateness of using the PLQY values obtained for the SrF2:Yb^{3+},Er^{3+} reference crystal inside the integrating sphere in Equation 31. To answer this question, it is essential to take into account the main difference between the measurements inside and outside the integrating sphere. It is the greater reabsorption of the emitted photons inside the sphere due to the multiple passes through the crystal. This leads to the conclusion that only the correction for the reabsorption in the crystal itself is required. Fortunately, the sample doped with only 1 mol.% of Er^{3+} shows no reabsorption and it is reasonable to assume that $\phi_{ref} \approx \phi_{UC}^{(a,exp)}$.

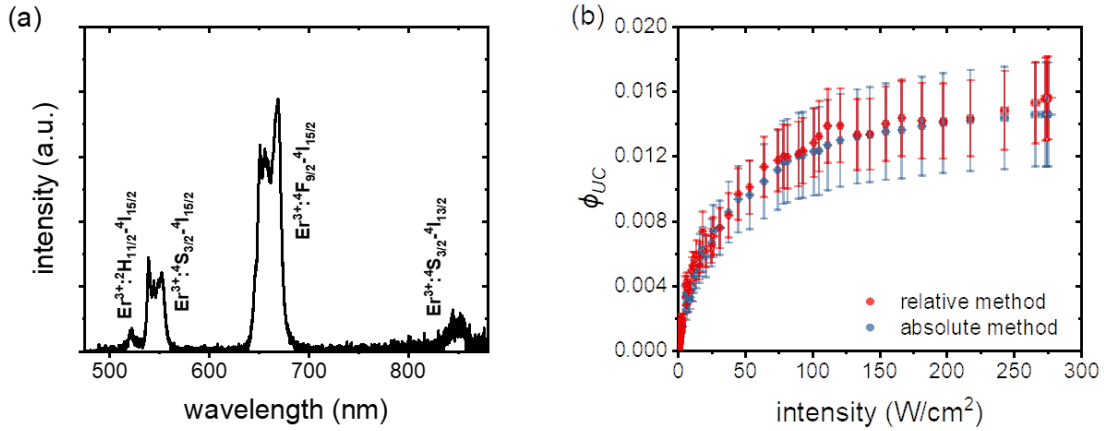

Figure 7.3 – a) emission spectrum under 976 nm, 290 W/cm^2 excitation; b) intensity dependence of UC PLQY under 976 nm excitation measured with the absolute and relative method of NaYF$_4$:18%Yb^{3+}2%Er^{3+}@CaF$_2$ nanoparticles.

To apply Equation 31, four additional parameters must be known: the absorptance of the reference (A_{ref}) and the sample (A_s) at 976 nm, and the integral emission intensity as a function of excitation intensity for both the reference (E_{ref}) and the sample (E_s). The refractive indices of toluene and SrF_2 in the range of 520 – 650 nm are 1.503 – 1.492 [201] and 1.439 – 1.437 [202], respectively. This gives a ratio of $\left(\frac{n_s}{n_s}\right)^2$ as 1.04, which allows for the following simplification of the Equation 31:

$$\phi^{(r)} = 1.04\phi_{ref}\left({}^{A_{ref}}\!/_{A_s}\right)\left({}^{E_s}\!/_{E_{ref}}\right), \qquad 32$$

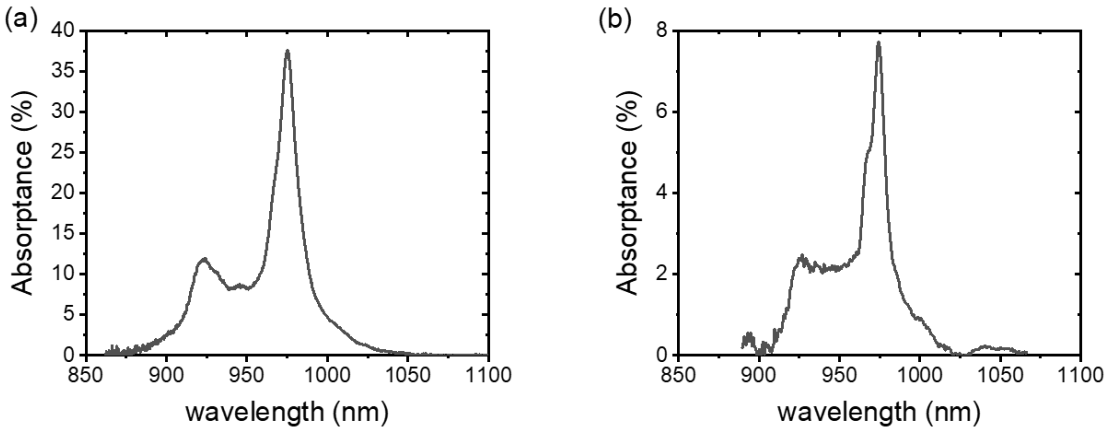

Figure 7.4 – absorption spectra of a) SrF2:Yb^{3+},Er^{3+} crystal; b) NaYF$_4$:18%Yb^{3+}2%Er^{3+}@CaF$_2$ nanoparticles.

The A_{ref} of the SrF2:Yb^{3+},Er^{3+} crystal and the A_s of the $NaYF_4$:18%Yb^{3+}2%Er^{3+}@CaF_2 nanoparticles can be determined by one of two methods: UV/Vis/NIR spectrometer (Figure 7.4) or an integrating sphere, where absorptance is calculated as the ratio of laser intensity $\left(1 - {}^{LD}/_{LI}\right)$ in Equation 18. Both methods give comparable results, with the absorptance of the reference crystal, A_{ref}, being 39%, and that of the nanoparticle sample, A_s, being 7%. The agreement between the two methods confirms the reliable measurement of the absorptance of reference crystals and upconversion nanocrystals in a cuvette with a 3 mm beam path using a standard UV/Vis/NIR spectrometer. The relative PLQY values obtained are shown in Figure 7.3b.

As UC is a non-linear process, the accuracy of the PLQY measurement for both absolute and relative methods depends on the excitation intensity and the absorbance of the sample. A remarkable agreement between the methods is observed at high excitation intensities (> 10 W/cm2). In contrast, the quantum yield values show a greater difference at low excitation intensities.

Considering the precision of the measurements, shown as error bars in Figure 7.3b, the observed differences are surprisingly satisfactory. Thus, the proposed relative method for estimating the UC PLQY of nanocrystals can be widely applied, given the strong agreement between the methods employed.

7.4 Analysis of the uncertainties of absolute and relative methods

The final step in the analysis is to estimate the uncertainty provided by both methods. Considering that UC PLQY is calculated according to Equation 18, the absolute error is expressed as:

$$\Delta\phi_{UC} = \sqrt{\left(\frac{\partial\phi_{UC}^{(a)}}{\partial PD}\Delta PD\right)^2 + \left(\frac{\partial\phi_{UC}^{(a)}}{\partial PI}\Delta PI\right)^2 + \left(\frac{\partial\phi_{UC}^{(a)}}{\partial LD}\Delta LD\right)^2 + \left(\frac{\partial\phi_{UC}^{(a)}}{\partial LI}\Delta LI\right)^2 + \left(\frac{\partial\phi_{UC}^{(a)}}{\partial ES}\Delta ES\right)^2}, \qquad 33$$

where ΔPD, ΔPI, ΔLD, ΔLI and ΔES represent the absolute uncertainty of the corresponding measurement. Considering that the same spectrometers are used for *ES*, *LI* and *LD* as well as *PI* and *PD*, the following relative (δ) errors are obtained: $\delta PD = \delta PI = \delta P = 0.06$ and $\delta LD = \delta LI = \delta ES = \delta L = 0.01$. Absolute errors can then be expressed using the relative errors as $\Delta PD = PD * \delta P$, $\Delta PI = PI * \delta P$, $\Delta LD = LD * \delta L$, $\Delta LI = LI * \delta L$ and $\Delta ES = ES * \delta L$.

Writing Equation 32 in explicit form and assuming $A = 1 - \frac{LD}{LI}$, the next expression is obtained:

$$\Delta\phi_{UC} = \sqrt{\frac{\Delta PD^2}{A^2 ES^2} + \frac{\Delta PI^2 (1-A)^2}{A^2 ES^2} + \Delta LD^2 \left(\frac{PD-(1-A)PI}{A^2\ LI\ ES} - \frac{PI}{A\ LI\ ES}\right)^2 + \\ + \Delta LI^2 \left(\frac{(1-A)PI}{A\ LI\ ES} - \frac{(1-A)(PD-(1-A)PI)}{A^2\ LI\ ES}\right)^2 + \frac{\Delta ES^2 (PD-(1-A)PI)}{A^2\ ES^4}}. \quad 34$$

To obtain the relative error the following expression is used:

$$\delta\phi_{UC} = \frac{\Delta\phi_{UC}}{\phi_{UC}}. \quad 35$$

Taking the δP as 0.06 and δL as 0.01 it is possible to plot the relative error of the absolute method as a function of absorbtance.

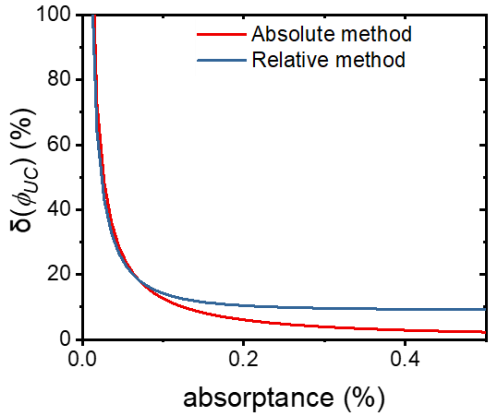

Figure 7.5 – Relative error of the ϕ_{UC} determination with the absolute and relative methods as a function of sample absorptance.

As the relative PLQY is calculated using the Equation 32 it is the product of the independent variables and the relative error is then calculated as:

$$\delta\phi^{(r)} = \sqrt{\left(\delta\phi_{ref}\right)^2 + (\delta A_s)^2 + \left(\delta A_{ref}\right)^2 + (\delta E_s)^2 + \left(\delta E_{ref}\right)^2}. \quad 36$$

The relative errors for each component of the expression can be approximated as $\delta\phi_{ref} = 0.04$, $\delta E_s = \delta E_{ref} = 0.06$. The uncertainties δA_{ref} and δA_s are determined based on the assumption that the absolute error of optical density measurement with a standard spectrophotometer is 0.005 according to [203]. For example, the datasheet for the Perkin Elmer Lambda 950 spectrophotometer specifies an accuracy of ±0.003 for an optical density of 1 at 546 nm. This assumption allows the relative errors δA_{ref} and δA_s to be calculated from Figure 7.4. The values obtained from Equation 35 are then converted to absolute errors and presented in Figure 7.3b as error bars for the relative method.

In assessing the absorptance dependence of $\delta\phi^{(r)}$ (Figure 7.5), the δA_s is varied while maintaining a fixed absolute error in optical density of 0.005. The optical density spans the range of 0 – 0.30, corresponding to absorptance values of 0 – 50%, respectively.

7.5 Summary

The main results presented in this chapter are:

- It is shown that the Er^{3+}/Yb^{3+} - doped SrF_2 crystal is an efficient up-conversion material, exhibiting the UC PLQY values up to 5.5% under 976 nm, 290 W/cm^2 excitation.
- The UC PLQY of the α-$NaYF_4$:18%Yb^{3+},2%Er^{3+}@CaF_2 nanocrystals measured by the relative method shows the highest value of 1.6% under 976 nm, 290 W/cm^2 excitation.
- The UC PLQY of the α-$NaYF_4$:18%Yb^{3+},2%Er^{3+}@CaF_2 nanocrystals measured by the absolute method shows the highest value of 1.5% under 976 nm, 290 W/cm^2 excitation. In general, there is good agreement between the results obtained with the two methods.
- The analysis of the uncertainties of the absolute and the relative methods shows that there is no difference in uncertainty for the samples with low absorptance (<10%), while for the samples with higher absorptance, the absolute method gives a lower uncertainty.

8. Promising new hosts for rare-earth ions

Two trends in material science stand out nowadays: the avoidance of harmful substances and the move towards biologisation. Both of these trends seem promising, as they lead to the development of new materials with unique properties as well as more advanced technological processes. However, it also brings new challenges, as this field is still far from being explored. Even if a theoretical solution exists, it must be translated into a reliable and feasible technical solution. Peptides and proteins can serve as interesting hosts for rare earth ions due to their unique structural and functional properties.

1. Peptides as molecular framework:

Peptides have a specific amino acid sequence that provides a unique structure. They can be designed to contain sites capable of coordinating rare earth ions. These peptide structures can be used to create nanoparticles or nanoclusters with rare earth ions.

2. Functional groups in proteins:

Proteins contain a variety of functional groups, including amino acids, which can serve as coordinating centres for rare earth ions. These ions can be incorporated into the structure of a protein, modifying its properties. For example, such modified proteins can be used as catalysts in chemical reactions.

3. Peptide nanotubes and nanodiscs:

Specific peptide designs can facilitate the formation of nanotubes or nanodiscs that can serve as hosts for the rare earth ions. These structures have potential for use in sensors, medical diagnostic devices, and other biotechnological applications.

4. Biomimetic protein materials:

Researchers are also seeking to create biomimetic materials that mimic the structures and functions of proteins in nature. These materials can be created using rare

earth ions to improve their properties. There are reports of the integration of rare-earth elements into peptides from solutions available [204].

There is certain progress in screening technology as the availability of peptide microarrays increases. Therefore, experiments that search for selective matrix elements can be carried out very efficiently using the high throughput screening approach. The invention of Merrifield solid-phase synthesis allowed the creation of DNA and peptide microarrays[205], which became an important tool for high-throughput study of oligonucleotide and protein interactions[206,207]. Today, the technical possibilities for the synthesis of molecular microarrays have been greatly enhanced by addressing monomers for in-situ solid-phase synthesis using a xerographic printer[208], the electric fields of a computer chip[209,210], light-induced forward transfer [211], and stochastic filling of microcavities with microparticles[212]. In addition, the molecular space of microarrays has been greatly expanded through the use of post-synthetic modification of peptides[213,214], the introduction of hundreds of new artificial amino acids and the realization of peptoid chemistry in array format[215]. Such progress has allowed the screening of both a large number of new specific molecular binders as well as new efficient chemical reactions.

Search for the host material is a complex process that includes screening, validation and integration into layers. Since this is new, it is important to first study the initial screening process.

To build on what is known, a peptide library is created from a previously reported peptide[204] with 10000 different twelve-mers of peptides placed on the chip in 120 μm spots. The peptide library contains both substitutions of the reported peptide by replacing all its amino acids at all 12 positions, as well as random variants created by combining positively charged and hydrophobic amino acids. Then the europium nitrate salt is preincubated with a concentration of 100 micrograms per milliliter for three hours at room temperature.

Optically the deposition of europium ions is investigated with a hyperspectral camera. To estimate the limitations of this approach the solution of europium nitrate with different concentration drop casted on a glass slide is analyzed. A hyperspectral camera is only capable of directing concentrations of 5 mg/ml and above (Figure 8.1). Therefore, other screening techniques such as Time-of-Flight Secondary Ion Mass Spectrometry for Molecular Imaging (TOF-SIMS) are required. This method allows for high lateral resolution, high chemical and surface selectivity, and sufficient mass resolution for the separation of major mass interferences[216,217].

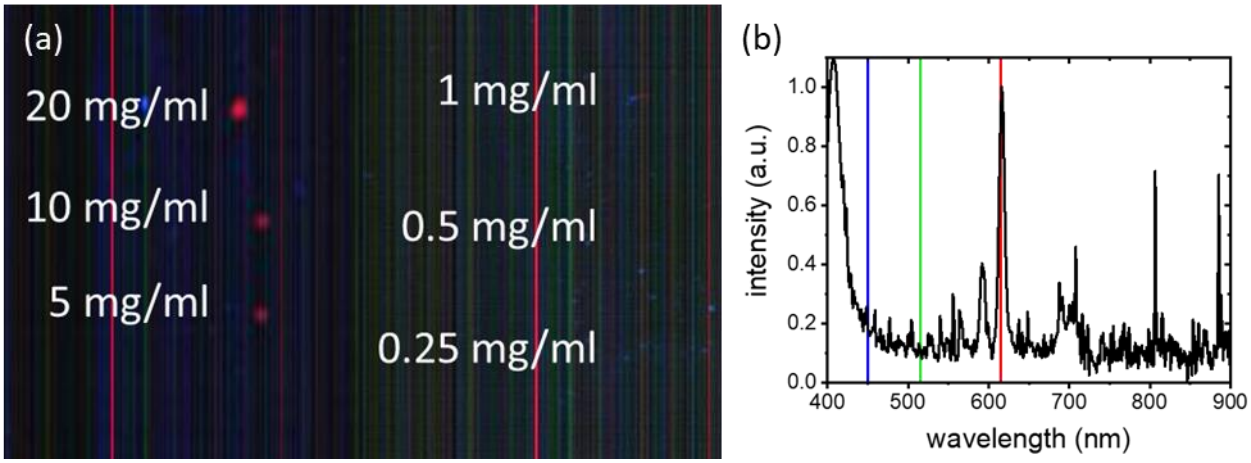

Figure 8.1 - a) Images of the drop-casted europium nitrate solution with different concentrations obtained with a hyperspectral camera under 386 nm excitation; b) Emission spectrum of the 20 mg/ml sample. Blue, Green and red lines show the wavelengths that are used for building the colour images.

The possible detection of selective deposition of europium ion on peptides is then studied. The imaging of the entire peptide library is performed using the TOF-SIMS approach. At each point of the 12-mer peptide, there is a different content of amino acids. In particular, phenylalanine is known for an aromatic side group in the formation of ordered structures. TOF-SIMS allows it to be detected well (Figure 8.2a). Similar detection of individual amino acids has been reported in the work [218].

Figure 8.2b shows the same chip scanned for europium ions. Distinct europium signals can be seen with the brightest one demonstrating a signal-to-noise ratio of more than ten. When analyzed it can be observed that different peptides have varying bonding strength, thus providing an opportunity to control the density of the matrix.

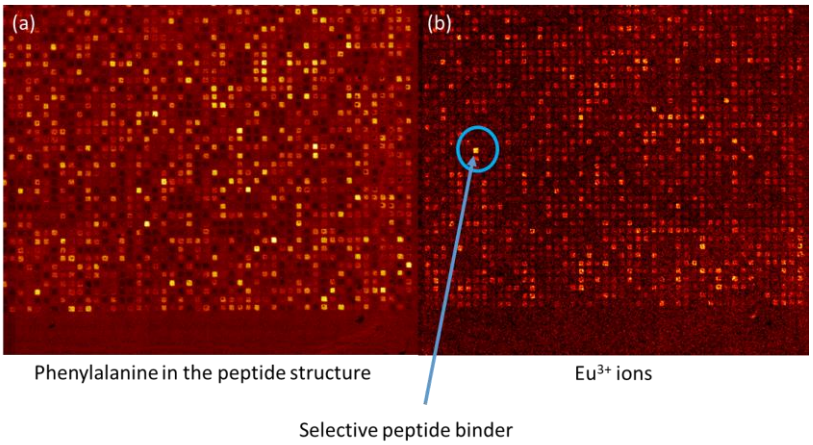

Figure 8.2 - a) TOF SIMS Imaging of phenylalanine at 120.08 m/z; b) Imaging of europium ion at 152.9 m/z.

Thus, the first step of matrix analysis is performed. The screening is demonstrated for the first time and a technique for the development of biological materials is studied. The present work illustrates a new promising direction to be developed in KIT as part of the digitalization of materials. The modular composition of peptides allows covering many possibilities compared to conventional methods, where it is only possible to vary the composition ratio or use certain additives. The application of peptides and proteins as hosts for rare earth ions offers unique opportunities to create innovative materials with controlled properties.

Conclusions and Outlook

In the current work complex research of up-conversion materials BaF_2: Er, Yb and PbF_2: Er, Yb as well as down-conversion materials BaF_2: Er and YF_3: Yb, Ce is carried out. The compositions which exhibit the highest luminescence quantum yield are determined. The possible application of BaF_2: Er crystals to increase the efficiency of photovoltaic devices is experimentally tested.

The main results obtained in the paper:

1. It is demonstrated that the Bridgman method provides Er^{3+}/Yb^{3+} co-doped and Er^{3+} single-doped BaF_2 and PbF_2 crystals that have high up- and down-conversion performance and that are suitable for combination with photovoltaic devices.
2. The concentration of doping ions in BaF_2:Er, Yb material that exhibits the highest luminescence quantum yield values is determined. It is 2 mol.% of Er^{3+} ions and 3 mol.% of Yb^{3+} ions and allows obtaining the value of up-conversion luminescence quantum yield equal to 10% under 976 nm excitation with an intensity of 490 W/cm^2. This value is comparable with the highest values observed in similar materials.
3. The concentration of doping ions in PbF_2: Er, Yb material that exhibits the highest luminescence quantum yield values is determined. It is 2 mol.% of Er^{3+} ions and 5 mol.% of Yb^{3+} ions and allows obtaining the value of up-conversion luminescence quantum yield equal to 4.4% under 976 nm excitation with an intensity of 350 W/cm^2.
4. Down-conversion with efficiency exceeding 100% is observed in BaF_2: Er crystals. The highest quantum yield is 153% and it is found in the sample doped with 5 mol.% Er^{3+} under 405 nm excitation. Maximum ebchancemennt of the Ge – photodiode J_{sc} is 0.6 mA/cm^2

5. It is demonstrated that like single crystals Ce^{3+} and Yb^{3+} - doped YF_3 powders exhibit down-shifting emission and have the potential to be used in combination with photovoltaic devices.
6. The values of the energy transfer coefficient from Ce^{3+} to Yb^{3+} ion in the YF_3 host under 266 nm excitation are determined. The obtained value is 37.5% and it is found in the sample with the doping concentrations of 0.05 mol.% of Ce^{3+} and 10.0 mol.% of Yb^{3+} ions. At the same time, the luminescence quantum yield is 0.91%.
7. It is demonstrated that SrF_2: Er, Yb can be used as a reference for relative UC PLQY measurements. Good agreement between relative and absolute methods is demonstrated using $NaYF_4$:18%Yb^{3+}2%Er^{3+}@CaF_2 nanoparticles as a test sample.
8. A new study of peptides as hosts for rare-earth ions is initiated. The detectable concentration of europium ions is clarified and the possibility of binding to peptides is investigated.

Based on the results of the present work, further research can be planned to extend the existing knowledge. Many of the results presented can be considered as proof of concept, but further progress should be made to make them viable for real-world applications.

- For UC to be used efficiently in photovoltaic systems, materials that exhibit high UC PLQY values at much lower excitation intensities should be explored. This could include the study of different hosts as well as doping ions. Compatibility with other types of solar cells should also be investigated. In addition, different device architectures should be tested to find a way to minimise emission losses.
- Although high DC PLQY values are possible, DC materials are limited by the low absorption of rare earth ions in the UV and Vis regions. To overcome this additional doping to increase the absorption in this region might be required.
- To extend the application as a reference material for PLQY determination, the range of both excitation and emission wavelengths should be extended. As with other applications, this will require the investigation of new combinations of dopant ions.
- Finally, the foundations have been laid for the study of peptides as hosts for the rare earth ions. Further research should include new peptides as well as other rare earth ions.

List of references

(1) *Photovoltaics Report - Fraunhofer ISE*. https://www.ise.fraunhofer.de/en/publications/studies/photovoltaics-report.html (accessed 2023-12-13).

(2) Green, M. A.; Hishikawa, Y.; Dunlop, E. D.; Levi, D. H.; Hohl-Ebinger, J.; Ho-Baillie, A. W. Y. Solar Cell Efficiency Tables (Version 51). *Progress in Photovoltaics: Research and Applications* **2018**, *26* (1), 3–12. https://doi.org/https://doi.org/10.1002/pip.2978.

(3) *Solar Cell Market Size, Share | Industry Report, 2022*. https://www.grandviewresearch.com/industry-analysis/solar-cell-market (accessed 2021-05-21).

(4) Vecchi, M. P. Integrated Tandem Solar Cells. *Solar Energy* **1979**, *22* (4), 383–388. https://doi.org/https://doi.org/10.1016/0038-092X(79)90193-2.

(5) Beard, M. C.; Luther, J. M.; Midgett, A. G.; Semonin, O. E.; Johnson, J. C.; Nozik, A. J. Third Generation Photovoltaics: Multiple Exciton Generation in Colloidal Quantum Dots, Quantum Dot Arrays, and Quantum Dot Solar Cells. In *2010 35th IEEE Photovoltaic Specialists Conference*; 2010; pp 370–375. https://doi.org/10.1109/PVSC.2010.5616850.

(6) Yamaguchi, M.; Takamoto, T.; Araki, K. Super High-Efficiency Multi-Junction and Concentrator Solar Cells. *Solar Energy Materials and Solar Cells* **2006**, *90* (18), 3068–3077. https://doi.org/https://doi.org/10.1016/j.solmat.2006.06.028.

(7) W.G.J.H.M. van Sark, A. Meijerink, R. E. I. S. Solar Spectrum Conversion for Photovoltaics Using Nanoparticles. In *Third Generation Photovoltaics*; Vasilis Fthenakis, Ed.; InTech: Rijeka, 2012; pp 1–30.

(8) Geisz, J. F.; France, R. M.; Schulte, K. L.; Steiner, M. A.; Norman, A. G.; Guthrey, H. L.; Young, M. R.; Song, T.; Moriarty, T. Six-Junction III–V Solar Cells with 47.1% Conversion Efficiency under 143 Suns Concentration. *Nat Energy* **2020**, *5* (4), 326–335. https://doi.org/10.1038/s41560-020-0598-5.

(9) Baiju, A.; Yarema, M. Status and Challenges of Multi-Junction Solar Cell Technology. *Front Energy Res* **2022**, *10*.

(10) Richards, B. S.; Hudry, D.; Busko, D.; Turshatov, A.; Howard, I. A. Photon Upconversion for Photovoltaics and Photocatalysis: A Critical Review. *Chem Rev* **2021**, *121* (15), 9165–9195. https://doi.org/10.1021/acs.chemrev.1c00034.

(11) Leblanc, M.; Maisonneuve, V.; Tressaud, A. Crystal Chemistry and Selected Physical Properties of Inorganic Fluorides and Oxide-Fluorides. *Chem Rev* **2015**, *115* (2), 1191–1254. https://doi.org/10.1021/cr500173c.

(12) Chaney, R. C.; Lafon, E. E.; Lin, C. C. Energy Band Structure of Lithium Fluoride Crystals by the Method of Tight Binding. *Phys Rev B* **1971**, *4* (8), 2734–2741. https://doi.org/10.1103/PhysRevB.4.2734.

(13) Richman, I. Longitudinal Optical Phonons in CaF2, SrF2, and BaF2. *J Chem Phys* **1964**, *41* (9), 2836–2837. https://doi.org/10.1063/1.1726360.

(14) Chen, X.; Xu, W.; Song, H.; Chen, C.; Xia, H.; Zhu, Y.; Zhou, D.; Cui, S.; Dai, Q.; Zhang, J. Highly Efficient LiYF4:Yb3+, Er3+ Upconversion Single Crystal under Solar Cell Spectrum Excitation and Photovoltaic Application. *ACS Appl Mater Interfaces* **2016**, *8* (14), 9071–9079. https://doi.org/10.1021/acsami.5b12528.

(15) Aarts, L.; Van Der Ende, B. M.; Meijerink, A. Downconversion for Solar Cells in NaYF4:Er,Yb. *J Appl Phys* **2009**, *106* (2), 023522. https://doi.org/10.1063/1.3177257.

(16) Lee, S. H.; Bae, S.-R.; Choi, Y. G.; Chung, W. J. Eu2+/Eu3+-Doped Oxyfluoride Glass Ceramics with LaF3 for White LED Color Conversion. *Opt Mater (Amst)* **2015**, *41*, 71–74. https://doi.org/https://doi.org/10.1016/j.optmat.2014.10.018.

(17) Yan, R. X.; Li, Y. D. Down/Up Conversion in Ln3+-Doped YF3 Nanocrystals. *Adv Funct Mater* **2005**, *15* (5), 763–770. https://doi.org/https://doi.org/10.1002/adfm.200305044.

(18) Liu, X.; Li, Y.; Aidilibike, T.; Guo, J.; Di, W.; Qin, W. Pure Red Upconversion Emission from CaF2:Yb3+/Eu3+. *J Lumin* **2017**, *185*, 247–250. https://doi.org/10.1016/j.jlumin.2017.01.023.

(19) Bouffard, M.; Jouart, J. P.; Joubert, M.-F. Red-to-Blue up-Conversion Spectroscopy of Tm3+ in SrF2, CaF2, BaF2 and CdF2. *Opt Mater (Amst)* **2000**, *14* (1), 73–79. https://doi.org/https://doi.org/10.1016/S0925-3467(99)00110-X.

(20) Kuznetsov, S.; Ermakova, Y.; Voronov, V.; Fedorov, P.; Busko, D.; Howard, I. A.; Richards, B. S.; Turshatov, A. Up-Conversion Quantum Yields of SrF2:Yb3+,Er3+ Sub-Micron Particles Prepared by Precipitation from Aqueous Solution. *J Mater Chem C Mater* **2018**, *6* (3), 598–604. https://doi.org/10.1039/c7tc04913g.

(21) Wang, G.; Peng, Q.; Li, Y. Upconversion Luminescence of Monodisperse CaF2:Yb 3+/Er3+ Nanocrystals. *J Am Chem Soc* **2009**, *131* (40), 14200–14201. https://doi.org/10.1021/ja906732y.

(22) Lei, L.; Xie, B.; Li, Y.; Zhang, J.; Xu, S. Improvement of the Luminescent Intensity of Yb/Er: CaF2 Nanocrystals by Combining Na+-Doping and Active-Core/Active-Shell Structure. *J Lumin* **2017**, *190*, 462–467. https://doi.org/10.1016/j.jlumin.2017.05.084.

(23) Saleta Reig, D.; Grauel, B.; Konyushkin, V. A.; Nakladov, A. N.; Fedorov, P. P.; Busko, D.; Howard, I. A.; Richards, B. S.; Resch-Genger, U.; Kuznetsov, S. V.; Turshatov, A.; Würth, C. Upconversion Properties of SrF2:Yb3+,Er3+ Single Crystals. *J Mater Chem C Mater* **2020**, *8* (12), 4093–4101. https://doi.org/10.1039/c9tc06591a.

(24) Madirov, E. I.; Konyushkin, V. A.; Nakladov, A. N.; Fedorov, P. P.; Bergfeldt, T.; Busko, D.; Howard, I. A.; Richards, B. S.; Kuznetsov, S. V; Turshatov, A. An Up-Conversion Luminophore with High Quantum Yield and Brightness Based on BaF<inf>2</Inf>:Yb^{3+},Er^{3+}Single Crystals. *J Mater Chem C Mater* **2021**, *9* (10), 3493–3503.

(25) Zhang, P.; Yin, J.; Zhang, B.; Zhang, L.; Hong, J.; He, J.; Hang, Y. Intense 2.8\&\#x2009;\&\#x2009;\&\#x3BC;m Emission of Ho3$+$ Doped PbF2 Single Crystal. *Opt. Lett.* **2014**, *39* (13), 3942–3945. https://doi.org/10.1364/OL.39.003942.

(26) Rast, H. E.; Caspers, H. H.; Miller, S. A. Lattice Vibrations and Infrared Properties of Yttrium Fluoride. *Physical Review* **1969**, *180* (3), 890–895. https://doi.org/10.1103/PhysRev.180.890.

(27) Nizamutdinov, A. S.; Kuznetsov, S. V; Madirov, E. I.; Voronov, V. V; Khadiev, A. R.; Yapryntsev, A. D.; Ivanov, V. K.; Semashko, V. V; Fedorov, P. P. Down-Conversion Luminescence of Yb^{3+} in Novel Ba<inf>4</Inf>Y<inf>3</Inf>F<inf>17</Inf>:Yb:Ce Solid Solution by Excitation of Ce^{3+} in UV Spectral Range. *Opt Mater (Amst)* **2020**, *108*.

(28) Nizamutdinov, A. S.; Kuznetsov, S. V.; Konyushkin, V. A.; Nakladov, A. N.; Voronov, V. V.; Madirov, E. I.; Khadiev, A. R.; Gorieva, V. G.; Semashko, V. V. Down-Conversion Luminescence of Ce-Yb Ions in YF3. *Opt Mater (Amst)* **2019**, *95*, 109256. https://doi.org/10.1016/j.optmat.2019.109256.

(29) Tanner, P. A. Some Misconceptions Concerning the Electronic Spectra of Tri-Positive Europium and Cerium. *Chem Soc Rev* **2013**, *42* (12), 5090–5101. https://doi.org/10.1039/c3cs60033e.

(30) Ofelt, G. S. Intensities of Crystal Spectra of Rare-Earth Ions. *J Chem Phys* **2004**, *37* (3), 511–520. https://doi.org/10.1063/1.1701366.

(31) Judd, B. R. Optical Absorption Intensities of Rare-Earth Ions. *Physical Review* **1962**, *127* (3), 750–761. https://doi.org/10.1103/PhysRev.127.750.

(32) Luo, W.; Liao, J.; Li, R.; Chen, X. Determination of Judd–Ofelt Intensity Parameters from the Excitation Spectra for Rare-Earth Doped Luminescent Materials. *Physical Chemistry Chemical Physics* **2010**, *12* (13), 3276–3282. https://doi.org/10.1039/B921581F.

(33) Zhang, Y.; Chen, B.; Xu, S.; Li, X.; Zhang, J.; Sun, J.; Zhang, X.; Xia, H.; Hua, R. A Universal Approach for Calculating the Judd–Ofelt Parameters of RE 3+ in Powdered Phosphors and Its Application for the β-NaYF 4 :Er 3+ /Yb 3+ Phosphor Derived from Auto-Combustion-Assisted Fluoridation. *Physical Chemistry Chemical Physics* **2018**, *20* (23), 15876–15883. https://doi.org/10.1039/C8CP02317D.

(34) Egaña, A.; Tardío, M.; de la Torre-Gamarra, C.; Várez, A.; Cantelar, E.; Muñoz Santiuste, J. E. Spectroscopy and Judd-Ofelt Analysis of Er3+ Ions in Li5La3Nb2O12 Garnet-Type Ceramic Powder. *J Lumin* **2018**, *202*, 232–238. https://doi.org/10.1016/J.JLUMIN.2018.05.068.

(35) de Mello Donegá, C.; Meijerink, A.; Blasse, G. Saturation Effects in the Excitation Spectra of Rare-Earth Ions. *J Lumin* **1994**, *62* (5), 189–201. https://doi.org/10.1016/0022-2313(94)90029-9.

(36) Rabouw, F. T.; Prins, P. T.; Villanueva-Delgado, P.; Castelijns, M.; Geitenbeek, R. G.; Meijerink, A. Quenching Pathways in NaYF4:Er3+,Yb3+ Upconversion Nanocrystals. *ACS Nano* **2018**, *12* (5), 4812–4823. https://doi.org/10.1021/acsnano.8b01545.

(37) Van Pieterson, L.; Reid, M. F.; Burdick, G. W.; Meijerink, A. 4fn - 4f(n-1)5d Transitions of the Heavy Lanthanides: Experiment and Theory. *Phys Rev B Condens Matter Mater Phys* **2002**, *65* (4), 1–13. https://doi.org/10.1103/PhysRevB.65.045114.

(38) Bünzli, J. C. G. Lanthanide Luminescence: From a Mystery to Rationalization, Understanding, and Applications. *Handbook on the Physics and Chemistry of Rare Earths* **2016**, *50*, 141–176. https://doi.org/10.1016/bs.hpcre.2016.08.003.

(39) Weissman, S. I. Intramolecular Energy Transfer the Fluorescence of Complexes of Europium. *J Chem Phys* **1942**, *10* (4), 214–217. https://doi.org/10.1063/1.1723709.

(40) Förster, T. Zwischenmolekulare Energiewanderung Und Fluoreszenz. *Ann Phys* **1948**, *437* (1–2), 55–75. https://doi.org/10.1002/andp.19484370105.

(41) Dexter, D. L. A Theory of Sensitized Luminescence in Solids. *J. Chem. Phys* **1953**, *21* (1953), 836. https://doi.org/10.1063/1.1699044.

(42) Kunkely, H.; Vogler, A. Photolysis of Aqueous Europium(III) Azide Complexes: Formation of Europium(II) Induced by Ligand-to-Metal Charge Transfer Excitation. *Inorg Chem Commun* **2005**, *8* (1), 117–118. https://doi.org/10.1016/j.inoche.2004.10.024.

(43) Carlos, L. D.; Fernandes, J. A.; Sá Ferreira, R. A.; Malta, O. L.; Gonçalves, I. S.; Ribeiro-Claro, P. Emission Quantum Yield of a Europium(III) Tris-β-Diketonate Complex Bearing a 1,4-Diaza-1,3-Butadiene: Comparison with Theoretical Prediction. *Chem Phys Lett* **2005**, *413* (1–3), 22–24. https://doi.org/10.1016/j.cplett.2005.07.033.

(44) Bünzli, J. C. G.; Froidevaux, P.; Harrowfield, J. M. Photophysical Properties of Lanthanide Dinuclear Complexes with P-Tert-Butylcalix[8]Arene. *Inorg Chem* **1993**, *32* (15), 3306–3311. https://doi.org/10.1021/ic00067a019.

(45) Kano, T. Principal Phosphor Materials and Their Optical Properties: Luminescence Centers of Rare-Earth Ions. In *Fundamentals of Phosphors*; 2006; pp 181–204.

(46) D'Aléo, A.; Pointillart, F.; Ouahab, L.; Andraud, C.; Maury, O. Charge Transfer Excited States Sensitization of Lanthanide Emitting from the Visible to the Near-Infra-Red. *Coord Chem Rev* **2012**, *256* (15–16), 1604–1620. https://doi.org/10.1016/j.ccr.2012.03.023.

(47) Nakazawa, E. Charge-Transfer Type Luminescence of Yb3+ Ions in LuPO4 and YPO4. *Chem Phys Lett* **1978**, *56* (1), 161–163. https://doi.org/10.1016/0009-2614(78)80210-3.

(48) Nikl, M.; Yoshikawa, A.; Fukuda, T. Charge Transfer Luminescence in Yb3+-Containing Compounds. In *Optical Materials*; Elsevier, 2004; Vol. 26, pp 545–549. https://doi.org/10.1016/j.optmat.2004.05.002.

(49) Van Pieterson, L.; Meijerink, A. Charge Transfer Luminescence of Yb3+ in Orthophosphates. *J Alloys Compd* **2000**, *300*, 426–429. https://doi.org/10.1016/S0925-8388(99)00756-2.

(50) Van Pieterson, L.; Heeroma, M.; De Heer, E.; Meijerink, A. Charge Transfer Luminescence of Yb3+. *J Lumin* **2000**, *91* (3), 177–193. https://doi.org/10.1016/S0022-2313(00)00214-3.

(51) Etchart, I.; Huignard, A.; Bérard, M.; Nordin, M. N.; Hernández, I.; Curry, R. J.; Gillin, W. P.; Cheetham, A. K. Oxide Phosphors for Efficient Light Upconversion: Yb3+ and Er3+ Co-Doped Ln2BaZnO5 (Ln = Y, Gd). *J Mater Chem* **2010**, *20* (19), 3989–3994. https://doi.org/10.1039/c000127a.

(52) Auzel, F. Upconversion and Anti-Stokes Processes with f and d Ions in Solids. *Chem Rev* **2004**, *104* (1), 139–173. https://doi.org/10.1021/cr020357g.

(53) Bloembergen, N. Solid State Infrared Quantum Counters. *Phys Rev Lett* **1959**, *2* (3), 84–85. https://doi.org/10.1103/PhysRevLett.2.84.

(54) Moncorgé, R.; Benyattou, T. Excited-State Absorption of Ni2+ in MgF2 and MgO. *Phys Rev B* **1988**, *37* (16), 9186–9196. https://doi.org/10.1103/PhysRevB.37.9186.

(55) Wenger, O. S.; Güdel, H. U. Chemical Tuning of the Photon Upconversion Properties in Ti2+-Doped Chloride Host Lattices. *Inorg Chem* **2001**, *40* (23), 5747–5753. https://doi.org/10.1021/ic010255t.

(56) Wermuth, M.; Güdel, H. U. Photon Avalanche in Cs2ZrBr6:Os4+. *J Am Chem Soc* **1999**, *121* (43), 10102–10111. https://doi.org/10.1021/ja990847z.

(57) Gamelin, D. R.; Güdel, H. U. Excited-State Dynamics and Sequential Two-Photon Upconversion Excitation of Mo3+-Doped Chloro- and Bromo-Elpasolites. *Journal of Physical Chemistry B* **2000**, *104* (44), 10222–10234. https://doi.org/10.1021/jp002132k.

(58) Baluschev, S.; Yakutkin, V.; Wegner, G.; Minch, B.; Miteva, T.; Nelles, G.; Yasuda, A. Two Pathways for Photon Upconversion in Model Organic Compound Systems. *J Appl Phys* **2007**, *101* (2), 023101. https://doi.org/10.1063/1.2409618.

(59) Liu, Q.; Yin, B.; Yang, T.; Yang, Y.; Shen, Z.; Yao, P.; Li, F. A General Strategy for Biocompatible, High-Effective Upconversion Nanocapsules Based on Triplet-Triplet Annihilation. *J Am Chem Soc* **2013**, *135* (13), 5029–5037. https://doi.org/10.1021/ja3104268.

(60) Van Den Hoven, G. N.; Snoeks, E.; Polman, A.; Van Dam, C.; Van Uffelen, J. W. M.; Smit, M. K. Upconversion in Er-Implanted Al2O3 Waveguides. *J Appl Phys* **1996**, *79* (3), 1258–1266. https://doi.org/10.1063/1.361020.

(61) Barnes, N. P.; Walsh, B. M.; Filer, E. D. Ho:Ho Upconversion: Applications to Ho Lasers. *Journal of the Optical Society of America B* **2003**, *20* (6), 1212. https://doi.org/10.1364/josab.20.001212.

(62) Hebert, T.; Wannemacher, R.; MacFarlane, R. M.; Lenth, W. Blue Continuously Pumped Upconversion Lasing in Tm:YLiF4. *Appl Phys Lett* **1992**, *60* (21), 2592–2594. https://doi.org/10.1063/1.106919.

(63) Suyver, J. F.; Grimm, J.; Krämer, K. W.; Güdel, H. U. Highly Efficient Near-Infrared to Visible up-Conversion Process in NaYF4:Er3+,Yb3+. *J Lumin* **2005**, *114* (1), 53–59. https://doi.org/10.1016/j.jlumin.2004.11.012.

(64) Guo, H.; Qiao, Y. M. Preparation, Characterization, and Strong Upconversion of Monodisperse Y2O3:Er3+,Yb3+ Microspheres. *Opt Mater (Amst)* **2009**, *31* (4), 583–589. https://doi.org/10.1016/j.optmat.2008.06.011.

(65) Chen, X. P.; Zhang, W. J.; Zhang, Q. Y. Towards Efficient Upconversion and Downconversion of NaYF 4:Ho3,Yb3 Phosphors. *Physica B Condens Matter* **2011**, *406* (6–7), 1248–1252. https://doi.org/10.1016/j.physb.2011.01.008.

(66) Pandey, A.; Rai, V. K.; Dey, R.; Kumar, K. Enriched Green Upconversion Emission in Combustion Synthesized Y 2O3:Ho3+-Yb3+ Phosphor. *Mater Chem Phys* **2013**, *139* (2–3), 483–488. https://doi.org/10.1016/j.matchemphys.2013.01.043.

(67) Vetrone, F.; Mahalingam, V.; Capobianco, J. A. Near-Infrared-to-Blue Upconversion in Colloidal BaYF5:Tm 3+, Yb3+ Nanocrystals. *Chemistry of Materials* **2009**, *21* (9), 1847–1851. https://doi.org/10.1021/cm900313s.

(68) Oliveira, A. S.; De Araujo, M. T.; Gouveia-Neto, A. S.; Medeiros Neto, J. A.; Sombra, A. S. B.; Messaddeq, Y. Frequency Upconversion in Er3+/Yb3+-Codoped Chalcogenide Glass. *Appl Phys Lett* **1998**, *72* (7), 753–755. https://doi.org/10.1063/1.120884.

(69) Yeh, D. C.; Sibley, W. A.; Suscavage, M.; Drexhage, M. G. Multiphonon Relaxation and Infrared-to-Visible Conversion of Er 3+ and Yb3+ Ions in Barium-Thorium Fluoride Glass. *J Appl Phys* **1987**, *62* (1), 266–275. https://doi.org/10.1063/1.339139.

(70) Da Vila, L. D.; Gomes, L.; Tarelho, L. V. G.; Ribeiro, S. J. L.; Messadeq, Y. Mechanism of the Yb-Er Energy Transfer in Fluorozirconate Glass. *J Appl Phys* **2003**, *93* (7), 3873–3880. https://doi.org/10.1063/1.1555679.

(71) Xu, D.; Liu, C.; Yan, J.; Yang, S.; Zhang, Y. Understanding Energy Transfer Mechanisms for Tunable Emission of Yb3+-Er3+ Codoped GdF3 Nanoparticles: Concentration-Dependent Luminescence by near-Infrared and Violet Excitation. *Journal of Physical Chemistry C* **2015**, *119* (12), 6852–6860. https://doi.org/10.1021/acs.jpcc.5b00882.

(72) Yu, D.; Yu, T.; Wang, Y.; Zhang, Q.; Meijerink, A. Multiphoton Near-Infrared Quantum Splitting of Er3+. *Phys Rev Appl* **2020**, *13* (2), 024076. https://doi.org/10.1103/PhysRevApplied.13.024076.

(73) Fan, S.; Wang, S.; Sun, H.; Sun, S.; Gao, G.; Hu, L. Efficient Dual-Mode up-Conversion and down-Shifting Emission in β-$NaYF_4$:Yb^{3+},Er^{3+} Microcrystals via Ion Exchange. *Journal of the American Ceramic Society* **2017**, *100* (7), 3061–3069. https://doi.org/10.1111/jace.14872.

(74) Pollnau, M.; Gamelin, D.; Lüthi, S.; Güdel, H.; Hehlen, M. Power Dependence of Upconversion Luminescence in Lanthanide and Transition-Metal-Ion Systems. *Phys Rev B Condens Matter Mater Phys* **2000**, *61* (5), 3337–3346. https://doi.org/10.1103/PhysRevB.61.3337.

(75) Suyver, J. F.; Aebischer, A.; García-Revilla, S.; Gerner, P.; Güdel, H. U. Anomalous Power Dependence of Sensitized Upconversion Luminescence. *Phys Rev B Condens Matter Mater Phys* **2005**, *71* (12), 125123. https://doi.org/10.1103/PhysRevB.71.125123.

(76) Kaiser, M.; Würth, C.; Kraft, M.; Hyppänen, I.; Soukka, T.; Resch-Genger, U. Power-Dependent Upconversion Quantum Yield of NaYF4:Yb3+,Er3+ Nano- and Micrometer-Sized Particles-Measurements and Simulations. *Nanoscale* **2017**, *9* (28), 10051–10058. https://doi.org/10.1039/c7nr02449e.

(77) Pokhrel, M.; Kumar, G. A.; Sardar, D. K. Highly Efficient NIR to NIR and VIS Upconversion in Er3+ and Yb3+ Doped in M2O2S (M = Gd, La, Y). *J Mater Chem A Mater* **2013**, *1* (38), 11595–11606. https://doi.org/10.1039/c3ta12205k.

(78) Qiao, X.; Fan, X.; Wang, M.; Zhang, X. Spectroscopic Properties of Er3+-Yb3+ Co-Doped Glass Ceramics Containing BaF2 Nanocrystals. *J Non Cryst Solids* **2008**, *354* (28), 3273–3277. https://doi.org/10.1016/j.jnoncrysol.2008.02.014.

(79) Tikhomirov, V. K.; Rodríguez, V. D.; Méndez-Ramos, J.; Del-Castillo, J.; Kirilenko, D.; Van Tendeloo, G.; Moshchalkov, V. V. Optimizing Er/Yb Ratio and Content in ErYb Co-Doped Glass-Ceramics for Enhancement of the up- and down-Conversion Luminescence. *Solar Energy Materials and Solar Cells* **2012**, *100*, 209–215. https://doi.org/10.1016/j.solmat.2012.01.019.

(80) Burns, P. A.; Dawes, J. M.; Dekker, P.; Piper, J. A.; Jiang, H.; Wang, J. Optimization of Er, Yb:YCOB for CW Laser Operation. *IEEE J Quantum Electron* **2004**, *40* (11), 1575–1582. https://doi.org/10.1109/JQE.2004.834935.

(81) Hinojosa, S.; Meneses-Nava, M. A.; Barbosa-García, O.; Díaz-Torres, L. A.; Santoyo, M. A.; Mosiño, J. F. Energy Back Transfer, Migration and Energy Transfer (Yb-to-Er and Er-to-Yb) Processes in Yb,Er:YAG. In *Journal of Luminescence*; North-Holland, 2003; Vol. 102–103, pp 694–698. https://doi.org/10.1016/S0022-2313(02)00626-9.

(82) Kuleshov, N. V.; Lagatsky, A. A.; Shcherbitsky, V. G.; Mikhailov, V. P.; Heumann, E.; Jensen, T.; Diening, A.; Huber, G. CW Laser Performance of Yb and Er, Yb Doped Tungstates. *Appl Phys B* **1997**, *64* (4), 409–413. https://doi.org/10.1007/s003400050191.

(83) Richman, I. Longitudinal Optical Phonons in CaF2, SrF2, and BaF2. *J Chem Phys* **1964**, *41* (9), 2836–2837. https://doi.org/10.1063/1.1726360.

(84) Quintanilla, M.; Zhang, Y.; Liz-Marzán, L. M. Subtissue Plasmonic Heating Monitored with CaF2:Nd3+,Y3+ Nanothermometers in the Second Biological Window. *Chemistry of Materials* **2018**, *30* (8), 2819–2828. https://doi.org/10.1021/acs.chemmater.8b00806.

(85) Kaminskii, A. A.; Rhee, H.; Eichler, H. J.; Bohatý, L.; Becker, P.; Takaichi, K. Wide-Band Raman Stokes and Anti-Stokes Comb Lasing in a BaF_2 Single Crystal under Picosecond Pumping. *Laser Phys Lett* **2008**, *5* (4), 304–310. https://doi.org/10.1002/lapl.200710130.

(86) Wu, H.; Hao, Z.; Zhang, L.; Zhang, X.; Xiao, Y.; Pan, G. H.; Wu, H.; Luo, Y.; Zhao, H.; Zhang, J. Phonon Energy Dependent Energy Transfer Upconversion for the Red Emission in the Er3+/Yb3+ System. *Journal of Physical Chemistry C* **2018**, *122* (17), 9611–9618. https://doi.org/10.1021/acs.jpcc.8b02446.

(87) Liarokapis, E.; Anastassakis, E.; Kourouklis, G. A. Raman Study of Phonon Anharmonicity in LaF3. *Phys Rev B* **1985**, *32* (12), 8346–8355. https://doi.org/10.1103/PhysRevB.32.8346.

(88) Bitam, A.; Khiari, S.; Diaf, M.; Boubekri, H.; Boulma, E.; Bensalem, C.; Guerbous, L.; Jouart, J. P. Spectroscopic Investigation of Er3+ Doped BaF2 Single Crystal. *Opt Mater (Amst)* **2018**, *82*, 104–109. https://doi.org/10.1016/j.optmat.2018.05.034.

(89) Zhang, X.; Chen, Z.; Qiu, J. Mechanistic Investigation of Upconversion Luminescence in Er3+-Doped BaCl2, BaF2 and NaYF4 Phosphors. *Mater Chem Phys* **2015**, *162*, 76–81. https://doi.org/10.1016/j.matchemphys.2015.05.003.

(90) Nicoara, I.; Stef, M.; Buse, G.; Racu, A. Growth and Characterization of ErF3 Doped BaF2 Crystals. *J Cryst Growth* **2020**, *547*, 125817. https://doi.org/10.1016/j.jcrysgro.2020.125817.

(91) Sang, R.; Li, Y.; Ma, X.; Cui, Z.; Liu, Y. Synthesis and Optical Properties of Erbium-Doped BaF2 Nanoparticles. *Mater Chem Phys* **2014**, *143* (3), 1315–1318. https://doi.org/10.1016/j.matchemphys.2013.11.040.

(92) Miller, M. P.; Wright, J. C. Single Site Multiphonon and Energy Transfer Relaxation Phenomena in BaF2:Er3+. *J Chem Phys* **1977**, *68* (4), 1548–1562. https://doi.org/10.1063/1.435924.

(93) Wells, J. P. R.; Dean, T.; Reeves, R. J. Site Selective Spectroscopy of the C3v Symmetry Centre in Er3+ Doped BaF2. *J Lumin* **2002**, *96* (2–4), 239–248. https://doi.org/10.1016/S0022-2313(01)00230-7.

(94) Miller, M. P.; Wright, J. C. Importance of Defect Clustering in the Analysis of BaF2: Er3+ Optical Spectra. *Phys Rev B* **1978**, *18* (7), 3753–3756. https://doi.org/10.1103/PhysRevB.18.3753.

(95) Doualan, J. L.; Camy, P.; Benayad, A.; Von Edlinger, M.; Ménard, V.; Moncorgé, R. Spectroscopic and Laser Properties of Yb3+ Doped CaF2, SrF2 and BaF2 Laser Crystals. In *Advanced Solid-State Photonics, ASSP 2008*; Optical Society of America, 2008; p WE11. https://doi.org/10.1364/assp.2008.we11.

(96) Stef, M.; Nicoara, I.; Vizman, D. Distribution of Yb^{3+} and Yb^{2+} Ions along YbF_3 -Doped BaF_2 Crystals. *Crystal Research and Technology* **2018**, *53* (12), 1800186. https://doi.org/10.1002/crat.201800186.

(97) Dantelle, G.; Mortier, M.; Goldner, P.; Vivien, D. EPR and Optical Study of Yb3+-Doped β-PbF2 Single Crystals and Nanocrystals of Glass-Ceramics. *Journal of Physics: Condensed Matter* **2006**, *18* (34), 7905. https://doi.org/10.1088/0953-8984/18/34/005.

(98) Castiglione, M. J.; Madden, P. A. Fluoride Ion Disorder and Clustering in Superionic PbF2. *Journal of Physics: Condensed Matter* **2001**, *13* (44), 9963. https://doi.org/10.1088/0953-8984/13/44/311.

(99) Yang, F.; Wu, C.; Hao, X.; Chen, Y.; Lu, J.; Yang, S. E. Luminescence of Hydrothermally Fabricated PbF2:Er3+ Particles and Their Application in Bifacial Silicon Solar Cells. *Optica Applicata* **2014**, *Vol. 44* (nr 3), 463–473. https://doi.org/10.5277/OA140310.

(100) Dantelle, G.; Mortier, M.; Patriarche, G.; Vivien, D. Er3+-Doped PbF2: Comparison between Nanocrystals in Glass-Ceramics and Bulk Single Crystals. *J Solid State Chem* **2006**, *179* (7), 1995–2003. https://doi.org/10.1016/J.JSSC.2006.03.038.

(101) Gouveia-Neto, A. S.; Da Costa, E. B.; Bueno, L. A.; Ribeiro, S. J. L. Upconversion Luminescence in Transparent Glass Ceramics Containing β-PbF2 Nanocrystals Doped with Erbium. *J Alloys Compd* **2004**, *375* (1–2), 224–228. https://doi.org/10.1016/J.JALLCOM.2003.11.040.

(102) Labéguerie, J.; Dantelle, G.; Gredin, P.; Mortier, M. Luminescence Properties of PbF2:Yb–Er Nanoparticles Synthesized by Two Different Original Routes. *J Alloys Compd* **2008**, *451* (1), 563–566. https://doi.org/https://doi.org/10.1016/j.jallcom.2007.04.111.

(103) Tikhomirov, V. K.; Adamo, G.; Nikolaenko, A. E.; Rodriguez, V. D.; Gredin, P.; Mortier, M.; Zheludev, N. I.; Moshchalkov, V. V. Cathodo- and Photoluminescence in Yb3$+$-Er3$+$ Co-Doped PbF2 Nanoparticles. *Opt. Express* **2010**, *18* (9), 8836–8846. https://doi.org/10.1364/OE.18.008836.

(104) Richards, B. S. Luminescent Layers for Enhanced Silicon Solar Cell Performance: Down-Conversion. *Solar Energy Materials and Solar Cells* **2006**, *90* (9), 1189–1207. https://doi.org/https://doi.org/10.1016/j.solmat.2005.07.001.

(105) Berkowitz, J. K.; Olsen, J. A. Investigation of Luminescent Materials under Ultraviolet Excitation Energies from 5 to 25 EV. *J Lumin* **1991**, *50* (2), 111–121. https://doi.org/https://doi.org/10.1016/0022-2313(91)90025-Q.

(106) Benitez, E. L.; Husk, D. E.; Schnatterly, S. E.; Tarrio, C. A Surface Recombination Model Applied to Large Features in Inorganic Phosphor Efficiency Measurements in the Soft X-ray Region. *J Appl Phys* **1991**, *70* (6), 3256–3260. https://doi.org/10.1063/1.350331.

(107) Piper, W. W.; DeLuca, J. A.; Ham, F. S. Cascade Fluorescent Decay in Pr3+-Doped Fluorides: Achievement of a Quantum Yield Greater than Unity for Emission of Visible Light. *J Lumin* **1974**, *8* (4), 344–348. https://doi.org/10.1016/0022-2313(74)90007-6.

(108) Oskam, K. D.; Wegh, R. T.; Donker, H.; van Loef, E. V. D.; Meijerink, A. Downconversion: A New Route to Visible Quantum Cutting. *J Alloys Compd* **2000**, *300–301*, 421–425. https://doi.org/https://doi.org/10.1016/S0925-8388(99)00755-0.

(109) Wegh, R. T.; Donker, H.; van Loef, E. V. D.; Oskam, K. D.; Meijerink, A. Quantum Cutting through Downconversion in Rare-Earth Compounds. *J Lumin* **2000**, *87–89*, 1017–1019. https://doi.org/https://doi.org/10.1016/S0022-2313(99)00514-1.

(110) Richards, B. S. Luminescent Layers for Enhanced Silicon Solar Cell Performance: Down-Conversion. *Solar Energy Materials and Solar Cells* **2006**, *90* (9), 1189–1207. https://doi.org/https://doi.org/10.1016/j.solmat.2005.07.001.

(111) Dexter, D. L. Possibility of Luminescent Quantum Yields Greater than Unity. *Physical Review* **1957**, *108* (3), 630–633. https://doi.org/10.1103/PhysRev.108.630.

(112) Auzel, F. Upconversion and Anti-Stokes Processes with f and d Ions in Solids. *Chem Rev* **2004**, *104* (1), 139–174. https://doi.org/10.1021/cr020357g.

(113) Wegh, R. T.; van Loef, E. V. D.; Meijerink, A. Visible Quantum Cutting via Downconversion in LiGdF4:Er3+, Tb3+ upon Er3+ 4f11→4f105d Excitation. *J Lumin* **2000**, *90* (3), 111–122. https://doi.org/https://doi.org/10.1016/S0022-2313(99)00621-3.

(114) Eilers, J. J.; Biner, D.; van Wijngaarden, J. T.; Krämer, K.; Güdel, H.-U.; Meijerink, A. Efficient Visible to Infrared Quantum Cutting through Downconversion with the Er3+–Yb3+ Couple in Cs3Y2Br9. *Appl Phys Lett* **2010**, *96* (15), 151106. https://doi.org/10.1063/1.3377909.

(115) Ishii, A.; Miyasaka, T. Quantum Cutting-Induced near-Infrared Luminescence of Yb3+ and Er3+ in a Layer Structured Perovskite Film. *J Chem Phys* **2020**, *153* (19), 194704. https://doi.org/10.1063/5.0030596.

(116) Fan, B.; Chlique, C.; Merdrignac-Conanec, O.; Zhang, X.; Fan, X. Near-Infrared Quantum Cutting Material Er3+/Yb3+ Doped La2O2S with an External Quantum Yield Higher than 100%. *The Journal of Physical Chemistry C* **2012**, *116* (21), 11652–11657. https://doi.org/10.1021/jp3016744.

(117) Huang, X.; Chen, D.; Lin, L.; Wang, Z.; Feng, Z.; Zheng, Z. Infrared Quantum Cutting in Er3+:NaYF4 Nanostructured Glass Ceramics for Solar Cells. *Optik (Stuttg)* **2014**, *125* (1), 565–568. https://doi.org/https://doi.org/10.1016/j.ijleo.2013.07.024.

(118) Sobolev, B. P.; Tkachenko, N. L. Phase Diagrams of BaF2-(Y, Ln)F3 Systems. *Journal of The Less-Common Metals* **1982**, *85* (C), 155–170. https://doi.org/10.1016/0022-5088(82)90067-4.

(119) Kuznetsov, S. V.; Fedorov, P. P. Morphological Stability of Solid-Liquid Interface during Melt Crystallization of M 1-x R x F 2+x Solid Solutions. *Inorganic Materials* **2008**, *44* (13), 1434–1458. https://doi.org/10.1134/S0020168508130037.

(120) Wen, S.; Zhou, J.; Zheng, K.; Bednarkiewicz, A.; Liu, X.; Jin, D. Advances in Highly Doped Upconversion Nanoparticles. *Nat Commun* **2018**, *9* (1), 1–12. https://doi.org/10.1038/s41467-018-04813-5.

(121) Wen, S.; Zhou, J.; Zheng, K.; Bednarkiewicz, A.; Liu, X.; Jin, D. Advances in Highly Doped Upconversion Nanoparticles. *Nat Commun* **2018**, *9* (1), 1–12. https://doi.org/10.1038/s41467-018-04813-5.

(122) Buchinskaya, I. I.; Fedorov, P. P. Lead Difluoride and Related Systems. *Russ. Chem. Rev.* **2004**, *73* (4), 371–400. https://doi.org/10.1070/RC2004v073n04ABEH000811.

(123) De Mello, J. C.; Wittmann, H. F.; Friend, R. H. An Improved Experimental Determination of External Photoluminescence Quantum Efficiency. *Advanced Materials* **1997**, *9* (3), 230–232. https://doi.org/10.1002/adma.19970090308.

(124) Faulkner, D. O.; McDowell, J. J.; Price, A. J.; Perovic, D. D.; Kherani, N. P.; Ozin, G. A. Measurement of Absolute Photoluminescence Quantum Yields Using Integrating Spheres - Which Way to Go? *Laser Photon Rev* **2012**, *6* (6), 802–806. https://doi.org/10.1002/lpor.201200077.

(125) Carl, F.; Birk, L.; Grauel, B.; Pons, M.; Würth, C.; Resch-Genger, U.; Haase, M. LiYF4:Yb/LiYF4 and LiYF4:Yb,Er/LiYF4 Core/Shell Nanocrystals with Luminescence Decay Times Similar to YLF Laser Crystals and the Upconversion Quantum Yield of the Yb,Er Doped Nanocrystals. *Nano Res* **2021**, *14* (3), 797–806. https://doi.org/10.1007/s12274-020-3116-y.

(126) Joseph, R. E.; Busko, D.; Hudry, D.; Gao, G.; Biner, D.; Krämer, K.; Turshatov, A.; Richards, B. S.; Howard, I. A. A Method for Correcting the Excitation Power Density Dependence of Upconversion Emission Due to Laser-Induced Heating. *Opt Mater (Amst)* **2018**, *82*, 65–70. https://doi.org/10.1016/j.optmat.2018.05.025.

(127) Yasyrkina, D. S.; Kuznetsov, S. V.; Ryabova, A. V.; Pominova, D. V.; Voronov, V. V.; Ermakov, R. P.; Fedorov, P. P. Dependence of Quantum Yield of Up-Conversion Luminescence on the Composition of Fluorite-Type Solid Solution NaY1-x-YYbxEryF4. *NANOSYSTEMS: PHYSICS, CHEMISTRY, MATHEMATICS* **2013**, *4* (5), 648–656. https://doi.org/10.1515/plm-2013-0013.

(128) Madirov, E.; Konyushkin, V. A.; Nakladov, A.; Fedorov, P. P.; Bergfeldt, T.; Busko, D.; Howard, I. A.; Richards, B. S.; Kuznetsov, S.; Turshatov, A. Up-Conversion Luminophore with High Quantum Yield and Brightness Based on BaF 2 :Yb 3+ ,Er 3+ Single Crystals . *J Mater Chem C Mater* **2021**. https://doi.org/10.1039/d1tc00104c.

(129) Singh, R.; Madirov, E.; Busko, D.; Hossain, I. M.; Konyushkin, V. A.; Nakladov, A. N.; Kuznetsov, S. V.; Farooq, A.; Gharibzadeh, S.; Paetzold, U. W.; Richards, B. S.; Turshatov, A. Harvesting Sub-Bandgap Photons via Upconversion for Perovskite Solar Cells. *ACS Appl Mater Interfaces* **2021**, *13* (46), 54874–54883. https://doi.org/10.1021/ACSAMI.1C13477/SUPPL_FILE/AM1C13477_SI_001.PDF.

(130) Shannon, R. D.; Prewitt, C. T. Effective Ionic Radii in Oxides and Fluorides. *Acta Crystallogr B* **1969**, *25* (5), 925–946. https://doi.org/10.1107/s0567740869003220.

(131) Anderson, A.; Cleveland, F. F. The Raman Effect, Vol. 2: Applications . *Phys Today* **1974**, *27* (2), 54–55. https://doi.org/10.1063/1.3128450.

(132) Mead, D. G.; Wilkinson, G. R. The Temperature Dependence of the Raman Spectra of Some Alkaline Earth Crystals with the Fluorite Structure. *Journal of Physics C: Solid State Physics* **1977**, *10* (7), 1063–1072. https://doi.org/10.1088/0022-3719/10/7/016.

(133) Guo, H.; Qiao, Y. M. Preparation, Characterization, and Strong Upconversion of Monodisperse Y2O3:Er3+,Yb3+ Microspheres. *Opt Mater (Amst)* **2009**, *31* (4), 583–589. https://doi.org/10.1016/j.optmat.2008.06.011.

(134) Suyver, J. F.; Grimm, J.; Krämer, K. W.; Güdel, H. U. Highly Efficient Near-Infrared to Visible up-Conversion Process in NaYF4:Er3+,Yb3+. *J Lumin* **2005**, *114* (1), 53–59. https://doi.org/10.1016/j.jlumin.2004.11.012.

(135) Labbe, C.; Doualan, J. L.; Camy, P.; Moncorgé, R.; Thuau, M. The 2.8 Mm Laser Properties of Er3+ Doped CaF2 Crystals. *Opt Commun* **2002**, *209* (1–3), 193–199. https://doi.org/10.1016/S0030-4018(02)01628-0.

(136) Piao, R.; Wang, Y.; Zhang, Z.; Zhang, C.; Yang, X.; Zhang, D. Optical and Judd-Ofelt Spectroscopic Study of Er^{3+} -doped Strontium Gadolinium Gallium Garnet Single-crystal. *Journal of the American Ceramic Society* **2018**, *102* (3), jace.16114. https://doi.org/10.1111/jace.16114.

(137) Auzel, F.; Lipinska-Kalita, K. E.; Santa-Cruz, P. A New Er3+-Doped Vitreous Fluoride Amplification Medium with Crystal-like Cross-Sections and Reduced Inhomogeneous Line Width. *Opt Mater (Amst)* **1996**, *5* (1–2), 75–78. https://doi.org/10.1016/0925-3467(95)00055-0.

(138) Boccolini, A.; Marques-Hueso, J.; Chen, D.; Wang, Y.; Richards, B. S. Physical Performance Limitations of Luminescent Down-Conversion Layers for Photovoltaic Applications. *Solar Energy Materials and Solar Cells* **2014**, *122*, 8–14. https://doi.org/10.1016/j.solmat.2013.11.005.

(139) Berry, M. T.; May, P. S. Disputed Mechanism for NIR-to-Red Upconversion Luminescence in NaYF4:Yb3+,Er3+. *Journal of Physical Chemistry A* **2015**, *119* (38), 9805–9811. https://doi.org/10.1021/acs.jpca.5b08324.

(140) Macdougall, S. K. W.; Ivaturi, A.; Marques-Hueso, J.; Krämer, K. W.; Richards, B. S. Broadband Photoluminescent Quantum Yield Optimisation of Er 3+-Doped β-NaYF4 for Upconversion in Silicon Solar Cells. *Solar Energy Materials and Solar Cells* **2014**, *128*, 18–26. https://doi.org/10.1016/j.solmat.2014.05.004.

(141) Siaï, A.; Haro-González, P.; Horchani Naifer, K.; Férid, M. Optical Temperature Sensing of Er3+/Yb3+ Doped LaGdO3 Based on Fluorescence Intensity Ratio and Lifetime Thermometry. *Opt Mater (Amst)* **2018**, *76*, 34–41. https://doi.org/10.1016/j.optmat.2017.12.018.

(142) Wong, K. L.; Bünzli, J. C. G.; Tanner, P. A. Quantum Yield and Brightness. *Journal of Luminescence*. Elsevier B.V. August 1, 2020, p 117256. https://doi.org/10.1016/j.jlumin.2020.117256.

(143) Lakowicz, J. R. *Principles of Fluorescence Spectroscopy*; Springer, 2006. https://doi.org/10.1007/978-0-387-46312-4.

(144) Dong, J.; Bass, M.; Mao, Y.; Deng, P.; Gan, F. Dependence of the Yb^3+ Emission Cross Section and Lifetime on Temperature and Concentration in Yttrium Aluminum Garnet. *Journal of the Optical Society of America B* **2003**, *20* (9), 1975. https://doi.org/10.1364/josab.20.001975.

(145) Hehlen, M. P.; Brik, M. G.; Krämer, K. W. 50th Anniversary of the Judd-Ofelt Theory: An Experimentalist's View of the Formalism and Its Application. *J Lumin* **2013**, *136*, 221–239. https://doi.org/10.1016/j.jlumin.2012.10.035.

(146) C, A. L.; Camarillo, I.; Camarillo, E.; Ramos, F.; Flores, M.; Caldiño, U. Spectroscopic Characterization of Er^{3+} Transitions in $Bi_4Si_3O_{12}$. *Journal of Physics: Condensed Matter* **2004**, *16* (32), 5925–5936. https://doi.org/10.1088/0953-8984/16/32/025.

(147) Ebendorff-Heidepriem, H.; Ehrt, D. Tb3+ F-d Absorption as Indicator of the Effect of Covalency on the Judd-Ofelt Ω2 Parameter in Glasses. *J Non Cryst Solids* **1999**, *248* (2), 247–252. https://doi.org/10.1016/S0022-3093(99)00243-4.

(148) Lachheb, R.; Herrmann, A.; Assadi, A. A.; Reiter, J.; Körner, J.; Hein, J.; Rüssel, C.; Maâlej, R.; Damak, K. Judd–Ofelt Analysis and Experimental Spectroscopic Study of Erbium Doped Phosphate Glasses. *J Lumin* **2018**, *201*, 245–254. https://doi.org/10.1016/j.jlumin.2018.03.087.

(149) Hashim, S.; Ghoshal, S. K.; Abdullahi, I. On the Lasing Potency of Samarium-Activated BaSO4–TeO2–B2O3 Glass Host: Judd–Ofelt Analysis. *Indian Journal of Physics* **2020**, *94* (11), 1811–1820. https://doi.org/10.1007/s12648-019-01631-3.

(150) Lei, Y.; Song, H.; Yang, L.; Yu, L.; Liu, Z.; Pan, G.; Bai, X.; Fan, L. Upconversion Luminescence, Intensity Saturation Effect, and Thermal Effect in Gd 2 O 3: Er 3, Yb 3+ Nanowires. *Journal of Chemical Physics* **2005**, *123* (17), 174710. https://doi.org/10.1063/1.2087487.

(151) Han, Y.; Li, H.; Wang, Y.; Pan, Y.; Huang, L.; Song, F.; Huang, W. Upconversion Modulation through Pulsed Laser Excitation for Anti-Counterfeiting. *Sci Rep* **2017**, *7* (1), 1–8. https://doi.org/10.1038/s41598-017-01611-9.

(152) Yu, D.-C.; Martín-Rodríguez, R.; Zhang, Q.-Y.; Meijerink, A.; Rabouw, F. T. Multi-Photon Quantum Cutting in Gd2O2S:Tm3+ to Enhance the Photo-Response of Solar Cells. *Light Sci Appl* **2015**, *4* (10), e344–e344. https://doi.org/10.1038/lsa.2015.117.

(153) Orlovskii, Y. V; Pukhov, K. K.; Basiev, T. T.; Tsuboi, T. Nonlinear Mechanism of Multiphonon Relaxation of the Energy of Electronic Excitation in Optical Crystals Doped with Rare-Earth Ions. *Opt Mater (Amst)* **1995**, *4* (5), 583–595. https://doi.org/https://doi.org/10.1016/0925-3467(95)00012-7.

(154) Madirov, E.; Busko, D.; Howard, I. A.; Richards, B. S.; Turshatov, A. Absolute Quantum Yield for Understanding Upconversion and Downshift Luminescence in PbF2:Er3+,Yb3+ Crystals. *Phys. Chem. Chem. Phys.* **2023**, *25* (17), 11986–11997. https://doi.org/10.1039/D3CP00936J.

(155) Sardar, D. K.; Bradley, W. M.; Perez, J. J.; Gruber, J. B.; Zandi, B.; Hutchinson, J. A.; Trussell, C. W.; Kokta, M. R. Judd–Ofelt Analysis of the Er3+ (4f11) Absorption Intensities in Er3+−doped Garnets. *J Appl Phys* **2003**, *93* (5), 2602–2607. https://doi.org/10.1063/1.1543242.

(156) Bergstrand, J.; Liu, Q.; Huang, B.; Peng, X.; Würth, C.; Resch-Genger, U.; Zhan, Q.; Widengren, J.; Ågren, H.; Liu, H. On the Decay Time of Upconversion Luminescence. *Nanoscale* **2019**, *11* (11), 4959–4969. https://doi.org/10.1039/c8nr10332a.

(157) Carnall, W. T.; Crosswhite, H.; Crosswhite, H. M. *Energy Level Structure and Transition Probabilities in the Spectra of the Trivalent Lanthanides in LaF_3*; Argonne, IL (United States), 1978; Vol. 1. https://doi.org/10.2172/6417825.

(158) Dodge, M. J.; Malitson, I. H.; Mahan, A. I. A Special Method for Precise Refractive Index Measurement of Uniaxial Optical Media. *Appl. Opt.* **1969**, *8* (8), 1703–1705. https://doi.org/10.1364/AO.8.001703.

(159) Baride, A.; May, P. S.; Berry, M. T. Cross-Relaxation from Er3+(2H11/24S3/2) and Er3+(2H9/2) in β-NaYF4:Yb,Er and Implications for Modeling Upconversion Dynamics. *Journal of Physical Chemistry C* **2020**, *124* (3), 2193–2201. https://doi.org/10.1021/acs.jpcc.9b10163.

(160) Ma, F.; Su, F.; Zhou, R.; Ou, Y.; Xie, L.; Liu, C.; Jiang, D.; Zhang, Z.; Wu, Q.; Su, L.; Liang, H. The Defect Aggregation of RE3+ (RE = Y, La ∼ Lu) in MF2 (M = Ca, Sr, Ba) Fluorites. *Mater Res Bull* **2020**, *125*, 110788. https://doi.org/https://doi.org/10.1016/j.materresbull.2020.110788.

(161) Chernov, S. V; Gunβer, W.; Murin, I. V. On Rare-Earth Clustering in Flourite Type Solid Solutions MF2□REF3. *Solid State Ion* **1991**, *47* (1), 67–70. https://doi.org/https://doi.org/10.1016/0167-2738(91)90181-A.

(162) Wilson, L. R.; Richards, B. S. Measurement Method for Photoluminescent Quantum Yields of Fluorescent Organic Dyes in Polymethyl Methacrylate for Luminescent Solar Concentrators. *Appl. Opt.* **2009**, *48* (2), 212–220. https://doi.org/10.1364/AO.48.000212.

(163) Ebendorff-Heidepriem, H.; Ehrt, D.; Bettinelli, M.; Speghini, A. Effect of Glass Composition on Judd–Ofelt Parameters and Radiative Decay Rates of Er3+ in Fluoride Phosphate and Phosphate Glasses. *J Non Cryst Solids* **1998**, *240* (1), 66–78. https://doi.org/https://doi.org/10.1016/S0022-3093(98)00706-6.

(164) Yao, G.; Lin, C.; Meng, Q.; Stanley May, P.; Berry, M. T. Calculation of Judd-Ofelt Parameters for Er3+ in β-NaYF4: Yb3+, Er3+ from Emission Intensity Ratios and Diffuse Reflectance Spectra. *J Lumin* **2015**, *160*, 276–281. https://doi.org/10.1016/j.jlumin.2014.12.025.

(165) Cantelar, E.; Marin-Dobrincic, M.; Jardiel, T.; Caballero, A. C.; Cussó, F. Judd–Ofelt Analysis of Powder Samples: LiNbO3:Er3+ Submicron-Sized Particles as a Model Case. *Opt Mater (Amst)* **2015**, *41*, 122–125. https://doi.org/https://doi.org/10.1016/j.optmat.2014.10.025.

(166) Cormier, J.-F.; Fortin, M.; Frechette, J.; Noiseux, I.; Vernon, M. L.; Long, W. The Effects of Self-Absorption and Detection Geometry on Fluorescence Intensity and Decay Lifetime. In *Optical Diagnostics and Sensing V*; Priezzhev, A. V, Cote, G. L., Eds.; SPIE, 2005; Vol. 5702, pp 123–134. https://doi.org/10.1117/12.591026.

(167) Madirov, E.; Busko, D.; Cardona, F. A.; Hudry, D.; Kuznetsov, S. V; Konyushkin, V. A.; Nakladov, A. N.; Alexandrov, A. A.; Howard, I. A.; Richards, B. S.; Turshatov, A. Comparison of Quantum Yield of Upconversion Nanocrystals Determined by Absolute and Relative Methods. *Adv Photonics Res* **2023**, *4* (2), 2200187. https://doi.org/https://doi.org/10.1002/adpr.202200187.

(168) Gao, G.; Busko, D.; Katumo, N.; Joseph, R.; Madirov, E.; Turshatov, A.; Howard, I. A.; Richards, B. S. Ratiometric Luminescent Thermometry with Excellent Sensitivity over a Broad Temperature Range Utilizing Thermally-Assisted and Multiphoton Upconversion in Triply-Doped La<inf>2</Inf>O<inf>3</Inf>:Yb^{3+}/Er^{3+}/Nd^{3+}. *Adv Opt Mater* **2021**, *9* (5).

(169) Saleta Reig, D.; Grauel, B.; Konyushkin, V. A.; Nakladov, A. N.; Fedorov, P. P.; Busko, D.; Howard, I. A.; Richards, B. S.; Resch-Genger, U.; Kuznetsov, S. V.; Turshatov, A.; Würth, C. Upconversion Properties of SrF2:Yb3+,Er3+ Single Crystals. *J Mater Chem C Mater* **2020**, *8* (12), 4093–4101. https://doi.org/10.1039/c9tc06591a.

(170) Joseph, R. E.; Jiménez, C.; Hudry, D.; Gao, G.; Busko, D.; Biner, D.; Turshatov, A.; Krämer, K.; Richards, B. S.; Howard, I. A. Critical Power Density: A Metric to Compare the Excitation Power Density Dependence of Photon Upconversion in Different Inorganic Host Materials. *Journal of Physical Chemistry A* **2019**, *123* (31), 6799–6811. https://doi.org/10.1021/acs.jpca.9b03851.

(171) Hossan, M. Y.; Hor, A.; Luu, Q.; Smith, S. J.; May, P. S.; Berry, M. T. Explaining the Nanoscale Effect in the Upconversion Dynamics of β-NaYF4:Yb3+, Er3+ Core and Core–Shell Nanocrystals. *The Journal of Physical Chemistry C* **2017**, *121* (30), 16592–16606. https://doi.org/10.1021/acs.jpcc.7b04567.

(172) Nizamutdinov, A. S.; Kuznetsov, S. V.; Konyushkin, V. A.; Nakladov, A. N.; Voronov, V. V.; Madirov, E. I.; Khadiev, A. R.; Gorieva, V. G.; Semashko, V. V. Down-Conversion Luminescence of Ce-Yb Ions in YF3. *Opt Mater (Amst)* **2019**, *95*, 109256. https://doi.org/10.1016/j.optmat.2019.109256.

(173) Sobolev, B. P.; Garashina, L. S.; Federov, P. P.; Tkachenko, N. L.; Seiranyan, K. B. Polymorphism and Crystallographic Properties of Yttrium and Rare-Earth Trifluorides. *Soviet Physics – Crystallography Reports* **1974**, *18* (4), 473–476.

(174) Sobolev, B. P.; Fedorov, P. P. Hexagonal YF3 Structure Type and High-Temperature Modifications of Rare-Earth Trifluorides Isostructural with YF3. *Sov Phys Crystallogr* **1973**, *18* (3), 392.

(175) Dorenbos, P. 5d-Level Energies of Ce3+ and the Crystalline Environment. IV. Aluminates and "Simple" Oxides. *J Lumin* **2002**, *99* (3), 283–299. https://doi.org/10.1016/S0022-2313(02)00347-2.

(176) Wang, X.; Sheng, T.; Fu, Z.; Li, W.; Jeong, J. H. Highly Uniform YF3:Ln3+ (Ln = Ce3+, Tb3+) Walnut-like Microcrystals: Hydrothermal Synthesis and Luminescent Properties. *Mater Res Bull* **2013**, *48* (6), 2143–2148. https://doi.org/10.1016/J.MATERRESBULL.2013.02.029.

(177) Stręk, W.; Bednarkiewicz, A.; Dereń, P. J. Power Dependence of Luminescence of Tb3+-Doped KYb(WO4)2 Crystal. *J Lumin* **2001**, *92* (3), 229–235. https://doi.org/10.1016/S0022-2313(00)00263-5.

(178) Pollnau, M.; Gamelin, D. R.; Lüthi, S. R.; Güdel, H. U.; Hehlen, M. P. Power Dependence of Upconversion Luminescence in Lanthanide and Transition-Metal-Ion Systems. *Phys Rev B* **2000**, *61* (5), 3337–3346. https://doi.org/10.1103/PhysRevB.61.3337.

(179) Lim, K.-S.; Hamilton, D. S. UV-Induced Loss Mechanisms in a Ce3+:YLiF4 Laser. *J Lumin* **1988**, *40–41*, 319–320. https://doi.org/10.1016/0022-2313(88)90212-8.

(180) Lim, K.-S.; Hamilton, D. S. UV-Induced Loss Mechanisms in a Ce3+:YLiF4 Laser. *J Lumin* **1988**, *40–41*, 319–320. https://doi.org/10.1016/0022-2313(88)90212-8.

(181) Semashko, V. V.; Dubinskii, M. A.; Abdulsabirov, R. Y.; Korableva, S. L.; Naumov, A. K.; Nizamutdinov, A. S.; Zhuchkov, M. S. Photodynamic Nonlinear Processes in UV Solid-State Active Media and Approaches to Improving Material Laser Performance; Kaplyanskii, A. A., Malkin, B. Z., Nikitin, S. I., Eds.; International Society for Optics and Photonics, 2002; Vol. 4766, p 119. https://doi.org/10.1117/12.475323.

(182) Semashko, V. V. Problems in Searching for New Solid-State UV- and VUV-Active Media: The Role of Photodynamic Processes. *Physics of the Solid State* **2005**, *47* (8), 1507. https://doi.org/10.1134/1.2014502.

(183) You, F.; Bos, A. J. J.; Shi, Q.; Huang, S.; Dorenbos, P. Electron Transfer Process between Ce^{3+} Donor and Yb^{3+} Acceptor Levels in the Bandgap of $Y_3Al_5O_{12}$ (YAG). *Journal of Physics: Condensed Matter* **2011**, *23* (21), 215502. https://doi.org/10.1088/0953-8984/23/21/215502.

(184) Laroche, M.; Girard, S.; Moncorgé, R.; Bettinelli, M.; Abdulsabirov, R.; Semashko, V. Beneficial Effect of Lu3+ and Yb3+ Ions in UV Laser Materials. *Opt Mater (Amst)* **2003**, *22* (2), 147–154. https://doi.org/10.1016/S0925-3467(02)00358-0.

(185) Nizamutdinov, A. S.; Semashko, V. V.; Naumov, A. K.; Abdulsabirov, R. Yu.; Korableva, S. L.; Marisov, M. A. Photodynamic Processes in CaF[Sub 2] Crystals Activated by Ce[Sup 3+] and Yb[Sup 3+] Ions. *Physics of the Solid State* **2005**, *47* (8), 1457. https://doi.org/10.1134/1.2014489.

(186) Nizamutdinov, A. S.; Marisov, M. A.; Semashko, V. V.; Naumov, A. K.; Korableva, S. L.; Abdulsabirov, R. Yu. Spectral Kinetics of Ce 3+ Ions in Double-Fluoride Crystals with a Scheelite Structure. *Physics of the Solid State* **2005**, *47* (8), 1460. https://doi.org/10.1134/1.2014490.

(187) Dorenbos, P. The Hole Picture as Alternative for the Common Electron Picture to Describe Hole Trapping and Luminescence Quenching. *J Lumin* **2018**, *197*, 62–65. https://doi.org/10.1016/J.JLUMIN.2018.01.013.

(188) Semashko V; Dubinskii M; Abdulsabirov R; Naumov A; Korableva S. Anti-Solarant Co-Doping of Ce-Activated Tunable UV Laser Materials and Their Laser Performance. In *V, Proceedings of the International Conference on LASERS 2000*; 2001; pp xi–xii.

(189) Semashko V; Dubinskii M; Abdulsabirov R; Naumov A; Korableva S. Anti-Solarant Co-Doping of Ce-Activated Tunable UV Laser Materials and Their Laser Performance. In *V, Proceedings of the International Conference on LASERS 2000*; 2001; pp xi–xii.

(190) Semashko, V. V. Problems in Searching for New Solid-State UV- and VUV-Active Media: The Role of Photodynamic Processes. *Physics of the Solid State* **2005**, *47* (8), 1507. https://doi.org/10.1134/1.2014502.

(191) Yu, D. C.; Rabouw, F. T.; Boon, W. Q.; Kieboom, T.; Ye, S.; Zhang, Q. Y.; Meijerink, A. Insights into the Energy Transfer Mechanism in Ce 3 + − Yb 3 + Codoped YAG Phosphors. *Phys Rev B* **2014**, *90* (16), 165126. https://doi.org/10.1103/PhysRevB.90.165126.

(192) Verweij, J. W. M.; Pédrini, C.; Bouttet, D.; Dujardin, C.; Lautesse, H.; Moine, B. Fluorescence of Ce3+ in LiREF4 (RE Gd, Yb). *Opt Mater (Amst)* **1995**, *4* (5), 575–582. https://doi.org/10.1016/0925-3467(95)00011-9.

(193) van der Kolk, E.; Ten Kate, O. M.; Wiegman, J. W.; Biner, D.; Krämer, K. W. Enhanced 1G4 Emission in NaLaF4: Pr3+, Yb3+ and Charge Transfer in NaLaF4: Ce3+, Yb3+ Studied by Fourier Transform Luminescence Spectroscopy. *Opt Mater (Amst)* **2011**, *33* (7), 1024–1027. https://doi.org/10.1016/J.OPTMAT.2010.08.010.

(194) Combes, C. M.; Dorenbos, P.; Van Eijk, C. W. E.; Pedrini, C.; Den Hartog, H. W.; Gesland, J. Y.; Rodnyi, P. A. Optical and Scintillation Properties of Ce3+ Doped LiYF4 and LiLuF4 Crystals. *J Lumin* **1997**, *71* (1), 65–70. https://doi.org/10.1016/S0022-2313(96)00118-4.

(195) Nizamutdinov, A. S.; Marisov, M. A.; Semashko, V. V.; Naumov, A. K.; Korableva, S. L.; Abdulsabirov, R. Yu. Spectral Kinetics of Ce 3+ Ions in Double-Fluoride Crystals with a Scheelite Structure. *Physics of the Solid State* **2005**, *47* (8), 1460. https://doi.org/10.1134/1.2014490.

(196) Sato, H.; Machida, H.; Shimamura, K.; Bensalah, A.; Satonaga, T.; Fukuda, T.; Mihokova, E.; Dusek, M.; Nikl, M.; Vedda, A. Color Centers in LiCaAlF6 Single Crystals and Their Suppression by Doping. *J Appl Phys* **2002**, *91* (9), 5666. https://doi.org/10.1063/1.1466525.

(197) Madirov, E.; Busko, D.; Cardona, F. A.; Hudry, D.; Kuznetsov, S. V; Konyushkin, V. A.; Nakladov, A. N.; Alexandrov, A. A.; Howard, I. A.; Richards, B. S.; Turshatov, A. Comparison of Quantum Yield of Upconversion Nanocrystals Determined by Absolute and Relative Methods. *Adv Photonics Res* **2023**, *4* (2), 2200187. https://doi.org/https://doi.org/10.1002/adpr.202200187.

(198) Saleta Reig, D.; Grauel, B.; Konyushkin, V. A.; Nakladov, A. N.; Fedorov, P. P.; Busko, D.; Howard, I. A.; Richards, B. S.; Resch-Genger, U.; Kuznetsov, S. V.; Turshatov, A.; Würth, C. Upconversion Properties of SrF2:Yb3+,Er3+ Single Crystals. *J Mater Chem C Mater* **2020**, *8* (12), 4093–4101. https://doi.org/10.1039/c9tc06591a.

(199) Kuznetsov, S.; Ermakova, Yu.; Voronov, V.; Fedorov, P.; Busko, D.; Howard, I. A.; Richards, B. S.; Turshatov, A. Up-Conversion Quantum Yields of SrF2:Yb3+,Er3+ Sub-Micron Particles Prepared by Precipitation from Aqueous Solution. *J Mater Chem C Mater* **2018**, *6* (3), 598–604. https://doi.org/10.1039/C7TC04913G.

(200) Arteaga Cardona, F.; Jain, N.; Popescu, R.; Busko, D.; Madirov, E.; Arús, B. A.; Gerthsen, D.; De Backer, A.; Bals, S.; Bruns, O. T.; Chmyrov, A.; Van Aert, S.; Richards, B. S.; Hudry, D. Preventing Cation Intermixing Enables 50% Quantum Yield in Sub-15 Nm Short-Wave Infrared-Emitting Rare-Earth Based Core-Shell Nanocrystals. *Nat Commun* **2023**, *14* (1), 4462. https://doi.org/10.1038/s41467-023-40031-4.

(201) Giessen, H.; Kedenburg, S.; Vieweg, M.; Gissibl, T. Linear Refractive Index and Absorption Measurements of Nonlinear Optical Liquids in the Visible and Near-Infrared Spectral Region. *Optical Materials Express, Vol. 2, Issue 11, pp. 1588-1611* **2012**, *2* (11), 1588–1611. https://doi.org/10.1364/OME.2.001588.

(202) Moore, H. H. Refractive Index of Alkaline Earth Halides and Its Wavelength and Temperature Derivatives. *J Phys Chem Ref Data* **1980**, *9* (1), 161–290. https://doi.org/10.1063/1.555616.

(203) Sooväli, L.; Rõõm, E. I.; Kütt, A.; Kaljurand, I.; Leito, I. Uncertainty Sources in UV-Vis Spectrophotometric Measurement. *Accreditation and Quality Assurance* **2006**, *11* (5), 246–255. https://doi.org/10.1007/S00769-006-0124-X/FIGURES/4.

(204) Bonnet, C. S.; Devocelle, M.; Gunnlaugsson, T. Luminescent Lanthanide-Binding Peptides: Sensitising the Excited States of Eu(Iii) and Tb(Iii) with a 1,8-Naphthalimide-Based Antenna. *Org. Biomol. Chem.* **2012**, *10* (1), 126–133. https://doi.org/10.1039/C1OB06567J.

(205) Merrifield, R. B. Solid Phase Peptide Synthesis. I. The Synthesis of a Tetrapeptide. *J Am Chem Soc* **1963**, *85* (14), 2149–2154. https://doi.org/10.1021/ja00897a025.

(206) Dikmans, A.; Beutling, U.; Schmeisser, E.; Thiele, S.; Frank, R. SC2: A Novel Process for Manufacturing Multipurpose High-Density Chemical Microarrays. *QSAR Comb Sci* **2006**, *25* (11), 1069–1080. https://doi.org/https://doi.org/10.1002/qsar.200640130.

(207) Fodor, S. P. A.; Read, J. L.; Pirrung, M. C.; Stryer, L.; Lu, A. T.; Solas, D. Light-Directed, Spatially Addressable Parallel Chemical Synthesis. *Science (1979)* **1991**, *251* (4995), 767–773. https://doi.org/10.1126/science.1990438.

(208) Stadler, V.; Felgenhauer, T.; Beyer, M.; Fernandez, S.; Leibe, K.; Güttler, S.; Gröning, M.; König, K.; Torralba, G.; Hausmann, M.; Lindenstruth, V.; Nesterov, A.; Block, I.; Pipkorn, R.; Poustka, A.; Bischoff, F. R.; Breitling, F. Combinatorial Synthesis of Peptide Arrays with a Laser Printer. *Angewandte Chemie International Edition* **2008**, *47* (37), 7132–7135. https://doi.org/https://doi.org/10.1002/anie.200801616.

(209) Loeffler, F.; Schirwitz, C.; Wagner, J.; Koenig, K.; Maerkle, F.; Torralba, G.; Hausmann, M.; Bischoff, F. R.; Nesterov-Mueller, A.; Breitling, F. Biomolecule Arrays Using Functional Combinatorial Particle

Patterning on Microchips. *Adv Funct Mater* **2012**, *22* (12), 2503–2508. https://doi.org/https://doi.org/10.1002/adfm.201103103.

(210) König, K.; Block, I.; Nesterov, A.; Torralba, G.; Fernandez, S.; Felgenhauer, T.; Leibe, K.; Schirwitz, C.; Löffler, F.; Painke, F.; Wagner, J.; Trunk, U.; Bischoff, F. R.; Breitling, F.; Stadler, V.; Hausmann, M.; Lindenstruth, V. Programmable High Voltage CMOS Chips for Particle-Based High-Density Combinatorial Peptide Synthesis. *Sens Actuators B Chem* **2010**, *147* (2), 418–427. https://doi.org/https://doi.org/10.1016/j.snb.2009.12.039.

(211) Loeffler, F. F.; Foertsch, T. C.; Popov, R.; Mattes, D. S.; Schlageter, M.; Sedlmayr, M.; Ridder, B.; Dang, F.-X.; von Bojničić-Kninski, C.; Weber, L. K.; Fischer, A.; Greifenstein, J.; Bykovskaya, V.; Buliev, I.; Bischoff, F. R.; Hahn, L.; Meier, M. A. R.; Bräse, S.; Powell, A. K.; Balaban, T. S.; Breitling, F.; Nesterov-Mueller, A. High-Flexibility Combinatorial Peptide Synthesis with Laser-Based Transfer of Monomers in Solid Matrix Material. *Nat Commun* **2016**, *7* (1), 11844. https://doi.org/10.1038/ncomms11844.

(212) Popov, R.; Shankara, G. K.; von Bojnicic-Kninski, C.; Barua, P.; Mattes, D.; Breitling, F.; Nesterov-Mueller, A. Stochastic Deposition of Amino Acids into Microcavities via Microparticles. *Sci Rep* **2019**, *9* (1), 16468. https://doi.org/10.1038/s41598-019-52994-w.

(213) Ridder, B.; Mattes, D. S.; Nesterov-Mueller, A.; Breitling, F.; Meier, M. A. R. Peptide Array Functionalization via the Ugi Four-Component Reaction. *Chem. Commun.* **2017**, *53* (40), 5553–5556. https://doi.org/10.1039/C7CC01945A.

(214) Roberts, K. D.; Lambert, J. N.; Ede, N. J.; Bray, A. M. Efficient Synthesis of Thioether-Based Cyclic Peptide Libraries. *Tetrahedron Lett* **1998**, *39* (45), 8357–8360. https://doi.org/https://doi.org/10.1016/S0040-4039(98)01843-7.

(215) Mattes, Daniela. S.; Streit, B.; Bhandari, D. R.; Greifenstein, J.; Foertsch, T. C.; Münch, S. W.; Ridder, B.; v. Bojničić-Kninski, C.; Nesterov-Mueller, A.; Spengler, B.; Schepers, U.; Bräse, S.; Loeffler, F. F.; Breitling, F. Combinatorial Synthesis of Peptoid Arrays via Laser-Based Stacking of Multiple Polymer Nanolayers. *Macromol Rapid Commun* **2019**, *40* (6), 1800533. https://doi.org/https://doi.org/10.1002/marc.201800533.

(216) Muenster, B.; Welle, A.; Ridder, B.; Althuon, D.; Striffler, J.; Foertsch, T. C.; Hahn, L.; Thelen, R.; Stadler, V.; Nesterov-Mueller, A.; Breitling, F.; Loeffler, F. F. Solid-Material-Based Coupling Efficiency Analyzed with Time-of-Flight Secondary Ion Mass Spectrometry. *Appl Surf Sci* **2016**, *360*, 306–314. https://doi.org/https://doi.org/10.1016/j.apsusc.2015.10.223.

(217) Lhoest, J.-B.; Wagner, M. S.; Tidwell, C. D.; Castner, D. G. Characterization of Adsorbed Protein Films by Time of Flight Secondary Ion Mass Spectrometry. *J Biomed Mater Res* **2001**, *57* (3), 432–440. https://doi.org/https://doi.org/10.1002/1097-4636(20011205)57:3<432::AID-JBM1186>3.0.CO;2-G.

(218) Schmidt, D.; Maier, J.; Bernauer, H.; Nesterov-Mueller, A. Label-Free Imaging of Solid-Phase Peptide Synthesis Products and Their Modifications Tethered in Microspots Using Time-of-Flight Secondary Ion Mass Spectrometry. *Int J Mol Sci* **2023**, *24* (21). https://doi.org/10.3390/ijms242115945.